Chapter 1

Introduction

This thesis presents an investigation into the mechanisms of Auroral Kilometric Radiation (AKR) that occurs naturally in the polar regions of the Earth's magnetosphere. AKR is a non-thermal radio emission of very high intensity that is generated by the Earth's auroral zone. This chapter explains key features of this emission along with details of satellite missions that have detected and measured it. This chapter ends with an outline of previous research conducted at the University of Strathclyde and research pursued in this thesis.

1.1 Auroral Kilometric Radiation (AKR) and astrophysical sources of cyclotron radiation

Kilometre band radiation from the terrestrial magnetosphere is a phenomenon that has attracted significant scientific interest for over thirty years. The phenomenon has led to several theories being produced based on a range of plasma dynamics many of which at least in part conflict with each other. Terrestrial Kilometric Radiation should be seen in the context of a range of astrophysical radio sources which have been observed by radio astronomers over a broad spectral range in recent years [Labelle & Treumann 2002]. As the kilometre band signals from the Earth were observed to be associated with the polar regions they are called Auroral Kilometric Radiation (AKR), Figure 1.1.

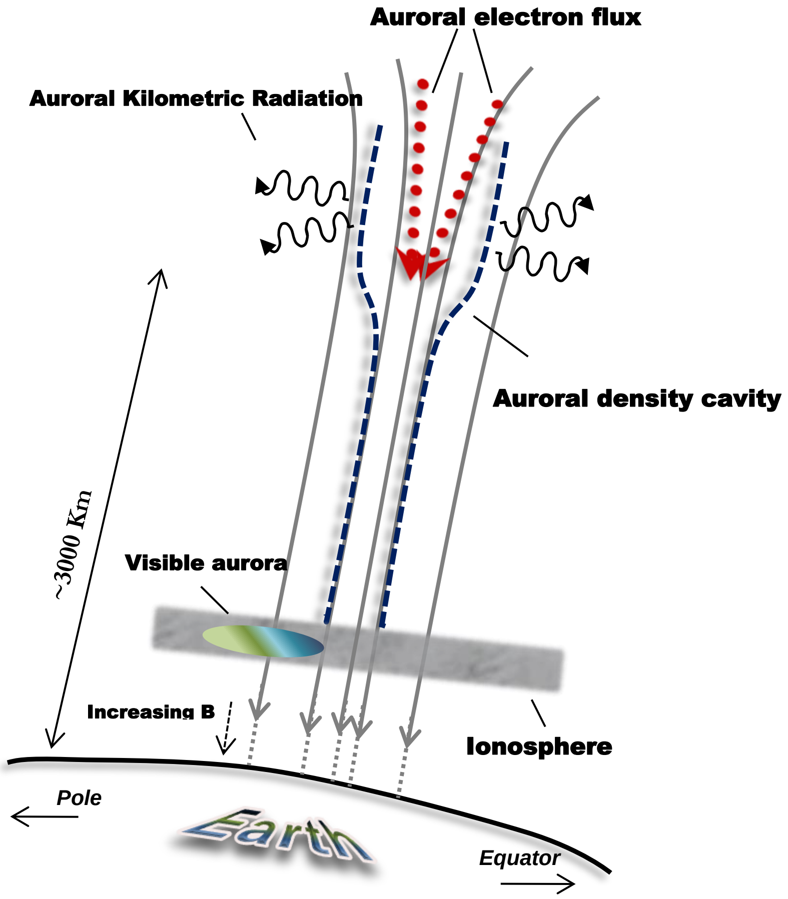

Figure 1.1: Representation of the AKR source region and terrestrial auroral process and the production of visible aurora as the electrons enter the ionosphere.

AKR was first observed as being extra-terrestrial noise of frequency around 1MHz by Beneditkov [Beneditkov et al. 1965]. The emission properties were later characterized in the mid 1970's through to the early 1980's by D.A. Gurnett and colleagues. Gurnett showed that the peak power emitted in AKR was ~10^9 W, about 1% of the total power arriving into the magnetosphere as auroral electron precipitation and centred around a frequency of ~300kHz, this data was collected by the IMP-6 and IMP-8 satellites [Gurnett 1974]. It is sourced at high altitudes (~3,000km - ~13,000km) within a large region of plasma depletion in the auroral zone known as the auroral density cavity [Benson 1985]. AKR is not readily observed on the ground as the radiation intensity peaks at several hundred kilohertz, and due to ionospheric shielding is normally observed by distant satellites equipped with suitable receivers [Benson & Calvert 1979][Bujarbarua et al. 1984**a**] [Schreiber 2005].

AKR occurs when electrons in the Earth's magnetosphere, sourced from the solar wind, are accelerated towards the Earth's ionosphere into the auroral zone. As the field aligned electron beam is accelerated towards the auroral zone it is subject to a magnetic compression, this will result in a 'horse-shoe' shaped velocity distribution of the electrons. The horseshoe shape arises from conservation of the magnetic moment, which causes an increase in their pitch angle. This produces a broad region on the distribution function where $\partial f_e / \partial v_\perp > 0$.

Measurements of AKR show that emissions are mainly polarised in the X plasma mode (extraordinary mode), meaning it is polarised and propagating perpendicular to the static magnetic field, and it is emitted at a frequency close to the cyclotron frequency (see theory section 1.1.1). This was identified in 1978 and noted by Kaiser et al. from data collected from Voyager 1 and 2 probes [Parrot et al. 2001] [Benson 1985] [Kaiser et al. 1978]. In 1979 the polarisation was confirmed by Benson and Calvert [Benson & Calvert 1979] using the data from the ISIS 1 satellite's swept frequency receiver. Then in 1981 the AKR source region was mapped out by Calvert [Calvert 1981].

Twiss proposed an explanation for the creation of solar radio bursts through his theory of electron cyclotron maser emissions. Twiss was one of the first scientists to produce theory in this area. In his theory he showed that in order for negative cyclotron absorption to arise at radio wavelengths (when the medium behaves like an amplifier to incident radiation) there is a need for the radiating electrons to have a kinetic energy distribution that is non-thermal, with an excess of high energy electrons such that the differential of the near-resonant electron density with respect to the kinetic energy of the electrons is positive. This theory of negative absorption, occurring due to electrons that undergo cyclotron motion, was a key contribution and the first description of coherent cyclotron emission spawning a wide range of astro and applied physics [Twiss 1958].

Numerous theories have been proposed for the mechanism of Auroral Kilometric Radiation [Melrose et al. 1982] [Melrose 2008] [Melrose et al. 1984] [Cole & Pokhotelov 1980]. The general consensus to date of the agreed mechanism for generating AKR is a collective coherent electron cyclotron maser instability similar to the proposal of Twiss [Vorgul et al. 2011]. This particular model was first proposed by Wu and Lee, in their theory they concluded that it was the ascending electrons that were responsible for the induced radiation emissions [Wu & Lee 1998]. The instability was predicted from plasma kinetic theory that resulted in a dispersion relation that indicated unstable growth of the R-X mode due to a positive gradient in the transverse velocity profile of the electron velocity space distribution function ($\partial f_e / \partial v_\perp > 0$). One condition for unstable growth is that the plasma frequency, ω_{pe} must be much less than the cyclotron frequency, ω_{ce}, this condition is met in the auroral density cavity [Ergun et al. 2000].

The ascending electron flux is formed by the portion of the precipitating auroral electron flux that gets magnetically mirrored by the convergent magnetic field in the auroral zone. The fraction having low initial $v_\perp$ is not mirrored and reaches the ionosphere where it is absorbed; this area of the velocity space is called the loss cone. The mirrored flux would thus have fewer electrons in the low pitch region of the distribution and might be expected to radiate more effectively. It was the proposal of Wu and Lee that resulted in the electron cyclotron-maser instability becoming the established theory of the mechanism for AKR. Also for a considerable time, the accepted theory was that the so called loss cone distribution in the mirrored flux provided the source of free energy for driving the instability [Zieball & Yoon 1995].

Satellite data from the auroral density cavity illustrated the absence of the “loss cone” particles in the ascending distribution, however it was never considered as being a strong feature of the data. Several published papers illustrated a clear representation of the electron horseshoe distribution in the descending flux [Delory et al. 1998] [Ergun et al. 2000] [Ungstrup et al. 1990] which appear as a strong, reproducible, feature in the same region as the AKR emission. A new theory was published by Bingham and Cairns [Bingham & Cairns 2000] which considered R-X mode dispersion and growth due to a horseshoe shaped velocity distribution in the Earth bound accelerated flux. The proposal by Bingham and Cairns is related to the previous model by Wu and Lee. It is a cyclotron resonant effect, however it realises the potential for radiation growth without requiring the elimination of the low pitch component of the beam current (as Wu and Lee achieved by invoking the loss cone and considering the mirrored flux). Instead, the theory recognises that the instability may be driven by the much more readily observed and much higher power descending flux providing that there exists a region of positive gradient of the particle distribution function in velocity space.

Auroral Kilometric Radiation is currently of particular interest as similar non-thermal radio emissions are known to originate from certain types of stars and other magnetised astrophysical objects which makes terrestrial Auroral Kilometric Radiation of wider interest to astronomers and astrophysicists [Melrose and Dulk 1982]. Examples include Jupiter [Oya 1974] and Saturn [Lamy et al. 2008]. Recent observations of the flare star UV-Ceti [Bingham & Cairns 2000] have revealed intense, 100% circularly polarised radiation originating from the polar regions of the star. This radiation has been observed at frequencies in the range of 5GHz – 15GHz and it has been proposed that the emission mechanism responsible for the kilometric and decametric planetary auroral radio emission may also be responsible for the UV-Ceti emission at centimetre wavelength [Bingham et al. 2001]. Understanding the emission mechanism responsible for terrestrial AKR therefore has wider significance.

Extensive observation continue to add to the connection of the AKR phenomenon to the magnetosphere environment. Auroral Kilometric Radio emissions have been observed to exhibit intense bursts of this radio emission [Mutel 2004] in a very wide wavelength range. Here the high magnetic field strength and a rather low density of cold plasma make it possible for hectometric emission bursts to arise. Short hectometric bursts were sometimes observed at frequencies of 1540kHz and 2160kHz [Yi-Juin et al. 2008] this was observed from the Prognoz 8 satellite. Bursts of hectometric auroral emission at frequencies of 992kHz and 1486kHz were observed on-board the Prognoz-10 satellite during the solar activity minimum period in April-November 1985. The appearance of short hectometric events is however a rare phenomenon. For more than five years of continuous observations no more than fifty such events were recorded in total. This is partly because of specific features of the orbital motion of the satellite (the orbit position in the northern hemisphere at comparatively low initial latitudes with gradual displacement of the orbit toward the Earth's equator by 2000) the hectometric events have been recorded only at orbital perigees (the point of lowest altitude when in orbit) close to the Earth.

The hectometric emission events were observed in the auroral regions of the corresponding hemispheres predominantly in the months of the autumn-winter season. In the Northern hemisphere they were completely absent, for example, in spring and summer from April till September. This did not exclude the presence of intense auroral emission in the kilometric wavelength range at that time. Unlike AKR emissions which can often occur nearly continuously for a long time, up to ten hours and longer, at the frequencies of the hectometric wave range this emission is highly sporadic [Kuril'chik 2007].

AKR has been studied and analysed in great depth [Poezd et al. 1987] [Kurth et al. 1975][Green et al. 1977][Imhof et al. 1999][Morgan et al. 2000] [Kurth & Gurnett 1998], by utilising various satellites many of its characteristics have been determined [Schreiber et al. 2002]. Through statistical analyses of observation data from the Akebono satellite [Kumamoto & Oya 1998] some recent studies of auroral phenomena have shown seasonal variations in AKR sources and precipitating auroral particles [Collin et al. 1998][Kumamoto et al. 2005].

A seasonal variation in AKR has also been identified in the distant magnetotail using data obtained by the GEOTAIL spacecraft [Kasaba et al. 1997]. As a control mechanism for the seasonal variation in auroral electrons, the conductivity of the ionosphere is thought to change the resonance conditions of the field aligned AC currents. Analysis of the seasonal variations in AKR suggest that up-welling plasma from the summer ionosphere hinders or violates the generation conditions required for the cyclotron maser instability. As previously noted the cyclotron maser model for AKR is associated with a cold and tenuous plasma, however the data obtained by the Akebono satellite show that AKR sources can be observed even in regions of relatively high-density plasma, $\omega_p/\omega_{ce}>0.5$ [Kumamoto et al. 2001][Atmospheric electrodynamics Vol II].

High resolution wave spectrograms provided by Polar (plasma wave investigation) electric field observations have shown some dynamical behaviour of AKR. The observations have revealed the existence of two AKR sources. A low-altitude AKR source appears prior to and during a substorm, a short magnetospheric disturbance (see theory section 1.4), over a rather narrow altitude range (4,000km to 6,000km in altitude). While a high-altitude AKR source suddenly appears with intense power at the substorm onset along a wider altitude range (6,000km to 12,000km in altitude) above the pre-existing low altitude AKR source. The existence of two AKR sources suggests the existence of two types of field-aligned accelerations in the M-1 coupling region during a substorm. Data from the FAST (Fast Auroral Snapshot Explorer) satellite suggested that the parallel electric fields are concentrated in at least two locations at high-altitude $E_{//}$ near ~1 R_E and low altitude $E_{//}$ between ~2,000km and ~5,000km along the magnetic field lines.

Morioka studied the phenomena of AKR breakup, an intensification of both low and high altitude AKR, defined in the particular study here as the explosive development of a high-altitude AKR source at the time of an auroral breakup. This suggests the abrupt formation of an acceleration region above a pre-existing and fairly stable low-altitude acceleration region. AKR breakups are usually preceded within 1-3 minutes by the appearance and/or gradual enhancement of low-altitude AKR, which suggests that low altitude acceleration is a necessary condition for the ignition of high-altitude bursty acceleration. They always accompany a full substorm.

1.1.1 AKR and other wave polarisation and propagation properties in the magnetosphere

The plasma in the magnetosphere is normally considered to be a cold and weakly ionised gas within the Earth's magnetic field. The plasma in the AKR source region, the auroral density cavity, is colder and more tenuous than the surrounding plasma. In this geophysical plasma the dynamics are significantly influenced by the Earth's magnetic field. Cold plasma theory shows that at high frequencies there are two characteristic electromagnetic wave modes that can propagate perpendicular to the B-field in a magnetoplasma. They are often referred to as the free-space ordinary (O) and extraordinary (X) modes. The X-mode means the wave is polarised and propagating perpendicular to the static magnetic field whereas the O-mode is polarised parallel and propagates perpendicular to the static magnetic field [Helliwell 2001].

The X-mode has several branches, one is the free space mode, whilst it also has a slow branch mode. The slow branch mode is so called because it is restricted to propagation velocities less than the vacuum speed of light, this is sometimes called the Z-mode [Benson et al. 2006]. It is a trapped mode of the plasma confined in frequency between the cut-off frequency f_L and the upper hybrid frequency f_{UH}.

Another mode of interest is the W, whistler, mode. Whistlers are triggered by lightning flashes, they travel along the Earth's dipole field and occur below the upper hybrid/R resonance. They are so called because they propagate in the ionosphere at audio-frequencies which can be heard, on a suitable receiver, as a whistle of descending pitch. The group velocity is a strong progressive function of frequency and therefore a wideband instantaneous signal spreads into a chirped note, i.e. in the initial pulse containing a spread of frequencies the high frequency waves travel faster arriving earlier at the detection point than the lower frequency waves and so a whistle of descending pitch is heard. The dispersion diagrams for electromagnetic wave propagation are explained in section 2.3.5. Figure 1.2 and Figure 1.3 illustrate these dispersions for X, O, Z, R and L modes.

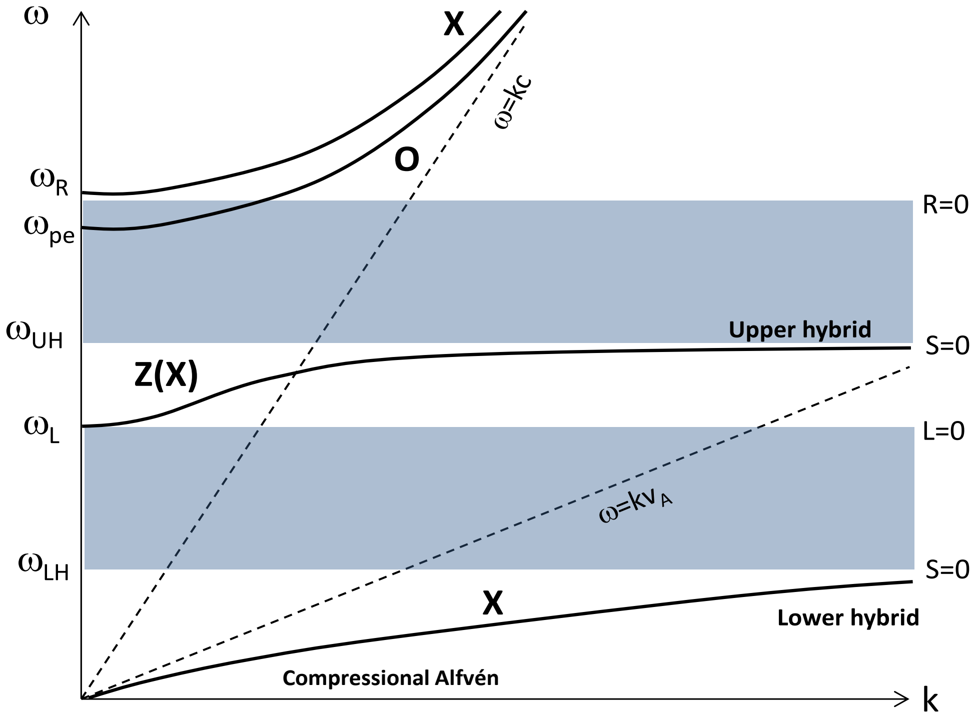

Figure 1.2: Dispersion diagrams for wave propagation, $k_\perp B$, showing the X, O & Z branches.

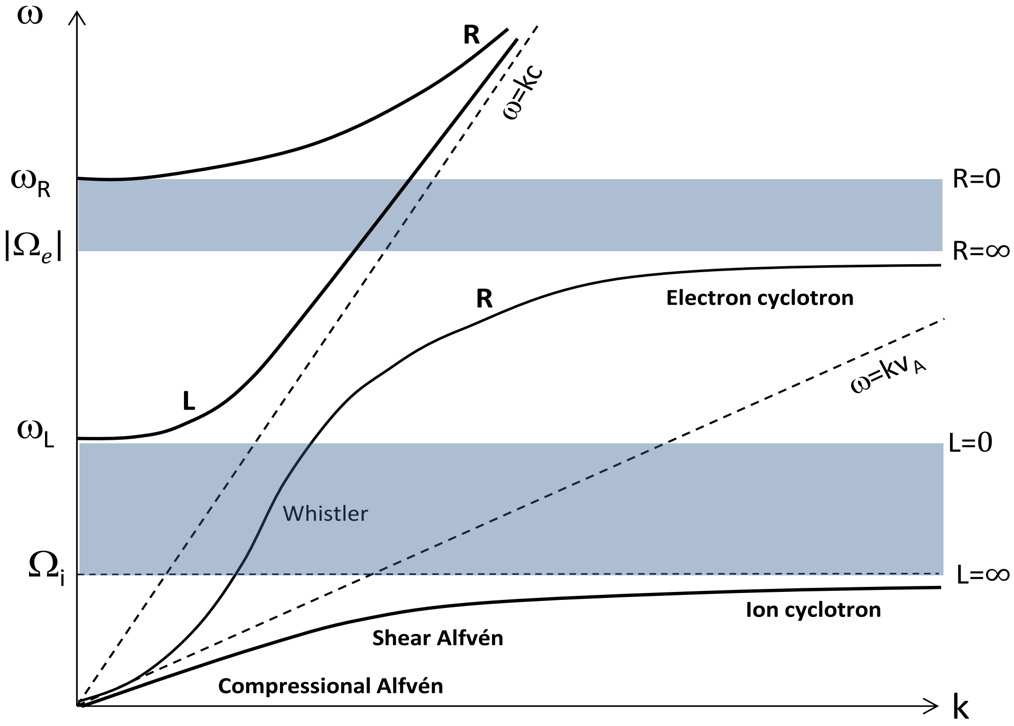

Figure 1.3: Dispersion diagrams for wave propagation, $k_{//}$ B, showing the R & L branches.

1.2 Satellite observations of AKR source regions

Progressively enhanced data collected by satellites, since the late 1960's, have provided invaluable information to inform the scientific analysis. Due to the higher temporal and spatial resolution the source region could be fully resolved which in turn allowed for new features of the AKR source region to be measured. Further research into this data has revealed areas with trapped electrons near the edge of the density cavity [Roux et al. 1993], and that the strongest AKR emissions occur in the density-depleted cavities that extend 30km to 300km in latitude [Ergun et al. 1998] [Louarn & Le Queau 1996]. Study of the source region densities have shown that there are some regions that are dominated by >100eV electrons. The abundance of hot and cold electrons is an important factor in the generation of AKR as hot electrons introduce relativistic modifications to the wave dispersion [Strangeway et al. 1998].

Data from satellites have indicated that for a given altitude the AKR emissions extend in frequency down to a lower limit of approximately the local relativistic electron-cyclotron frequency. The "Hawkeye" satellite was used by the University of Iowa for density measurements within the auroral plasma cavity i.e. the AKR source region. Although not originally equipped for plasma density measurements, estimates of the density were possible exploiting the natural wave signals it receives. Hawkeye showed a region of plasma depletion up to 100km wide and 8,000km long where densities are as low as 1cm^{-3}, equating to a plasma frequency of 9kHz which is much less than the electron cyclotron frequency $f_{ce} \sim 10^2$kHz. Other satellite missions have also collected data about the AKR source region mainly Viking and Cluster.

The Viking spacecraft has allowed for numerous observations to be performed inside and near the sources of Auroral Kilometric Radiation [Louarn et al. 1990] [Perraut et al. 1990][Ungstrup et al. 1990][Louarn & Le Queau 1996**a**]. Viking collected data during ~50 AKR source region crossings in the altitude range between 4,000km and 9,000km. Results revealed that the frequency peak is close to the gyrofrequency and that the lower cut-off frequency is on average at the gyrofrequency and confirms that in the source region the density is typically less than 1.5cm^{-3}. This is the order of the density of hot electrons illustrative that the Auroral

Kilometric Radiation is generated in thin source regions where the plasma is hot and tenuous, very different from the surrounding colder and denser plasma. It has been shown that these thin regions (with a transverse width of a few kilometres) correspond to the acceleration structures associated with discrete auroral arcs [Saflekos et al. 1989][Moen et al. 1998]. Due to the high electron energy present inside the AKR source region, relativistic effects should be taken into account in the study of the beam dispersion. Such effects can strongly modify the beam–wave coupling. One of the important consequences of this is that, in the presence of positive $\partial f / \partial v_\perp$ slopes in the electron distribution function an instability can develop and lead to an amplification of electromagnetic waves. It is generally accepted that this instability is the generation mechanism of AKR [Louarn et al. 1990**b**][Roux et al. 1993][Bujarbarua et al. 1984**b**].

Some of the best and most recent data comes from the FAST auroral snapshot satellite, yielding numerous high time and frequency resolution measurements of the AKR region. FAST was launched in August 1996 and was inserted into a polar orbit with an altitude range of 350km to 4200km above the Earth and carries instruments to measure energetic electrons and ions, electric fields, and magnetic fields above the Earth's auroral zones, Figure 1.4. As a direct result of the FAST mission, several features of the AKR source region were noted [Delory et al. 1998][Sato et al. 2002][Strangeway et al. 1998][Yi-Jiun et al. 2008][Ergun et al. 1998][Sigsbee et al. 1998]. Strong temporal variations were observed in the AKR emissions with every source crossing of the FAST satellite. Rather than extending across the entire auroral density cavity the strongest emissions were often observed to be at the edge of a small region in the density cavity and typically appeared in bursts <1s in duration [Menietti et al. 2006**b**][Benson 1984].

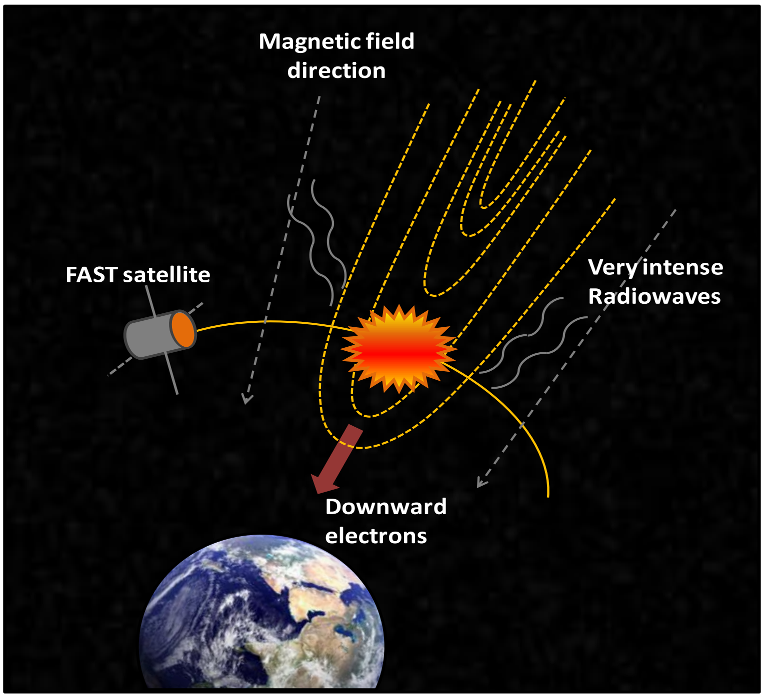

Figure 1.4**:** Orbit of FAST satellite crossing the AKR region.

The four Cluster [Aikio et al. 2004][Gurnett et al. 2001][Pickett et al. 2010][Pickett et al. 2008] spacecraft passed over Northern Scandinavia on 6 February 2001 from South-East to North-West at a radial distance of ~4.4 Earth's radii in the post-midnight sector. When mapped along geomagnetic field lines, the separation of the spacecraft in the magnetosphere was 110km in latitude and 50km in longitude. This constellation allowed the study of the temporal evolution of plasma with a time scale of a few minutes. The main findings from Cluster were that the auroral arcs, which describes the aurora as a simple curving arc of light across the sky, were located close to the equator-ward and pole-ward edge of a large-scale density cavity [Gurnett et al. 2001][Mutel et al. 2008][Mutel 2006][Mellott et al. 1988][Yoon & Weatherwax 1998]. Cluster has identified over 6,000 individual Auroral Kilometric Radiation bursts between 2002 and 2003 [Pickett et al. 2008]. Burst locations were determined by triangulation using differential delays from cross-correlated wideband (WBD) radio waveforms. The WBD instrument used for these measurements consisted of four identical receiving antenna systems [Aikio et al. 2004][Mutel et al. 2000].

Another satellite which took data from the auroral zone is the Swedish Freja satellite which was launched in October 1992 for investigations of auroral plasma physics and fine scale auroral processes [Zanetti et al. 1994]. The Freja orbit was at an inclination of 63 degrees, which is unusually small for a spacecraft dedicated to the aurora, but due to the offset of the Earth's magnetic field from the geographic pole, latitudes above 70 degrees were regularly achieved with occasional excursions up to 77 degrees. Frejas small inclination proved useful for auroral studies, as it skimmed the auroral oval in the West-East direction for extended time intervals, rather than getting the brief North-South crossings achieved by the polar orbits conventional for satellites investigating auroral physics [Eriksson & Wahlund 2006][Marklund 1997].

The International Satellites for Ionospheric Studies (ISIS I and II launched in January 1969 and April 1971 respectively) were the third and fourth satellites launched in a series of Canadian missions to investigate the ionosphere. Observations from these satellites have informed the study of harmonic AKR emissions and emission polarisation [Hosotani et al. 2003]. Harmonic signals are observed to be associated with X-mode and O-mode AKR (see theory section 1.1.1). The 2nd harmonic X-mode AKR observations are consistent with a propagating signal whereas the 3rd and 4th harmonics are likely to be heavily damped signals that do not propagate far from their low density source region. 2nd harmonic signals observed in the O-mode are more often observed at frequencies below 2 ω_{ce} when ω_p/ω_{ce} is small and above 2 ω_{ce} when it is large [Benson 1984].

The second harmonic wave properties of AKR were also examined using the previously mentioned Akebono satellite. The analysis of the data indicated that the probability of harmonic emission being observed was 60% of all AKR events. The fundamental signals sometimes reveal a component structure. The frequency separation between these components is far greater than predicted frequency differences between any two spatially co-incident fundamental growth bands in the Doppler shifted cyclotron mechanism and it is probably due to the two signals having spatially separate source regions. The main points to note concerning the X-mode AKR emissions are that the high order (>3rd) X-mode harmonics may have a moderate intensity providing ω_p/ω_{ce} is sufficiently small (~0.1), whereas the harmonic intensities are much weaker at higher ω_p/ω_{ce} ratios [Benson 1984].

Referring to section 1.1.1 for the theoretical dispersion of the X,O,W and L modes, observations from the ISIS satellites have shown strong AKR is commonly observed in the X-mode when $\omega_p/\omega_{ce} < 0.3$, but rarely in the O-mode and never in the Z-mode or W-mode. Moderate strength AKR is observed in the X-mode out to $\omega_p/\omega_{ce} \sim 1.0$; it is occasionally observed in the Z-mode but never in the W-mode. Weak AKR is observed in the X-mode and O-modes out to $\omega_p/\omega_{ce} > 1.1$, in the Z-mode over nearly all ω_p/ω_{ce} sampled and in the W mode when $\omega_p/\omega_{ce} > 0.6$. There is some evidence that the W-mode is stronger at lower altitudes [Benson & Calvert 1979]. Figure 1.5 illustrates the ISIS projected AKR X-mode and O-mode source region (ω_p/ω_{ce}) values compared with theoretical normalized maximum temporal growth rates [Omidi et al. 1984].

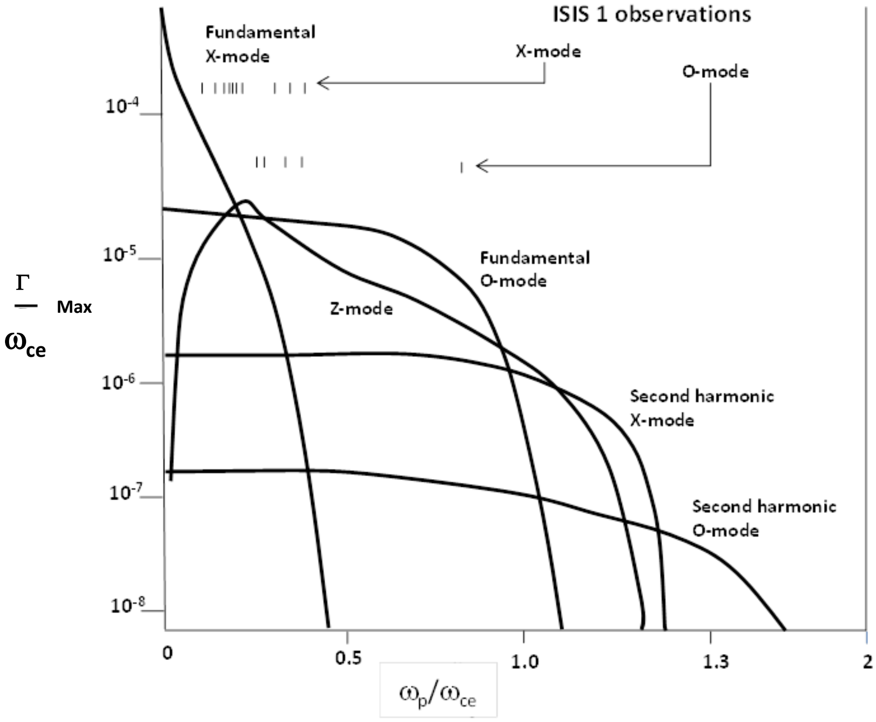

Figure 1.5**:** Predicated normalised growth rates for X, O, Z mode cyclotron emissions for the range of (ω_p/ω_{ce}) mapped by ISIS.

Fine structure patterns have been identified with intense R-X mode AKR. Data collected from the ISEE 1 & 2 illustrated that AKR consisted of many discrete narrow-band (<1kHz line width) emissions. Debate has arisen over the mechanism for these structures, from disturbances along the magnetic field lines to it being a natural consequence of the feedback model. Fine structure has also been observed by the Dynamics Explorer 1 satellite in the L-O mode. It has been suggested that any L-O mode AKR would be produced as a by-product of intense R-X mode AKR due to a polarization mismatch at the source boundary. Very narrowband, negative drifting patterns have been identified in ~6% of the high-resolution wideband spectrograms of L-O mode signals when X-mode AKR is present. The fine structure in the L-O mode AKR has important bearing on the theoretical interpretation of AKR. In the cyclotron maser mechanism, R-X mode AKR dominates over the L-O mode only in a low density plasma. From the point of view of the cyclotron maser mechanism, the question is whether the L-O mode revealing fine structures is the result of a direct generation from relatively high plasma density regions or an R-X to L-O mode conversion at the boundary of a low density region [Grabbe et al. 1982][Menietti et al. 2006**a**][Shepherd et al. 1998][Menietti et al. 2000][Morozova et al. 2002][Pottelette et al. 2001].

1.3 The terrestrial auroral lights

The phenomenon most commonly associated with the terrestrial auroral regions [Lysak & Andre 2001] are the optical ionospheric emissions known as the “Aurora Borealis” in the northern hemisphere (or the northern lights) and in the southern counterpart named “Aurora Australis”. Aurora are a natural phenomena that occur mostly in the polar regions of the Earth. It presents a complex behaviour that arises from interactions between plasma and the Earth’s electromagnetic fields [Andre 1997][Pazamickas et al. 2005][Huff et al. 1988]. It takes the form of colourful irregular lights in the night sky, caused by excitation of atmospheric oxygen and nitrogen, with no two Aurora ever being the same.

One of the terms used to describe the Aurora is the “Arc” (which describes the Aurora as a simple curving arc of light across the sky). Another term is “band” which refers to Aurora that have an irregular shape with kinks or folds. In the striking image in Figure 1.6**a**, the aurora was taken during a geomagnetic storm from the International Space Station (ISS). Figure 1.6**b** was also taken from the ISS also illustrating the green aurora. Aurora occur most often in regions known as the “Auroral oval” rings roughly 2,400km around the Earth’s North and South geomagnetic poles, Figure 1.7.

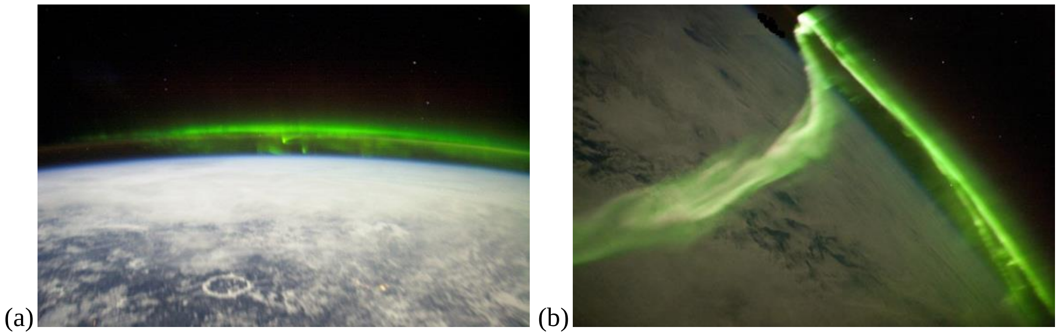

Figure 1.6**:** (a) Image of the aurora taken during a geomagnetic storm from International Space Station (ISS) (b) Aurora above the Earth taken from the ISS illustrating the green aurora [NASA space agency].

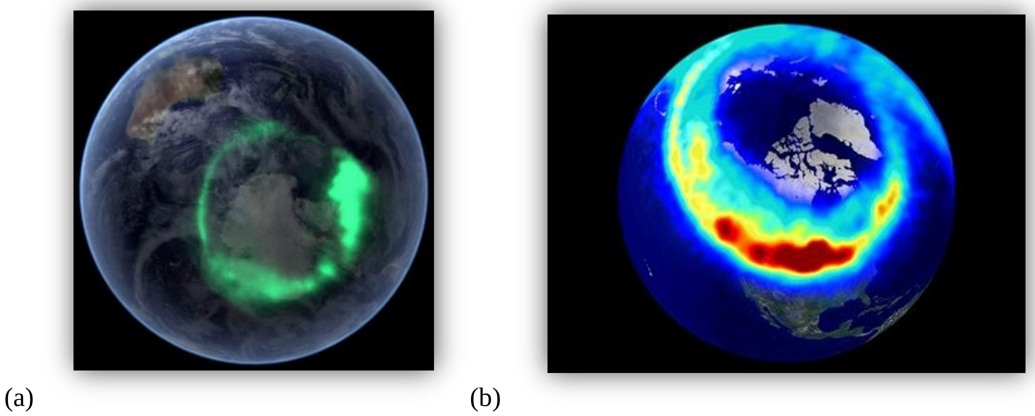

Figure 1.7**:** Illustration of auroral arcs (a) Aurora Australis captured by NASA’s IMAGE satellite, (b) Image taken from Cluster satellite [NASA space agency].

These ovals are constantly in motion and changing in brightness, moving by either expanding towards the equator or contracting towards the pole, due to the effect of solar wind. The Aurora are a product of the same accelerated electrons that cause AKR. As previously described some of the electrons form a loss cone which penetrates the Earth’s ionosphere exciting the atoms and molecules which decay resulting in visible aurora. It was noticed that there are gaps in normal bright aurora which are frequently recorded but rarely questioned. Recent research using data from four Cluster spacecraft orbiting the Earth has now suggested that these effects are black aurora which are actually anti-auroras. In black anti-auroras negatively charged particles are sucked out from the Earth's ionosphere along adjoining magnetic field lines. These dark anti-auroras can climb to over 20,000km and last for several minutes. Refer to Appendix 1 for extended detail.

1.4 The magnetosphere and the magnetotail

A magnetosphere is that area of space, around a planet, that is controlled by the planet's magnetic field, Figure 1.8. The shape of the Earth's magnetosphere is distorted as a direct result of being impacted by the solar wind. The solar wind creates an asymmetry in the noon-midnight meridian plane and flows around the planet enclosing its field in a cavity, it is this cavity we call the magnetosphere. The Earth's magnetosphere is a highly dynamic structure that responds dramatically to solar variations.

A substorm, is a short magnetospheric disturbance that occurs when the interplanetary magnetic field turns Southward which permits interplanetary and terrestrial magnetic field lines to merge at the dayside magnetopause and energy to be transferred from the solar wind to the magnetosphere. It is these substorms that are regarded as the dominant dynamical process of the magnetosphere.

The magnetosphere is compressed on the day-side by the pressure of the solar wind and stretches out on the night-side in a magnetotail [Meng 2001], this boundary of the magnetosphere is called the magnetopause. Energetic particles can be trapped in closed orbits within the Van Allen belts located in the magnetosphere [Morioka et al. 2008][Menietti 2008].

Another boundary which lies beyond the magnetopause is the magnetosheath, this is the region between the bow shock and the magnetopause. The magnetosheath is defined by the fact that the solar wind speed is greater than the fast magnetosonic wave speed. At the bow shock the plasma in the solar wind is slowed, compressed and heated. It then partly flows into the magnetosheath and partly around the magnetosheath.

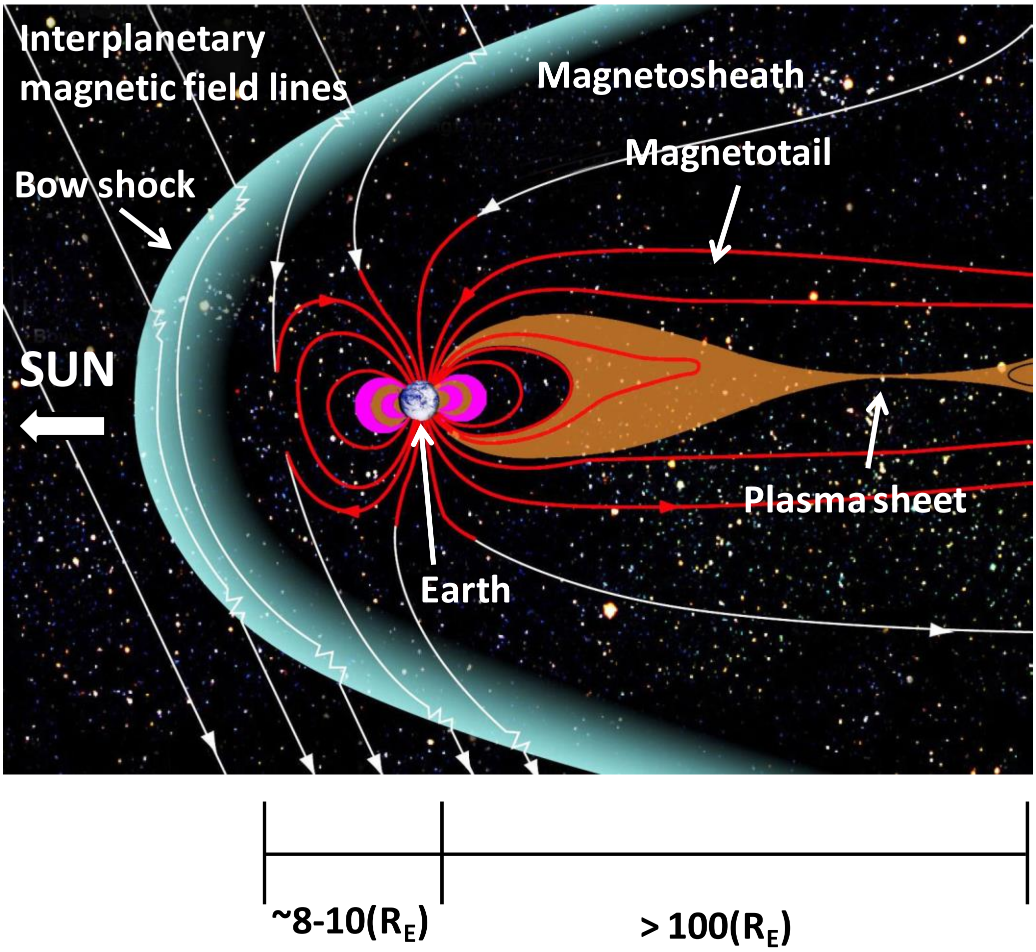

Figure 1.8**:** Illustration of the Earth's magnetosphere; an area of space around a planet where the plasma dynamics are controlled by the planet's magnetic field [NASA space agency].

1.5 Principles of a scaled laboratory experimental reproduction

Investigation into Auroral Kilometric Radiation at the University of Strathclyde has been primarily an experimental and numerical research programme, in collaboration with both the University of St Andrews, which led the theoretical analysis and the Rutherford Appleton Laboratory (RAL) which led the observational studies and participated in the theoretical and numerical work. It was possible to replicate important aspects of the dynamics of the source region of AKR emission in a controlled laboratory experiment, to reproduce major features of the natural phenomena, since the vital parameters in the theoretical model scale with ω_{ce}. Results from the experiment can be compared to the natural phenomena, numerical simulations and theoretical predications considerably enhancing the understanding of the cyclotron emission mechanisms. The interaction region in the magnetosphere is ~9,000km long and the frequencies of emissions are 10’s - 100’s kHz, since the dynamics of the instability scales as ω_p/ω_{ce} [Bingham and Cairns 2000] the experiment was scaled to laboratory dimensions by increasing the magnetic flux density, resulting in the experiment being ~1-2m length with frequencies in the GHz range.

In the auroral density cavity (within the Earth's magnetosphere) it has been hypothesised that there is an effective boundary which occurs when the plasma frequency exceeds the cyclotron frequency, causing the waves to 'reflect' back into the auroral density cavity, potentially providing a feedback mechanism for the instability providing a boundary similar to the metal wall of a waveguide. The mechanisms for the formation of this density cavity are a subject of current debate. The AKR emissions are observed to be predominantly polarised in the X-mode. This implies a Doppler term near zero for the resonance which in turn allows for strong coupling between the wave and the beam even in the case of large velocity spread.

In waveguides, Chapter 2, the propagation and polarisation properties of the plasma X-mode are best approximated by near to cut off TE modes (transverse electric) of a waveguide aligned with a static bias magnetic field. These propagate and are polarised perpendicularly to the waveguide axis and therefore to the magnetic field, similar to the propagation and polarisation of the X-mode. Conversely near to cut-off

TM (transverse magnetic) modes are close approximations to the O-mode (propagating perpendicular to the magnetic field but polarised parallel to the magnetic field) (see theory section 1.1.1).

The experimental set-up permits control of the beam current and magnetic compression ratio, leading to accurate measurements of the impact of these parameters on the radiation power and frequency which allows direct comparisons to the theoretical predictions and astrophysical data. One of the key aims of this work is to investigate whether there is enough free energy [Louarn et al. 1990] in electron beams formed by magnetic compression to account for the efficiency of radiation emission ~1-2%, as is measured in the magnetosphere.

1.5.1 Previous AKR research at the University of Strathclyde

The earliest experimental work focused on the emissions from the electron beam as it traversed through the system whilst experiencing an increasing magnetic field. The magnetic field plateau in this case was B=0.48T corresponding to a resonant frequency 11.7GHz, coupling to the $TE_{0,3}$ mode of a cylindrical waveguide. At this resonance the apparatus is highly overmoded with a wavelength substantially less than the smallest experimental dimension, this made mode differentiation analysis more difficult than say for a single mode resonance, however the magnetosphere also presents an ill-defined transverse electromagnetic structure [Speirs et al. 2005] [Cairns et al. 2005][Cairns et al. 2011].

Subsequent work focused on more detailed beam characterisation to enhance the understanding of the impact of the electron distribution on the microwave radiation. This was achieved by lowering the resonance frequency to 4.42GHz enabled by coupling to the $TE_{0,1}$ mode. This was done whilst operating with a plateau magnetic field of B=0.18T. The advantage of this modification was that it gave a reserve of additional magnetic field with which to further map the electron distribution [McConville et al. 2008]. Further experiments were carried out to improve comparison to the magnetospheric conditions by introducing a background plasma. This was achieved by design and construction of a ‘Penning type’ trap which was inserted into the interaction region of the experiment. This work was compared with that previously documented by Speirs [Speirs et al. 2005, 2008].

The apparatus was modelled in a 2D computer PiC (particle in cell) programme, KARAT, to enable numerical simulations of the experiment. This meant that as well as comparing results in the laboratory with theoretical predictions and geophysical measurements, a comparison to numerical simulations could also be undertaken. The simulations were also used to aid the design of the experimental apparatus and develop an understanding of its internal dynamics. Predictions from these 2D simulations were in good agreement with experimental results. Simulations were conducted for electron beam energies of 75-85keV, and electron cyclotron frequencies of 4.42GHz and 11.7GHz. At 11.7GHz, beam-wave coupling was predicted with the $TE_{0,3}$ mode and at 4.42GHz excitation of the $TE_{0,1}$ mode was predicted [Speirs et al. 2008]. The predicted RF conversion efficiencies, ~1-3%, were also comparable with the experiment and with estimates for the AKR generation efficiency [Speirs et al. 2008].

1.6 Research pursued in this thesis

This thesis presents a significantly extended investigation into the mechanisms of AKR that occur naturally in the polar regions of the Earth's magnetosphere. The methods used are numerical simulation and scaled experimental reproduction.

Using a time dependent particle in cell (PiC) code (in this case KARAT) it is possible to model various bounded and unbounded interaction geometries for different magnetic field configurations and electron beam parameters. Previous 2D PiC simulations were conducted to study beam transport and electron cyclotron wave coupling within the experimental geometry [Speirs et al. 2006][McConville et al. 2008]. As a significant development of this work, an initial objective was to conduct comparable full 3D PiC simulations to facilitate resolution of cyclotron-wave coupling with transverse electric waveguide modes having an azimuthal field variation/structure. Previous 2D simulations were unable to account for observed mode competition and harmonic coupling in the laboratory experiment. By being able to account for azimuthal structure it was possible to study the diverse radiation modes in the experiments' high magnetic field regime of B=0.48T.

New 2D simulations were conducted to study the role of the electron velocity distribution on the efficiency of the emission. These 2D simulations confirmed the dominant role of the high pitch electrons as free energy source for the AKR emissions.

As the electron velocity distribution had been shown to strongly affect the wave generation, a scheme was developed to inject electrons into the 3D model of the interaction space with a velocity distribution matched to the experimental measurements. This allowed the RF output signal from the experiment to be predicted in terms of its spectrum, output power/Poynting's flux and RF conversion efficiencies along with the excited mode spectrum with a realistic electron beam, these predictions were compared to prior experiments. The impact of the electron distribution was quantified and analysed as a function of electron beam current, electron velocity distribution and cyclotron detuning for resonances with near cut-off

TE modes, representing the expected excitation of X like modes in the magnetosphere.

It was observed in some single mode (geometry was adjusted to allow only one mode to propagate) 3D simulations that there was preference for wave emission in the backwards propagating mode. This was investigated further as it may be important with regard to the direction of wave emission in the magnetosphere, and the ultimate escape of the wave energy from the magnetosphere into space. The predictions from these preliminary simulations led to a combined experimental and 3D experimentally consistent numerical investigation into off perpendicular wave emission, testing the premise that the wave emission would favour backward wave propagation. The experimental investigation encompassed precise mapping of electron velocity space and measurements of the wave generation efficiencies, polarisation and propagation properties as a function of the shift from perpendicular propagation. These parameters were compared to the numerical simulations.

New experiments were also undertaken to test the suggestion that beams like those observed in the magnetosphere may from time to time emit directly into the O-mode whilst the potential for generation in R-X modes at the cyclotron frequency relatively far from perpendicular resonance has been quantified. The experiments determined the output power, spectrum and polarisation of the generated signal as a function of magnetic compression experienced by the beam and the cyclotron detuning for travelling TE (R like) resonances.

Throughout this research, the numerical predictions and experimental measurements were compared with each other and with magnetospheric observations.

Chapter 2

Theory of guided electromagnetic waves, cyclotron electron beams and beam-wave instabilities

In the research described in this thesis, a waveguide is typically used to constrain the transverse structure of the radiation. A waveguide is a structure that supports electromagnetic waves that can travel along its length. Therefore, this chapter discusses the theory of waveguides and electromagnetic waves, beginning with the theory of rectangular and circular waveguides. Following from waveguide theory, it is appropriate to consider the interactions that occur between an axially propagating electron beam undergoing cyclotron motion in a cylindrical waveguide. As mentioned in chapter one the measurements of electron distribution functions within the AKR source region display a characteristic crescent shaped or horseshoe distribution. The theory of the formation of this distribution is explained.

2.1 Electromagnetic (EM) waves

2.1.1 Introduction

The theory of microwaves, the term referring to alternating electomagnetic signals with frequencies between 300MHz and 300GHz, is based on a rich history that extends back to the nineteenth century. The foundations for electromagnetism began as far back as 1831 when Faraday discovered electromagnetic induction continuing through 1864 when Maxwell presented a complete theory of electromagnetism in a fundamental set of equations that predicted electromagnetic waves. The first observation of such waves began with the historic experiments of Heinrich Hertz between the years of 1886–1889 [Vanderlinde 1993].

Hertz work in electromagnetics was first put to practical use with the wireless telegraphy system, the high power pulses of RF energy from the Hertzian Dipole could be formed into a series of dots and dashes of Morse code for the transmitted signal in Marconi’s wireless telegraph system in 1896. By the twentieth century radio broadcasting was replacing wireless telegraphy and with the introduction of continuous wave (CW) microwave signal sources microwave system applications centred on communications. Radar is another important application, since Hertz discovered in 1886 that electromagnetic waves are reflected from solid objects. Applications of this appeared in 1903 when Hulsmeyer in Germany patented a system for detection of obstacles and navigation for ships using reflected radio waves.

At present, the majority of applications of microwave technology are in communications, radar and medical systems. As previously mentioned radar systems are used in the military to locate air, ground and seagoing targets along with missile guidance and fire control. Commercially, radar is used for air traffic control, weather monitoring and distance measurement. Other applications include medical accelerators for patient treatment/diagnostics, particle physics and industrial and scientific heating applications of normal materials and plasmas [Collin 2001].

2.1.2 Maxwell's equations

The foundations of electromagnetic theory were formulated by James Clerk Maxwell, his work was based on a large body of knowledge which was developed by Gauss, Ampère, Faraday and others. Maxwell's equations are a fundamental set of equations of which describe the laws that electromagnetic fields comply with, and are considered one of the most important scientific advances in history. Maxwell's equations are as follows;

$$\nabla \cdot \boldsymbol{D} = \rho_q$$ Gauss's Law

$$\nabla \cdot \mathrm{B} = 0$$ Gauss's Law for magnetic fields

$$\nabla \times \boldsymbol{E} = -\frac{\partial \boldsymbol{B}}{\partial t}$$ Faraday's Law

$$\nabla \times \boldsymbol{H} = \boldsymbol{J} + \frac{\partial \boldsymbol{D}}{\partial t}$$ Ampère-Maxwell Law

where, $\boldsymbol{E}$ *is the electric field,* $\boldsymbol{B}$ *is magnetic field flux density,* $\boldsymbol{D}$ *is electric displacement field,* $\boldsymbol{H}$ *is the magnetic field intensity,* $\boldsymbol{J}$ *is the current density,* ρ_q *is charge density and* t *is time.*

Any electromagnetic field must satisfy all of Maxwell's equations and the constituent equations which account for material properties;

$$\boldsymbol{D} = \varepsilon_0 \varepsilon_r \boldsymbol{E}$$ Equation 2.1

$$\boldsymbol{B} = \mu_0 \mu_r \boldsymbol{H}$$ Equation 2.2

where, ε_0 *is the permittivity of free space,* ε_r *is the permittivity of the medium,* μ_o *is the permeability of free space, and* μ_r *is the permeability of the medium*

2.1.3 Free space propagation

When electromagnetic energy travels in free space it always spreads out. The spreading of electromagnetic energy in free space can be illustrated as follows from Maxwell's equations and the wave equation in a uniform charge free region;

$$\nabla^2 \boldsymbol{D} - \frac{1}{C^2}\frac{\partial^2 \boldsymbol{D}}{\partial^2 t}=0 \qquad \text{Equation 2.3}$$

$$\nabla \cdot \boldsymbol{D} = 0 \qquad \text{Equation 2.4}$$

The general solution for Equation 2.3 that transports energy in a particular direction is given by;

$$\boldsymbol{D}(r,t) = \boldsymbol{F}(\boldsymbol{k}\cdot\boldsymbol{r} - ct) \qquad \text{Equation 2.5}$$

*where **k** is the wave vector and **F** is any function that satisfies the divergence condition*

The general form of an electromagnetic wave that transports energy in the z direction but localised as a beam can be written as;

$$D_i(r,t) = G_i(x,y)F_i(z-ct) \qquad \text{Equation 2.6}$$

where, i runs over the components, i.e. x,y,z polarisations.

This solution can be substituted into Equation 2.3 which gives an equation for each component;

$$F(z-ct)\left[\frac{\partial^2 G(x,y)}{\partial x^2} + \frac{\partial^2 G(x,y)}{\partial y^2}\right] = 0 \qquad \text{Equation 2.7}$$

The function F cannot be zero as this would mean it would be impossible to transport energy, hence;

$$\frac{\partial^2 G(x,y)}{\partial x^2} + \frac{\partial^2 G(x,y)}{\partial y^2} = 0 \qquad \text{Equation 2.8}$$

By definition a localised solution must have G(x,y) = 0 for large $|x|$ and $|y|$. The only solutions to Laplace's equation that is zero on the boundary is zero everywhere i.e. G(x,y) = 0 for all x and y. This means that we cannot have a finite unidirectional beam in free space [Pozar 2005]. Waveguides allow for a finite unidirectional beam because the metallic walls impose boundary conditions on the components of G(x,y) on the edge of the waveguide. Whilst $E_{\text{tangential}}$ and B_{normal} must be zero, E_{normal} and $B_{\text{tangential}}$ are not.

2.2 Waveguide mode theory and dispersion

It is an essential requirement in a microwave circuit to be able to transfer signal power from one point to another without unnecessary radiation loss. A waveguide is a structure that supports electromagnetic waves that can travel along its length; this is used to efficiently carry EM energy and also signals between two points. Using a waveguide is the most efficient way of transmitting energy over short distances at frequencies greater than about 1GHz up to ~200GHz. All metal tubes act as waveguides, whether they are hollow, or with one or more central conductors, providing they have translational symmetry in one dimension (although practical systems often have carefully designed bends). The walls reflect the waves to and fro, and for certain frequencies there exists modes produced by the superposition of these fields in such a way as to produce a new wave that propagates down the length of the pipe with very little attenuation. If the walls are perfectly conducting there is no attenuation at all since all of the incident energy would be reflected every time. The following theory focuses on waveguides with continuous translational symmetry; both cylindrical and rectangular waveguide mode theory will be discussed.

2.2.1 Transverse electric and magnetic modes

All the x and y field components can be expressed in terms of the z field components, whilst the solutions for the E_z and B_z components are independent of each other – we may write the wave equation for E_z and B_z;

$$\frac{\partial^2 E_z}{\partial x^2}+\frac{\partial^2 E_z}{\partial y^2}-k_z{}^2 E_z=\frac{\omega^2}{c^2}E_z \qquad \text{Equation 2.9}$$

$$\frac{\partial^2 B_z}{\partial x^2}+\frac{\partial^2 B_z}{\partial y^2}-k_z{}^2 B_z=\frac{\omega^2}{c^2}B_z \qquad \text{Equation 2.10}$$

These equations are independent of each other and therefore represent distinct allowed propagating waves. From the solutions to these two equations, Faraday’s and the Ampère-Maxwell laws give the transverse field components. Waves associated with the E_z field will have $B_z = 0$ and therefore are called a transverse magnetic solution, or a TM solution. To solve for TM modes we set $B_z = 0$ and solve for E_z subject to appropriate boundary conditions on the waveguide wall. Likewise, energy associated with the B_z field will have $E_z = 0$ and are therefore called a transverse electric, or a TE solution. So to solve for TE modes one sets $E_z = 0$ and solves Equation 2.10 for B_z subject to appropriate boundary conditions on the waveguide wall. TEM modes may also exist where both $E_z = 0$ and $B_z = 0$. In this case both the electric and magnetic fields are transverse, and the dispersion relation is simply $\omega = ck_z$. These modes will not be analysed in detail here but they arise only in multiconductor transmission lines and free space.

2.2.2 Rectangular waveguide mode theory

Consider a hollow metal pipe of rectangular cross-section, with width ‘a’ in the x-direction and width ‘b’ in the y-direction as shown in Figure 2.1. The direction of propagation of the waves is along the z-direction. As noted above there are two sets of waves that can propagate with low attenuation. These comprise of TE waves where the electric field is perpendicular to the direction of propagation, and TM, waves where the magnetic field is perpendicular to the direction of propagation.

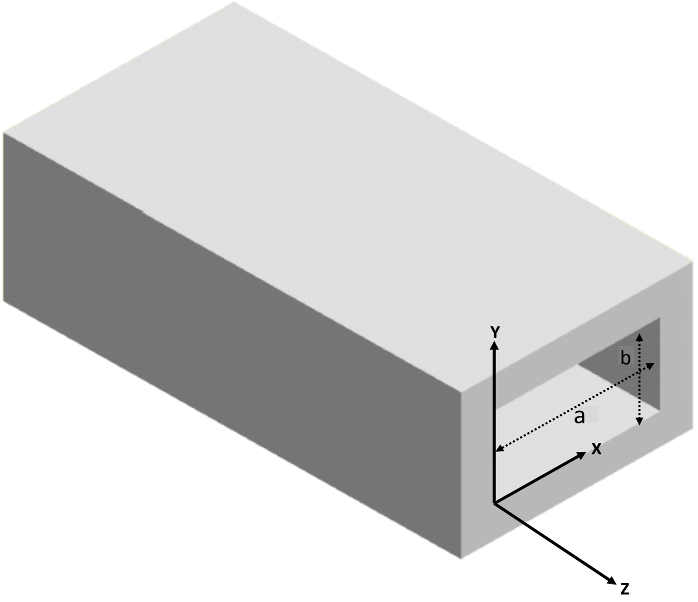

Figure 2.1**:** Coordinate system used for rectangular waveguides.

2.2.2.1 Cut-off and boundary conditions

Consider a rectangular metallic waveguide with walls at x = 0, x = a, y = 0 and y = b. As the boundaries are approached the tangential E field must go to zero. This means that $E_y=0$ at x=0,a and $E_x=0$ at y=0,b whilst E_z must be zero at all four interfaces.

For TM modes; when x=0 and x=a (as the boundaries are approached) the tangential electric field must vanish i.e. $E_y = 0$ and $E_z = 0$, for all values of y. Similarly on y = 0 and y = b the tangential electric field must vanish i.e. $E_x = 0$ and $E_z = 0$ for all values of x .

For TE modes $E_z=0$ and we require E_y to be zero at the walls x=0 and x=a. Similarly we require $E_x=0$ at y=0 and y=b.

2.2.2.2 Rectangular transverse electric and magnetic modes

Solutions of Equation 2.9 that satisfy the boundary condition are given as;

$$E_z^{TM} = A_{kz}\sin\left(\frac{m\pi x}{a}\right)\sin\left(\frac{n\pi y}{b}\right) m, n = 1, 2, 3....\qquad \text{Equation 2.11}$$

where, A_{kz} *is a constant multiplier that can be changed for differing modes.*

Solutions of Equation 2.10 that satisfy the boundary condition are given as;

$$B_z^{TE} = A_{kz}\cos\left(\frac{m\pi x}{a}\right)\cos\left(\frac{n\pi y}{b}\right)\qquad \text{Equation 2.12}$$

m, n = 0,1,2,3…(m = n = 0 not allowed)

For fixed values of a, b and m, n there is a minimum frequency at which waves propagate. This frequency is known as the *cut-off frequency;*

$$\omega_{cut-off} = c\sqrt{\left(\frac{m\pi}{a}\right)^2 + \left(\frac{n\pi}{b}\right)^2}\qquad \text{Equation 2.13}$$

Figure 2.2 illustrates TM and TE modes in a rectangular waveguide.

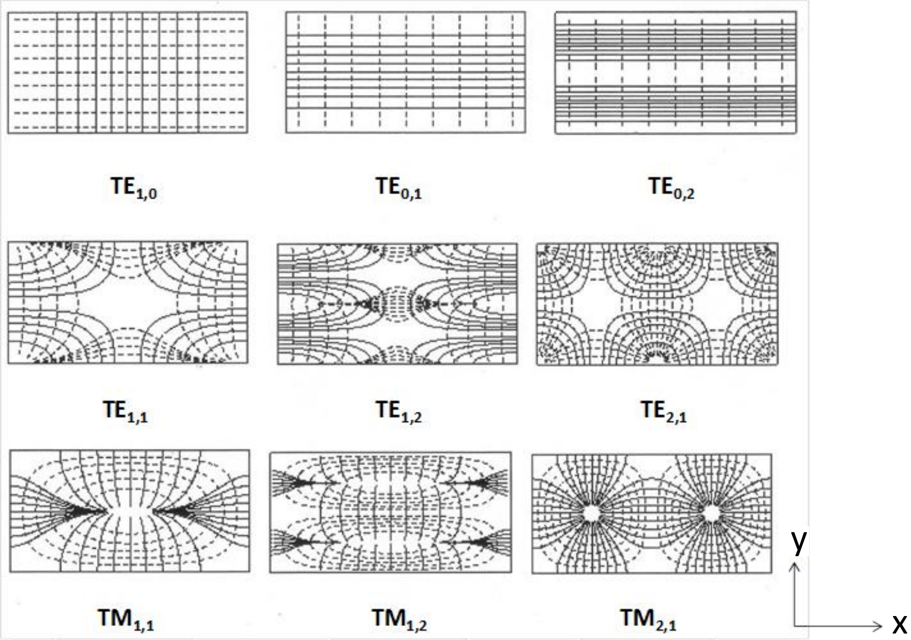

Figure 2.2**:** Diagram illustrates TM and TE modes in rectangular waveguides. Electric and magnetic fields are depicted by solid and dashed lines respectively.

2.2.3 Cylindrical waveguide mode theory

Much of the theory that holds for rectangular waveguides also holds for cylindrical waveguides aside from the mathematical complications associated with the vector calculus operator in cylindrical co-ordinate systems.

Hollow metal tubes of circular cross section i.e. cylindrical waveguides also support TE and TM waveguide modes. The geometry under consideration in the context of this theory is seen in Figure 2.3; a circular waveguide with inner radius a. It is of course appropriate to use cylindrical coordinates here since a cylindrical geometry is involved. Therefore in this case the components of the fields are expressed in terms of the cylindrical polar coordinates, r, φ and z.

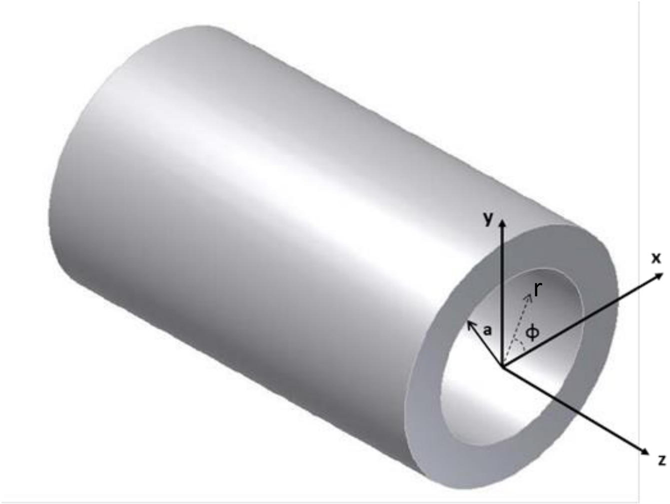

Figure 2.3**:** Coordinate system used for discussion of cylindrical waveguides.

Just like in the rectangular coordinate situation, the transverse fields in cylindrical coordinates can be derived from the E_z and H_z field components, for TM and TE modes respectively.

Notice that magnetic field intensity **H** is used here instead of the magnetic flux density. The electric and magnetic fields respectively $E_{0,z}(r,\varphi)$ and $H_{0.z}(r,\varphi)$, satisfy the wave equation;

$$\left(\nabla_t{}^2 + k_c{}^2\right)\begin{pmatrix} E_{0,z} \\ H_{0,z} \end{pmatrix} = 0 \qquad \text{Equation 2.14}$$

$$where,\, k_c{}^2 = \varepsilon_0 \varepsilon_r \mu \omega^2 - k_z{}^2 \,,\ \nabla_t{}^2 = \nabla^2 - \frac{\partial^2}{\partial z^2}$$

Writing the transverse Laplacian operator in cylindrical polar coordinates;

$$\left[\frac{1}{r}\frac{\partial}{\partial r}(r\frac{\partial}{\partial r}) + \frac{1}{r}\frac{\partial^2}{\partial \phi^2}\right]\begin{pmatrix} E_{0,z} \\ H_{0,z} \end{pmatrix} = -k_c{}^2 \begin{pmatrix} E_{0,z} \\ H_{0,z} \end{pmatrix} \qquad \text{Equation 2.15}$$

If the variables are separated and by applying a periodic boundary condition to the azimuthal component, a general solution can be obtained for the longitudinal field components [Vanderlinde 1993];

$$E_{0,z}, H_{0,z} = R_m(r)e^{\pm im\varphi}$$ Equation 2.16

where, m is an integer

The radial function $R_m(r)$, satisfies Bessel's equation and so has the general form;

$$E_{0,z}(r,\varphi), H_{0,z}(r,\varphi) = AJ(\gamma r)e^{\pm im\varphi}$$ Equation 2.17

2.2.3.1 Cylindrical transverse electric and magnetic modes

Cyclotron maser devices most commonly use TE modes for interaction and energy extraction. In the current context therefore the TE mode will be examined in depth.

In cylindrical waveguides TE modes have the following field components;

$$E_{0,z} = 0$$

$$H_{0,z} = AJ_m\left(\frac{\rho'_{m,i}\, r}{a}\right)e^{\pm im\varphi}$$

$$H_{0,t} = \frac{ik_z a^2}{\rho'^{\,2}_{m,i}}\nabla_t H_{0,z}$$

$$E_{0,t} = -\frac{i\mu\omega a^2}{\rho'^{\,2}_{m,i}}\left(\hat{k}\times\nabla_t H_{0,z}\right)$$

Equation 2.18

These components are derived from Equation 2.16 and 2.17, by applying the boundary condition for a cylindrical waveguide which is $B_{\perp} = 0$ & $E_{//} = 0$ at r = a. Figure 2.4 and Figure 2.5 illustrate the electric field intensities and also the electric field distributions of the TE modes in a cylindrical waveguide respectively.

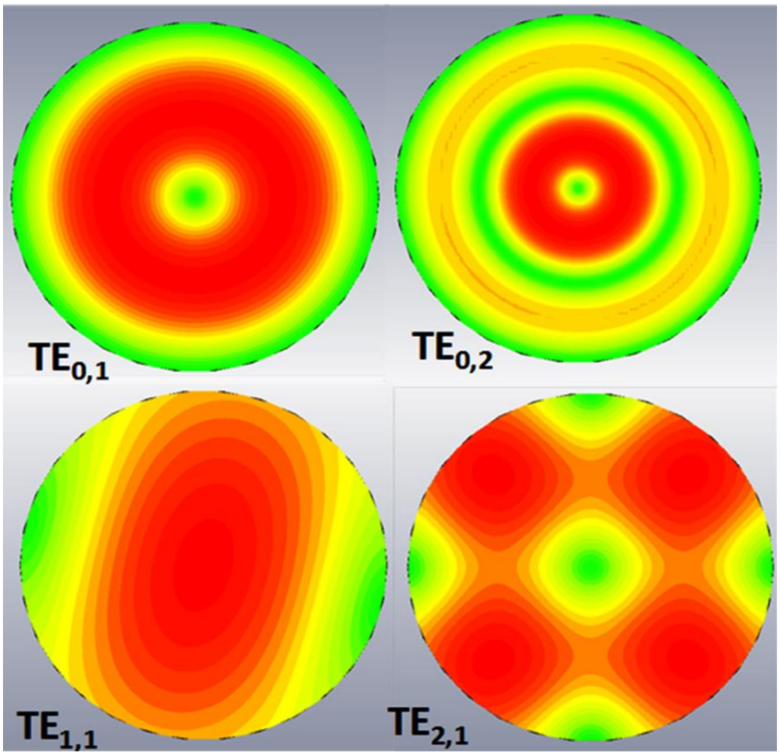

Figure 2.4**:** Electric field amplitude profiles for various TE modes in a cylindrical waveguide. The different colours indicate the intensities of the electric field.

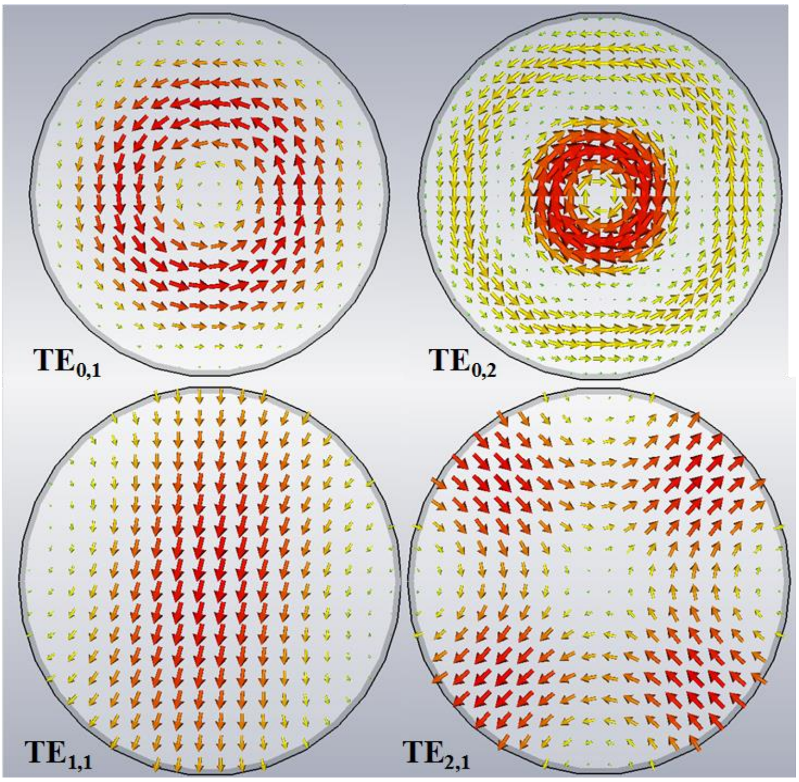

Figure 2.5**:** Field distributions of the TE modes in cylindrical waveguides.

The term $\rho'_{m,i}$ is the i-th root of the Bessel function derivative $J'_m(k_c a)$ this effectively means $k_c a = \rho'_{m,i}$. The smallest root of all the Bessel function derivatives is the first root of J'_1, $\rho'_{1,1}$, which makes the corresponding $TE_{1,1}$ mode the smallest cut-off frequency of any TE mode.

The dispersion equation is;

$$k_z^{\,2} = \varepsilon_0 \varepsilon_r \mu \omega^2 - \frac{\rho'^{\,2}_{m,i}}{a^2} \qquad \text{Equation 2.19}$$

The cut-off frequency is given by;

$$\omega_c = \frac{1}{\sqrt{\mu \varepsilon_0 \varepsilon_r}} \frac{\rho'_{m,i}}{a} \qquad \text{Equation 2.20}$$

It would be complete to note that a characteristic of Bessel functions is;

$$\frac{\partial}{\partial x} J_m(x) = -J_{m+1}(x) + \frac{m J_m(x)}{x}$$

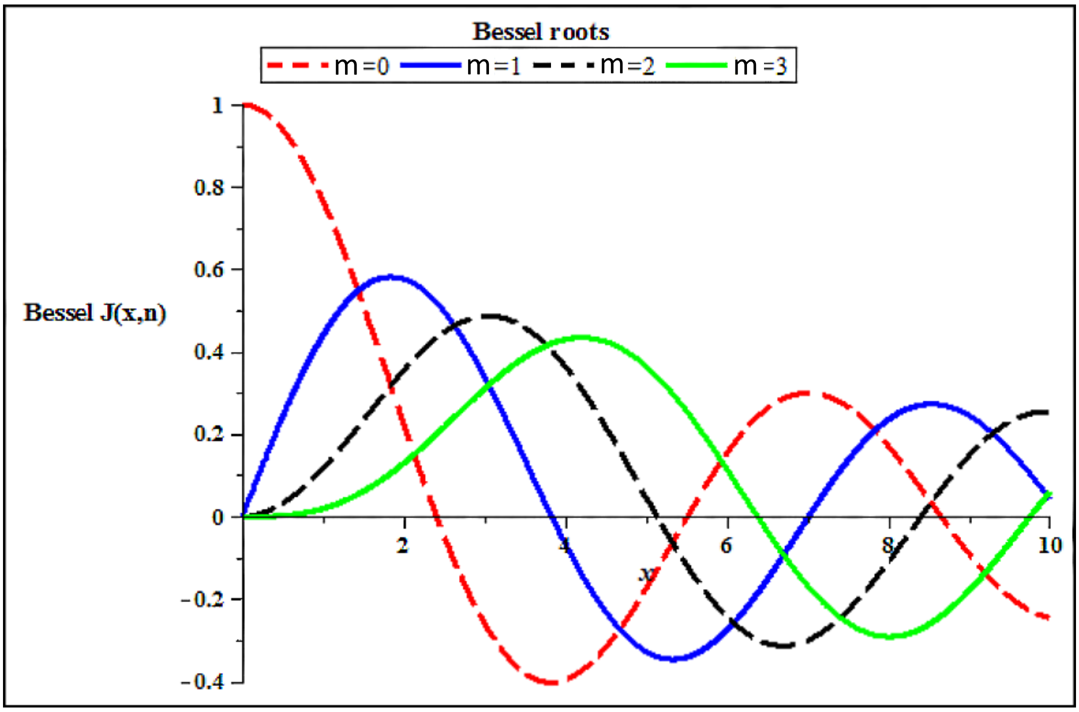

Figure 2.6**:** Plot of the first four Bessel functions.

For the case of TM modes, $B_z = 0$ and $E_z = AJ(k_c r)e^{\pm im\varphi}$, at the waveguide wall, E_z must vanish which would imply $J_m(k_c a) = 0$. This would mean that $k_c a$ must be a root of J_m. Figure 2.6 illustrates a plot of the first four Bessel functions. The turning points of this curve obviously correspond to the roots of the differentiated Bessel functions required for TE modes.

2.3 Electron cyclotron maser theory

2.3.1 Introduction

The electron cyclotron maser instability is a powerful mechanism which can produce non-thermal coherent stimulated radiation in plasmas. It is the instability that is believed to give rise to the AKR and the non-thermal auroral emission from other magnetized planets [Kurth & Zarka 2001].

The first description of Electron Cyclotron Maser (ECM) theory came from independent studies from three researchers, Twiss, Schneider and Gaponov between 1958 and 1959 [Schneider 1959] [Gaponov 1959] [Twiss 1958]. Twiss first put forward a theoretical description of the ECM in an astrophysical context whilst in 1959 Schneider & Gaponov each published calculations which investigated stimulated emission of electromagnetic waves from relativistic mono-energetic electrons in a magnetic field. Schneider’s approach was quantum mechanical whilst Gaponov used a classical description. It wasn’t until 1964 that the first fully understood experimental demonstration took place [Hirshfield & Granatstein 1977] [Hirshfield & Wachtel 1964]. Although earlier experiments had seen effects which were probably due to ECM instability [Pantell 1959].

R.H. Pantell observed the ECM mechanism in 1959; he reported the first results with a fast-wave cyclotron resonance interaction. He described a device that oscillated at frequencies between 2.5GHz - 4.0GHz with a 3μA beam at 1kV. Pantell claimed that the radiation arose from synchronism between the backward cyclotron wave and the waveguide $TE_{1,1}$ mode [Pantell 1959]. Chow and Pantell [Chow & Pantell 1964], Feinstein [Feinstein 1964] and Bott [Bott 1964] also verified this mechanism in the early 1960's.

In 1964 Bott, of the Royal Radar Establishment (RRE), reported the generation of radiation between 0.95mm and 2.2mm using a 10kV, 50mA beam in a spatially converging pulsed magnetic field of up to 100kG. Chow and Pantell showed that axial bunching could result from the combined forces due to the RF electric and RF magnetic fields [Hirshfield & Granatstein 1977]. These devices used low voltage, low current electron beams with a total mm-wave output power << 1kW. However there was ongoing debate about the relative roles and importance of the axial and rotational bunching effects.

In the early 1970's in Washington D.C., studies focussed on cold cathode, megavolt-level CRM devices whilst in the mid-1970s, in the former USSR, major developmental breakthroughs that yielded high average power millimetre-wave oscillators, were first published. The breakthrough occurred when using a tapered, open ended waveguide cavity in conjunction with a beam-forming system based on the magnetron injection gun, i.e. a MIG. A MIG works by forming an electron beam, with most of the energy in cyclotron motion [Granatstein & Alexeff 1987] [Nusinovich 2004]. This gave rise to research in long pulse, high power systems, which became known as gyrotrons.

In the millimetre and sub-millimetre (<1mm) wavelength regions the power radiated from a gyrotron, in continuous wave and long pulse regimes, greatly exceeds the power produced by a classical microwave tube (klystrons and magnetrons etc.) by many orders of magnitude. Hence the gyrotron is recognised as being an important addition to the range of high-power sources of coherent electromagnetic radiation.

The superiority (in this regard) of CRM systems arises since classical "conventional" devices usually operate by using periodic structures and cavities to manipulate and control the interacting wave and generate coherent bunching. Due to construction of the walls in these cavities there is a miniaturisation of the interaction space as the wavelength becomes shorter. Thus, there is a reduced potential for efficient high power output as the power that can be handled by such structures decreases significantly [Nusinovich 2004]. This is addressed in the gyrotron which operates in the fast wave limit in smooth bore and highly overmoded waveguides.

The gyrotron is the most efficient experimental example of the electron cyclotron maser to date. Between frequencies of ~10GHz - 450GHz gyrotrons can operate with efficiencies of up to 40%; however, they are most efficient below 250GHz. This is due to the need to operate at harmonics of the electron cyclotron frequency in the sub-mm wavelength band. Variations of the cyclotron maser such as the cyclotron autoresonance maser (CARM) [Speirs et al. 2004] have potentially the best performances at these frequencies, although these have problems associated with stringent requirements on the electron beam quality.

A classic picture of CRM action emerges by considering the relative phases of the electrons rotating about a magnetic field. This classic picture is due to azimuthal phase bunching by RF electric fields. A bunching mechanism for the electrons is required to impart an ac component to the beam current. Close synchronism of the electron-cyclotron motion with the EM wave is required for bunches to build up and to allow sustained energy transfer. Bunching and synchronism are two essential conditions to produce coherent radiation in vacuum-electronic devices [Chu 2004].

2.3.2 Particle orbit theory

As previously mentioned, the plasma in the AKR source region, the auroral density cavity, is colder and more tenuous than the surrounding plasma. In this geophysical plasma the dynamics are significantly influenced by the Earth's magnetic field.

The equation of motion for a particle moving at non-relativistic velocities in a static uniform magnetic field is given by;

$$m\frac{d\boldsymbol{v}}{dt} = q(\boldsymbol{v} \times \boldsymbol{B}) \qquad \text{Equation 2.21}$$

where, $q(\boldsymbol{v} \times \boldsymbol{B})$ *is the Lorentz force*

The scalar product of the above equation with the velocity vector gives;

$$m\boldsymbol{v}\cdot\frac{d\boldsymbol{v}}{dt} = q\boldsymbol{v}\cdot(\boldsymbol{v}\times\boldsymbol{B}) = 0$$ Equation 2.22

showing, the kinetic energy is unaffected by the Lorentz force since the rate of work $\boldsymbol{v}\cdot(\boldsymbol{v}\times\boldsymbol{B}) = 0$

Resolving the velocity into components conveniently allows the particle trajectories, relative to the magnetic field, to be described i.e. $\boldsymbol{v} = \boldsymbol{v}_{\perp} + \boldsymbol{v}_{//}$. Since the $\boldsymbol{v}\times\boldsymbol{B}$ force has no component parallel to the magnetic field, the parallel component of the velocity is constant, so the particle moves at a constant velocity along the magnetic field. The radius of the orbit, r_L, also known as the Larmor radius, of the motion in a plane perpendicular to the magnetic field can be obtained from the perpendicular component of the equation of the motion which can be written as;

$$m\frac{v_{\perp}^{2}}{r_L} = |q|v_{\perp}B$$ Equation 2.23

Hence the Larmor radius is given by;

$$r_L = \frac{mv_{\perp}}{|q|B}$$ Equation 2.24

where, $v_{\perp}$ *is constant which in turn makes the cyclotron radius constant (this means that the motion in a plane perpendicular to the magnetic field is a circle)*

The frequency of the circular motion around a magnetic field is known as the cyclotron frequency given (in angular form) by;

$$\omega_c = \frac{v_{\perp}}{r_L} = \frac{|q|B}{m}$$ Equation 2.25

Following this analysis, it is shown that the uniform motion along the magnetic field plus the circular motion around the magnetic field generates a helical trajectory. When observed looking along the direction of the magnetic field, positively charged particles rotate in the anti-clockwise sense around the magnetic field whilst negatively charged particles rotate in the clockwise sense. The instantaneous centre of the rotational motion is called the guiding centre. For relativistic particles the Lorentz factor is also present in the denominator for ω_c thus;

$$\omega_c = \frac{|q|B}{\gamma m_o}$$ Equation 2.26

$$r_L = \frac{\gamma m_0 v_\perp}{|q|B}$$ Equation 2.27

where, m_o is the rest mass of the particle and γ is the relativistic mass factor

$$\gamma = \frac{1}{\left[1 - \frac{v^2}{c^2}\right]^{1/2}}$$ Equation 2.28

where, c- speed of light, v *–magnitude of the velocity of the electron*

2.3.3 Magnetic moment

The term magnetic moment of a system refers to its magnetic dipole moment, and is a measure of the strength of the system's interaction with magnetic fields. A moving charge produces a current, if the charge is moving around a magnetic field in a uniform circular path then this constitutes a current loop. The magnetic moment μ of this current loop is the product of the current and the area of the loop,

$$\mu = IA$$ Equation 2.29

The magnitude of the current is the charge divided by the cyclotron period;

$$I = \frac{|q|}{T_c} = \frac{q^2 B}{2\pi m}$$ Equation 2.30

The area of the current loop is the area of the circular orbit;

$$A = \pi r_L{}^2 = \pi \left(\frac{m v_\perp}{qB} \right)^2$$ Equation 2.31

The expression for the magnetic moment is formed by combining Equation 2.30 and Equation 2.31 and is written as;

$$\mu = \frac{m v_\perp{}^2}{2B}$$ Equation 2.32

2.3.4 Magnetic mirrors

As stated in section 2.1.2, Maxwell’s second equation states that the net flux of magnetic field, B, emerging through any closed surface is zero i.e. the divergence of the magnetic flux density is zero. If this is expressed in cylindrical polar coordinates, assuming $B_\phi=0$, and rearranging;

$$\frac{\partial}{\partial r}(rB_r) = -r\frac{\partial B_z}{\partial z} \qquad \text{Equation 2.33}$$

If $\partial B_z / \partial z$ is varying slowly compared to any r scale of interest. Integrating Equation 2.33 gives;

$$B_r = -\frac{1}{r}\int_0^r r'\frac{\partial B_z}{\partial z}dr' \cong -\frac{r}{2}\frac{\partial B}{\partial z}\bigg|_{r=r_0} \qquad \text{Equation 2.34}$$

Introducing the z component of the Lorentz force on a particle, in cylindrical co-ordinates;

$$F_z = q(v_r B_\varphi - v_\varphi B_r) \qquad \text{Equation 2.35}$$

$B_\varphi = 0$ and substituting from Equation 2.35 gives;

$$F_z = -qv_\varphi B_r = \frac{qv_\varphi r}{2}\frac{\partial B_z}{\partial z} \qquad \text{Equation 2.36}$$

Since $v_\varphi = \mp v_\perp$ and considering particles rotating about the magnetic axis, so that $r = r_L$, the Larmor radius, substituting this gives the mirror force;

$$F_{//} = \mp \frac{qv_\perp r_L}{2}\frac{\partial B_z}{\partial z} \qquad \text{Equation 2.37}$$

The $\mp$ signs correspond to particles of opposite charge which will orbit the field in opposite directions, so can generalise this in 3D to;

$$F_{//} = \pm\mu\frac{\partial B}{\partial s} \qquad \text{Equation 2.38}$$

where, s is the coordinate in the direction of B and $\mu = \frac{qv_\perp r_L}{2}$

The parallel force arises from the interaction between the magnetic field and the magnetic moment produced by the cyclotron motion of the particle. The direction of the force is always such that the particle tends to be repelled from the region of strong magnetic field. If the magnetic field lines are converging, the Lorentz $(v \times B)$ force has a component opposite to the direction of convergence thereby producing a force away from the region of the stronger magnetic field.

2.3.5 Resonance relationships

In any gyro-device, the electron beam-wave interaction occurs when the cyclotron resonance condition is met, this is a synchronism between the Doppler shifted electron cyclotron frequency and the dispersion of the electromagnetic wave mode. The Doppler upshifted electron cyclotron frequency is defined as;

$$\omega_D = n\omega_{ce} + k_{//} v_{//} \qquad \text{Equation 2.39}$$

where, ω_D *= Doppler shifted cyclotron frequency, i.e. the operating frequency,* ω_{ce} *= Relativistic cyclotron frequency of the electrons in the presence of a magnetic field*

$$\omega_{ce} = eB / m_o \gamma \qquad \text{Equation 2.40}$$

where $n\omega_{ce}$ *is the harmonic cyclotron frequency. The term* $k_{//} v_{//}$ *is the Doppler upshift term.*

The waveguide mode oscillation frequency ω is defined by;

$$\omega^2 = c^2 k_{\perp}{}^2 + c^2 k_{//}{}^2 \qquad \text{Equation 2.41}$$

where, ω *= Guided electromagnetic radiation frequency,* $k_{\perp}$ *= Perpendicular wavenumber of the guided electromagnetic radiation.*

When the Doppler up-shifted cyclotron frequency ω_D is sufficiently close to the wave oscillation frequency ω then the cyclotron resonance condition is satisfied and wave particle interaction is possible. Dispersion diagrams are used to identify interactions that may occur, or cyclotron-wave resonances that may be available from the beam-wave dispersion characteristics. Examples of such dispersion diagrams are illustrated in Figure 2.7. Three dispersions are shown, each diagram illustrating a dispersion regime that may occur for different sets of beam parameters in a given waveguide geometry.

From Figure 2.7**a** it can be seen that the grazing incident beam-wave resonance occurs very close to waveguide mode cut-off. This interaction regime is typical of an electron cyclotron maser device i.e. a gyro-device such as a gyrotron. Beam-wave resonances of this nature that occur at superluminal phase velocity ($v_p > c$) are referred to as fast-wave resonances.

Optimum wave-particle interaction takes place at the grazing incidence of the waveguide mode with the Doppler up-shifted cyclotron frequency of the electrons in the extreme fast wave region (i.e. $k_\perp >> k_{//}$). In the fast wave region the group velocity of the wave $v_g = \frac{d\omega}{dk_{//}} \rightarrow 0$ and the phase velocity is $v_p = \frac{\omega}{k_{//}} \rightarrow \infty$.

Figure 2.7**b** illustrates a case where both far and close to waveguide mode cut-off resonances are present on a single beam line. By plotting these resonances it is possible to deduce useful information about the differences between their sensitivity to velocity spread. Notice the effect the Doppler upshift term from Equation 2.39 has at higher axial wavenumbers, $k_{//}$. This is seen by the extreme impact of any change in the pitch factor $\alpha = v_\perp / v_{//}$ has in the marked shift in frequency in the far from cut-off resonance.

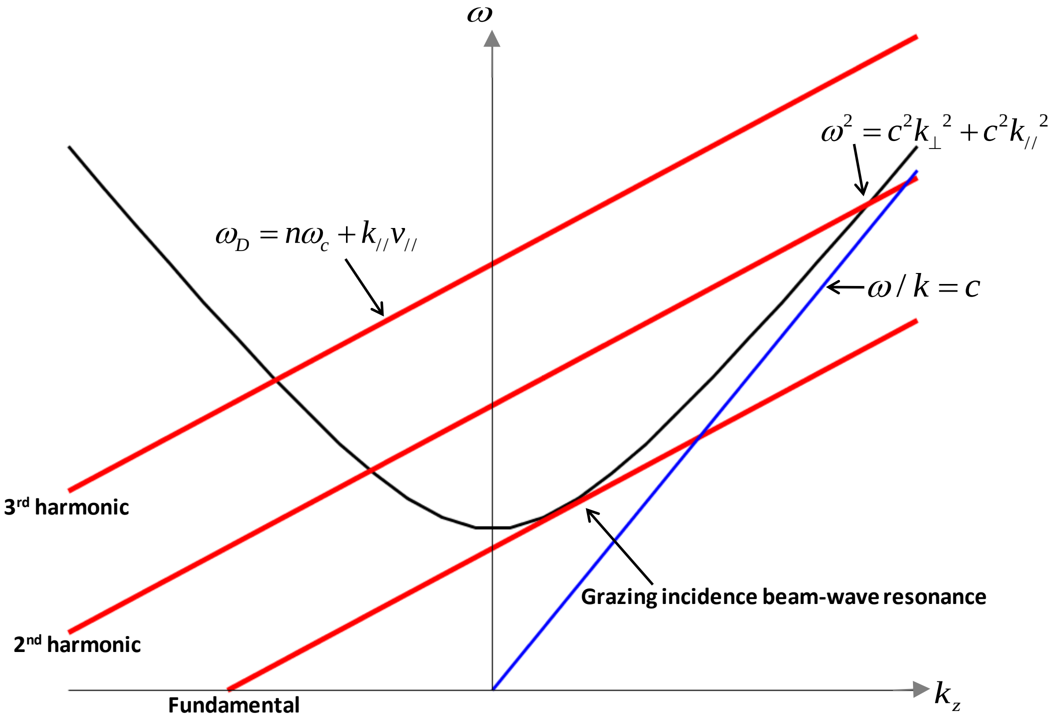

(a) Beam-wave dispersion plot illustrating beam wave harmonics.

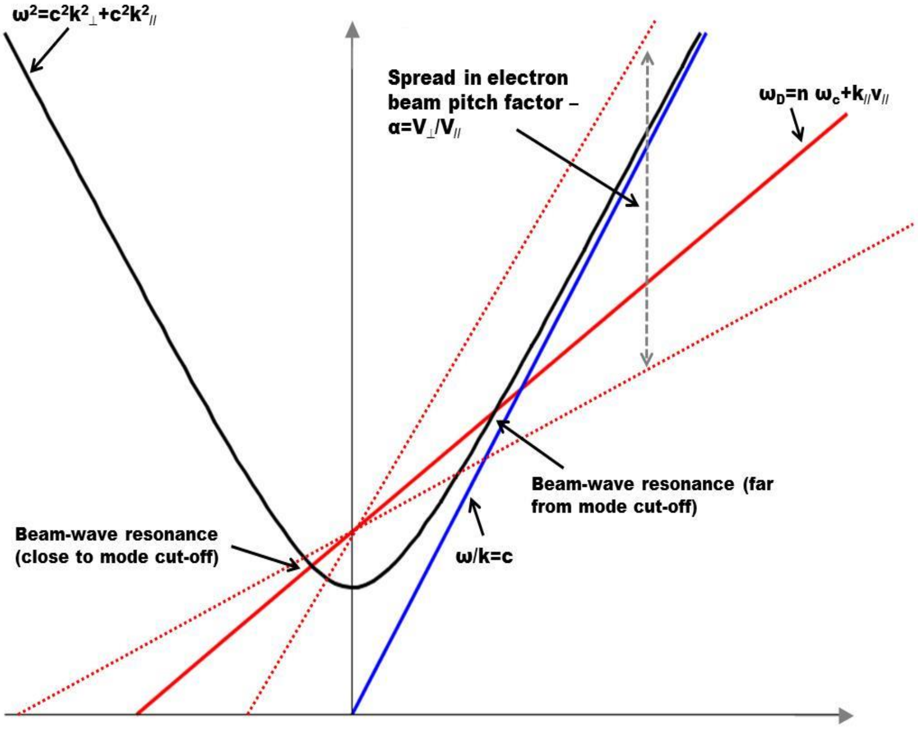

(b) A dispersion illustrating an interaction scenario where both a near to cut-off (backward wave) and far from cut-off resonance is present.

Figure 2.7: Beam-wave dispersion plots for two individual interaction scenarios.

At higher axial wavenumbers the Doppler upshift term has more influence which in turn means a greater sensitivity of the Doppler upshifted cyclotron frequency ω_D to spread in the electron axial velocity $v_{//}$. In the case for close to cut-off resonance with $k_{//} \to 0$ the Doppler upshift term plays a minor role in influencing the frequency of the beam-wave resonance, which means the interaction efficiency is less sensitive to a spread in the electron pitch factor.

2.3.6 Energy extraction & instability mechanism

It has been stated previously that electromagnetic radiation may be extracted from relativistic electrons gyrating about an external magnetic field via the CRM instability. There are two additional mechanisms associated with cyclotron energy extraction from the transverse cyclotron motion of electrons. These are the Weibel instability and the peniotron interaction.

The most common or widely recognised mechanism however is the CRM instability [Hirshfield & Granatstein 1977][Sprangle & Drobot 1977]. The CRM and Weibel are two manifestations of a single physical process, observed in two extreme conditions. Although they occur simultaneously, it is usual for one to dominate in a given interaction.

To allow net flow of energy from the transverse electron motion into the electromagnetic wave, the electrons go through two key processes. These two processes are a common factor between the Weibel and CRM instabilities,

(i) *Bunching of the electrons in relative phase to produce a coherent state for energy extraction*

(ii) *Energy extraction via a slippage in phase of the electron bunches relative to the rotating E-field vector of the EM mode.*

These two processes occur simultaneously, as whilst the electron bunching is occurring a detuning between the RF and cyclotron frequencies causes a progressive relative phase shift. This phase shift brings the bunched electrons into a phase (with respect to the EM wave) where energy extraction can occur.

The change in ω_D as the electron velocity changes through interaction with the RF fields can be determined by taking its time derivative. This derivative can be evaluated by using the z component of the Lorentz force equation $d\boldsymbol{p}/dt = -e(\boldsymbol{E} + \boldsymbol{v} \times \boldsymbol{B})$ with the energy equation $mc^2\, d\gamma/dt = -e\boldsymbol{v}.\boldsymbol{E}$ and also Faraday's law which relates the transverse E and B fields for a TE waveguide mode $\mathbf{B}_\perp = (\mathrm{k_z}/\omega)\mathbf{z} \times \mathbf{E}_\perp$resulting in;

$$\frac{d\omega_D}{dt} = \frac{-ek_z^{\ 2}}{m\gamma\omega}\left[1 - \frac{\omega^2}{k_z^{\ 2}c^2}\right]\vec{v}_\perp.\vec{E}_\perp \qquad \text{Equation 2.42}$$

{Term 1} {Term 2}

Term 1 comes from the Lorentz force which moves electrons in the z direction. This force produces the phase bunching in the Weibel mechanism. The second term comes from the energy change due to acceleration or deceleration of the electron, which is the phase bunching associated with the CRM mechanism. Even though both instabilities share a common physics process, the physical motion of the particles in the individual mechanisms is completely different. Also, the CRM instability dominates when $v_p/c > 1$, i.e. the fast wave region. However when $v_p/c < 1$ the Weibel instability dominates.

2.3.7 Cyclotron resonance maser (CRM) instabilities – azimuthal bunching

In order to study the mechanism responsible for the CRM instability it is useful to refer to the rotational particle trajectories. It is beneficial at this stage to note that the CRM instability is also known as the azimuthal instability as it occurs in an azimuthal direction. From Figure 2.8, the orbital dynamics of electrons uniformly distributed around a gyro orbit can be seen. The electrons are rotating in a *clockwise direction* (observed looking along the magnetic field) about a uniform constant magnetic field, $B_0\hat{e}_z$. The radius of the electron orbit is the Larmor radius,

$$r_L = v_\perp / (\omega_{ce}) \qquad \text{Equation 2.43}$$

where, $v_\perp$ *is the perpendicular velocity*

Under the influence of an electric field, $E_y = \varepsilon_0 \cos(\omega_o t)\hat{e}_y$, the particles' orbit will change. When the frequency of the electric field is equal to the initial relativistic cyclotron frequency, ω_{ce}, electrons 8, 1 and 2 will lose energy and tend to spiral inwards.

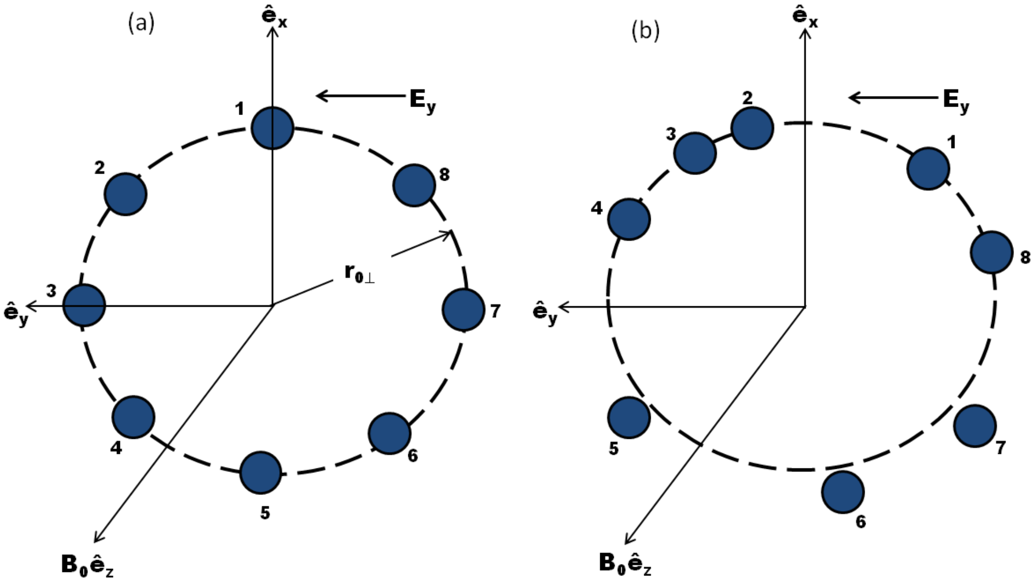

Figure 2.8**:** Electron cyclotron maser mechanism. Illustrated by orbits of particles in velocity space in the presence of a small external field (a) initial particle positions (b) bunched electrons after several gyrotron cycles.

Referring again to Figure 2.8, the relativistic cyclotron frequency of these electrons will increase, since γ decreases. The phase of the electrons will tend to slip ahead the wave. Particles on the other side 4, 5 and 6 will gain energy and so their cyclotron frequency will decrease and they will spiral outwards. The phase of these particles will slip behind the wave. After this process has evolved over several cycles the electrons will start to bunch around the positive y axis. The bunching effect is relativistic since it depends on the rotational frequency of the electrons being energy dependent.

In order to achieve a net energy transfer between the electrons and the wave the Doppler shifted relativistic cyclotron frequency, ω_{ce}, must be slightly less than ω_0. If ω_{ce} is slightly less than ω_0 the particles in the bunch will then slip behind the wave, and the particles will distribute in the upper half of the plane as in Figure 2.8**b**. This will mean the net kinetic energy, $E_{k,}$ of the collection of electrons will decrease as a result of the phase slippage between the electrons and the field. This differential frequency resulting in the slippage in phase is known as detuning. Conservation of the total energy implies that the field amplitude will increase.

Whilst the relativistic cyclotron frequency remains less than ω_0 the particles will continue to slip behind the wave. If the field amplitude is sufficiently high then at some point as the electrons drift through the interaction system, the electrons will lose sufficient energy that their cyclotron frequency matches the wave frequency. Continued interaction will eventually bring the electrons back through the phase path (at the top of the orbit in Figure 2.9) to the accelerating condition. This corresponds to a saturation limit, called ‘phase trapping’, on the efficiency of the interaction.

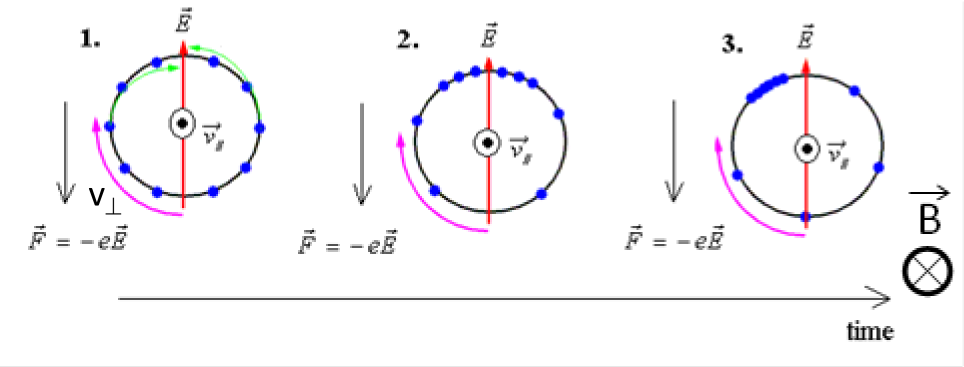

Figure 2.9**:** Phase bunches forming from the progression of CRM instability.

2.3.8 Weibel instabilities – Axial bunching

Phase bunching due to the Weibel mechanism occurs as a result of the axial movement of the electrons perpendicular to the cyclotron orbit, shown in Figure 2.10. The electrons’ transverse velocity interacts with the transverse magnetic field component of the waveguide mode modulating the axial velocity.

Phase bunching is produced in the Weibel mechanism by the Lorentz force $-e(v_\perp \times B_\perp)$ which moves the electrons in the z direction. The electrons that are situated on the left hand side of the E-field plane will experience a longitudinal Lorentz force directed forwards along the direction of $v_{//}$ and will therefore shift forwards in phase with respect to the electromagnetic field. However, on the right hand side of the field plane the electrons are forced backwards both longitudinally and in phase. This will result in a bunching mechanism as shown in Figure 2.10.

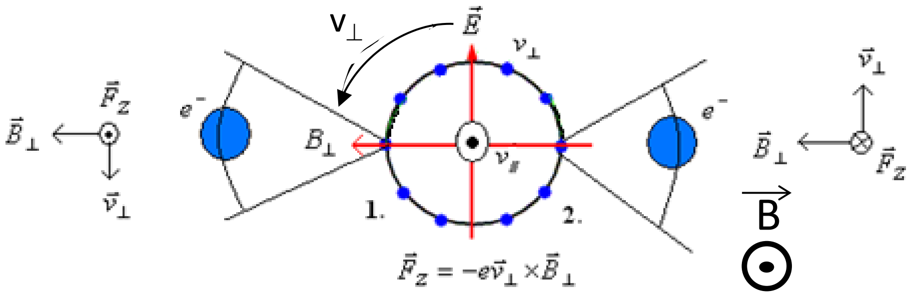

Figure 2.10**:** Representation of the Weibel instability.

Note that in Figure 2.11 the orbital circle does not represent the absolute geometrical coordinates of electrons; it only shows their orbital phase with respect to the local electromagnetic field vectors. As the electrons on the left hand side and the right hand side of the E-field plane are sent forwards or backwards in space respectively a bunch is formed at the bottom of the orbit. This is 180^{o} out of phase with the transverse electric field.

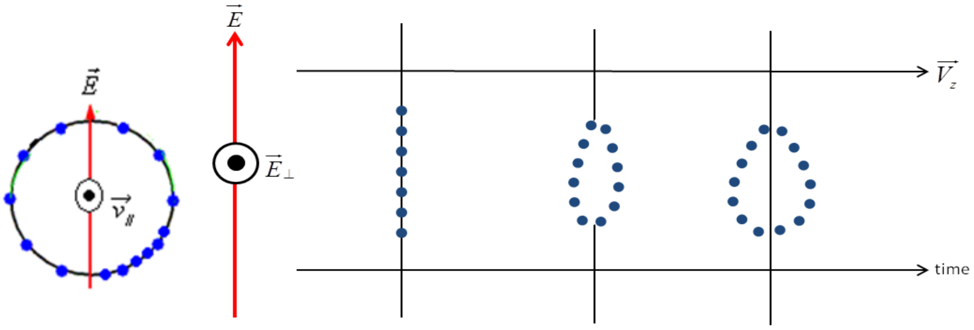

Figure 2.11: Beam cross-section and side profile of electron bunching occurring due to the Weibel instability.

As mentioned, both instabilities share a common overall arrangement, however when considering the physical motion of the particles the individual mechanisms are markedly different. For energy extraction by the Weibel interaction, the bunch drifts forward in phase which is due to an axial magnetic field set slightly higher than that for perfect resonance. The energy is extracted with deceleration of the orbits through interaction with the electric field, which is common with the CRM instability.

2.3.9 The autoresonance condition

From the cyclotron dispersion, that took into account the Doppler shift $\omega_D = n\omega_{ce} + k_{//}v_{//}$, it can be seen that the changing electron energy may change the axial velocity and/or the cyclotron frequency i.e. the axial velocity may decrease along with the Doppler term if the electron energy decreases (and therefore the cyclotron frequency increases). These two changes can compensate for each other. Research by scientists between 1962 and 1987 [Davydovskii 1962] [Granatstein & Alexeff 1987] showed that if the resonant EM wave propagated along an external guiding magnetic field with a phase velocity $v_{ph} = \omega / k_z$ equal to the speed of light c, the two changes compensate each other. This means that if the resonance condition is already fulfilled in such a system, then this resonance will be met automatically at all points regardless of how large the variations in the electron energies are. This condition, associated with the relative strengths of the CRM and Weibel instabilities, is referred to as the autoresonance condition. In short, it occurs when $\omega \approx k_z c$ and there is very little or no phase change even although the energy of the electrons is changing. This condition is employed by the CARM, or the cyclotron autoresonance maser [Speirs et al. 2004]. This phenomenon can in principle be used to extract large amounts of energy from the beam without losing synchronism. The autoresonant interaction is attractive when working with relativistic beams as autoresonant tuning causes v_z to decrease such that $\omega = \omega_c + v_z k_z$ remains constant, and allowing the instability to access the substantial translational energy. However, it is exceptionally sensitive to velocity spread.

2.3.10 Evolution of horseshoe electron distribution

The horseshoe distribution arises when an electron beam, that is mainly rectilinear, propagates into a region of increasing axial magnetic field. This occurs as the conservation of the magnetic moment, μ, results in the conversion of axial velocity

$v_{//}$ into perpendicular velocity $v_\perp$. The result is an increase in electron pitch factor, $\alpha = v_\perp / v_{//}$.

Equation 2.32 can be used to explain this phenomenon. As B_0, the axial magnetic field, increases $v_\perp$ must also increase to keep the magnetic moment constant. Since we know that the B-field does not affect the kinetic energy the resultant velocity distribution will develop as a half-horseshoe shaped profile (Assuming an initial drifting distribution as shown in Figure 2.12.(a)). Hence it is referred to as a horseshoe distribution, Figure 2.12. The horseshoe distribution is characterised by a broad region in velocity space where, $\partial f_e / \partial v_\perp$ is positive with f_e being the distribution function.

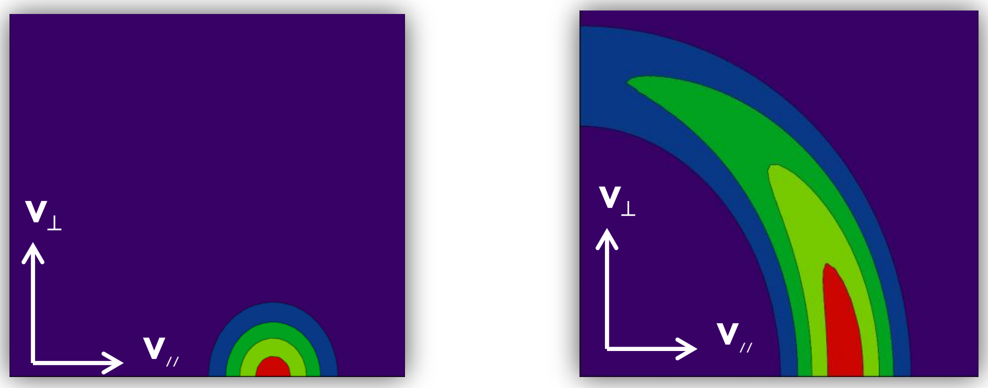

(a) (b)

Figure 2.12: (a) shows a beam before entering the increasing magnetic field. (b) represents the horseshoe distribution that arises from the conservation of magnetic moment.

Horseshoe shaped electron velocity distributions are believed to occur in numerous astrophysical environments where a suitable convergent magnetic field configuration exists [Bingham et al. 2002**b**]. The horseshoe distribution may also arise in any charged particles in these conditions of magnetic compression.

In recent times it has been proposed that the AKR is driven by electrons existing across a positive transverse velocity gradient $({}^{\partial f_e}/_{\partial v_\perp})$ at high pitch factors within an electron horseshoe distribution. Such a distribution has been observed in the AKR source region by various satellite missions [Sato et al. 2002] [Aikio 2004] [Strangeway 1998].

2.3.11 The loss cone

As the horseshoe distribution continues to expand in velocity space, electrons at the tip of the distribution will be magnetically mirrored as they pass $v_{//} = 0$ and enter into the region of negative axial velocity, Figure 2.13.

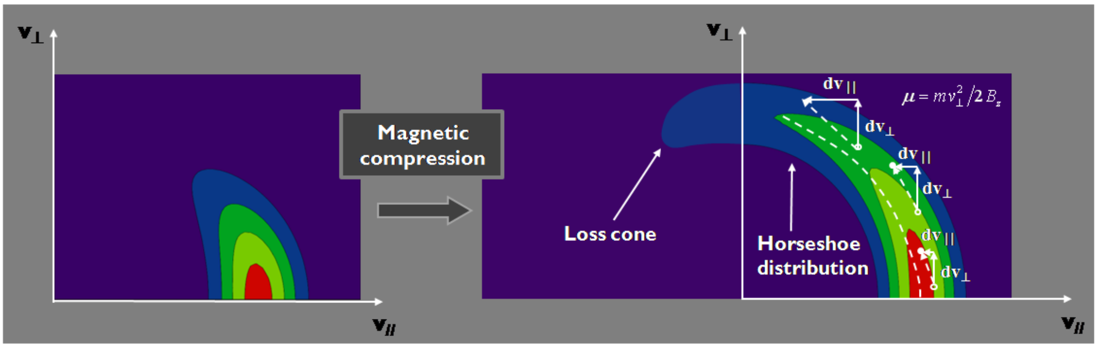

Figure 2.13: Loss cone distribution in velocity space. As the guide magnetic field increases, the beam distribution function progressively develops a horseshoe-like profile with an increasing number of electrons residing across a positive gradient in transverse momentum at the tip of the distribution.

This mirrored component has a gap at low $v_\perp$, and high $v_{//}$ and is referred to as the “loss cone” distribution and has also been shown to be unstable to cyclotron maser emission [Wu & Lee 1979].

2.3.12 Instabilities in loss cone and horseshoe distributions

It is now a well-established theory that the electron cyclotron maser instability is the mechanism responsible for the generation of AKR [Wu & Lee 1979] [Louarn & L’Queau 1996] [Yoon & Weatherwax 1998].

It has been shown that the loss cone distribution produces cyclotron radiation above the electron cyclotron frequency with a finite axial wave-number component parallel to the magnetic field [Wu & Lee 1979].

In 2000 Bingham and Cairns used plasma kinetic theory to derive the dispersion and growth of the R-X plasma mode due to a horseshoe shaped electron velocity distribution [Bingham & Cairns 2000].

The analysis conducted by Bingham and Cairns uses the susceptibility tensor [Stix 1992] to derive a dispersion relation for the R-X mode. The derivation assumes a weakly relativistic hot plasma component and a wave frequency that is close to the relativistic electron cyclotron frequency. In terms of the refractive index;

$$n^2 = 1 - \frac{\omega_p{}^2}{(\omega^2 - \Omega_{e0}{}^2)} - i\alpha_i - \frac{\left[-\frac{\omega_p{}^2 \Omega_{e0}}{\omega(\omega^2 - \Omega_{e0}{}^2)} - i\alpha_i \right]^2}{1 - \frac{\omega_p{}^2}{(\omega^2 - \Omega_{e0}{}^2)} - i\alpha_i} \qquad \text{Equation 2.44}$$

where, ω_p *is the angular plasma frequency,* Ω_{e0} *is the non-relativistic electron cyclotron frequency,* ω *is the wave frequency.*

The coefficient α_i for the imaginary component is given in terms of the momenta variables, p, μ_p;

$$\alpha_i = \frac{1}{4} \frac{\omega_{pe}{}^2}{\Omega_{e0}{}^2} 2\pi m^2 c^2 \int_{-1}^{1} d\mu_p (1 - \mu_p{}^2) p^2 \left(\frac{\partial f_e}{\partial p} - \frac{\mu_p}{p} \frac{\partial f_e}{\partial \mu_p} \right) \Bigg|_{p=p_0} \qquad \text{Equation 2.45}$$

where, $\mu_p = \cos\theta = \frac{p_{//}}{p}$ *, p is the electron momentum,* $p_{//}$ *is the parallel component of electron momentum,* p_0 *= is the resonant momentum.*

The first term in Equation 2.45 is destabilising which results in a growth of the R-X mode if $\partial f / \partial p$ is positive. The second term, however, tends to stabilise and is negative.

The stabilising term will tend to zero for μ_p becoming uniform on the interval $\mu_p \in [-1,1]$. If μ_p becomes uniform across the full range of pitch factors, a pronounced horseshoe shaped electron velocity distribution has been formed. When a full horseshoe shaped velocity distribution is formed then $\partial f_0/\partial p$ is maximised and the first term is dominant, this results in a large positive α which means there will be significant growth in the R-X mode, Figure 2.14.

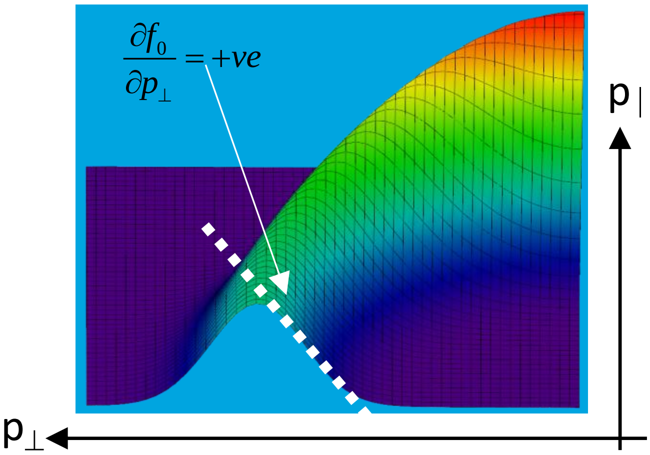

Figure 2.14**:** A visual representation of the horseshoe distribution.

Chapter 3

Electron beam sources and physics

This chapter presents the theory of electron beams, electron guns and emission mechanisms. Various emission processes are discussed, with a focus on explosive electron emission as this is the type of emission employed by the velvet coated electron gun in the experiment. The chapter also has descriptions of properties characterising an electron beam.

3.1 Emission regimes

For the purpose of electron beam production, there are three primary regimes of electron emission from a cathode surface that can be identified. The regimes comprise of space charge limited emission, temperature limited emission, and field dominated emission. For a given material, each behaviour occurs over a different range of values in the applied electric field. For each electron emission regime there is a different theoretical description and governing equation. Figure 3.1 below contains a summary of the mechanisms which dominate current flow for a low work function cathode emitter surface with respect to the applied electric field.

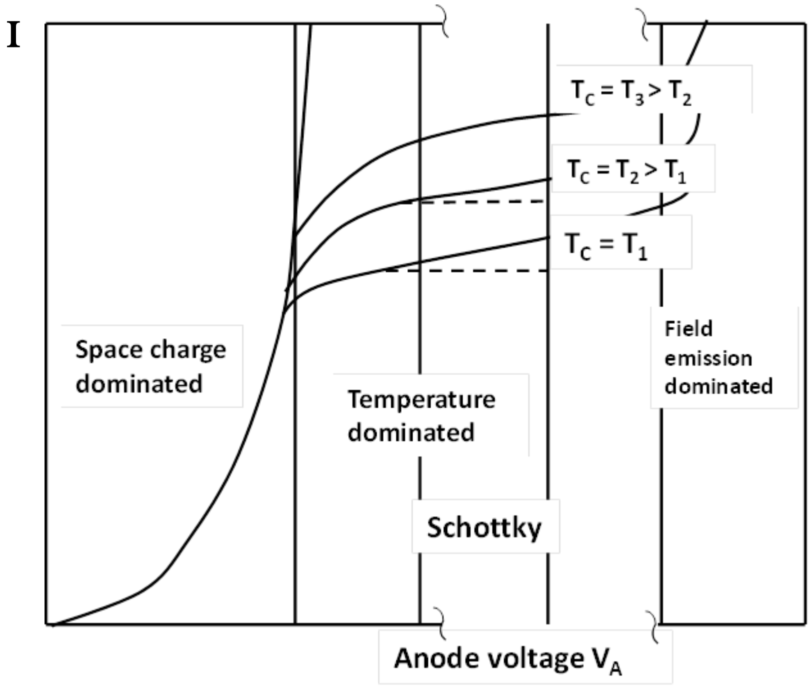

Figure 3.1: Plot representing various electron emission regimes in terms of applied electric field and resultant emitted current density.

3.1.1 Thermionic emission

At temperatures above absolute zero, some electrons have sufficient energy to escape from the surface of a solid. As the temperature increases the number of electrons with sufficient energy to escape increases. Electron emission resulting from the heating of a surface is referred to as thermionic emission.

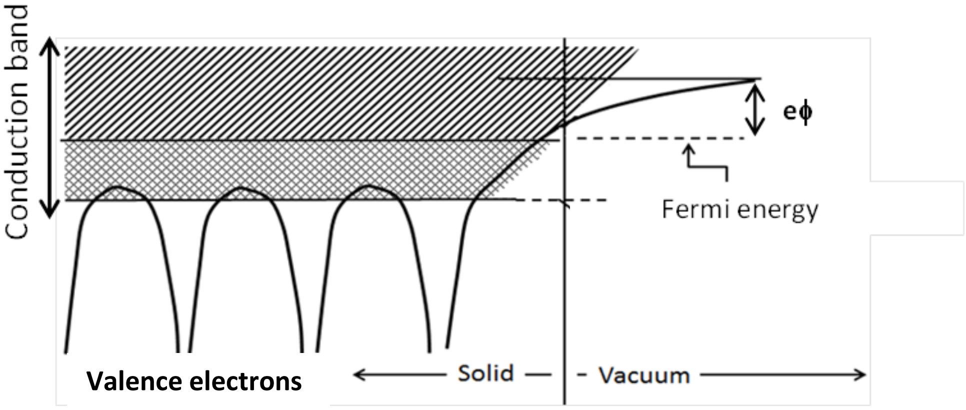

Figure 3.2**:** Energy level diagram for electrons near the surface of a metal.

Thermionic emission can be explained through Figure 3.2. The figure is an energy level diagram for electrons near the interface between a metallic solid and vacuum. In the solid, the parabolic curves represent electron energy levels adjacent to atoms. The upper energy levels merge in metals to form a conduction band. The difference in energy between the Fermi energy in the conduction band and the vacuum level adjacent to the solid is known as the work function and is denoted by $e\phi$.

Electron emission, from a solid, results from electrons in the solid having sufficient momentum directed toward the surface to overcome the potential barrier (work function) and to escape from the solid. The thermionic emission current can be predicted by considering the density of the allowed electron energy states and the probability of their occupation. An electron energy distribution can be obtained by multiplying the density of states by the probability of occupation, the density of states is illustrated in Figure 3.3.

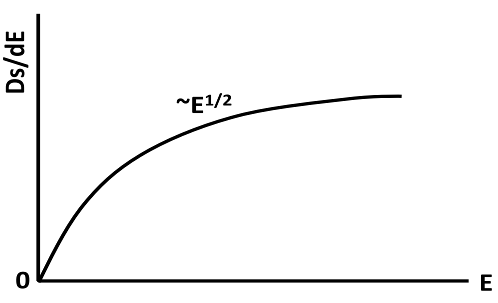

Figure 3.3**:** Density of states as a function of energy.

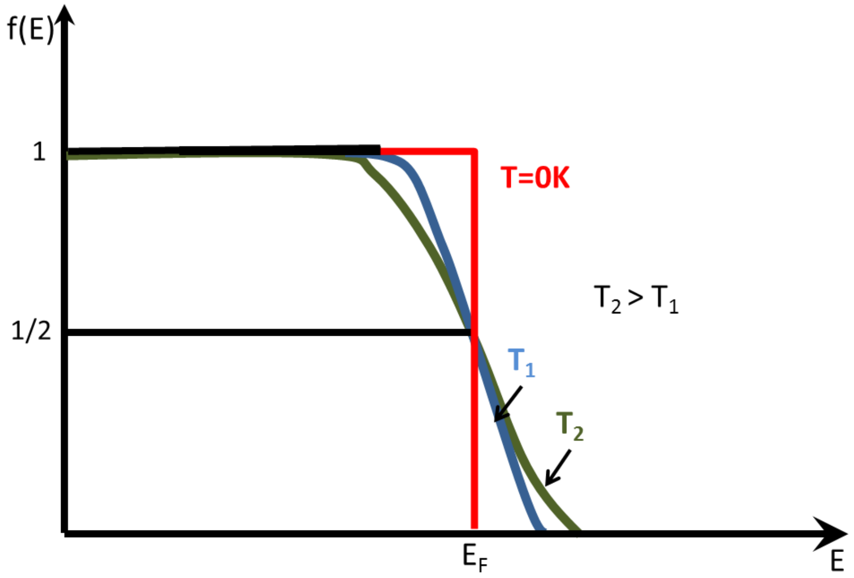

Figure 3.4**:** Fermi-Dirac distribution function.

Only electrons at the “tail” of this distribution i.e. the high energy end will have sufficient energy to overcome the work function barrier and escape from the emitter. The strong dependence of electron density in the high energy “tail” on temperature is shown in Figure 3.4 which illustrates the occupancy probability for an available quantum state as a function of energy. The emission current density, J, is given by the Richardson-Dushman equation;

$$J = A_o T^2 e^{-\frac{e\phi}{kT}} \qquad \text{Equation 3.01}$$

where, e *= electron charge = 1.6 x* 10^{-19} *C,* k *= Boltzmann constant = 1.381 x* 10^{-23} *J/K,*

T *= temperature (K),* A_o *= 1.20 x* 10^6 *A/*m^2 *deg*^{2}*,* ϕ *= work function in eV.*

The most significant aspect of this equation is the exponential variation of current density with work function and the even stronger dependency on temperature. It is clear from looking at the Richardson-Dushman equation that to obtain high values of emission current density the work function must be low and the temperature must be high [Gilmour 1986].

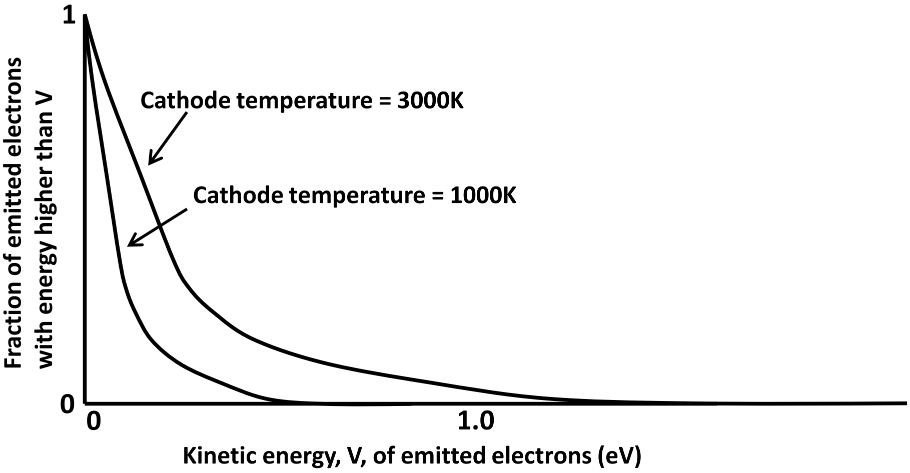

Figure 3.5**:** Kinetic energy distribution of thermionically emitted electrons.

3.1.2 Schottky effect

The Richardson-Dushman equation does not take into consideration the effect of an electric field at the cathode surface, although it has been found that when an electric field applied towards an emitting surface is increased the emission increases. This phenomenon can be explained by considering Figure 3.6, the applied field reduces the energy barrier that an electron must overcome in order to escape the emitter. The work function energy is reduced by $e\Delta\phi$ to become $e\phi - e\Delta\phi$;

$$\Delta\phi = \left(\frac{eE}{4\pi\varepsilon_o}\right)^{\frac{1}{2}}$$ Equation 3.02

where, E is applied electric field

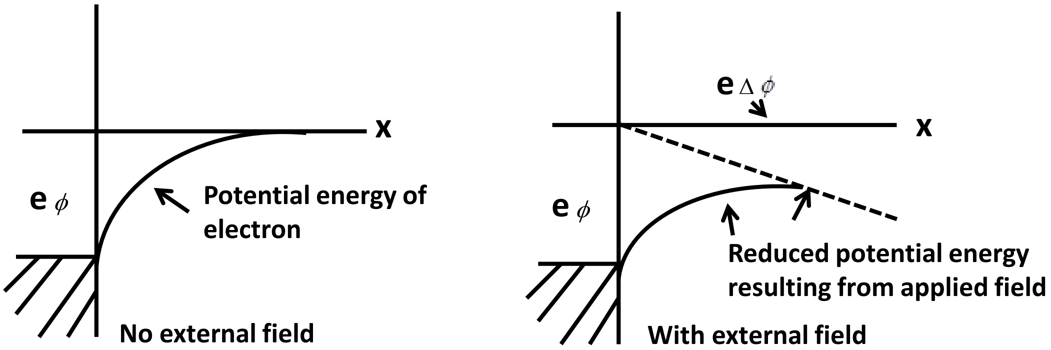

Figure 3.6**:** Illustration of the Schottky Effect.

With a new work function the Richardson-Dushman equation can be re-written for the modified current density as;

$$J = J_0 \; e^{\frac{e\left(\frac{eE}{4\pi\varepsilon_0}\right)^{1/2}}{kT}} \qquad \text{Equation 3.03}$$

where, J_o = Richardson-Dushman current density (“zero field” current density)

In determining J_o experimentally it is necessary to extrapolate from values measured at relatively high electric fields, as at low electric field levels electrons near the cathode surface alter the applied electric field. This is known as the *electron space charge effect*.

3.1.3 Space charge limit

The space charge effect can be explained as the effect of the negative charge of an electron reducing the potential that is present in the absence of the electrons. In the region near an emitting cathode where many electrons are present, the reduction in potential can be appreciable. This is shown for a parallel-plane diode in Figure 3.7.

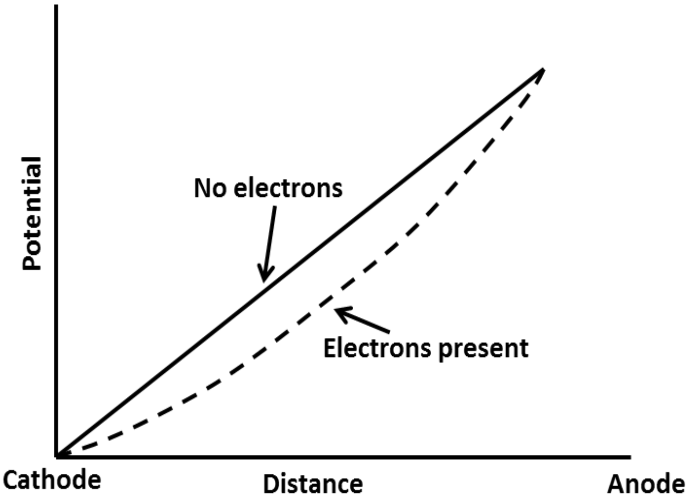

Figure 3.7**:** Potential distribution with and without electrons in a parallel-plane diode.

In the absence of electrons the potential increases linearly from the cathode to the anode. When electrons are present, the potential profile is depressed as indicated by the dashed line. As the electron emission rate is increased the potential is further decreased. There is a limit to how far the electron emission can be increased. This limit occurs when the density of electrons adjacent to the cathode surface becomes so large that it tends to depress the potential below zero. If the potential were to be negative, electrons would be forced back to the cathode. When the voltage is increased to a value high enough so that the cathode cannot supply sufficient current to maintain the space charge condition the cathode is said to be temperature (or possibly field) limited. Many RF and microwave tubes are designed to operate in the space charge limited (SCL) regime as this means that the current only depends on the anode voltage geometry and not the material properties of the cathode. The emission current limit is given by the Child-Langmuir Law;

$$J = \frac{4\varepsilon_0}{9D^2}\left(\frac{2e}{m}\right)^{\frac{1}{2}} V^{\frac{3}{2}} \qquad \text{Equation 3.04}$$

where, D is the gap separation, m is the mass of the emitted particle, V the gap voltage, ε_0 is the permittivity of free space, e the charge of the emitted particle.

3.2 Field emission

When an electric field is applied to an emitting surface the emission increases. It has been found that when the electric field applied to the surface of a cathode is increased to the 10^9-10^{10} V/m level the electron emission rate increases very rapidly, and much faster than the Schottky model will allow.

The potential energy profile of the surface barrier in this regime is like that of the Schottky effect except that the applied field is much larger. This makes the width of the potential barrier at the surface of the cathode very narrow, so narrow that some of the electrons can pass through the barrier, even though they don’t have sufficient kinetic energy to overcome it. The width of the barrier is a feature of the material and the electric field strength. This effect is known as the tunnelling effect and results from the quantum mechanical nature of the electron. The resulting electron emission is called field emission.

3.2.1 Fowler-Nordheim equation

The resulting electron current density due to the barrier tunnelling may be calculated. This is given by the Fowler-Nordheim equation.

$$J = \frac{AE^2}{\phi} e^{-\frac{B\phi^{\frac{3}{2}}}{E}} \qquad \text{Equation 3.05}$$

where, A and B are largely independent of electric field, A is 1.54 x 10^{-6} *[*$10^{4.54\varphi^{-1/2}}$*] and B is* 6.53×10^{9}*, E electric field in V/m, J current density in A/*m^2*,* ϕ *work function in eV.*

Fowler-Nordheim plots of log $1/E^2$ vs 1/E are the normal method for demonstrating field emission.

3.2.2 Field enhancement

If on an electrode, there exist small narrow formations of bulk metal, termed ‘whiskers’, then there will be a reduction in the field required for enhanced electron emission as they strongly influence the local surface electric field. There are different ways that whiskers can be formed; one of which is when a gap has been left unstressed for a period of time resulting in the commonly observed clean-up stressing of a diode or by exposing a diode to a DC electric field. Explosive electron emission can also result in the formation of whiskers, explosive emission creates whiskers when the cathode surface becomes locally molten and undergoes rapid cooling. An illustration of the form of such whiskers can be seen in Figure 3.8. At the tip of these whiskers the electric field is subject to enhancement. This means that even when the overall electric field is too small to support a field emission current over the macroscopic surface, due to the existence of the field enhancement a field emission current can initiate from the tip of the whisker. The field enhancement factor, β, characterises the field enhancement.

Figure 3.8**:** Illustration of the form of whiskers on the surface of stainless steel cathodes after exposure to fields of around 200kV/cm.

As whiskers occur on a microscopic level the complexity of the surface geometry makes an analytical approach to determine the local surface fields impractical, however a computer simulation can be used to determine these fields and thus the currents by applying the Fowler-Nordheim model [Feng & Verboncoeur 2005].

3.2.3 Latham hot electron model

The most appealing feature of the hot electron model is that it provides an alternative physical explanation of the Fowler-Nordheim pre-breakdown log $(1/V^2)$ vs $(1/V)$ trend. Although the Fowler-Nordheim emission from surface deformities is commonly accepted and has been demonstrated with manufactured surfaces it is likely that in the case of field enhanced electron emission from a bulk surface the conducting whisker theory is not enough to fully explain the experimental experience [Garven 1994], specifically there are not always whiskers observed in areas associated with field emission. There is an alternative model which was proposed by Latham and his co-workers. This model provided the first physical interpretation of the non-metallic emission processes, referred to as the ‘Hot electron model’, and is based on experimental observations. It has been assumed that the emitting micro-region is an insulating inclusion in the surface of the cathode, Figure 3.9.

In this regime when an external field is initially applied to the surface it will be able to penetrate the inclusion through to the metal substrate and therefore any electrons that manage to cross the metal-insulator interface will be accelerated.

For this reason very few of these electrons would be needed to cause a current avalanche through scattering processes. This particular type of inclusion switches between a non-conducting “off” state to a conducting “on” state. This model assumes that an initial threshold switching process occurs approximately every nanosecond in highly localised filaments or channels with high charge-carrier concentrations.

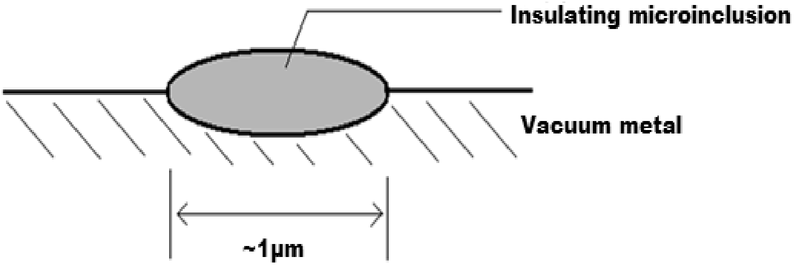

Figure 3.9**:** The physical micro-regime assumed to be responsible for non-metallic electron emission processes.

The Richardson-Dushman equation was applied to the emission process at the insulator-vacuum interface by Latham. This was done by expressing the electron temperature in terms of the applied potential and the resulting equation is shown in Equation 3.06.

$$I = A_0 a\left[\frac{2e\Delta d}{3k_B \varepsilon d}\right]^2 V^2 e^{\left[\frac{x}{\left(\frac{2\Delta d}{3d\varepsilon}\right)V}\right]} \qquad \text{Equation 3.06}$$

where, A_0 is the Richardson-Dushman proportionality constant, a is the area of emission site, Δd width of the insulating inclusion, ε the relative permittivity of the insulator, d electron gap separation, χ height of the surface potential barrier, V potential across the diode gap, I current.

This equation is very similar to the equation shown in Equation 3.05 which is the Fowler-Nordheim relationship. This resulted in Latham suggesting that there may be many situations where this type of emission occurs and was mistaken for field enhanced emission, similar to whisker type emission.

3.3 Explosive electron emission

3.3.1 Cathode flare formation

Explosive emission occurs due to plasma formation around the front of a cathode face, the mechanism responsible for the plasma formation is generally believed to be either electric field enhancement at the tip of individual metallic whiskers on a surface or a surface flashover process and/or dielectric breakdown induced along the length of an insulating inclusion. A space charge limited current can be drawn from the plasma which behaves much like a cathode surface with a low work function. The emission current will lead to Ohmic heating of the plasma cloud which expands away from the cathode surface and into the anode-cathode gap.

Explosive electron emission arises due to rapid Ohmic (Joule) heating, when the electric field exceeds the limit for stable field emission of an enhanced emission site, caused by the emission current which it is carrying. Typically the process may become a ‘runaway’ as the resistivity increases and thermal conductivity decreases with temperature, the material reaches melting point which causes the emission site to explosively sublimate/vaporise. Once the explosion event has occurred, the gas cloud that has resulted expands and becomes ionised by the emission current from the extremely hot underlying cathode. The field enhanced emission current (see theory section 3.2.2 & 3.2.3) is strongly localised so the heating effect can be severe even at low total current.

3.3.2 Flare expansion velocity

Experimental techniques have measured the cathode flare expansion velocity [Mesyats & Proskurovsky 1989]. Analysis has shown that the cathode material has a strong influence on the expansion velocity, however, it is not strongly affected by the electric field strength applied in the gap. The influence of the magnetic field has also been investigated, and it was found that the flare velocity could be reduced by a factor of about 25% by application of a magnetic field transverse to the electric field. The expansion velocity of the outer surface of the plasma flare was constant, independent of the distance from the cathode, which suggests an adiabatic nature for the expansion, the driving energy being the stored thermal energy of the exploded enhanced emission site. Mesyats and Proskurovsky [Mesyats & Proskurovsky 1989] estimate the thermal energy stored in the microemitter and use the adiabatic model for the expansion in order to derive an expression that predicts the plasma front expansion velocity.

$$v_e = \sqrt{\left(\frac{4\gamma_A}{\gamma_A - 1}\right)\frac{j^2 \kappa t_d}{\pi^2 \rho_c}} \qquad \text{Equation 3.07}$$

where, $\frac{j^2 \kappa t_d}{\pi^2 \rho_c}$ $=E_T$, γ_A *is the adiabatic parameter,* v_e *is the expansion velocity,* κ *is the resistivity,* ρ_c *is the cathode material density, and* E_T *is the thermal energy (per unit mass) heating the solid whisker.*

Equation 3.07 gives an estimate of the value of the expansion velocity. The expansion velocity of the front of the cathode flare is a particularly significant parameter in the operation of long pulse plasma flare cathode systems. The outer limit of the expanding plasma is effectively the emission surface as far as the Child-Langmuir law is concerned; therefore the electrical behaviour of the diode is influenced by the evolving geometry. If this type of diode is used as a beam source in a microwave generator then the geometry changes that are caused by the expanding plasma are frequently found to be responsible for terminating the operation of the instability in the source [Ronald 1996][Ronald et al. 2011]. It is possible nonetheless to operate such devices in rapid sequences of short pulses [Spark et al. 1994].

The experiment discussed in this thesis utilises a velvet coated cathode, velvet has a plasma expansion velocity of ~2x10^{6}cm/s. Approximate values for other materials include; tungsten 2-2.5x10^{6}cm/s, aluminium 2.4x10^{6}cm/s and copper 2.4x10^{6}cm/s [Mesyats & Proskurovsky 1989].

3.3.3 Interaction between emission sites

If a cathode has not had micro-protrusions created artificially on the surface the explosive emission sites can potentially occur anywhere there is an enhanced emission site. Only a few of these actually need to convert to explosive emission to support current up to the space charge limit. The screening effect and the relay effect can explain the manner in which emission sites interact with each other. The screening effect, suppression of new sites, occurs in the surrounding area of a ‘primary’ or initial explosive electron emission site which will have formed at the site of a particular efficient field emitter. The electrons emitted from the plasma cause a space charge depression of the electric field at the cathode surface. The suppressed field is insufficient to cause the conversion of any other field enhanced emission sites to the explosive emission mode; this increases the inhomogeneity in the electron emission current density at the cathode. The screening effect can be suppressed by applying a magnetic field, as the field confines the electrons close to their point of origin, Figure 3.10.

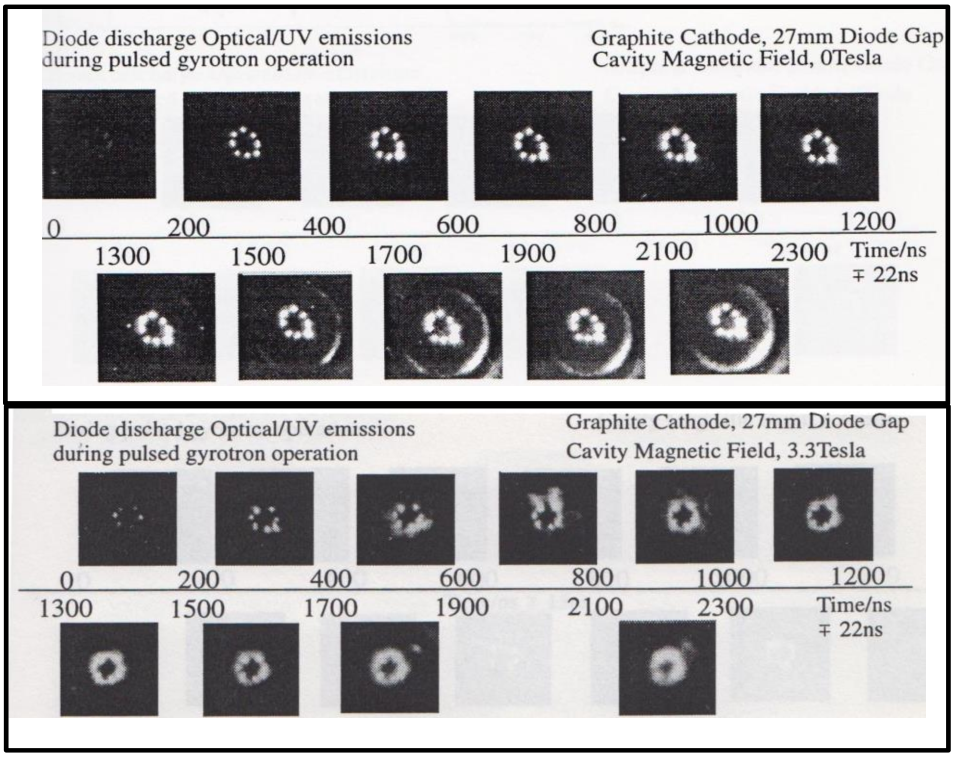

Figure 3.10**:** Illustration of the magnetic field effect on the cathode flare distribution density in a coaxial diode with a cylindrical graphite cathode, increasing from a cathode magnetic field value of 0T to ~0.1T [K. Ronald, 1996].

This is significant in the case of the co-axial magnetically insulated type of diode commonly used as the beam source in high current microwave tubes. The influence of the magnetic field upon the screening effect in this type of diode is usually at its greatest when the magnetic field is at relatively low magnitudes; where the Larmor radius of the electron orbits is greater than the magnitude of the cathode flare plasma itself [Mesyats and Proskurovsky 1989].

The regeneration effect refers to the activation of new sites nearby a site of explosive emission. The high pressure of a plasma in the region above a primary explosive electron emission site causes the formation of a new potential sites of explosive emission very close to the area of the original. A relay effect exists that can cause the formation of emission sites at much greater distances. Periodical variations in the plasma density profile can cause the emission current to have a ‘burst’ nature. This type of behaviour has been noted to coincide with periods of high potential in the fringes of the cathode flare plasma, this may cause sufficient enhanced electron emission resulting in the explosion of microprotrusions. Many cathode surfaces contain insulating inclusions and/or layers and charging of these layers by the particle flux can result in the layers breaking down due to the high field. Magnetic fields can influence the relay effect, which appears to progress preferentially in the direction of the Lorentz force on the particles.

3.4 Electron beam transport

A collective of charged particles can be defined in several ways depending on its characteristics, for instance if a group of charged and neutral particles exhibits collective behaviour within a quasi-neutral gas then it is called plasma. However if the particles concerned are mostly moving in the same direction i.e. the flow of particles is coherent and they have little kinetic velocity spread then this is regarded as a beam. Beams are characterised macroscopically by the type of particle, the average kinetic energy of the particles, the current, the power and also the pulse length. The orbits and trajectories of a beam depend on the fields surrounding it and the fields arising from the particles within the beam. Beam characteristics are important in applications such as particle accelerators, microwave devices and laser plasma interactions. Beams are often cylindrical in shape however other forms are possible such as a sheet beam. Here the beam has very large transverse dimensions in one dimension in comparison with the other.

In the transportation of beams it is sometimes necessary to be able to “distort” the beam by deflecting or curving it in some way, this is possible with the use of a transverse electric or a magnetic field. Typically the divergent space charge forces are countered by the Lorentz force of the particles interacting with a strong axial magnetic field. This section focuses on the fundamental physics behind beam transport, which describes what happens when an electron beam has left the electron gun.

3.4.1 Phase space

As previously mentioned, a beam is an ordered flow of particles. It becomes beneficial to examine the particle dynamics of such a large number of particles in six dimensional phase space. At any given point in time, phase space represents the complete parameters of the particle orbits, so now instead of a particle being described by the vector (x(t), y(t), z(t)) it is described by both space and velocity axes, becoming (x(t),y(t),z(t), v_x(t), v_y(t), v_z(t)) for non-relativistic particles. In the case of relativistic particles it is better to use momentum axes (x(t),y(t),z(t), p_x(t), p_y(t), p_z(t)). Velocity is not a very useful quantity to characterize relativistic beams because all the particles will be travelling at approximately the speed of light and their kinetic energy is comparable to or greater than their rest energy.

3.4.2 Liouville’s theorem

Liouville’s Theorem, named after the French mathematician Joseph Liouville, states that the phase space distribution function must be constant along the trajectories of a system i.e. the phase space density of the system remains constant with time. It describes the time evolution of the phase space distribution function.

In describing the equation governing this, consider a dynamical system with canonical coordinates q_i and conjugate momenta p_i, where i=1,...,n. The phase space density ρ(p,q) determines the probability ρ(p,q) d^nqd^np that a particle will be found in the infinitesimal phase space volume d^nqd^np.

The Liouville equation governs the evolution of ρ(p^n,q^n;t) in time t:

$$\frac{d\rho}{dt} = \frac{\partial\rho}{\partial t} + \sum_{i=1}^{n}\left[\frac{\partial\rho}{\partial q_i}\dot{q}_i + \frac{\partial\rho}{\partial p_i}\dot{p}_i\right] = 0$$ Equation 3.08

where, $\dot{q}_i = \frac{\partial H}{\partial p_i}$ *and* $\dot{p}_i = -\frac{\partial H}{\partial q_i}$ *. H is the Hamiltonian (H=H(q,p,t) which corresponds to the total energy of the system).*

The expected total number of particles is the integral over phase space of the distribution:

$$N = \int d^n q d^n p \rho(p,q)$$ Equation 3.09

In the simple case of a non-relativistic particle moving in Cartesian space under a force with coordinates q and momenta p, Liouville's theorem can be written;

$$\frac{\partial\rho}{\partial t} + \frac{p}{m}\cdot\nabla_x\rho + F\cdot\nabla_P\rho = 0$$ Equation 3.10

This equation illustrates that in a conservative system the distribution function is constant along any trajectory in phase space [Swann 1933].

3.4.3 Laminar and non-laminar beams

When considering beam transport it is important to understand the order and disorder in beams.

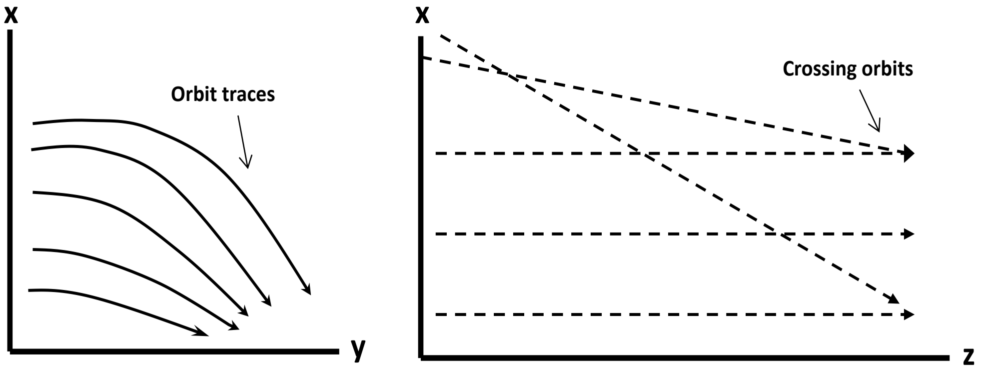

(a) (b)

Figure 3.11**:** Motion of beam particles viewed in configuration space (a) particle orbits in a laminar beam (b) downstream projection of particle orbits for a non-laminar distribution.

A brief definition of beam order is presented here. A beam that is ideal has laminar particle orbits. A pure laminar flow cannot be achieved in practice but it is often possible to achieve a good approximation. For a beam to be laminar the three velocity components must have values uniquely defined for each spatial position in the beam. Particles close to each other remain neighbours throughout the spatial extent of the beam. Referring to Figure 3.11**a** this illustrates the motion of a laminar beam in configuration space and Figure 3.11**b** illustrates a non-laminar beam in configuration space as two particles at the same position have different transverse velocities, thus breaking one of the conditions for a beam to be laminar. Here, the particles may have multiple values of transverse velocity at a single point in space. A laminar beam can be focussed by an ideal lens to a point of zero dimension. The lens displaces the distribution in the v_x direction in a manner appropriate to the spatial distribution of the particle's velocity, while preserving the projected length along the x axis. As particles in a non-laminar beam have a range of transverse velocities at a given location, it is impossible to focus the beam by aiming all particles from all given locations in the beam towards a common point with a simple ideal lens.

3.4.4 Phase fluid

When plotted in phase space, the trajectories of large numbers of particles have a high degree of order if forces vary smoothly in space. Beams which have good parallelism are easier to transport than beams with diverse transverse velocity components. Orbits in phase space, with similar phase space coordinates and no collisions, will always be neighbours.

As mentioned in section 3.4.3, beams that have orbits in a laminar beam flow will never intersect, as two trajectories approach each other the forces acting on both particles becomes identical. These rules of phase space allow for the study of a large number of particles by developing theory and equations for their collective behaviour. As phase space allows for the description of collective behaviour for a large number of particles, it can follow that this is very similar to the description of a fluid, hence why the phase space for a collection of particles can be referred to as a *phase fluid*.

3.4.5 Beam emittance

In reality beams are not perfectly formed. The quality of a beam is a prime factor determining how well it may be transported over large distances, focused into a small space with a minimum divergence and form high-resolution images. The net volume occupied by a beam may be constant in phase space (see theory section 3.4.1) but it is possible for variations in magnetic fields to distort the distribution which in principle can be reversed by reversing the particles orbits. It is helpful to define a quantitative representation of the quality of a beam. This is achieved through measuring how parallel and localised it is, quantified as its emittance. The smaller the phase space occupied by the beam the higher the quality of the beam.

The term beam brightness was defined for conventional optics in order to quantise the quality of a light source. In particle beams it is the current density per unit solid angle in the axial direction. A beam which is bright has high current density and has highly parallel particle trajectories. The concept of beam brightness was introduced by Van Steenbergen as $B=I/V_4$ where V_4 is the hypervolume in the four dimensional trace space. Brightness is normally expressed in terms of the current divided by the product of the emittances along the transverse x and y axes, which can be related to the volume by assuming a simple geometrical shape [Rhee 1992] [Worster 1968].

The minimum phase-space volume is established by the characteristics of the region of formation. Emittance is typically measured in terms of position and transverse angle rather than transverse velocity because the inclination of particle orbits can be measured directly. The angle the beam makes with the axis of symmetry is denoted as x'=dx/dz and y'=dy/dz.

If the beam is near paraxial the relationship between the inclination angles and the transverse velocities is, x`= $v_x/v_z$ and y' = $v_y/v_z$. The coordinates (x, x`, y, y') are generally treated as functions of z rather than time t. As they describe the trace of a particle orbit along the axial direction the space defined by these coordinates is called trace space. Transverse emittance is the effective 4D volume occupied by a distribution in trace space and may be quantified by a designated distribution boundary.

This boundary is designated by the representation in Figure 3.12; the area is defined by an ellipse denoted by the dashed line.

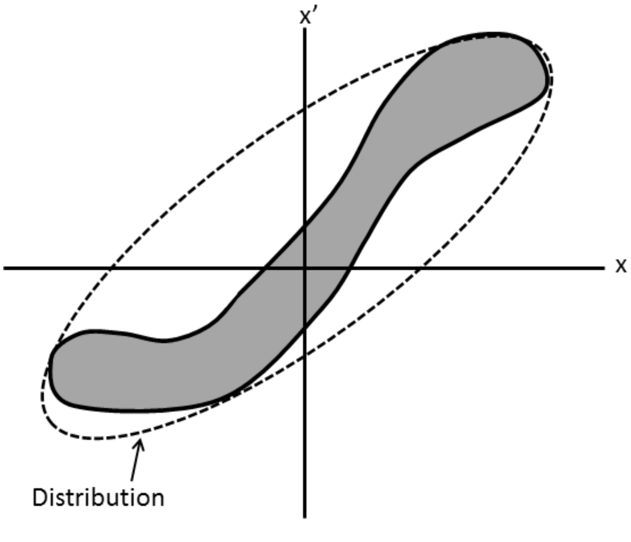

Figure 3.12**:** Particle velocity/position distribution denoted by the grey area. The dashed line round the outside represents a minimum area ellipse, enclosing the distribution.

The curve represents the smallest elliptical area that contains all the orbit vector points, the area of this ellipse divided by π is the emittance;

$$\varepsilon_x = \iint dx dx' / \pi \qquad \text{Equation 3.11}$$

Figure 3.12 illustrates an ellipse which is defined around a distribution with the major and minor axes aligned with the x-x' coordinate axes.

An ideal lens allows a laminar beam to be focused to a smaller dimension. As a beam is focussed through an ideal lens the dimension of the ellipse in the x direction will decrease, however the values of x' will necessarily increase with increasing 'x' to allow the focussing to take place. The minimum space in the ellipse remains consistent with Liouville's theorem (see theory section 3.4.2).

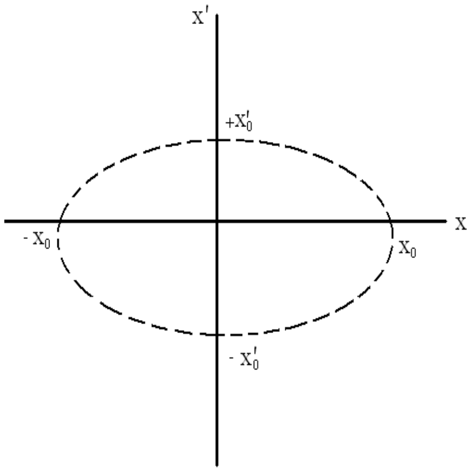

Figure 3.13**:** Upright trace-space ellipse, enclosed emittance equals $x_0x'_0$ in units of π-m-rad.

If we consider a beam with no initial divergence in its velocity, spread over a range Δx, i.e. along the x axis in Figure 3.13, the lens will displace the distribution in the v_x direction although conserving the projected length along the x axis. During transit through the drift region, of length f, the orbit vectors will converge towards x=0. The orientation of the distribution will change until it aligns with the v_x axis at the focal point. Since the particles in a non-laminar beam have some random distribution in their transverse velocity at any location; at a position x the particles will have different values of v_x and a spread in directions. Stemming from the disorder of a non-laminar beam it becomes impossible to aim all of the particles to a single point, a point focus.

The phase space representation of the incident beam is no longer a simple line as it is for the case of a laminar beam. Non-laminar beams occupy a finite area in phase space, when the ellipse transforms as it did for the case of the laminar beam it also ends up aligned along the v_x axis.

In an ideal focussing system emittance is a conserved quantity; which makes it possible to detect imperfections in a confinement channel by analysis of growth in emittance [Agapov et al. 2007][Anderson et al. 2002][Felba 1999][O'Shea 1998].

3.4.6 Busch's theorem

Busch's theorem [Humphries 1999][Tsimring 2006] states that, when beam optics consist of non-dissipative axial invariant elements, such as drift solenoids, or axisymmetric RF fields then the canonical angular momentum of any particle is preserved. Busch's theorem relates the angular velocity of a charged particle in an axially symmetrical magnetic field to the flux enclosed in a circle centred on the axis and passing through the particle.

$$mr^2\dot{\theta} + \frac{q}{2\pi}\psi = p_\theta = const \qquad \text{Equation 3.12}$$

where, ψ is the magnetic flux enclosed by the particle in the equilibrium region. The value of p_Θ is determined by the magnetic field configuration at the emitter surface of the source and $\omega = \dot{\theta}$is the angular frequency.

Consider two special cases which can each be achieved with two co-axial solenoids, axially displaced and separated by an annular iron plate, where the magnetic field at the source is B_S and in the downstream region, B_0. If the source solenoid is off, then all of the magnetic flux generated by the other solenoid passes radially outward through the iron plate and the source is in a field free region. If the magnets produce a magnetic field of the same strength but opposite polarity the system presents a magnetic cusp. The geometrical contribution to the canonical angular momentum is determined by the magnetic flux ψ enclosed by the particle's initial orbital radius r_S.

$$P_\theta - mr^2\dot{\theta} = \frac{q}{2\pi}\psi_s = \frac{q}{2}B_s r_s^{\,2} \qquad \text{Equation 3.13}$$

In each of these two field geometries, the particles start with zero initial rotational velocity and cross magnetic flux lines and rotate in the uniform field of the downstream equilibrium region. The rotation frequency, ω, in the cusp case is twice as large as in the configuration of a magnetically shielded source. From Busch's theorem it is possible to obtain the angular frequency of the particles in the downstream equilibrium region;

$$\dot{\theta} = \omega = \frac{1}{mr^2}\left(\frac{q}{2\pi}\psi_s - \frac{q}{2\pi}\psi\right) \qquad \text{Equation 3.14}$$

where $\psi = B_0 r^2 \pi$ is the flux enclosed downstream, it is possible to write the relation as;

$$\omega(r) = \omega_L\left(\frac{\psi_s}{\psi} - 1\right) \qquad \text{Equation 3.15}$$

where, ω_L is the Larmor frequency, and ω is the angular frequency perceived from the axis of the centre of the solenoids not the guide centre of the particles which is ω_{ce}.

3.5 Beam focusing

In order for a beam to be of an adequate quality for most applications, it must be transported in an efficient and proper manner. Beam transport can be affected by several factors one of which is disorder in the beam; difficulty arises in transportation if the beam is composed of large diverse transverse velocity components. The most conventional way of transporting a beam is to apply a strong unidirectional magnetic field generated by long solenoids to confine the beam, whilst another effective way is to use sequences of electrostatic or magnetostatic lenses. This section discusses the use of electric and magnetic fields to shape the transverse motion of these particles.

Particles in beams will always have components of velocity perpendicular to the main direction of motion. This can arise from many different factors; it can originate from the injector as fields here can have imperfections of shape (or in certain applications may be specifically designed to induce transverse motion). As charged particle sources normally work at high temperatures so the particles may have random thermal motions. Velocity spreads and space charge repulsion act to increase the beam radius.

The main function of a lens is to sort particles according to their points of exit from the object and organise their convergence to corresponding points of the image. Two of the most important qualities a lens must provide is a stigmatic image and also geometric similarity of an image to an object. Explaining these respectively, rays emanating from any point of an object through a plane perpendicular to the optical axis must intersect after the lens at one point of the image in a plane perpendicular to the axis. The beam formed by the rays diverging from or converging to some point is called a homocentric beam. To achieve geometric similarity of an image, the distances between any points of an image have to be proportional to the distances between corresponding points of an object.

3.5.1 Focusing with magnets – the solenoid

A magnetic lens is a focusing system with a purely magnetic field. One of the most widely utilised magnetic focussing systems is the solenoid, as it is the only possible magnetic lens geometry which is consistent with cylindrical paraxial beams. The magnetic lens consists of a region of cylindrically symmetric radial and axial magnetic fields which are produced by axi-centered coils carrying azimuthal current, I, Figure 3.14 (or sections of magnetised material). This method is extensively used in cathode ray tubes, electron microscopes and electron accelerators.

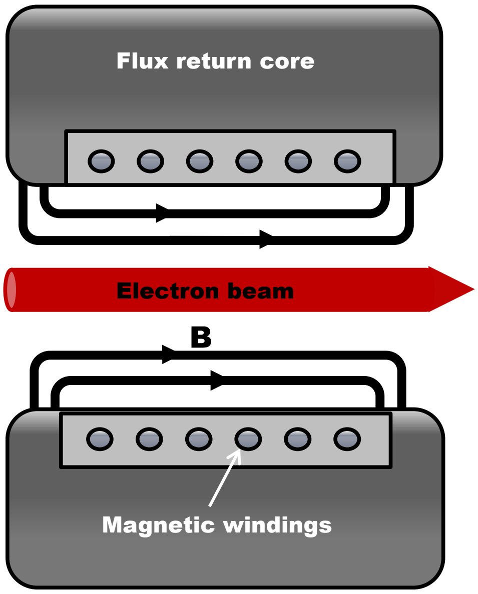

Figure 3.14**:** Schematic of solenoid magnet lens.

Since the magnetic field is static there is no change of particle energy passing through the lens. The magnitude of the magnetic field produced (by a long solenoid) can be determined using Equation 3.16 below.

$$B = \mu_o \frac{N}{L} I \qquad \text{Equation 3.16}$$

The particles enter the lens through a region of radial magnetic fields where the dominant Lorentz force, $qv_z \times B_r$, is azimuthal which gives rise to a v_θ component leading to a radial force when crossed into the B_z field inside the solenoid. The net effect is a deflection towards the axis, independent of charge state or direction. However, since there is a azimuthal velocity the radial and axial force equations must include terms for centrifugal and Coriolis forces.

$$\gamma m_o(dv_r/dt) = - qv_\theta B_z + \gamma m_0 v_\theta{}^2/r \qquad \text{Equation 3.17}$$

$$\gamma m_o(dv_\theta/dt) = - qv_z B_z - \gamma m_0 v_r v_\theta/r \qquad \text{Equation 3.18}$$

The equation of axial motion, v_z is constant. The motion of the particles through the lens can be described by the equations below, assuming γ, the relativistic correction factor, and r are constant and that the particle orbit has a small net rotation in the lens, so the Coriolis force can be ignored in Equation 3.16. By then using the substitution of $dv_\theta/dt = v_z \, dv_\theta/dz$, and by making use of $B_r = -\frac{r}{2}\frac{dB_z}{dz}$.

Equation 3.18 can be expressed in terms of canonical angular momentum,

$$v_\theta - qrB_z/2\gamma m_o = \mathit{constant} = 0 \qquad \text{Equation 3.19}$$

Equation 3.19 implies that particles gain no net azimuthal velocity passing completely through the lens, this occurs because the particles must cross negatively directed radial magnetic field lines at the exit that cancel out the azimuthal velocity gained at the entrance. However as the particles transit through the magnetic field, the Lorentz force may be used to balance the space charge and centrifugal drives to increase the radial profile of the beam or it may be used to lens the trajectories inwards. Systems which depend on a well-defined cyclotron motion of their operation will typically have one focussing system where all the B-fields point in the same direction, typically formed by an electromagnet. If only the axial motion is important then focussing can be achieved with sequential counter polarised magnetic elements in a lens chain, typically by permanent magnets.

Chapter 4

Experimental apparatus & diagnostics

This chapter presents details of the experimental apparatus explaining the function of each component, including the experimental accelerator and interaction region; the pulsed power system and the magnet coils. Measurement devices are also described; a Faraday cup for beam diagnostics; voltage probe techniques and diode current measurements; systems used for measuring microwave signal amplitude, spectrum, polarisation and propagation directions.

4.1 Experiment overview

4.1.1 Overall experimental set-up

As previously mentioned, a scaled laboratory apparatus was constructed to form an electron beam with a horseshoe distribution in velocity space and investigate the RF emissions produced by this beam. This chapter details the design of the various components and their assembly.

Figure 4.1 shows a photograph taken from the laboratory showing a frontal view of the full experiment and its position in the laboratory's shielded enclosure. Figure 4.2 also shows a photograph taken in the laboratory illustrating the electron injector region, the solenoids and the output waveguide. Figure 4.2 outlines the complete set-up including the water cooled solenoids and connection of the interaction waveguide to the vacuum pumps (see section 4.2). The experiment was operated under vacuum (see Appendix 1) in order to eliminate collisions between beam electrons and neutral gas particles.

Figure 4.3 is a drawing illustrating the main components of the experiment and Figure 4.4 illustrates the location of the experiment within the bay and illustrating the main components of the apparatus. Figure 4.5 and Figure 4.6 provide a detailed schematic diagram of the experimental layout and a list of the experimental components respectively.

A key element to the laboratory experiment is being able to reproduce elements of the magnetospheric environment. To mimic the auroral electrons travelling through a convergent magnetic field, it is necessary to inject an electron beam from an electron emitter which already exhibits an initial spread in velocity into an increasing magnetic field. The electron emitter and other components forming the electron gun are discussed in section 4.2.

Figure 4.1**:** Photograph showing a frontal view of the full experiment and its position within the surrounding lead and concrete walls. The metre stick against the wall gives a sense of scale.

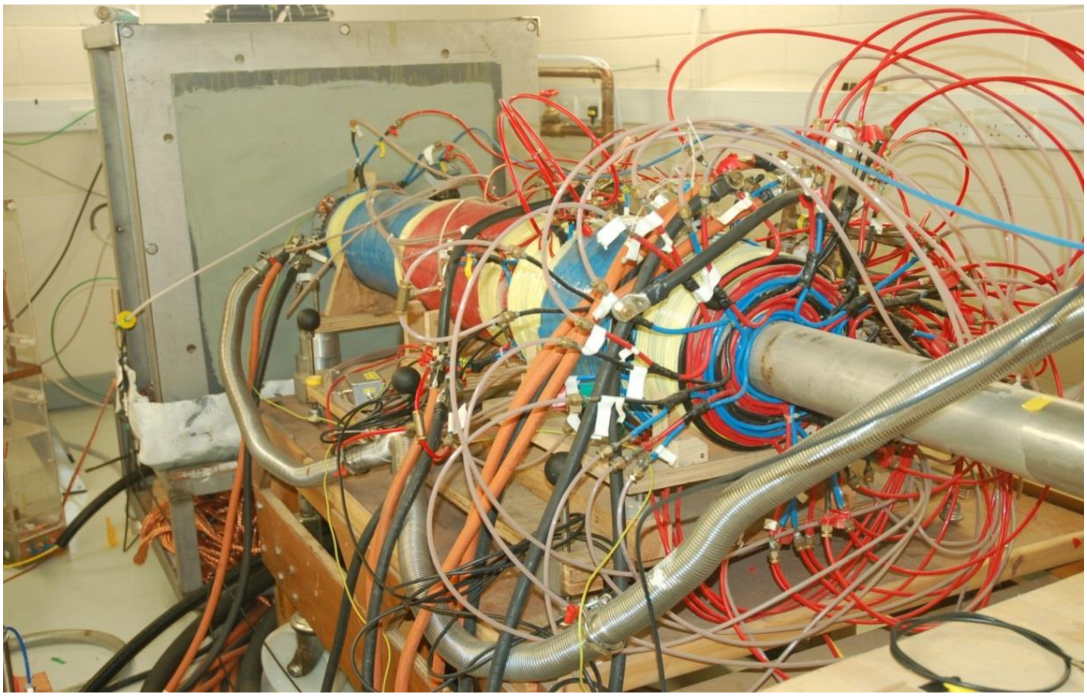

Figure 4.2**:** Photograph showing different aspects of the laboratory experiment, the cathode region, solenoids and the interaction waveguide.

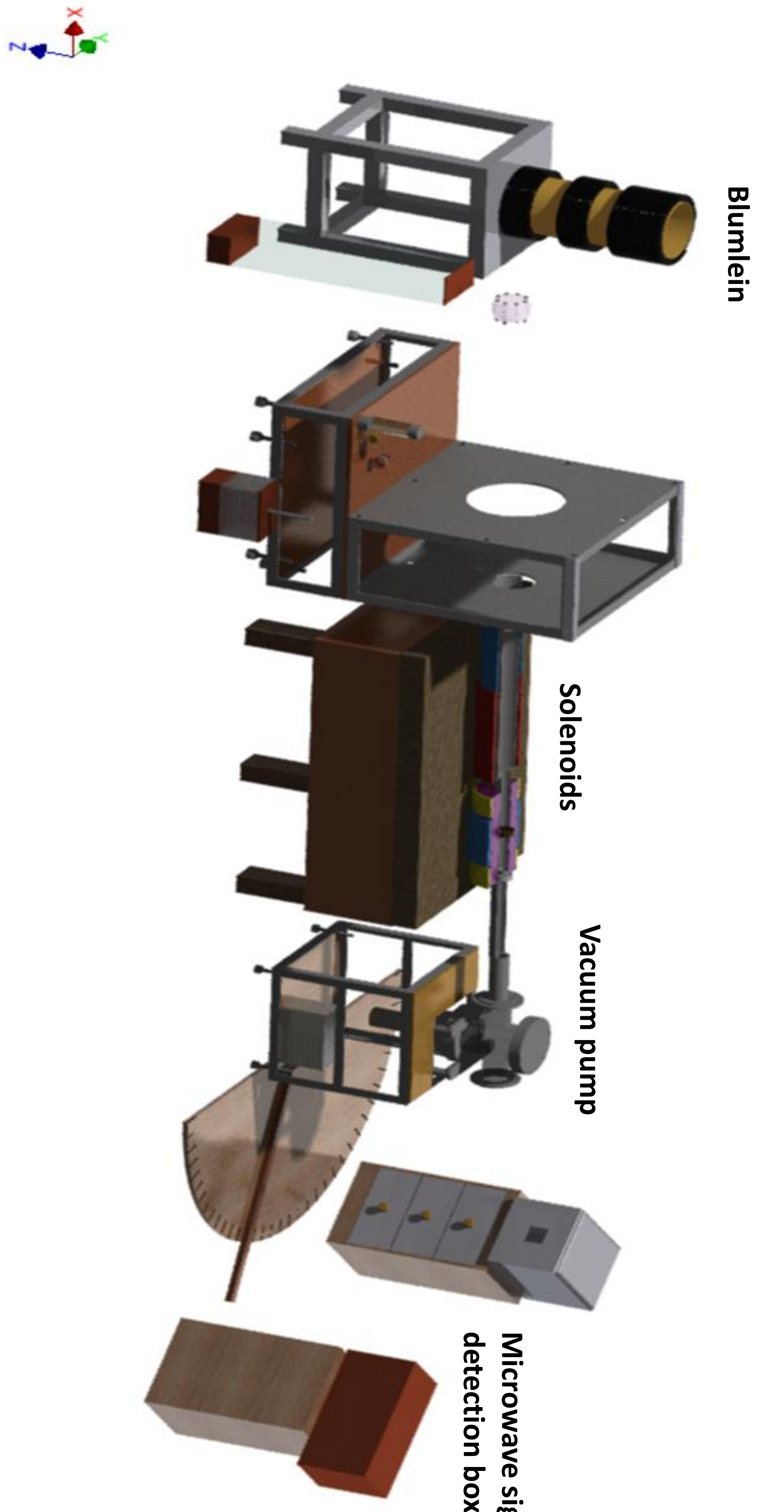

Figure 4.3**:** Perspective drawing of experiment illustrating main components.

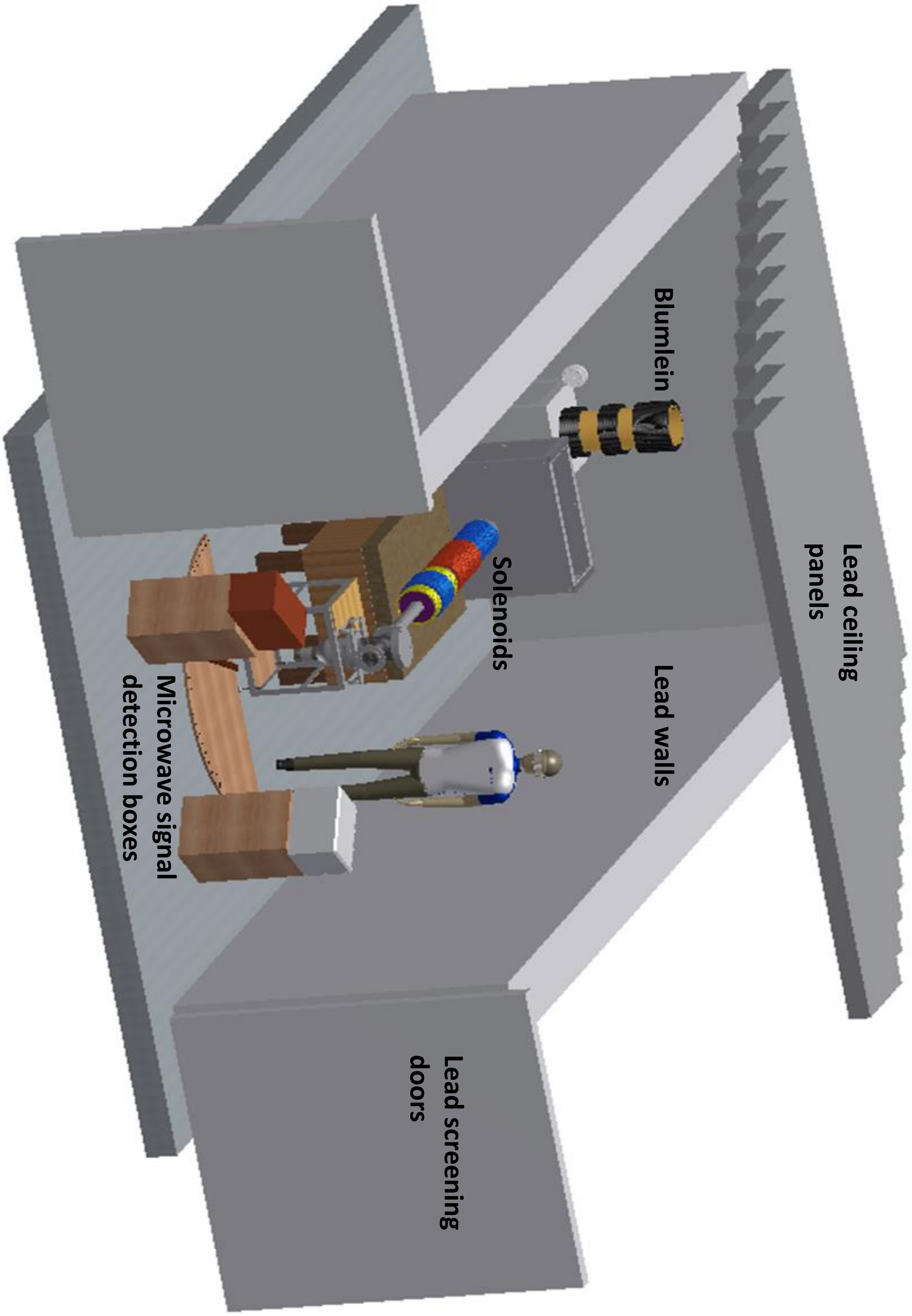

Figure 4.4**:** Drawing of experimental layout with position and relative size of various components in the lead and concrete shielded enclosure.

An HT firing circuit (see section 4.3) was created to energise the electron gun with pulses of 75kV-100kV. The magnet coils which focus the beam and their cooling system, are discussed in section 4.4. Section 4.5 discusses the microwave receiver diagnostics used to carry out the antenna scans and spectral measurements.

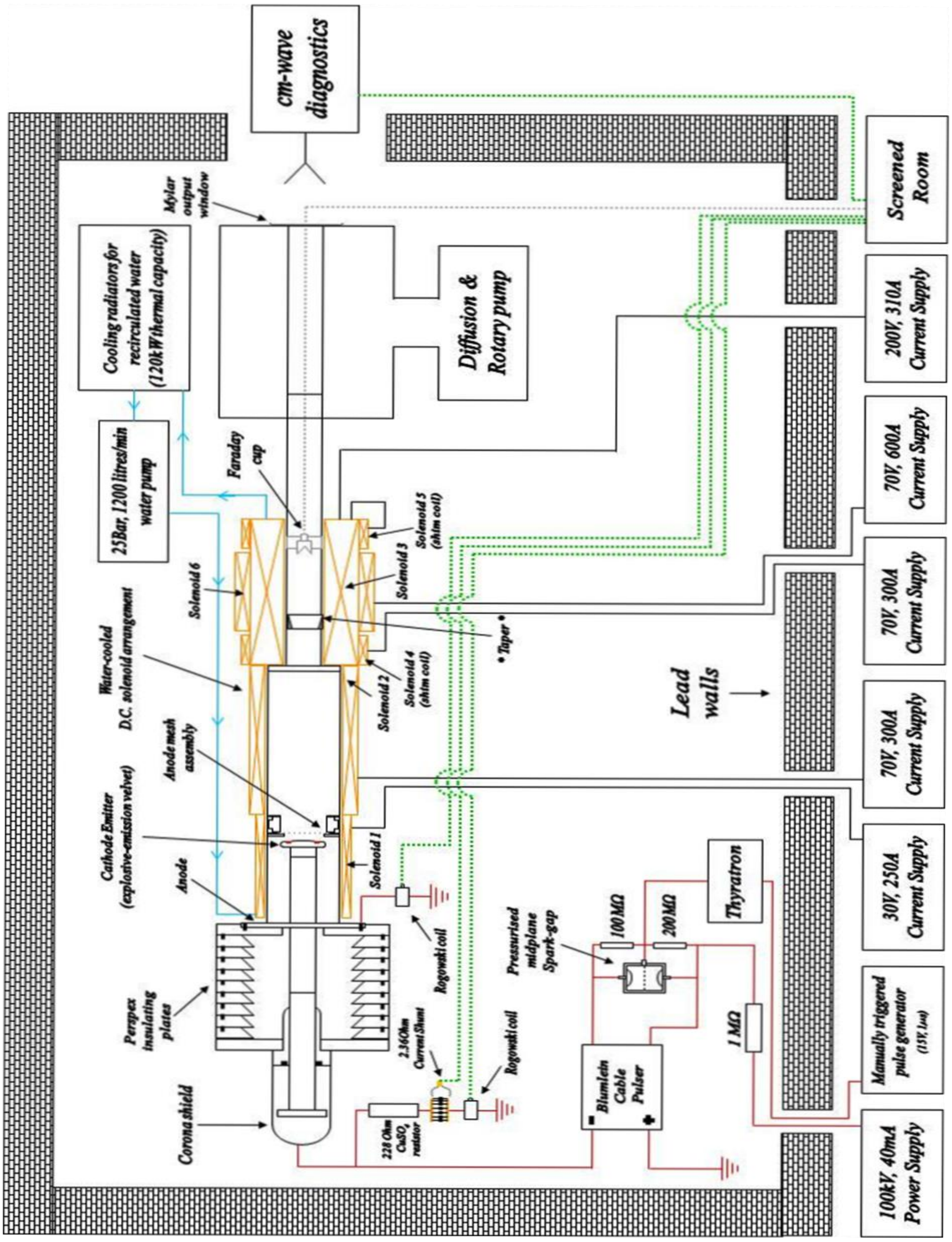

Figure 4.5: Schematic diagram of experimental layout, showing the interconnection of key components including the power supplies, diagnostics, vacuum envelope and magnetic field systems.

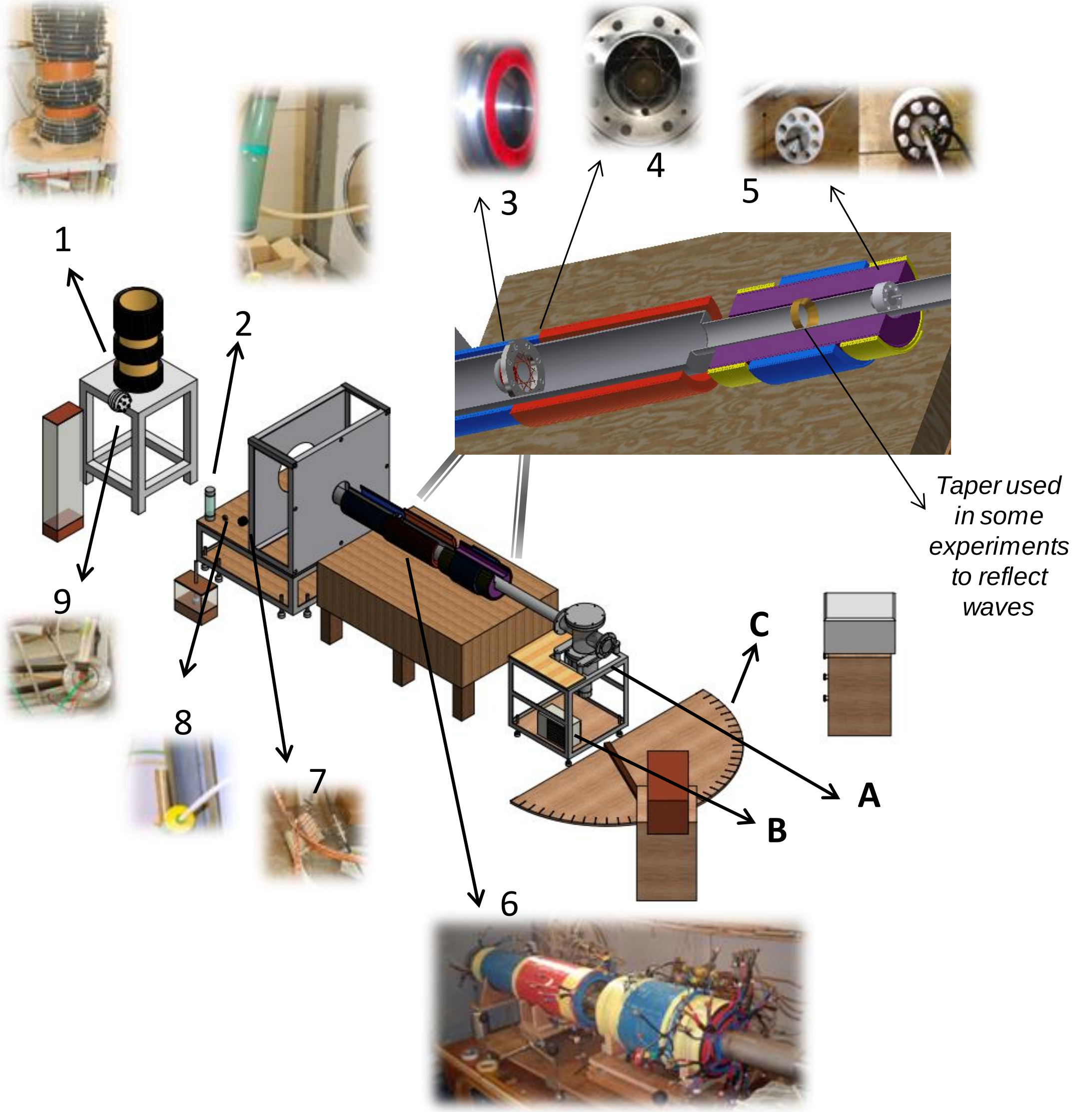

Part list: (1) Blumlein, section 4.3.1; (2) Copper sulphate resistor, section 4.3.2; (3) Velvet coated cathode, section 4.2.1; (4) Anode mesh, section 4.2.1; (5) Faraday cup, section 4.3.5; (6) Solenoids, section 4.4; (7) Shunt resistor, section 4.3.4; (8) Rogowski coil, section 4.3.3; (9) Spark gap, section 4.3.7; (A) Diffusion pump, Appendix 1; (B) Rotary pump, Appendix 1; (C) Microwave measuring equipment, section 4.5.4.

Figure 4.6**:** Detailed experimental layout, illustrating each component and relating this to the relevant section within the thesis.

4.2 Experimental vacuum and interaction region

The magnetospheric environment is highly non-collisional, this means that the electrons pass through all areas of interest without being subject to scattering by colliding with other particles. Conducting the laboratory experiments under vacuum, removing the majority of the gas molecules from the system, provides the capability to replicate this aspect of the magnetospheric environment in the laboratory. Here the mean free path must be increased until it significantly exceeds the distance travelled by the particles from their origin at the emitter until they reach the collector. The electrons are primarily subject to a collision with nitrogen molecules with a collision cross section of $q=15x10^{-20}m^2$ [Von Engel 1997]. The mean free path for a background pressure $\sim 10^{-6}$mBar is of the order $\lambda=\sim 1$km, which significantly exceeds the 2m trajectories of the electrons.

Figure 4.3 - Figure 4.6, is the Strathclyde experiment, the main vacuum envelope comprises a 16.12cm inner diameter, 1m long drift tube which is interfaced with an 8.28cm inner diameter 1.2m long interaction waveguide. The drift tube provides a sufficiently large bounding radius to accommodate the annular cathode emitter and large Larmor radii of electrons undergoing cyclotron motion at increasing pitch factors in relatively weak magnetic fields at the start of the magnetic compression system.

All flanges in the experiments are sealed with rubber O-rings. The vacuum was obtained using an Edwards RV12 rotary pump to reach the roughing pressure of $\sim 10^{-3}$mBar and to achieve a high vacuum, $\sim 10^{-6}$mBar, an Edwards Diffstak 100/300M oil diffusion pump was used. A baffle valve is used coupled with a roughing/backing diverter valve to isolate or engage the oil diffusion pump from the experiment.

A gas admittance valve and rotary pump isolation valve allows the vacuum system to be slowly and safely brought back up to atmospheric pressure for disassembly or maintenance. The vacuum pumps are interfaced with the internal volume of the experiments interaction waveguide via a sleeve-coupling vacuum flange.

4.2.1 Velvet coated cathode

The type of cathode used in the experimental simulation of AKR is an explosive emission (EE) velvet cathode. The surface of a velvet emitter consists of a layer of velvet cloth, ~0.5mm - 1mm thick, which is fixed to a metallic baseplate. Velvet is used as it is characterised by fine tufts of rather uniform dielectric fibres and it is these fibres that are responsible for initiation of the field emission process leading to plasma formation around the dielectric tufts.

The velvet cathode emitter surface has an annular configuration which can be seen in Figure 4.7. An important factor in the velvet cathode operation is the rate of plasma expansion, the plasma expansion of the velvet material used is ~$2x10^{6}$cm s^{-1}, with an associated drop-off in diode impedance. These factors dictate the maximum duration of the high voltage electron beam current pulse that may be generated by a given diode configuration (i.e. anode/cathode gap spacing).

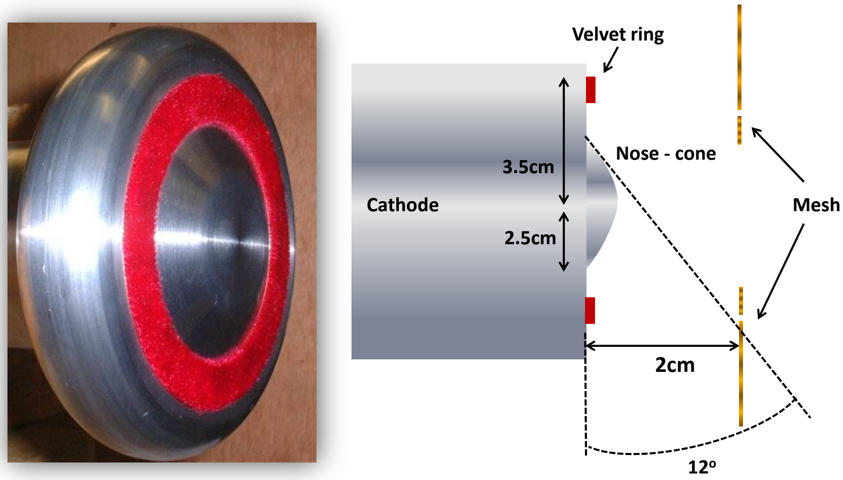

Figure 4.7**:** View of an annular dielectric velvet cathode surface, with schematic diagram illustrating dimensions and nose cone angle.

The maximum pulse duration for velvet cathode operation is determined by the point at which breakdown occurs within the anode-cathode gap due to the expanding plasma's proximity to the anode [Speirs et al. 2005].

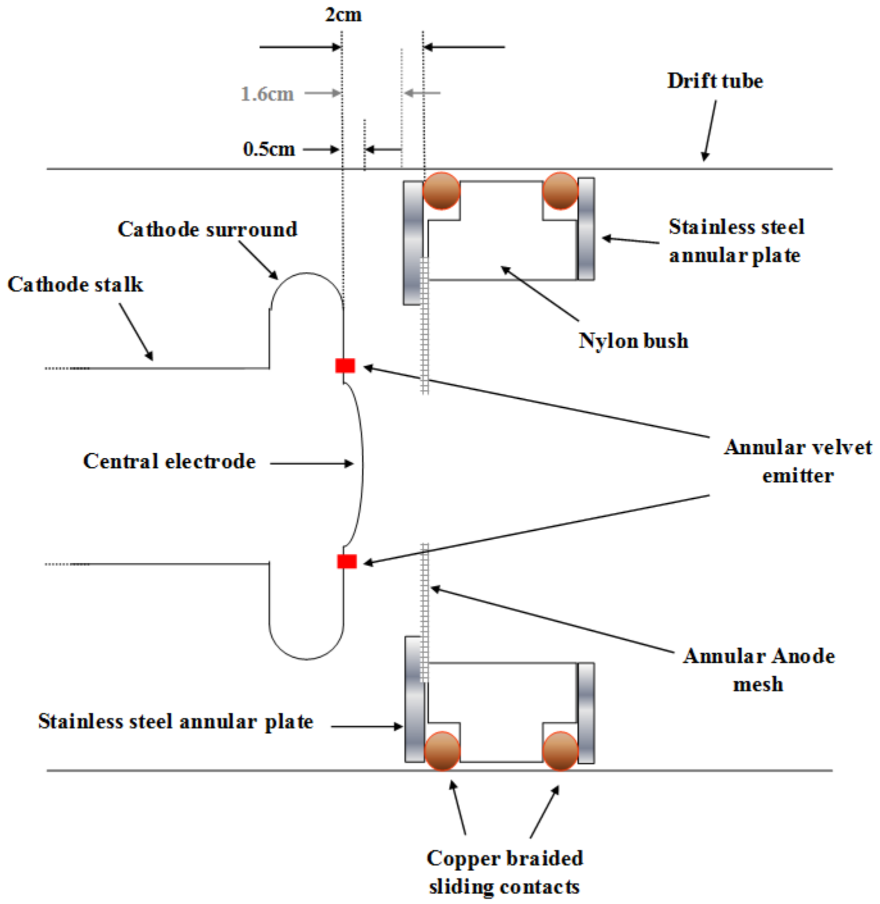

Figure 4.8**:** Schematic of the velvet cathode emitter and acceleration gap.

Figure 4.8 shows the position of the cathode and anode mesh, Figure 4.9, within the experiment. The nose-cone of the cathode face points towards the hole in the centre of the anode mesh, which is downstream of the cathode face. The anode mesh is made from copper wires spread sparsely so that the propagation of the beam is not significantly inhibited. The mesh was placed in front of the cathode in order to increase the electric field on the cathode surface to further enhance field emission. To initiate explosive emission in the experiment an electric field of ~30kVcm^{-1} is necessary. The anode and cathode flanges were separated by an acrylic insulating stack with a corona shield covering the rear of the cathode stalk where screwed rods allowed the distance between the two electrodes to be adjusted, the spacing in the AKR experiment was typically 1.5cm - 2cm. This corresponds to a plasma gap closing time ~1µs.

The nose-cone of the cathode results in a range of angles between the electric and magnetic field in the area surrounding the emitter, as at the inner edge E_r is greater than at the outer edge. The variation in this angle means that the electrons, as they are injected into the vacuum, will have an initial spread in axial velocity. An angle of 12^o was determined by simulations [Speirs 2006] and was tuned experimentally. This spread in velocity will form a horseshoe distribution in velocity space as they are magnetically compressed by the solenoids. The motion of the particles past the point of the anode mesh can be described by Busch's theorem (see theory section 3.4.6).

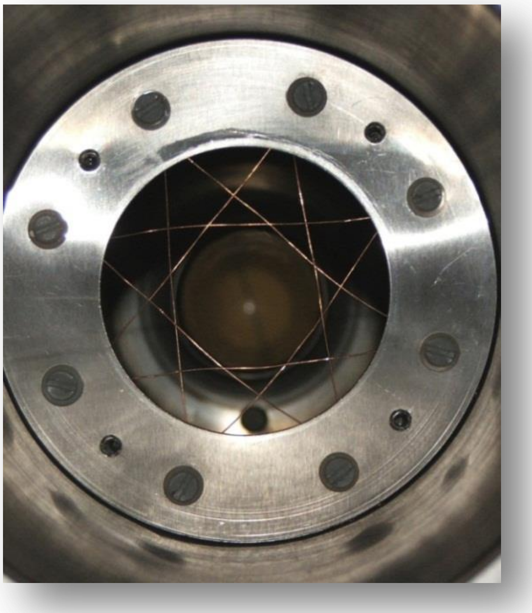

Figure 4.9**:** View of the anode mesh.

4.3 HT pulsed electrical diagnostics & supply

The HT pulsed circuit for the experiment is shown in Figure 4.10, each component is discussed within this section.

The explosive emission electron gun is powered by 75kV-85kV, 100ns pulses from a double Blumlein power supply. The quad cable supply discharges into the electron gun which is in parallel with an ionic resistor. The ionic resistor which is connected between the high voltage end of the Blumlein and ground provides a match to the output impedance of the cable pulser during the ignition phase of the cathode and consists of saturated copper sulphate ($CuSO_4$) solution. This solution can withstand very high peak powers without any damage.

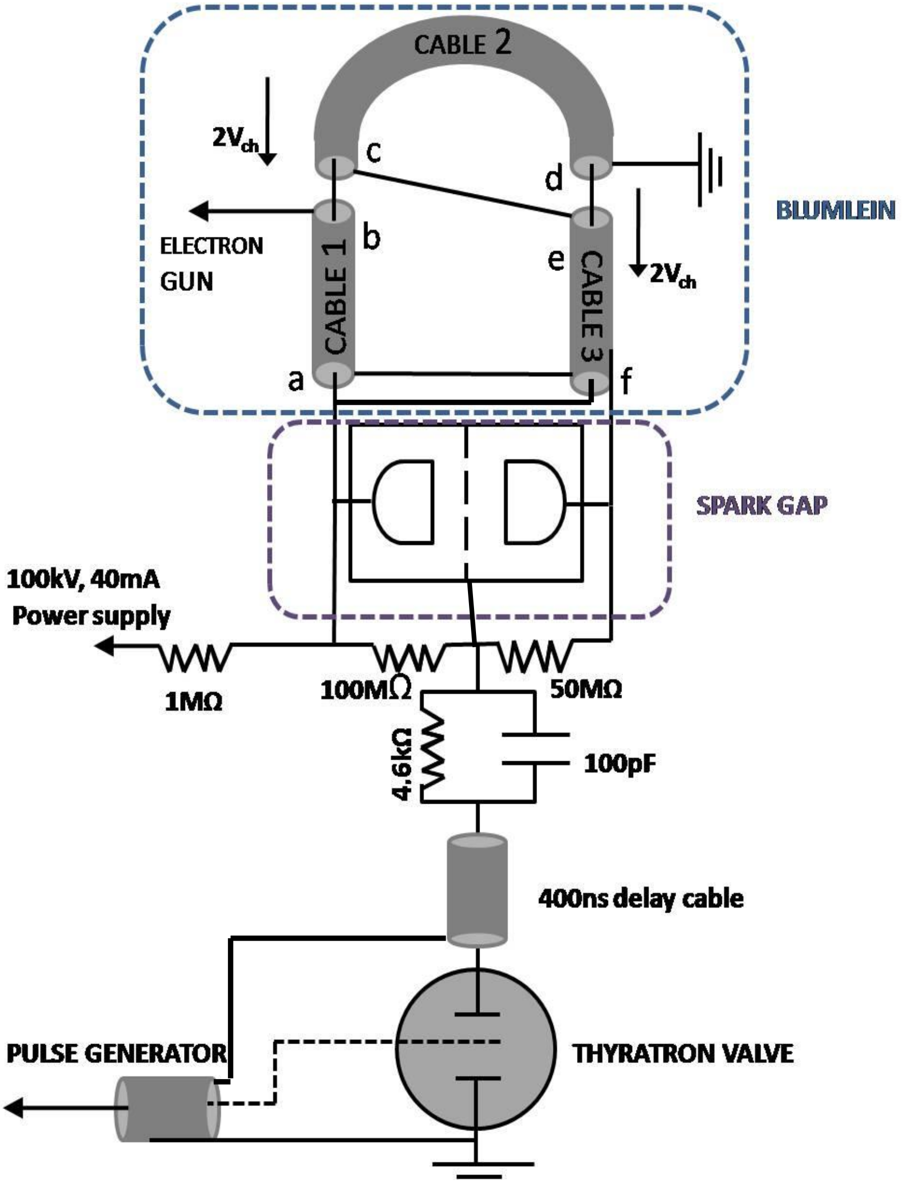

Figure 4.10: HT pulse generation circuit.

The combination of the known value of the matching resistor and a Rogowski coil to measure the current through this branch of the experiment in turn allowed the measurement of the value of the Blumlein output voltage. This trace being recorded on an oscilloscope.

4.3.1 Blumlein generator

High voltage pulse generators are used in a wide variety of research. These include power supplies for high-power pulsed accelerators, lasers and microwave generators and also X-ray generation. High voltage pulse generators broadly fall into three different categories; Marx impulse generators, pulse transformers and coaxial/stripline generators. In deciding which type of generator to use one considers the desirable output voltage, voltage rise-time, wave shape, duration and the pulse repetition rate and cost. A Blumlein pulse generator was used in the experimental set-up, seen in Figure 4.11. A Blumlein is used to produce a flat pulse, <1μs.

Figure 4.11**:** Experiment’s inverting double Blumlein pulse generator.

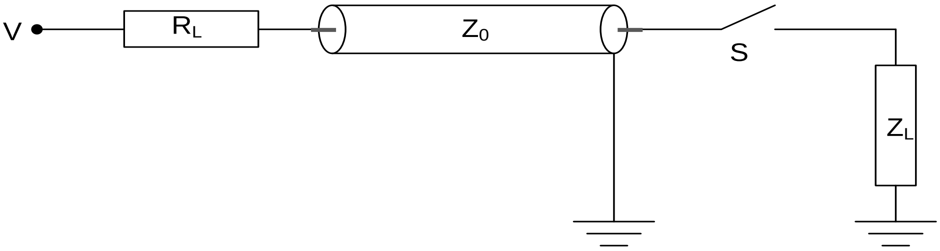

Figure 4.12**:** Simple DC charged single cable pulser circuit.

Consideration of the most primitive form of the device, the DC charged single cable pulser is a convenient point to describe the operational principles of the Blumlein cable pulser, Figure 4.12 illustrates such a circuit. It is constructed from a single length of coaxial cable, where the outer sheath is earthed and the inner conductor is charged by an input DC power supply to a given potential ‘V’ through the charge current limiting resistor R_L. When the inner conductor has reached the desired potential the output is gated into an output load Z_L via a fast switch S, which is most commonly a pressurised spark gap.

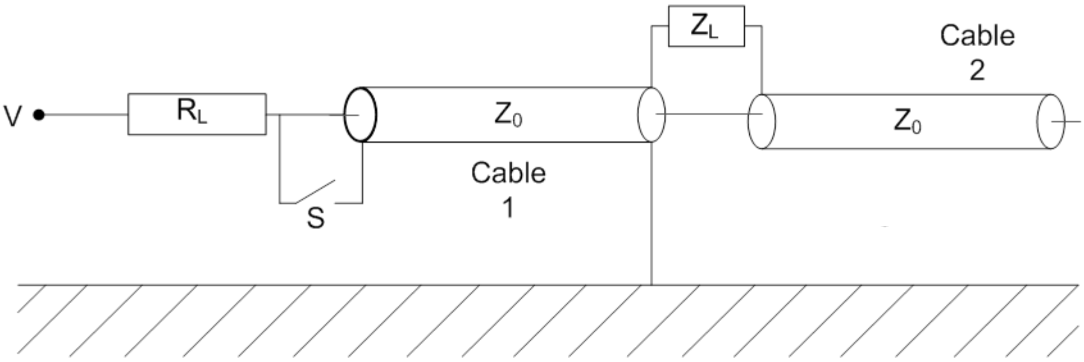

Figure 4.13**:** Blumlein cable pulser circuit.

The output voltage, V, is calculated from the ratio of the load impedance Z_L to the cable impedance Z_0, this relationship is shown in the following equation;

$$V = \frac{V_c Z_L}{Z_0 + Z_L}$$ Equation 4.01

The output voltage is maximised for $Z_L >> Z_0$, so the output voltage cannot exceed the input voltage for this configuration. It becomes clear that this is not particularly well suited for a high voltage pulse generation as no multiplication factor or voltage gain is obtainable and into a matched load (desirable to prevent reflections in the co-axial line) $Z_0 = Z_L$, $V = V_C/2$. The amplitude of the voltage pulse is however very flat with the limiting factor to the output voltage rise time being typically the speed of the high voltage switch S. The pulse length is given by $\tau = {2L\sqrt{\varepsilon_r}}/{c}$ where L is the length of the co-axial line and ε_r the relative permittivity of the cables dielectric filling. To be able to achieve such a desirable voltage pulse profile whilst obtaining voltage multiplication, a more advanced variant of the circuit in Figure 4.12 should be used. Referring to Figure 4.13, the circuit consists of two lengths of coaxial cable that are charged in parallel and discharged in series. This type of circuit is referred to as a Blumlein cable pulser.

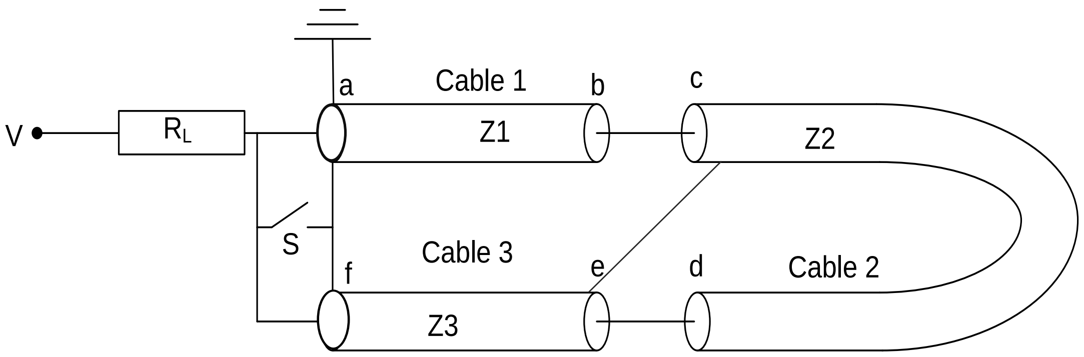

Figure 4.14: Inverting double Blumlein pulser circuit, usually $Z_1=Z_2=Z_3=Z_0$.

The way in which this system works is by charging the two sections of the coaxial cable to a desired potential through the current limiting resistor R_L. Although the inner conductors are wired in series with the high voltage supply, the capacitance of the circuit path exists between the inner and outer conductors of the coaxial cables, which means the two lengths of cable are charged effectively in parallel. After the high voltage switch S is triggered a negative voltage pulse is launched through the inner conductor of cable 1. Assuming the load impedance $Z_L >> Z_0$, the amplitude of this pulse will double upon reaching the bridging load Z_L between the outer conductors of cables 1 & 2. This occurs as a result of the large impedance mismatch. The more general output across the load Z_L is given by;

$$V_L = \frac{2V_c Z_L}{2Z_0 + Z_L}$$ Equation 4.02

The DC resistive impedance to ground of most elements of the circuit is close to zero, or to the relatively low Z_L, once the switch has closed. It is desirable that very little current flows along this path as it would discharge the cables rapidly and very substantially attenuate the output pulse. For this reason the cables may be wound into a coil, ensuring the voltage gradient from turn to turn is not excessive. The inductance L, of the wound high voltage cables, should be such that the value of L/τ for the pulse duration τ is much greater than the other impedances in the circuit. In this limit the internal impedance reverts to the serial superposition of the natural impedances of the component lines, as shown in Equation 4.02.

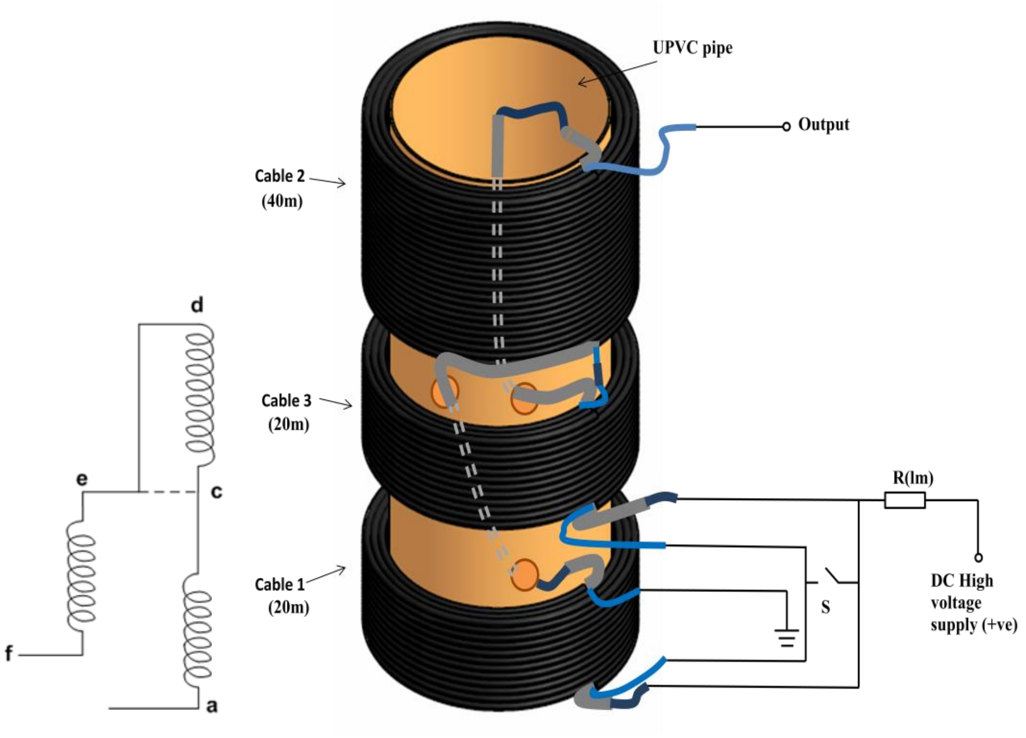

Figure 4.15**:** Experimental inverting double Blumlein generator layout and winding arrangement.

Theoretically the highest maximum output voltage in this case is $2V_c$. This technique is exactly that adopted in a more complex but flexible implementation of the Blumlein cable pulser circuit named the inverting double Blumlein cable pulser. The output across the load Z_L for this circuit is given by;

$$V_L = \frac{4V_c Z_L}{Z_1 + 2Z_2 + Z_3 + Z_L} \qquad \text{Equation 4.03}$$

The key benefits of this system is that it is possible to obtain a greater voltage gain than the Blumlein cable pulser. To produce this circuit the simplest way is to use a single length of coaxial cable which is folded back on itself. Referring to Figure 4.14 and Figure 4.15, by removing the outer braiding between the points b-c and d-e three single transmission lines are created one double the length of the other two. Cables 1, 2 & 3 are charged to a desired potential through the current limiting resistor R_L. In this case, from Equation 4.03 we can see that if $Z_L >> Z_0$ ($Z_0 = Z_{1,2,3}$) then $V_L = V_{ch} \times 4$. If $Z_L = 4Z_0$, the match condition, then $V_L = 2V_{ch}$. In the experiments described here, the Blumlein is used in a 'matched' configuration. Figure 4.16 illustrates the 'load' side of the Blumlein connections used in the present experiments.

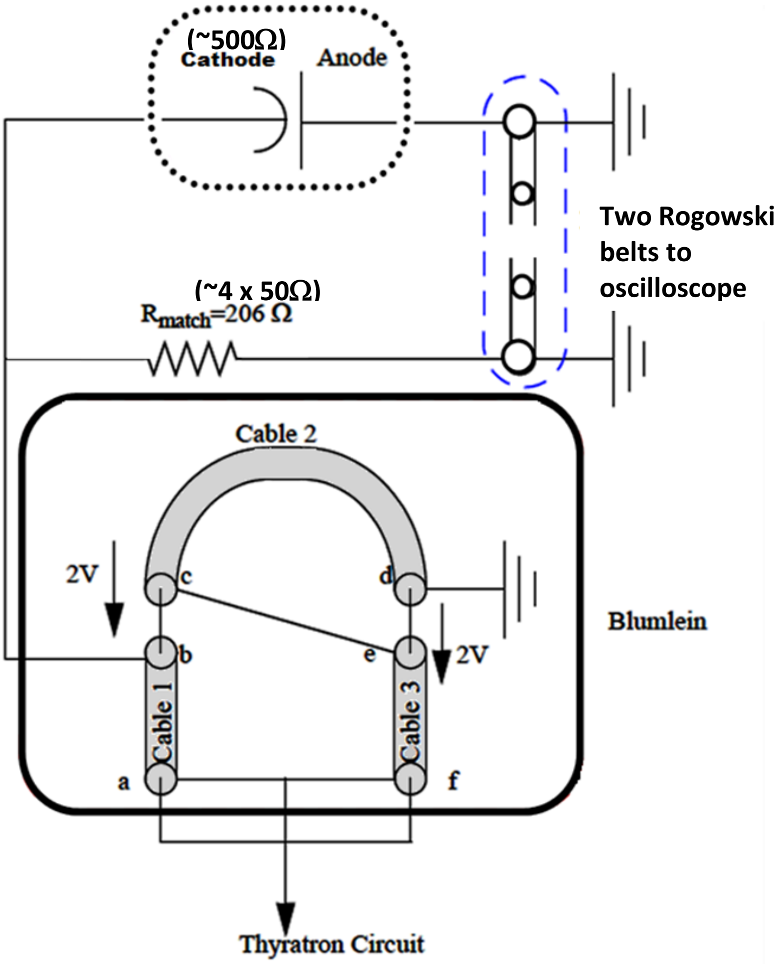

Figure 4.16: Blumlein 'load' side connections, the section inside the blue dotted lines are Rogowski belt current sensors transmitting to oscilloscopes along co-axial lines.

4.3.2 Ionic ($CuSO_4$) resistor

The experiment uses a copper sulphate ionic resistor, Figure 4.17, attached to the output of the Blumlein. Copper sulphate is an ionic crystal which when diluted with water produces a solution which has a finite conductivity. As the majority of the resistor consists of water it can withstand large peak powers without being damaged (specific heat capacity of water 4.2kJkg^{-1}K^{-1}). When a voltage is applied across this resistor the cations, positively charged ions, travel towards the cathode. The anions, negatively charged ions, will travel towards the anode. The accelerating potential was measured by sensing the current through this 206Ω matching ionic resistor by a Rogowski belt and was recorded by an oscilloscope. This resistance varies with temperature, and also slightly with voltage. It is therefore important to calibrate the resistor. The resistance of the ionic resistor was calibrated at a voltage, ~30kV. This was done using an all metal voltage probe and checked for linearity against the charging voltage up to the operating voltage of the apparatus.

Figure 4.17**:** Photograph of the copper sulphate ionic resistor connected to the output of the Blumlein.

4.3.3 Rogowski coil

Rogowski coils, also known as air-cored coils or worm coils, were introduced in 1912. Rogowski coils are useful for measurement of alternating or transient currents from tens to many thousands of ampères.

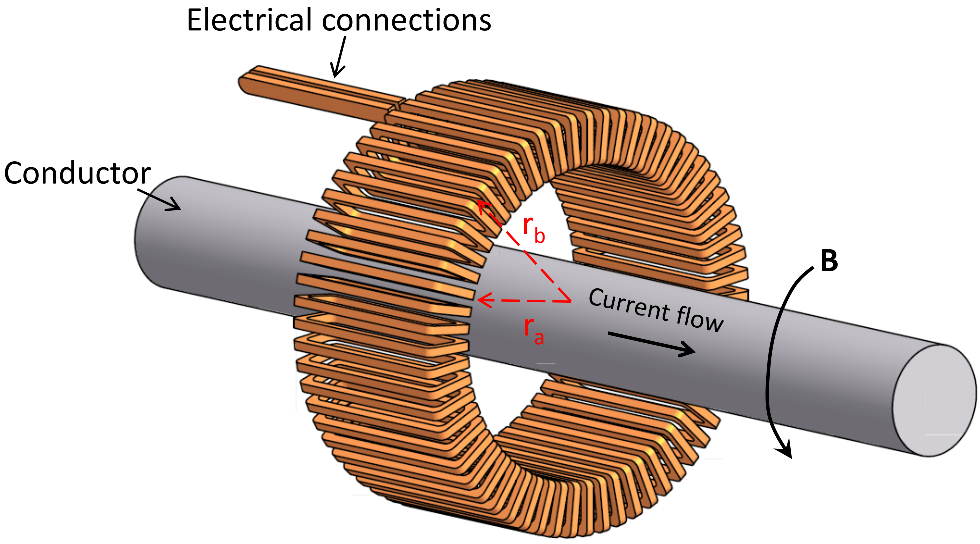

Figure 4.18**:** Arrangement of a Rogowski coil.

The general arrangement of a Rogowski coil is that of a transformer. The primary coil is in the form of a linear current vector which is encircled by the secondary coil that is formed by looping its conductor round a toroidal former, Figure 4.18.

The theory of Rogowski coils is based upon Faraday's laws that state "the total electromotive force induced in a closed circuit is proportional to the time rate of change of the total magnetic flux linking the circuit." When a wire loop moves through a magnetic field or when a wire is placed in a time varying magnetic field, then a voltage can be induced which is proportional to the rate of change of magnetic flux $V=-\delta\Phi_B/\delta t$. As the voltage developed in the secondary coil is proportional to the rate of change of the linking flux we can use an integrator circuit to measure the instantaneous flux (if we know the initial condition if time constants of circuit to be measured are known).

The theory of a Rogowski coil is also dependent on Ampères Law, as the line integral of the magnetic field around any loop is equal to the net current enclosed by it no matter what path the loop takes, if the loop encloses no net current the line integral is zero. Mathematically this is expressed as;

$$\oint_l \boldsymbol{B}.d\boldsymbol{l} = \mu \boldsymbol{I} \qquad \text{Equation 4.04}$$

If a Rogowski coil has an inner radius r_a and an outer radius r_b, which is encircling a centrally located long straight conductor carrying a current, I, in a section of length t with n turns, then the total flux linking the secondary coil is found by integrating over the turns;

$$\Phi_B = n \int_{z=0}^{t} \int_{r=r_a}^{r_b} B_\phi .dt\,\underline{dr} \qquad \text{Equation 4.05}$$

Evaluating equation 4.04 round a circular path centred on the primary current reveals that $B = \frac{\mu I}{2\pi r}$ Substituting we find;

$$\Phi_B = \frac{\mu In}{2\pi} \int_{z=0}^{t} \int_{r=r_a}^{r_b} \frac{dtdr}{r} = \frac{\mu Int}{2\pi} ln\left[{}^{r_b}\!/_{r_a} \right] \qquad \text{Equation 4.06}$$

This in turn means the voltage out of the Rogowski coil is;

$$V = -{}^{\partial\Phi}\!/_{\partial t} = -\frac{\mu nt}{2\pi} ln\left(\frac{r_b}{r_a} \right) \frac{dI}{dt} \qquad \text{Equation 4.07}$$

The AKR laboratory experiment utilises two Rogowski coils one is a measurement of the total diode current along the experiment’s ground return line. The other is the diode voltage measured by determining the current flow through the matching ionic resistor in the firing circuit. Both these measurements were recorded on an oscilloscope with suitable attenuation. Figure 4.19 illustrates the position of the coils in the experimental set-up. The Rogowski belts were calibrated using a current shunt, see Section 4.3.4.

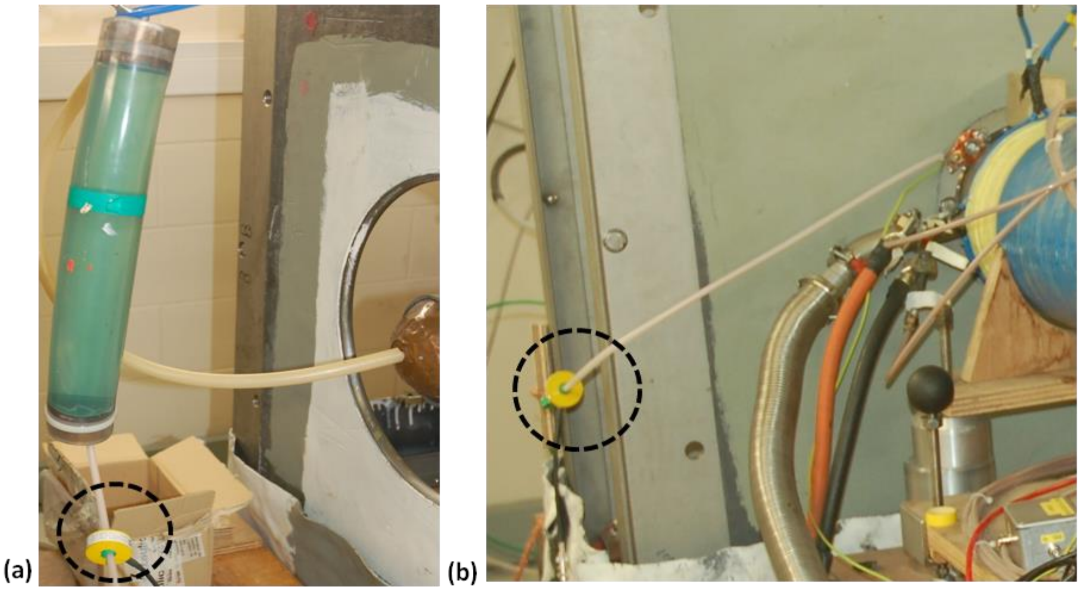

Figure 4.19**:** Rogowski coil circuit, (a) Rogowski coil measurement taken of the current through $CuSO_4$ resistor, for analysis of the diode voltage. (b) Rogowski coil measurement taken along the ground return of the experiment for analysis of the diode current.

4.3.4 Current shunt resistor

Although Rogowski coils were used as current diagnostics in the AKR laboratory experiment, a current shunt resistor was also used as a secondary diagnostic on the $CuS0_4$ resistor in parallel with the diode.

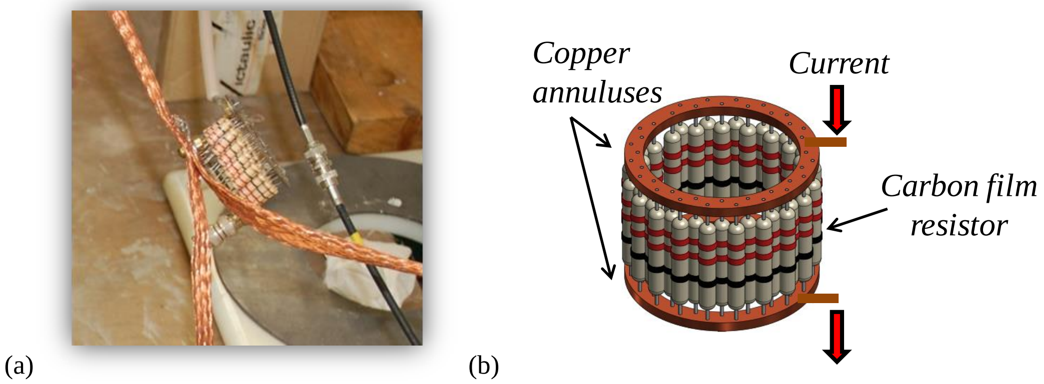

Figure 4.20**:** Current shunt (a) the current shunt connected into the experiment (b) current shunt resistor, illustrating the arrangement of the resistors and copper plates with connections for current flow.

The current shunt was used to verify and calibrate the Rogowski belt current measurement and provide a reliable method of measuring current with unlimited low frequency response. Figure 4.20 illustrates the current shunt connected into the experiment. The high frequency response in a current shunt is dominated by the self-capacitance (i.e. the resistors are very low inductance) of the resistor cluster. It is necessary to minimise this capacitance such that R << $1/\omega C$, this is done by arranging a parallel cluster of forty 22Ω, 1W carbon film resistors between two copper rings. These rings were wired to a BNC connector in order for a measurement of the voltage drop across the current shunt. Ohm's law allows this diagnostic to provide the current measurement.

4.3.5 Faraday cup

A Faraday cup is a metal cup or cylinder which intercepts a particle beam, Figure 4.21. It is used to measure the current of the electron beam, slightly downstream from the peak of the axial magnetic field in the laboratory experiment. As the particles impact the cup they induce a potential across the resistor that links the cup to the ground. Monitoring the voltage drop across this resistor and using Ohms law it is possible to evaluate the intercepted beam current. A co-axial cable transmits the resulting signal to a digital oscilloscope located in a screened room.

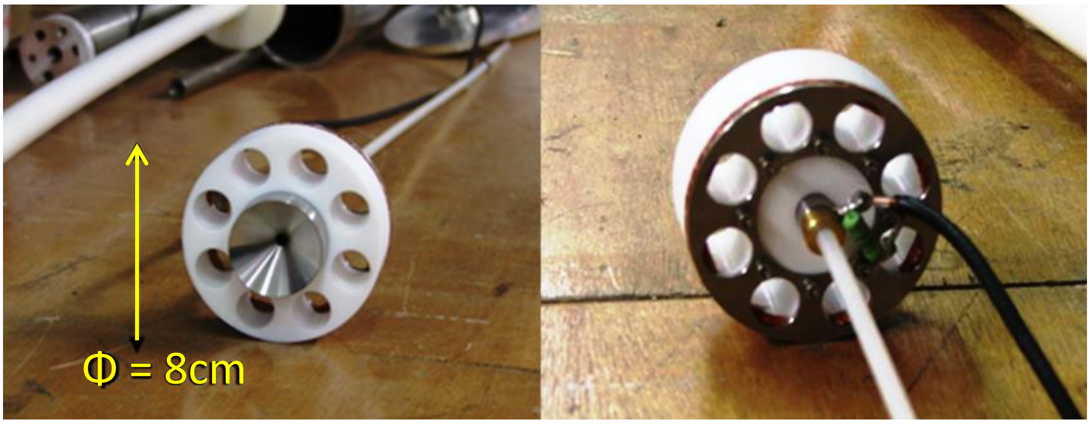

Figure 4.21**:** Photograph of Faraday cup used in the experiment, surrounded by PTFE bush. This fits within the interaction waveguide of the experiment.

Ideally the Faraday cup is large and deep enough so secondary electrons escaping from the surface due to the energetic electrons being collected do not distort the measurement.

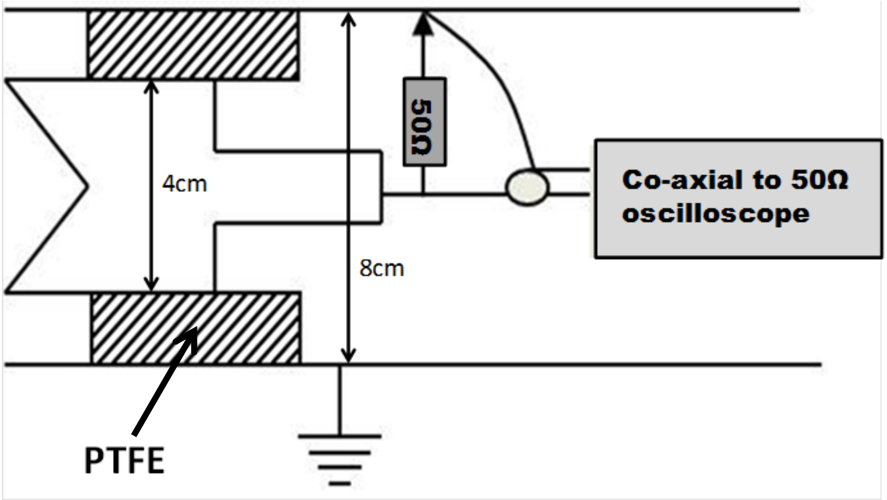

Figure 4.22**:** Faraday cup schematic illustrating the position of the resistor and the connection for the co-axial cable to the oscilloscope.

It is necessary to insulate this diagnostic from the anode so that the current incident on the cup can be measured; this is done by a PTFE insulator bridged by a very low inductance resistor connected to the grounded beam tube, Figure 4.22.

4.3.6 Thyratron

The hydrogen thyratron, Figure 4.23, is a high peak power electrical switch which uses hydrogen gas as the switching medium. The switching action is achieved by a transfer from the insulating properties of neutral gas to the conducting properties of ionised gas.

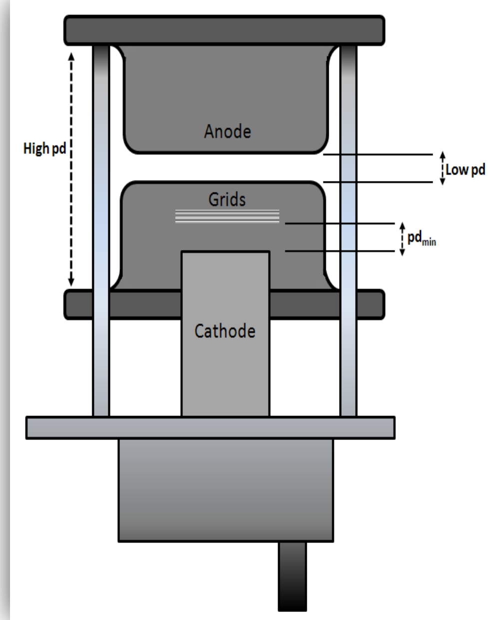

Figure 4.23**:** Schematic of the inside of a thyratron.

This is achieved by using a set of grids to localise a reservoir of ionised hydrogen, switching the grid allows the hydrogen to drift into the main gap. Thyratrons are robust devices which can tolerate fault conditions well in excess of normal ratings.

4.3.7 Spark gap

Although the spark gap shown in Figure 4.24 is a simple device, it is an effective form of closing switch. The basic concept of a self closing spark gap consists of an arrangement of two electrodes separated by a gap usually filled with a gas. When the voltage exceeds a critical value determined by the gas and pressure an electric spark closes the switch.

There are several different configurations of triggered spark gap (used to control the time at which the switch closes). The specific geometry adopted for the experiment is a mid-plane spark gap which consists of two domed electrodes, one of which is grounded and the other is charged, with a trigger electrode in between them, held at an intermediate potential by a voltage divider. The gap is filled with N_2 gas of pressure up to 2bar.

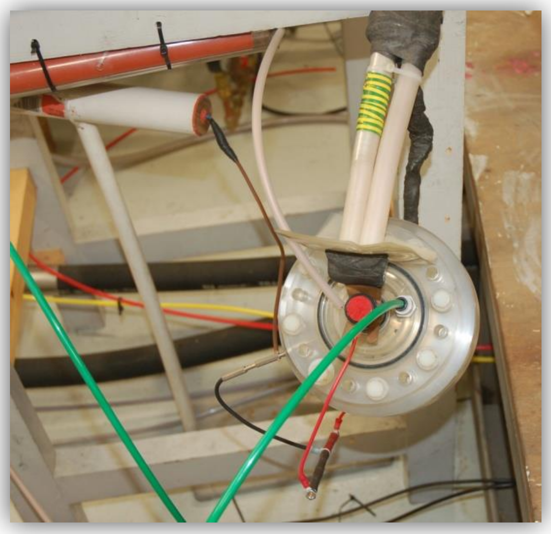

Figure 4.24**:** Photograph of the spark gap, used as a closing switch in the double Blumlein circuit, in the experiment.

The circuit of the mid-plane spark gap is seen in Figure 4.25, the voltage of the middle electrode is adjusted through changing the resistor values R_{b1} and R_{b2}.

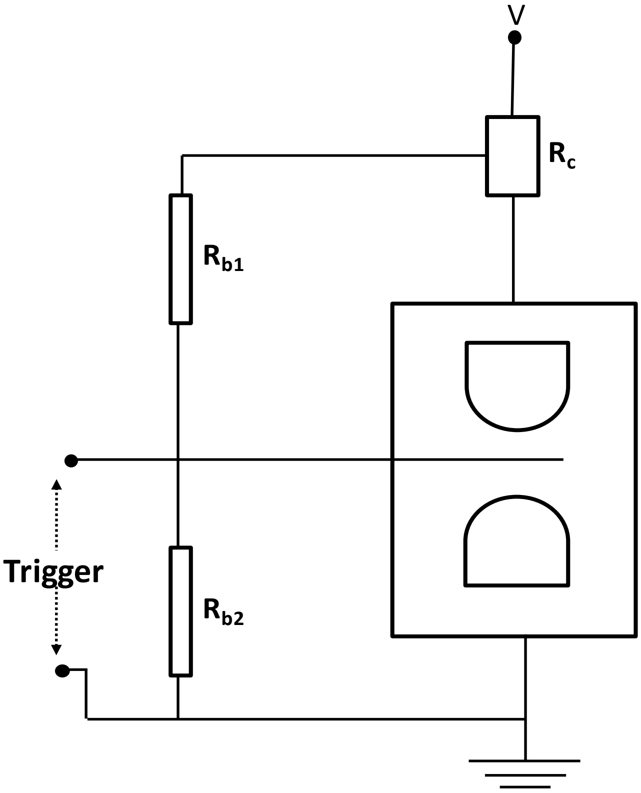

Figure 4.25**:** Circuit diagram for the mid-plane spark gap.

The trigger pulse, in this case grounding of the mid-plane gap by the thyratron switch, results in over-volting of the other half of the gap. Gas diffusion through the mid-plane causes a discharge between the two primary electrodes. The spark gap has a triggered timing jitter ~10ns.

Once the spark has been ignited, an electric current then flows until the path of ionized gas is broken or the current reduces below a minimum value called the 'holding current'. This usually happens when the voltage drops due to depletion of stored energy in the circuit.

4.4 Solenoids

A key aspect of the AKR emission process is the converging magnetic field upstream from the source region. In order to replicate this in the laboratory experiment a system of magnet solenoids was used to create a converging magnetic field as seen by the electron beam as it traversed the system, Figure 4.26.

The solenoids were constructed in separate sections with a different number of layers in each in order to provide a controlled degree of magnetic compression. They were constructed using more than 1km of OFHC (Oxygen Free High Conductivity) copper tubing which had an inner diameter of 2mm and an outer diameter of 7mm coated with a thin plastic sheath for electrical insulation and wound around non-magnetic formers.

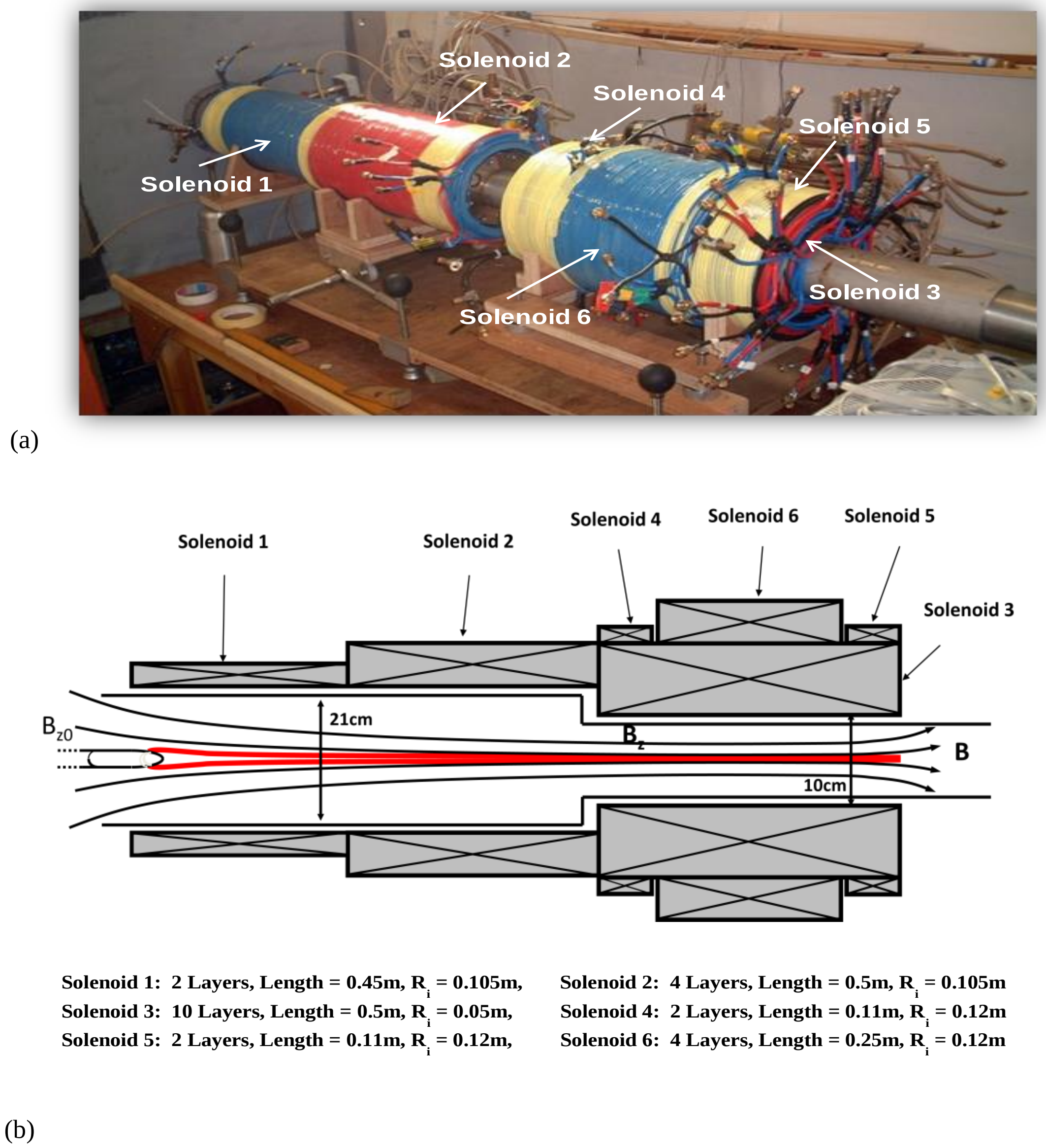

Solenoid 1: 2 Layers, Length = 0.45m, R_i = 0.105m, **Solenoid 2:** 4 Layers, Length = 0.5m, R_i = 0.105m
Solenoid 3: 10 Layers, Length = 0.5m, R_i = 0.05m, **Solenoid 4:** 2 Layers, Length = 0.11m, R_i = 0.12m
Solenoid 5: 2 Layers, Length = 0.11m, R_i = 0.12m, **Solenoid 6:** 4 Layers, Length = 0.25m, R_i = 0.12m

Figure 4.26**:** Experimental solenoid arrangement (a) Photo of experimental solenoid arrangement, illustrating the various different coils (b) Schematic, with dimensions, of the solenoid arrangement illustrating position of the electron beam.

Solenoid 1, 0.45m long, is the coil that controls the cathode. It is run by a 30V, 250A switched mode power supply and is made up of 2 layers with an ID of 0.21m. This coil surrounded the electron accelerator and was used to create the magnetic field which the electrons would experience as they were injected from the gun into the anode can (the region 21cm in diameter between the electron emitter and interaction space). Solenoid 2, 0.5m long, is made up of four layers and is run by a 70V 300A switched mode power supply. In practice it was always used at 40A. Its purpose is to transport the electrons into the interaction region of the experiment and acts as the transition between the low field electron gun region and the high field interaction region.

Solenoid 3, 0.5m long, is made up of 10 layers and has an ID of 0.10m. This coil encases the interaction region and holds the magnetic field plateau at a steady maximum magnetic field. Solenoids 4 and 5, called the shimming coils, are made up of 2 layers and are 0.11m long. Solenoid 4 is powered separately by a 70V, 300A supply, and solenoids 3 and 5 are driven in series by a 210V, 310A linear regulator. Solenoid 4's independent drive enables it to compensate for the asymmetric impact of Solenoid 2 on the magnetic plateau in the centre of Solenoid 3.

The shim coils allow solenoid 3 to provide a flat central plateau, 20cm in length at approximately a metre and a half downstream from the cathode. The plateau can reach up to B=0.5T in magnitude. Solenoid 6 was a reserve coil, capable of providing a high, > B=0.7T, peaked magnetic field profile to aid in mirroring the electrons should it be required. Refer to Figure 4.27 for an illustration of solenoid layers.

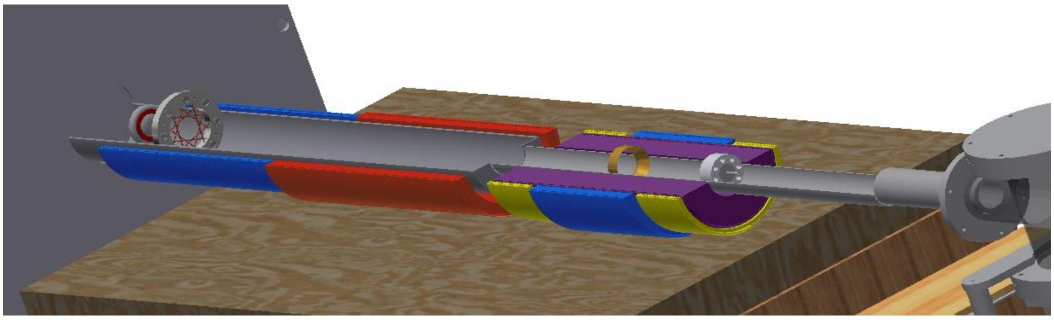

Figure 4.27**:** Illustration of the experimental solenoid arrangement illustrating the layers of the solenoids.

Figure 4.28 shows a schematic of the magnet coils alongside the magnetic field profile along the length of the system. The electrons were subject to magnetic compression as they passed into solenoid 2 and reached a maximum magnetic field in the centre of solenoid 3. Adiabatic motion of the electrons must be satisfied as much as possible during the magnetic compression stage, to correctly form the electrons into the desired horseshoe distribution in velocity space, Section 2.3.10.

The magnetic field profile and hence the coils were designed to satisfy this requirement as far as possible whilst producing a maximum field in the order of B=0.7T and compression ratio of up to 70 within the capacity of the laboratory's power supplies.

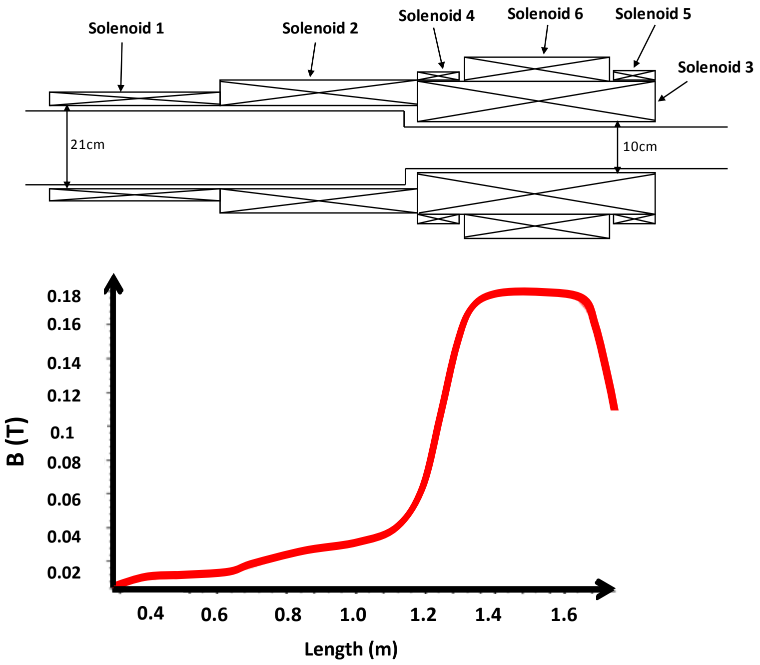

Figure 4.28**:** Experimental solenoid arrangement.

The laboratory was equipped with a $10m^3hr^{-1}$, 4bar water cooling system and so to provide the necessary 20+Bar cooling water; a boost pump was installed rated at $5\ m^3hr^{-1}$ and 16Bar. This provided an acceptable flow rate of water through the 20m long, 2mm ID pipes enabling each one to carry 300A. This was sufficient to allow the solenoids to be driven by a total electrical power of 120kW.

Figure 4.29 shows the Hall probe measurements that were taken before experiments were conducted to verify Maple code calculations of the magnetic field profile. The magnetic field profiles for both B=0.18T and B=0.48T plateau fields are shown. The magnetic field rises and then has a plateau for 20cm before decreasing again at the end of the coils. As can be seen in Figure 4.29 the Maple script predicts the fields with an accuracy ~1% which is within the tolerance range of the detuning of the cyclotron instability. The verified Maple code could then be used to calculate the PSU currents required for any experimental configuration required.

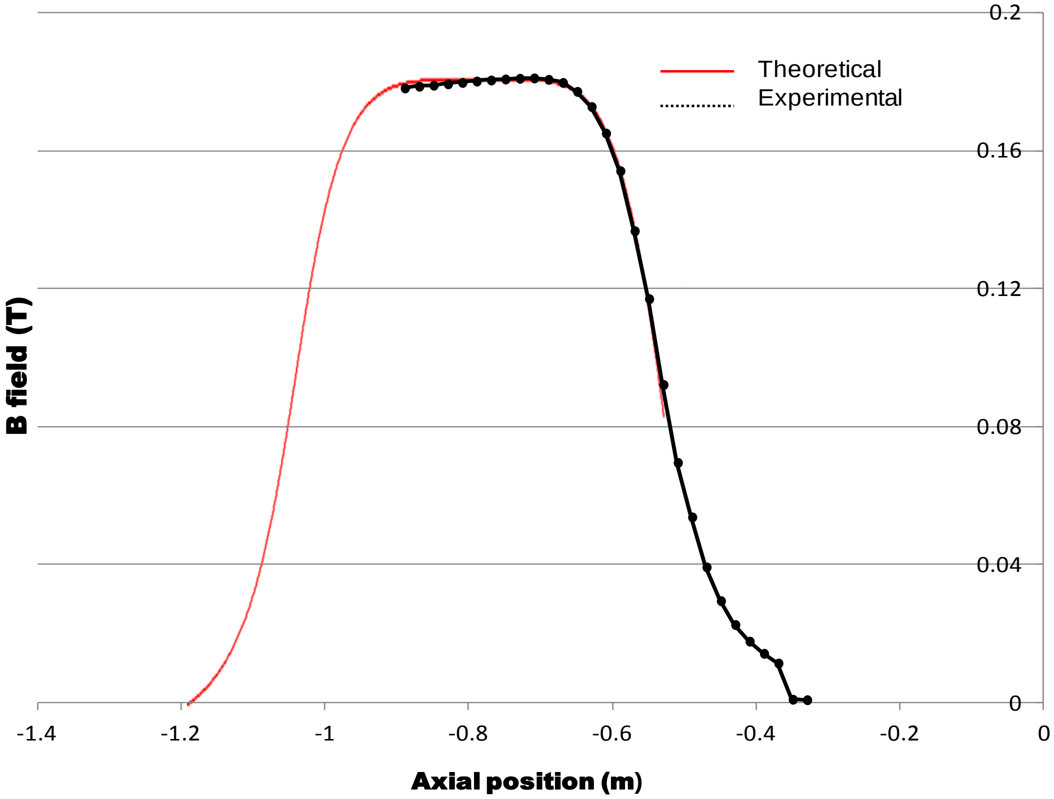

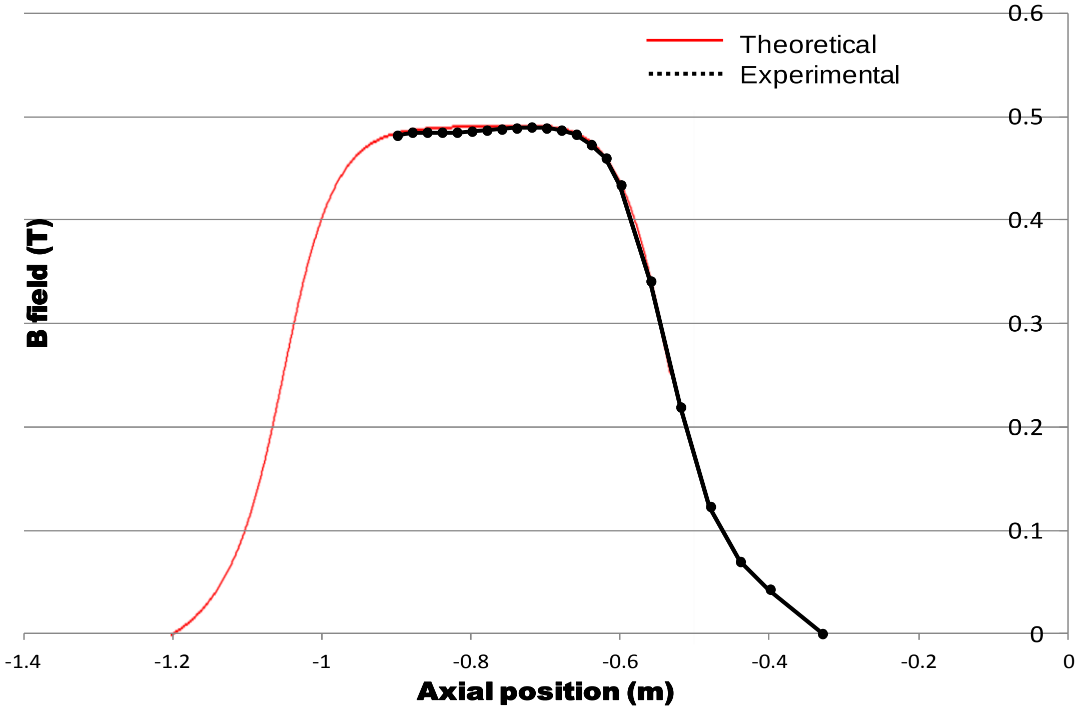

Figure 4.29**:** Experimental B-field measurement with corresponding Maple script predictions of B-field profiles.

4.5 Microwave detection

4.5.1 Spectral analysis

In order to record the microwave emissions a deep memory 12GHz real time digital oscilloscope was used to capture the complete microwave wave forms, Figure 4.30. A Fast Fourier Transform (FFT) was performed on the AC signals to yield a measurement of the wave frequency from each individual experimental pulse.

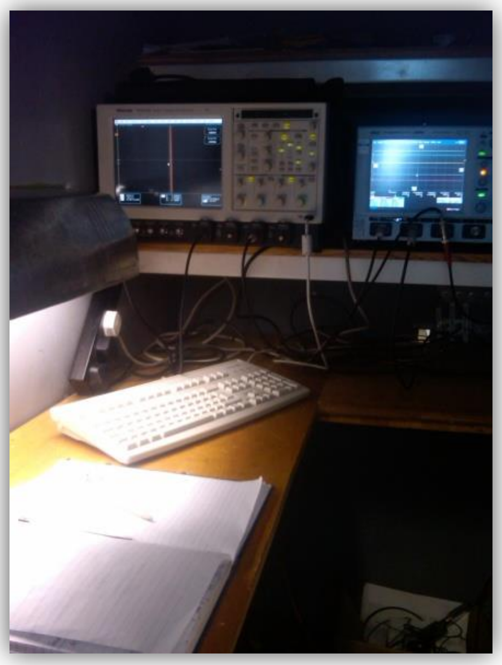

Figure 4.30**:** Screened room containing deep memory oscilloscopes, where microwave measurements were taken.

4.5.2 Attenuators

An attenuator is a passive device that reduces the amplitude or power of a signal without appreciably distorting its waveform. Figure 4.31 illustrates the co-axial attenuators that were used in the experiment.

Various AntlanTec RF attenuators of 6dB, 10dB and 20dB were used. The body is made from anodised aluminium and the connectors are of Type N and fabricated from stainless steel outers and Be-Cu inner contacts. These attenuators were rated to several watts of power, hence the finned heatsinks. The single attenuator at the top is an Inmet 3dB attenuator. Connectors are made from passivated stainless steel and the conductors are made from gold plated beryllium copper or brass whilst the body is made from anodised aluminium and the connectors are Type N and fabricated in stainless steel. The use of calibrated attenuators is vital if a power estimate is to be obtained. Therefore the performance of all attenuators was verified by measurements on Network Analysers.

These fixed attenuators were used to lower signal voltages, dissipate power, and to improve impedance matching, (by lowering the SWR and hence supressing cavity resonances at the cost of ultimate sensitivity). They serve to protect the measuring device from signal levels that might damage it.

Figure 4.31**:** Attenuators used in the experiment.

At microwave frequencies it is also common to load a waveguide transmission line with a lossy dielectric. By inserting a resistive material into an RF/microwave electric field, attenuation of the signal is obtained. This can be achieved by inserting a vane of lossy thin film glass into a waveguide which can be moved from a zero electric field position, at the wall, to a maximum, in the middle, thus creating a variable attenuator. Where higher precision attenuation is needed, a rotary vane attenuator can be used, if the vane is rotated from a position where it is perpendicular to the E-field of the waveguide to one where it is parallel then the attenuation changes from zero to a maximum respectively. Such sliding vane or rotary vane attenuators were however not used in these experiments.

4.5.3 Echosorb foam attenuators

The receiver system used for experiments at a cyclotron frequency of 4.42GHz, exploited a loss loaded material (Echosorb) to add attenuation to the WG12 waveguide sections (used as receiving waveguides in the 4.42GHz experiments, See Section 4.5.4). This approach was favoured over vane attenuators as it is effective at high harmonics of the expected frequency. This type of attenuator however has rather a complex spectral response. Calibrating a Vector Network Analyser with a Line-Reflect-Line (LRL) technique it is however possible to measure the attenuation accurately.

A piece of this absorbing material was used to aid in the matching of each waveguide receiving antenna and to provide an initial attenuation of the signal. The waveguide antenna used for the scanning arm of the antenna pattern measurements system had 17dB transmission loss due to this Echosorb. The reference arm antenna had an Echosorb foam section with a transmission loss of 13dB, shown in Figure 4.32. In both cases this was measured at a frequency of 4.42GHz.

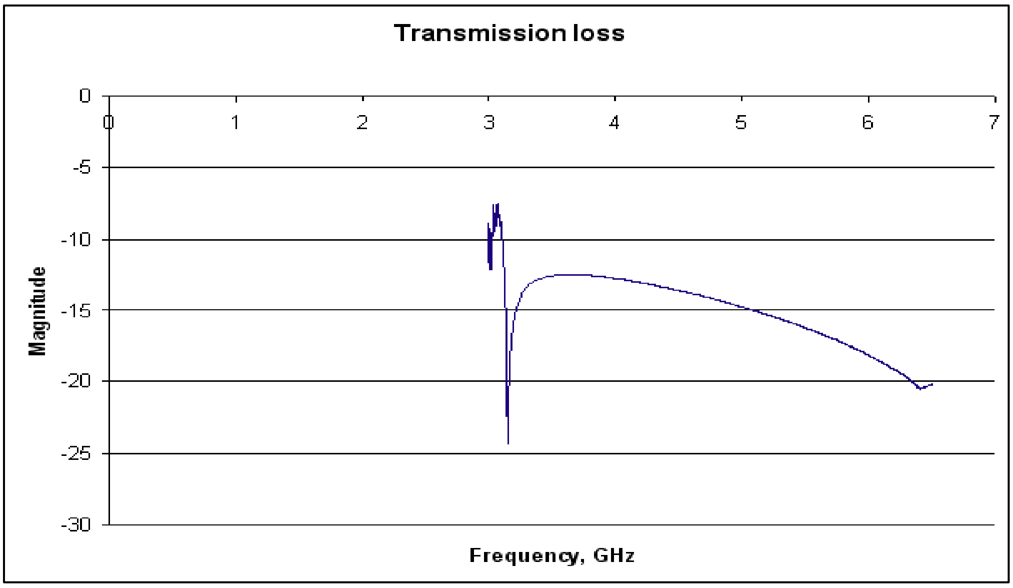

Figure 4.32: Transmission loss diagram for one of the ‘Echosorb’ foam attenuators used in the 4.42GHz waveguide receivers.

4.5.4 Receiving antenna, antenna pattern and power analysis

Pairs of waveguide 12 (WG12) stub receiver systems were built using single mode linearly polarised rectangular waveguide components with simple open ended waveguide apertures for detection of 4.42GHz radiation, and were filled with lossy dielectric attenuators. At the lower frequency, 2.7GHz, pairs of waveguide 10 (WG10) stub receiving antennae were substituted. These receivers operated in a single transverse mode [$TE_{1,0}$] at their respective frequency ranges. These were used to measure the radiation antenna pattern emitted by the experiment in radial (E parallel to scanning plane) and azimuthal polarisations (E perpendicular to scanning plane), and to receive signals for spectral analysis.

The two waveguide stub receiving antenna were placed in the far field region of the experiment output to capture the radiation emitted from the output window. Figure 4.33 and Figure 4.34 illustrate how the stub antennae are connected to the oscilloscope through the rectifying diodes. The emitted radiation power was measured at different angles around the experimental aperture. There were two receiving antennae, one antenna used to scan the radiation pattern and one used as a control 'reference' signal to ensure that any random statistical variation in the signal amplitude is small.

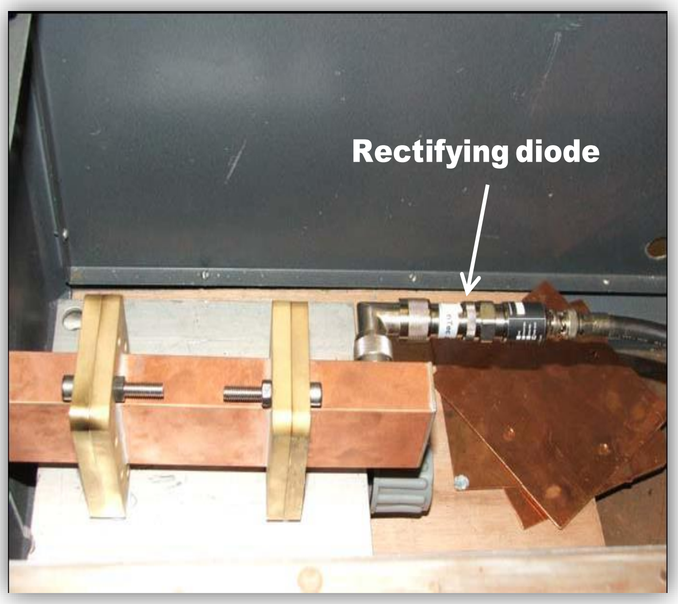

Figure 4.33**:** Waveguide antenna (in this case WG12) with rectifying diode.

This system allowed the radiated power flux as a function of polarisation (depending on the orientation of the waveguide stubs) and azimuthal position with respect to the output aperture of the experiment to be measured.

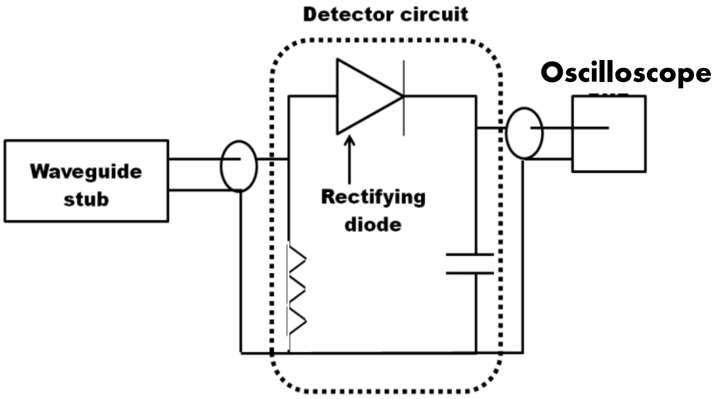

Figure 4.34**:** Schematic circuit diagram of rectifying diode.

Measurements were taken for azimuthal angles of up to 55°, angles greater than 55° could not be measured due to the walls of the output flange obstructing the radiation emission, Figure 4.35. The radiation was launched from a circular aperture 8.28cm in diameter.

The signals that were captured by the antennae were fed to calibrated rectifying diodes which enabled voltage readings to be obtained on a 2GHz deep memory digital oscilloscope. The detectors were calibrated with a source in turn calibrated against a thermal power meter. The readings from these measurements could then be analysed to determine the mode radiated and also the output power and efficiency of the system [Ronald et al. 2008**a**][Ronald et al. 2008**b**], exploiting the rectifier calibration curves.

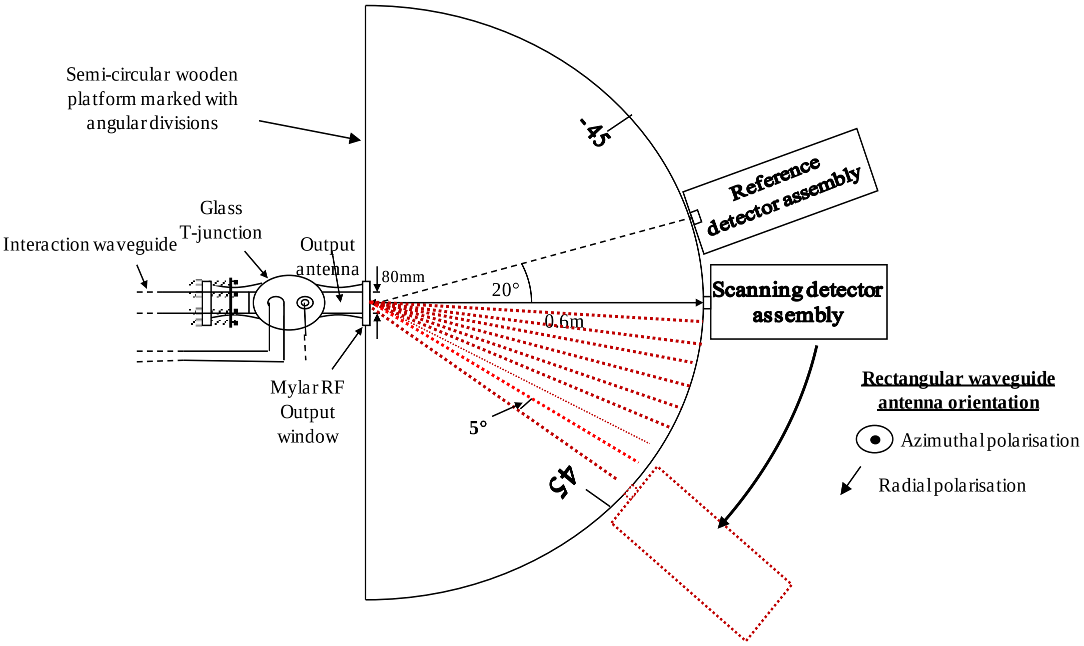

(a)

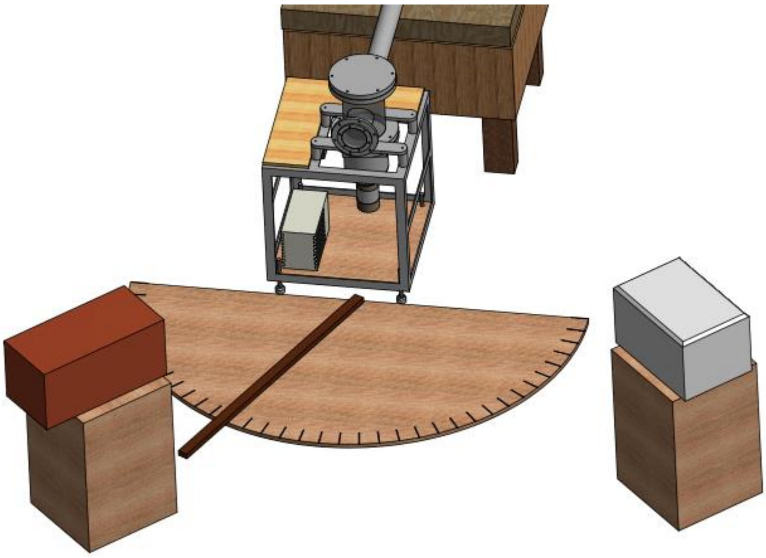

(b)

Figure 4.35**:** (a) Schematic microwave detection set-up and (b) drawing of position in the experiment.

4.5.5 Rectifying diodes

In order to be able to allow high frequency RF signals to be measured with relatively low bandwidth detection systems a rectifying diode is used. The specific rectifying diodes used in the experiment were made commercially. They are crystal detectors mounted inside a coaxial package. In this case the diodes used were fast gallium arsenide devices connected as shown in Figure 4.34 which short the E-field in one direction but present an open circuit in the other. The polarity of the signal that was obtained is dependent on the orientation of the diode and the half sine wave that was obtained was then capacitively smoothed. By calibration of the devices output voltage into a 50Ω load for pulsed input signals generated by a levelling synthesised microwave source calibrated against a calorimetric detector one can use the rectifier output voltage to determine the amplitudes and power of short duration input signals arriving at the detector input.

It is helpful to plot the output voltage against input power to provide calibration data for the rectifiers. Fitting polynomial curves of sufficient order to these curves allows automatic conversion of the recorded output voltage data into input power levels. Figure 4.36 illustrates the calibration plot used in the experiments.

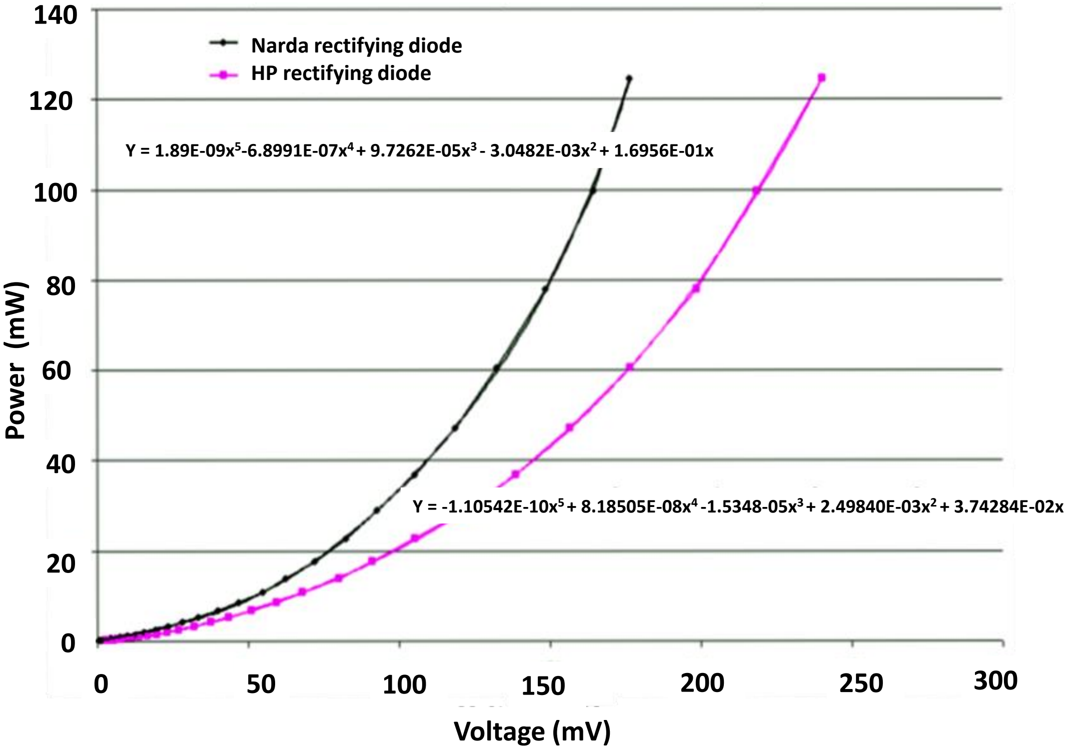

Figure 4.36**:** Calibration curves for Narda and HP rectifying diodes, showing fitted 5th order polynomial.

4.6 Numerical simulation

Numerical simulations were conducted using a particle in cell code called KARAT in both two and three dimensions. Computer simulations are a valuable aid to design experimental apparatus and to extend ones understanding and insight into the behaviour of an experiment or scientific phenomenon. They can be used to predict the results or behaviour of an experiment or to investigate aspects which are hard for the experiment to directly measure. Here KARAT was used to predict the frequency, power and modal structure of the radiation generated by the experiment. The behaviour of the electrons was also predicted, such as the phase space evolution of the beam. This is an example of a process that was difficult to directly measure. An example of the use of simulations in experimental design was the modelling of the electron optics and the formation of the velocity profile of the electron beam, because it is not possible in the laboratory experiment to achieve large degrees of magnetic compression whilst keeping the adiabatic conditions required for simple theoretical analysis.

An analytic code, Maple, was used to calculate the magnetic fields generated by the solenoids. Maple is primarily an analytical algebra solver with significant numerical computation capability. It offers the advantage of developing as far as possible an algebraic representation of a problem which can often be faster than direct numerical solution.

4.6.1 KARAT and its modelling method

4.6.1.1 KARAT introduction

The beam wave interaction simulations in this thesis were conducted using the PiC code KARAT.

KARAT is available in both 2 Dimensional and 3 Dimensional geometry forms. The 2.5D version (2.5D means the geometry and fields are described in 2D but all three components of the particles velocities are retained) treats slab x-z, polar r-θ, and axisymmetric r-z geometries. In a 2.5D axisymmetric geometry Maxwell's equations are solved on the cylindrical coordinates (r,φ,z) assuming that $\frac{\partial}{\partial\varphi} \equiv 0$. The simulated 2-D region on the r-z plane is covered by a rectangular mesh with cells having the dimensions h_r and h_z.

In the 3D version the three electromagnetic field components and three momentum components are free to vary without constraint in each spatial dimension. Here, Maxwell's equations are solved in a Cartesian system x,y,z. The problem region to be simulated is covered by a rectangular volume mesh with the cells having the dimensions h_x, h_y, and h_z [Tarakanov]. Due to time and memory constraints not every single real particle in the simulation can be reasonably computed. KARAT therefore uses a merging factor to group real particles together into one PiC particle. In the simulations presented here, one PiC particle is representing $3x10^7$ real particles unless otherwise stated.

The code is fully electromagnetic (being based on the Maxwell curl equations and hence allowing the fields to evolve in time) and based on the particle in-cell (PiC) method. Its main use is to provide solutions to non-stationary electrodynamic problems having complicated geometry and involving the dynamics of relativistic electrons and non-relativistic ions. It is particularly suited to the simulation of high-current electron devices such as vircators, FEL's and gyrotrons. It can also be used to model physical phenomena in laboratory and space plasmas. In the present case it was selected due to its highly flexible system for defining the distribution of electrons in a complex electron beam.

4.6.1.2 Finite difference scheme of modelling

KARAT works on the basis of solving Maxwell's equations by a finite difference scheme with overstepping on a rectangular shearing grid. On each time step it computes the motion of the particles within each cell. Within this cell each particle will have a position and velocity. The current source terms in Maxwell's equations are derived by taking an average of all the particles in a cell. The average can then be smoothed between cells to enhance the stability and accuracy of a computation. The electric field in the simulations is corrected by using Boris' method. This scheme provides the unique feature of a special grid shear yielding satisfaction of the boundary conditions without requiring any extrapolation. When modelling particles in plasma systems they may be simulated by either macro particles or by a linear model.

Externally applied magnetic fields are treated in three ways. The field can be defined (in axi-symmetric systems) by means of a set of on-axis values and their corresponding positions, or the magnetic fields of current carrying coils can be computed; finally external files with information about the magnetic field can be loaded, having been generated in another code or from experimental measurement. The main particle attributes, namely the charge and mass are user specified input parameters for beam particles. The plasma macro particle charge and mass are defined by the merging factor. The merging factor is chosen by the user based on the maximum number of particles that may reasonably be solved for, and an estimate of the total numbers of real particles filling the system at any instant.

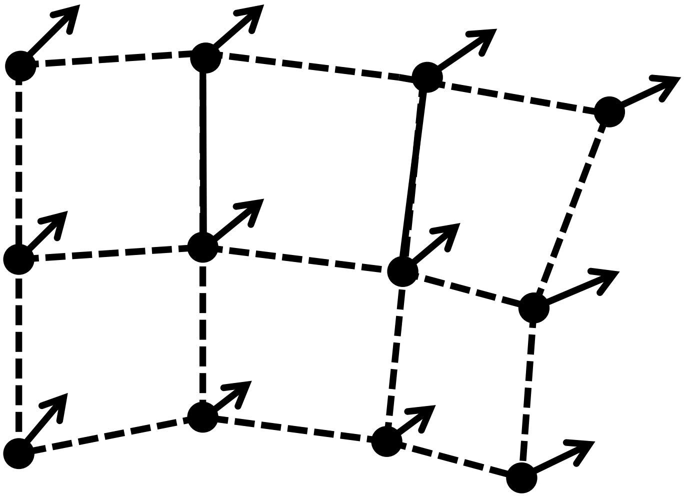

Figure 4.37**:** Vector representation of a field evaluated at the nodes of a lattice.

Maxwell's equations allow one to predict how the electromagnetic field changes from one instant to the next instant. To work out what the electric or magnetic field is going to be everywhere in a volume of space at a future instant one has to know its value at the current instant, and also the local curl of the other field and the location and motion of the charged particles.

Finite difference implies that derivatives will be estimated from a Taylor expansion. A Taylor expansion will give the value of a displaced point as a function of its value and derivatives at the un-displaced point. Spatial derivatives are estimated from knowledge of a function at two or more points. Approximate solutions can be constructed for the fields at some arbitrary location by interpolating from the known values of the fields at discrete points on a lattice. Combining values at more points increases the accuracy to which the derivative is estimated. Reducing the lattice spacing can also increase the accuracy; however a higher order estimation of derivatives will increase the accuracy slightly faster than reducing the lattice spacing. For solving vector equations like Maxwell's equations a finite difference scheme can be set up by specifying the value and direction of the vector E and H fields at every point on a pair of interleaved grids.

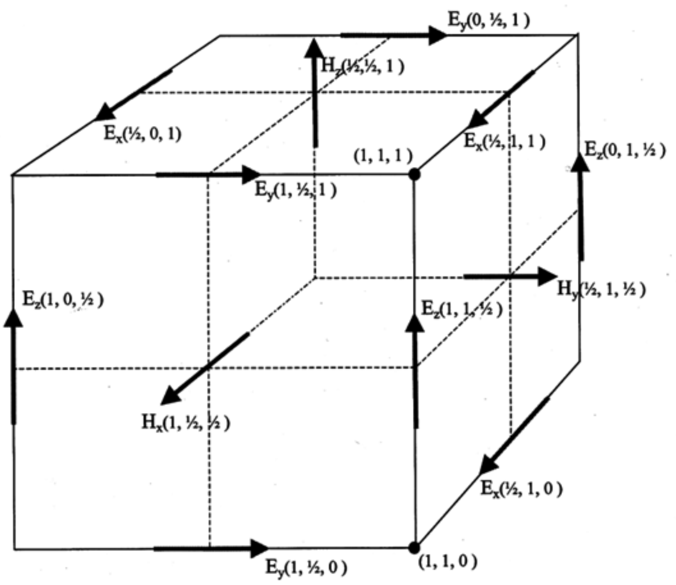

Figure 4.38**:** The Yee cell, this gives a representation of the integrated form of Maxwell's equations.

This is represented by a lattice shown in Figure 4.37. Figure 4.38 illustrates a Yee cell. The Yee cell gives a representation of the integrated form of Maxwell's equations. The average value of a field component, over the face of the square through which it passes, is represented by a vector defined through the centre of the face. The time derivative of this component is given by Maxwell's curl equations using the boundary vectors of the other field type on the alternate grid.

4.7 Using Maple to solve the simulation magnetic field configuration

As seen in section 4.4, the solenoids of the experiment are able to provide detailed control of the profile of the magnetic field. In order to input this magnetic field into the simulations Maple was used to predict the axial field profiles by defining the solenoid geometry and currents. It equally allowed the design and configuration of the solenoids for experiments with accurate definition of the magnetic field by predicting the current required in each coil. The experimental measurements of B_z are used to verify the Maple script. The figures of the Hall probe measurements from the experiment are seen in section 4.4, along with the Maple script predictions. For the Maple script see Appendix 2.

Chapter 5

Results & analysis

This chapter presents the results gained from conducting 2D and 3D KARAT particle in cell code (PiC) simulations and scaled laboratory experiments. The chapter is split into various regimes or specific studies that were undertaken. Where both experimental and numerical investigations were conducted for similar conditions these are presented together to create a natural progression and to facilitate comparison of the data from each method.

5.1 Initial 3D simulations

An early objective of the research in this thesis was to conduct 3D finite difference time domain PiC simulations that built on results obtained from previous 2D PiC simulations of the experimental apparatus. Those 2D simulations had been conducted in a geometry consistent with the experiment. The key parameters of the resonant structure and magnetic field were carried over to the 3D simulation [Gillespie et al. 2008].

In the previous 2D simulations the impact of parameters such as the magnetic field configuration, detuning, compression, the electron current and energy on the formation of the horseshoe distribution and its subsequent evolution including the microwave output power, wave frequency and mode structure were analysed. These predictions were compared to the experimental measurements and also gave an insight into certain dynamics that could not be directly measured, for example, the evolution of the horseshoe distribution function due to RF emission. In these 2D PiC models, plots were generated that illustrated the formation of the horseshoe distribution as the electron beam is travelling through the magnet system from the electron gun. These simulations were also able to partially predict the mode structure and frequency of the emitted RF radiation [Speirs et al. 2008].

The focus of the initial 3D numerical simulations was to study excitation of the $TE_{0,1}$ and the $TE_{0,3}$ modes within a waveguide of 8.28cm diameter by an electron beam having a horseshoe distribution in velocity space. The resonant magnetic fields for these modes were close to B=0.18T and B=0.48T respectively.

The 3D PiC simulations were not only intended to corroborate the predictions of the 2D simulations but also to provide a more realistic picture of the interaction as they can account for azimuthal structure in the radiation modes. This will permit coupling to and excitation of a larger range of modes than the 2D version could show (the 2D PiC codes impose azimuthal invariance in all variables). Hence 3D simulations would yield, in principle, a better representation of the experiment.

Figure 5.1 illustrates the geometry of the simulation. The cylindrical waveguide radius matched the experimental geometry, 4.14cm. The magnetic plateau region was

20cm long, Figure 5.2, and the beam can be seen impacting into the walls at z=50cm. At around z=225cm there is a ‘numerical’ absorber, which has a conductivity that increases from zero moving from left to right in the absorber. The function of this element was to absorb radiation within the interaction waveguide. It effectively represents the output window of the experiment. The guide magnetic field is seen Figure 5.2. Unlike the 2D simulations, the solenoids and electron gun are not defined in the 3D simulations due to memory constraints. The beam is instead injected with a predefined horseshoe distribution (see theory section 2.3).

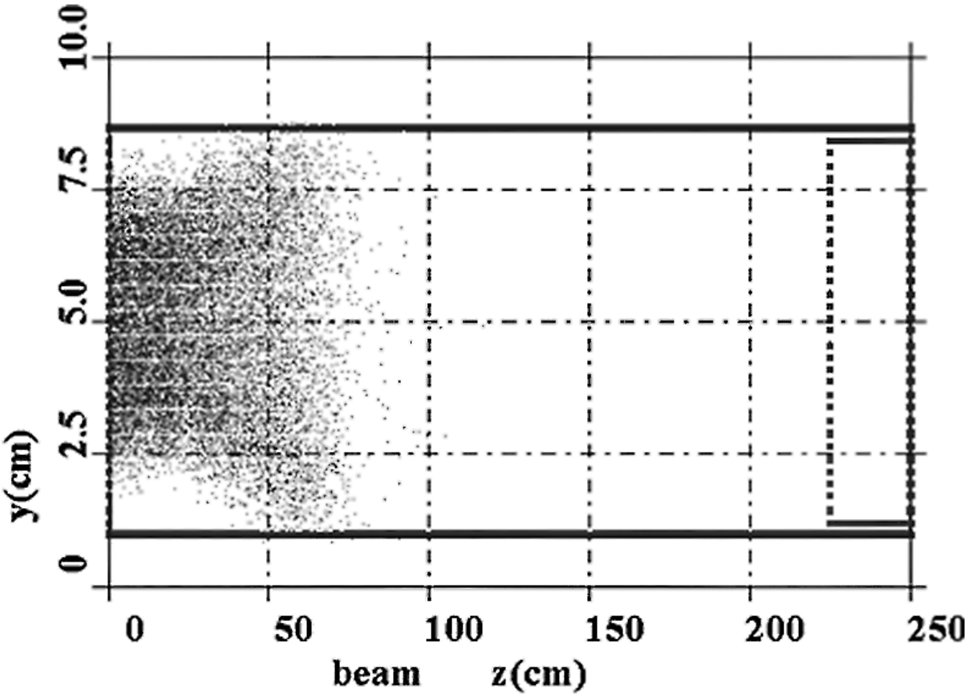

Figure 5.1**:** Experimentally consistent simulation geometry, illustrating waveguide with the electron beam PiC particle trajectories of a pre-defined horseshoe distribution.

Plots of the electron beam phase space are generated, Figure 5.3, illustrating the evolution of the transverse momentum of the beam along the waveguide. Referring to the highlighted area, corresponding to the plateau of the magnet system, Figure 5.3**a**, one notes that initially the electrons have a spread in their transverse and axial momentum, due to the injected horseshoe distribution. From z=0-20cm the action of the AKR mechanism induces a further spreading of the momentum. The arrow path in Figure 5.3**a** shows net loss of rotational momentum due to the instability.

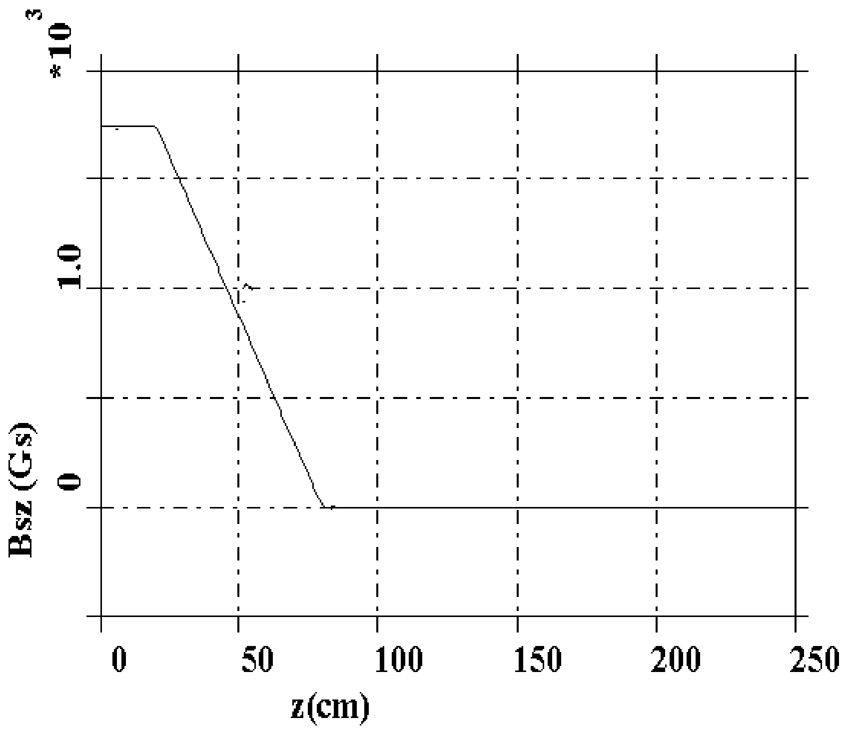

Figure 5.2**:** Magnetic field profile for initial 4.42GHz simulations (peak B-field B=0.18T), 11.7GHz simulations used a similar profile with a peak B field of B=0.48T.

At the point where the magnetic field declines, conservation of magnetic moment results in a conversion of transverse momentum to field aligned axial momentum. The spread in momentum due to the horseshoe distribution is also evident in the axial momentum, Figure 5.3**b**, which is unperturbed by the cyclotron emission mechanism.

As mentioned, the initial regimes investigated in the 3D simulations were kept consistent with the geometry and magnetostatic configuration of previous experimental studies. These being resonant magnetic fields of close to B=0.18T and B=0.48T with resonant frequencies of ~4.42GHz and ~11.7GHz respectively. At the lower resonant magnetic field of B=0.18T the experiment had a reserve of magnetic flux that could be used by the mirroring process to analyse the electron beam distribution in velocity space (see section 5.3). At a magnetic field of B=0.48T the waveguide is very overmoded (D>>λ), which therefore better represents the auroral source region.

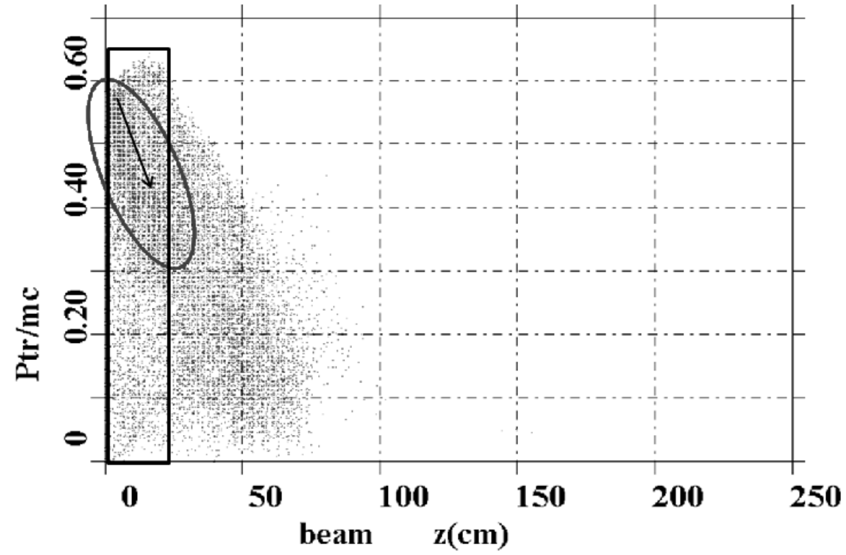

(a)

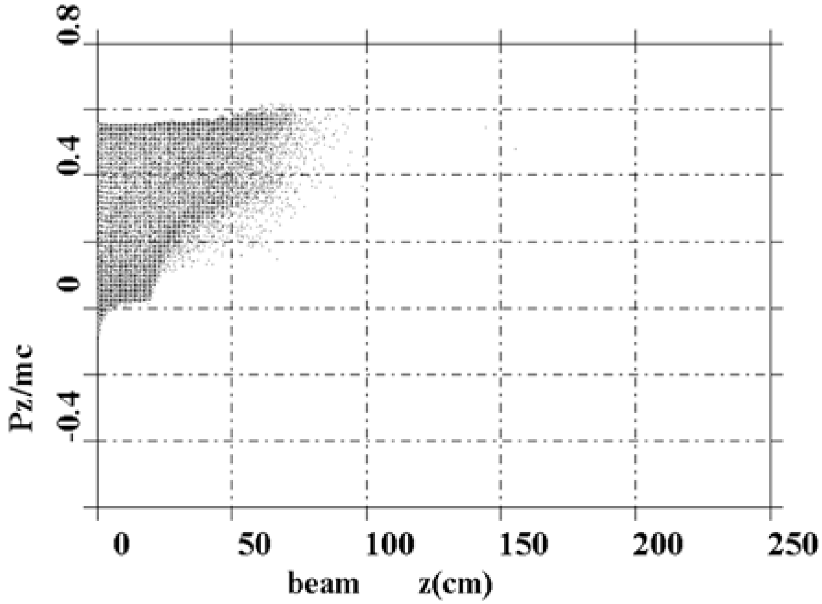

(b)

Figure 5.3**:** Phase space plots of the electron beam in simulations, illustrating the spread in (a) transverse and (b) axial momentum due to horseshoe distribution.

Table 5.1 below summarises the key parameters of the 4.42GHz simulation. The peak magnetic field was chosen to complement the 4.14cm radial bounding geometry. At z=0.2m in the simulation geometry (the experiment has a plateau field 20cm in length) the magnetic field declines linearly towards zero at z=0.8m. This causes the beam to diverge radially and terminate on the waveguide wall. Again this is reproducing the broad behaviour of the experiment and ensures that there is a region downstream of the resonant volume where the radiation may be measured in isolation from the electron beam. At the end of the simulation region a gradated density dielectric region, 0.25m long, is defined at z=2.25m. This absorbs the radiation before it reaches the simulation boundary. The beam current in the simulation is shown in Figure 5.4.

Geometrical Parameters	***Value or Range***
Axial length	2.5m
Radial width of interaction waveguide	0.0414m
Axial mesh spacing	0.2cm
Radial mesh spacing	0.2cm
Electron beam parameters	***Value or Range***
Electron beam current I_b	11A
Electron beam energy E	-75kV
Injected electron beam pitch-factor spread	$\alpha = 0.36 \rightarrow 11.4$
PiC particle merging factor	3×10^7 electrons/PiC particle
Number of PiC particles in system	~80,000 PiC particles
Constant magnetic field parameters	***Value or Range***
Axial magnetic field B_z0	0.18T
Length of constant axial field region	0.2m
Dielectric absorbent region post beam	***Value or Range***
Radial limits	$0 \rightarrow 0.0414$m
Axial limits	2.25 - 2.5m
Conductivity	Isotropic with linear gradation 0-0.1Siemens/m
Relative dielectric permittivity $\boldsymbol{\varepsilon_r}$	3.2
Relative dielectric permeability μ_r	1

Table 5.1: Parameters for initial 4.42GHz simulations.

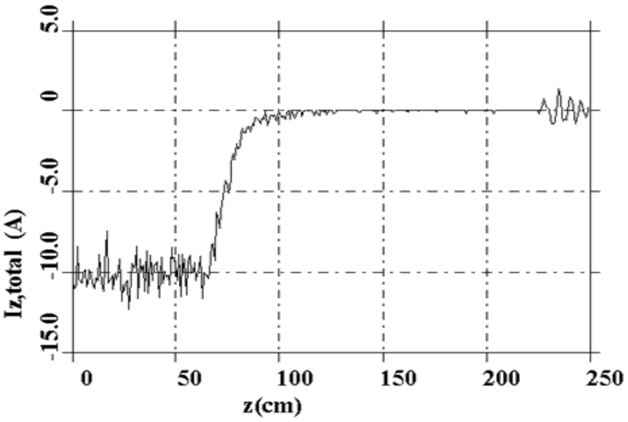

Figure 5.4**:** Beam current plot for 4.42GHz simulations, ~11A.

Figure 5.5 is a plot generated by 3D KARAT illustrating the electric field pattern of the excited modes in the output area of the system. Here it can be seen that the mode is the $TE_{0,1}$, the mode expected to be in resonance at 4.42GHz.

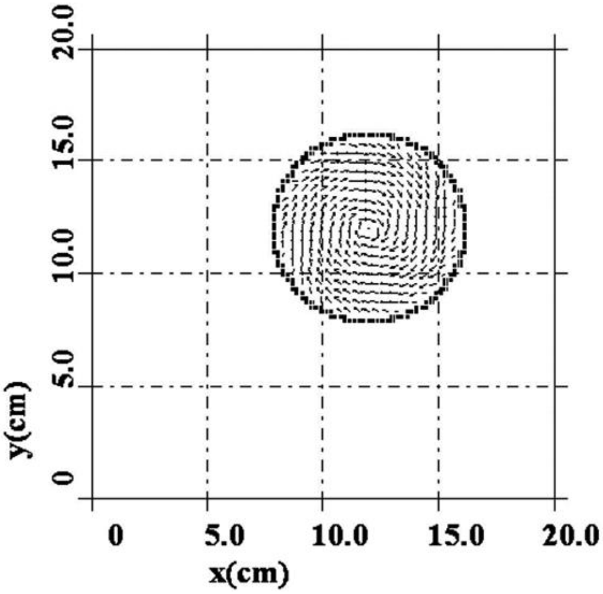

(a)

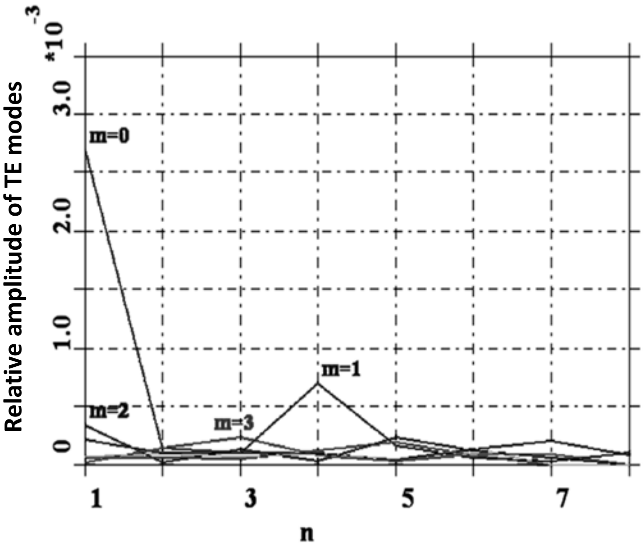

(b)

Figure 5.5: KARAT output illustrating (a) Electric field vector plots from simulation illustrating excitation of the $TE_{0,1}$ mode (b) Spatial analysis of the modes excited in the interaction. Here it can be seen the $TE_{0,1}$ is the predominant mode.

Figure 5.6 is the Fourier transform of the time history of the electric field when the simulation is tuned to a 4.42GHz resonance. A signal close to 4.42GHz was excited as expected. It can be seen that there is a 2nd harmonic signal. A 2nd harmonic signal was observed in the previous experiments [McConville et al. 2008] but had not been predicted by the 2D simulations [Speirs et al. 2008]. The advantage of the 3D simulation is that it can model non-axisymmetric field structures and this explains why the 3D simulations were able to resolve this harmonic generation.

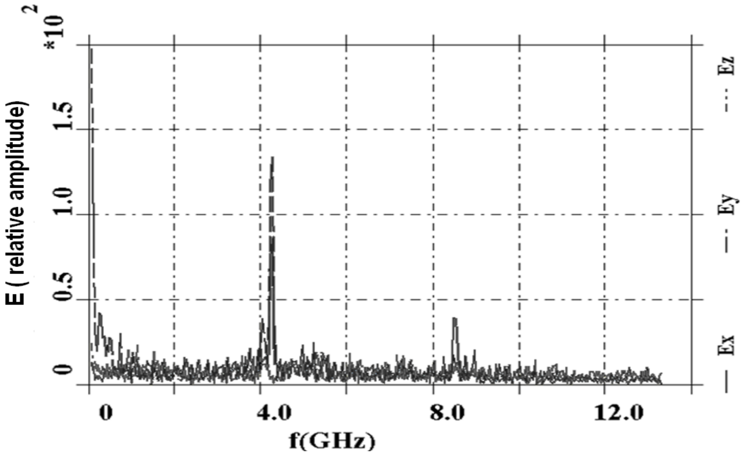

Figure 5.6: Fourier transform of electric field in a simulation tuned for 4.42GHz illustrating 2nd harmonic.

Figure 5.7 is a plot of the Poynting flux integrated over the end of the waveguide, this allows the output power of the radiation to be determined. The fast oscillation corresponds to twice the wave frequency and the average power is given by averaging over this sin^2 function. The maximum power output predicted for the system is ~28kW. This yields an efficiency of ~3% which is comparable to both the experimental measurements ~1-2% and the magnetospheric observations, ~1% [Gurnett 1974][McConville et al. 2008].

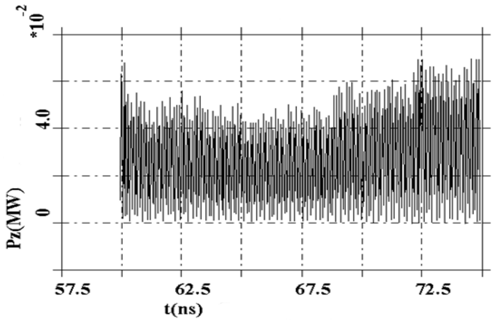

Figure 5.7: Power output from 4.42GHz simulations, illustrating an average power ~28kW corresponding to an efficiency of ~3% which is comparable to experimental values.

Table 5.2 below summarises the key parameters of the 11.7GHz simulation. Here the magnetic field is B=0.48T and the beam current is 16A, with an energy of 85keV. Note that the voltage and current was changed slightly between the 4.42GHz and the 11.7GHz.

Geometrical Parameters	***Value or Range***
Axial length	2.5m
Radial width of interaction waveguide	0.0414m
Axial mesh spacing	0.2cm
Radial mesh spacing	0.2cm
Electron beam parameters	***Value or Range***
Electron beam current I_b	16A
Electron beam energy E	-85kV
Injected electron beam pitch-factor spread	$\alpha = 0.36 \rightarrow 11.4$
PiC particle merging factor	3×10^7 electrons/PiC particle
Number of PiC particles in system	~80,000 PiC particles
Constant magnetic field parameters	***Value or Range***
Axial magnetic field B_{z0}	0.48T
Length of constant axial field region	0.2m
Dielectric absorbent region post beam	***Value or Range***
Radial limits	0 → 0.0414m
Axial limits	2.25 - 2.5m
Conductivity	Isotropic with linear gradation 0 - 0.1Siemens/m
Dielectric permittivity ε_r	3.2
Dielectric permeability μ_r	1

Table 5.2: Parameters for initial 11.7GHz simulations.

Figure 5.8 illustrates the modes excited in the simulation, it can be seen that the predominant mode is the $TE_{0,3}$. Figure 5.9 shows the electric field patterns from the output of the simulation, it can be seen that in (a) the mode is the $TE_{0,3}$ and (b) there is a $TE_{2,3}$ pattern excited. There is a possibility that this is indicative of mode competition and this will be investigated further in section 5.6.

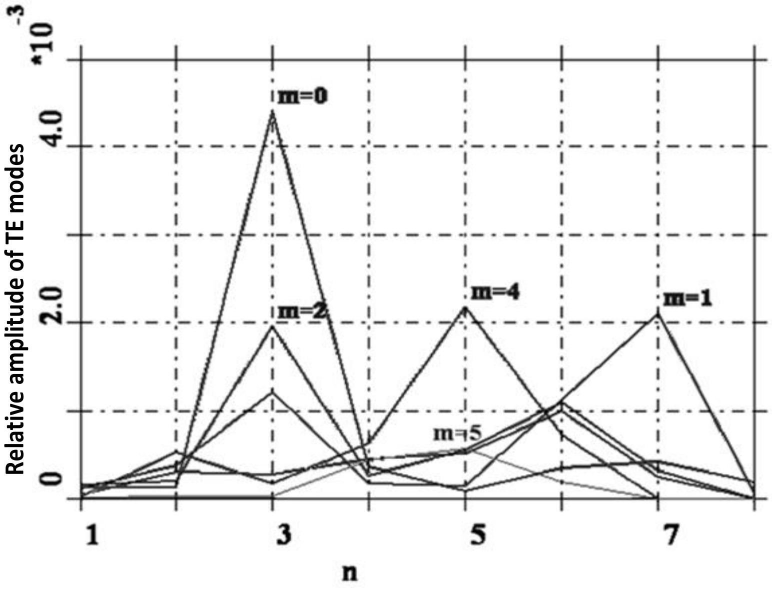

Figure 5.8**:** KARAT output predicting the modes excited in the high frequency (11.7GHz) interaction. Here it can be seen the $TE_{0,3}$ is the predominant mode.

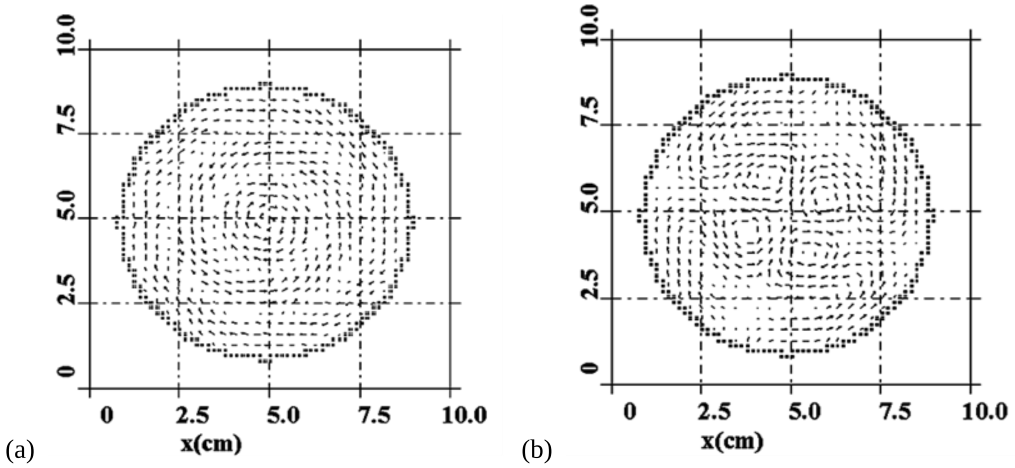

(a) (b)

Figure 5.9**:** (a) Electric field vector plots illustrating $TE_{0,3}$ mode. (b) Electric field vector plots illustrating $TE_{2,3}$ mode.

Figure 5.10 & Figure 5.11 illustrate the Fourier transform of the electric field. The resonant frequency excited is ~11.7GHz, which was as expected, close to f_{ce}. There are also small peaks which occur at 11.3GHz and 11.5GHz, this could also be representative of mode competition in the interaction. This confirms mode patterns observed from the experiment which in this resonance regime indicated competition between two modes, the $TE_{0,3}$ and $TE_{2,3}$ [McConville et al. 2008]. Figure 5.12 shows the Poynting flux from the simulations, predicting a peak output power of 17kW yielding an efficiency of ~2%, the efficiency of the experiment was ~1-2%.

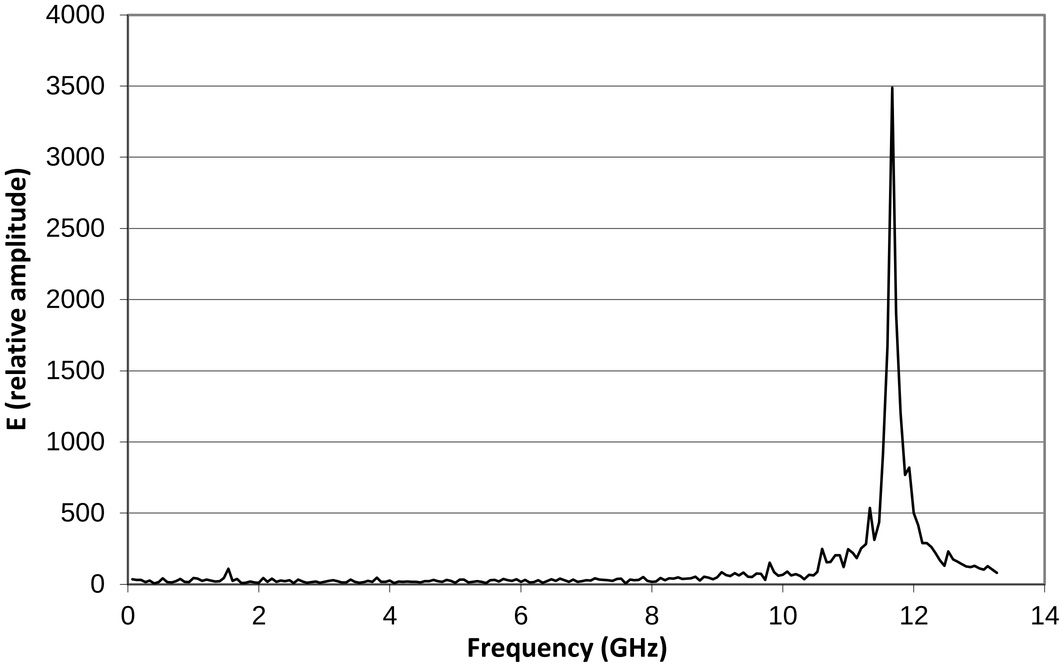

Figure 5.10**:** Fourier transform of the E-field taken close to the source region at 0.05m over a period of t= 75-80ns, illustrating the primary resonance at a peak frequency of 11.6GHz. There is also a small peak at ~11.3GHz, indicating possible mode competition.

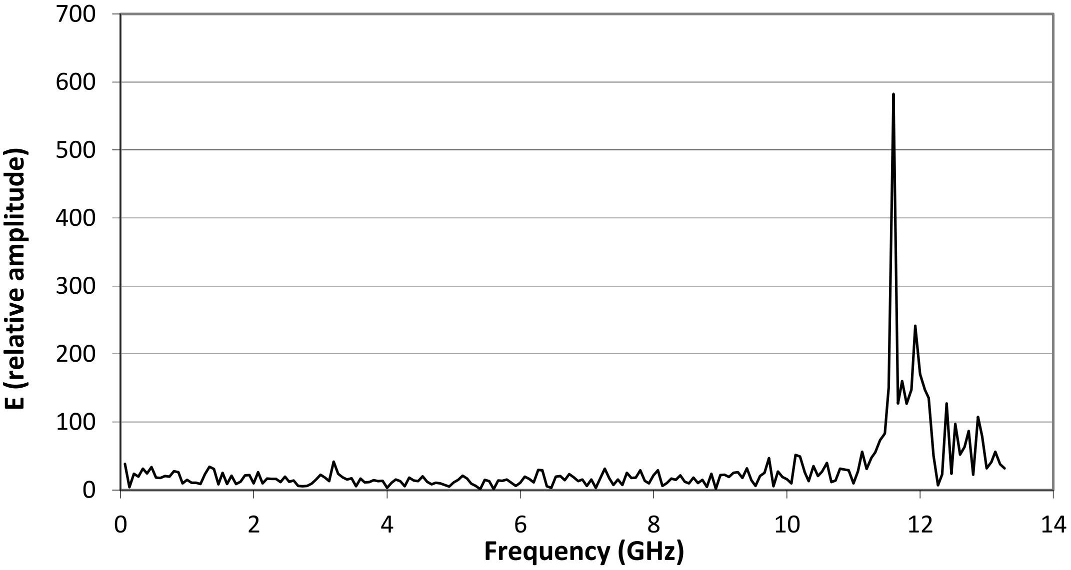

Figure 5.11**:** Fourier transform of E-field of 1.2m downstream from the source region showing that several nanoseconds earlier the spectra has peaks at ~11.6GHz and ~12GHz.

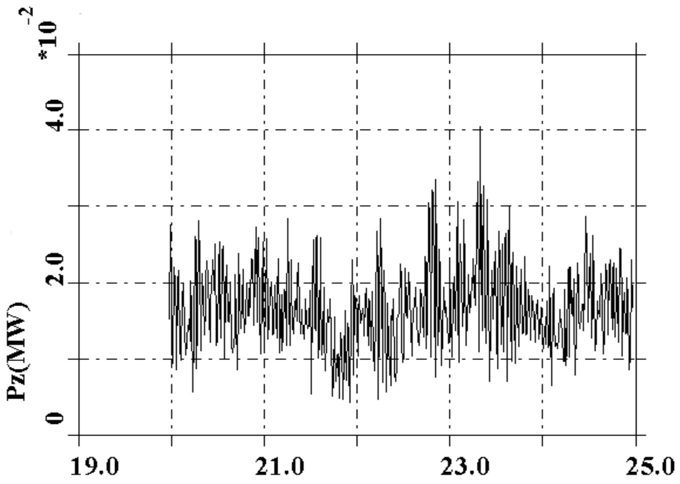

Figure 5.12**:** Output power for 11.7GHz simulations. Peak power around 17kW, which equates to an efficiency of ~2%, comparable to experiment and magnetospheric efficiencies. Note the power does not have a typical $\sin^2$ transient minima at zero due to the overmoding in the simulation.

These initial simulations tested the 3D method against previous 2D simulations and experimental data. The results they produced were broadly consistent with both previous results. However they also provided insight that could not be predicted by previous 2D simulations (mode competition, harmonic excitation).

5.2 Analysing the impact of beam current, detuning and velocity distribution

The effect of varying the beam current, electron distribution and magnetic detuning were investigated. These simulations were conducted initially in 2D KARAT, the reasoning for this was to be able to study and analyse a wide range of parameters rapidly within a simpler simulation system. In 2D simulations azimuthal structure is discounted, eliminating the requirement to mesh one of the transverse dimensions (θ in this case). However, as previously mentioned, it means a limited mode spectrum may be coupled to the electron beam.

The geometry for the simulation is shown in Figure 5.13, the solenoid can be seen at the top of the waveguide. The crosses indicate points where detailed data is recorded for analysis. It can be seen that a taper has been added in the injection side of this simulation, the taper allows transport of the beam, Figure 5.14, correct positioning of the emitter surface gave minimal beam scraping. The small neck on the beam tunnel cuts off all radiation modes, thus ensuring that all the reverse propagating signals would be reflected to the output. The magnetic field profile is seen in Figure 5.15. The impact of the beam current, particle distribution and detuning (see theory section 2.5.2) on the output power and the resonant frequency was analysed.

Referring to Table 5.3, seventy two different regimes were studied; four different values of beam current were tested over a range of magnetic detuning for two electron distributions. To distinguish between the two different velocity distributions tested they have been assigned the titles of Distribution 1 and Distribution 2; these refer to an electron distribution from 10^{o} to 80^{o} pitch angle and an electron distribution from 50^{o} to 80^{o} pitch angle respectively.

A further distribution was investigated, defined here as Distribution 3. The pitch angle spread is the same as Distribution 1, from 10 degrees to 80 degrees, but with a progressively increasing density distribution (with twice the number of particles at 80 degrees compared to 10 degrees).

Distribution 1		**Distribution 2**	
Bo (T)	0.1854	***Bo (T)***	0.1854
Pitch angle range (degrees)	10 – 80	***Pitch angle range (degrees)***	50 – 80
Energy (keV)	75	***Energy (keV)***	75
Current (A)	1.7 - 12	***Current (A)***	1.7 – 12
Density distribution	Uniform	***Density distribution***	Uniform

Distribution 3	
Bo (T)	0.1854
Pitch angle range (degrees)	10 – 80
Energy (keV)	75
Current (A)	1.7 - 12
Density distribution	Increasing

Table 5.3: Parameters for beam current and detuning simulations.

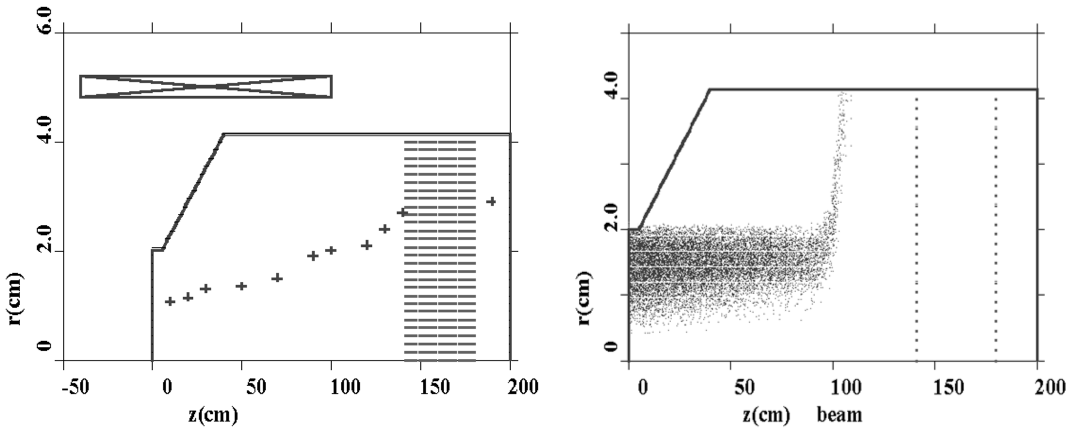

Figure 5.13**:** KARAT simulation geometry used for investigation of the impact of the electron distribution function, beam current and detuning, illustrating the waveguide, the interaction solenoid, dielectric, and cross reference points and the simulation geometry. Also illustrated is the beam trajectory, and collection into the walls at z=100cm. The dielectric can be seen at z=135cm.

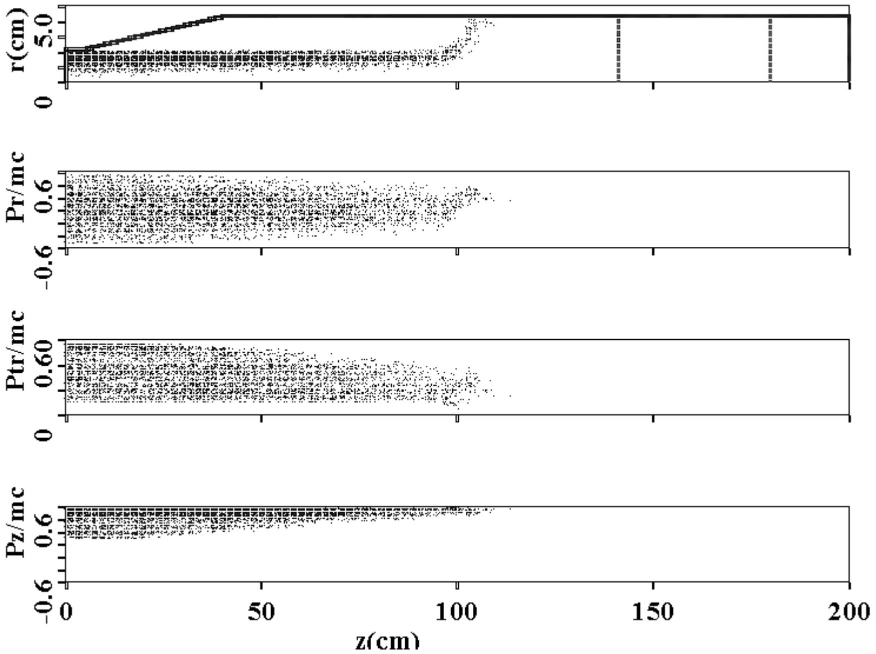

Figure 5.14**:** KARAT simulation geometry illustrating electron distribution in normalised momentum space in P_r, P_t and P_z.

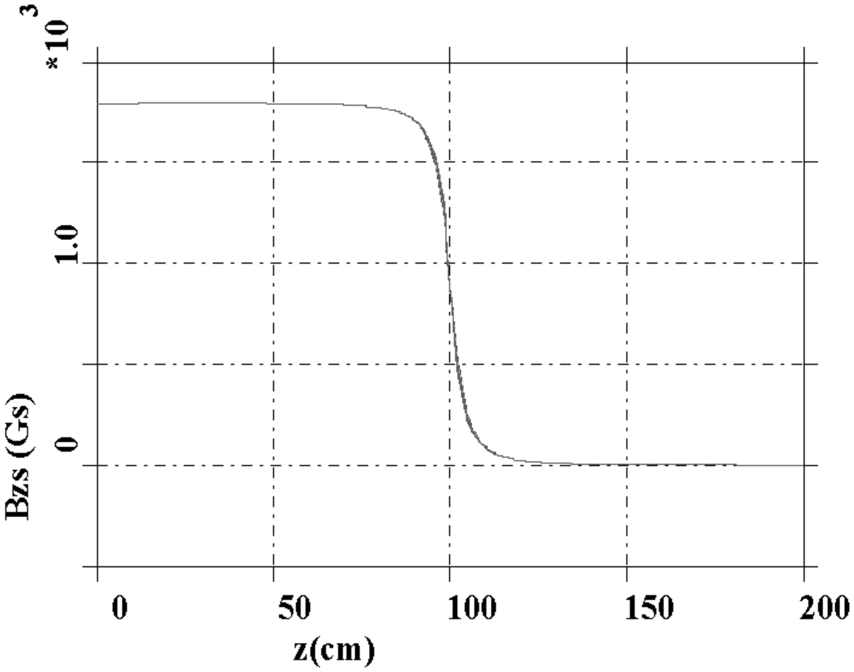

Figure 5.15: The magnetic field profile for the simulations. The plateau, B=0.1854T (which was varied in the simulations to control the detuning), is longer than the experimental magnetic field plateau of 20cm, this is to transport the beam through the tapered section in the geometry, the 'resonant' length remains 20cm.

Figure 5.16 shows the electron distribution in velocity space, illustrating the horseshoe distribution.

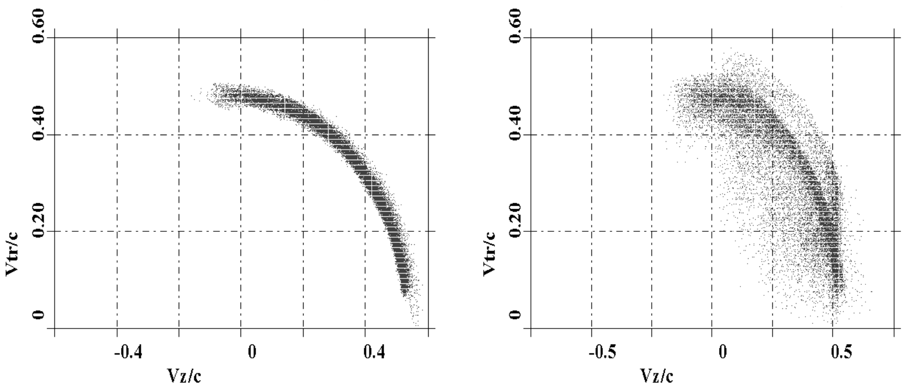

Figure 5.16: Electron distribution in velocity space (for distribution 1), illustrating the injection and evolution of the horseshoe distribution from the start of the simulation t=20ns (prior to RF wave generation) to the end at t=120ns (saturated RF wave generation).

Figure 5.17 and Figure 5.18 illustrate the trends of the emission frequency and the output power with increasing detuning. The electrons in the horseshoe distribution are initially uniformly distributed in gyro phase (phase asynchronous) extending from 0^{o} to 360^{0}.

It is clear to see that, from Figure 5.17, the output power increased with the input beam current. With the current increasing by a factor of seven the output power increases by over a factor of thirteen, increasing from ~6kW to ~80kW. However there is a sharp resonance when the cyclotron frequency is close to the waveguide cut-off frequency (corresponding here to 0% detuning) with sharp drops in emission efficiency for either increasing or decreasing detuning although the power still (typically) increases with current.

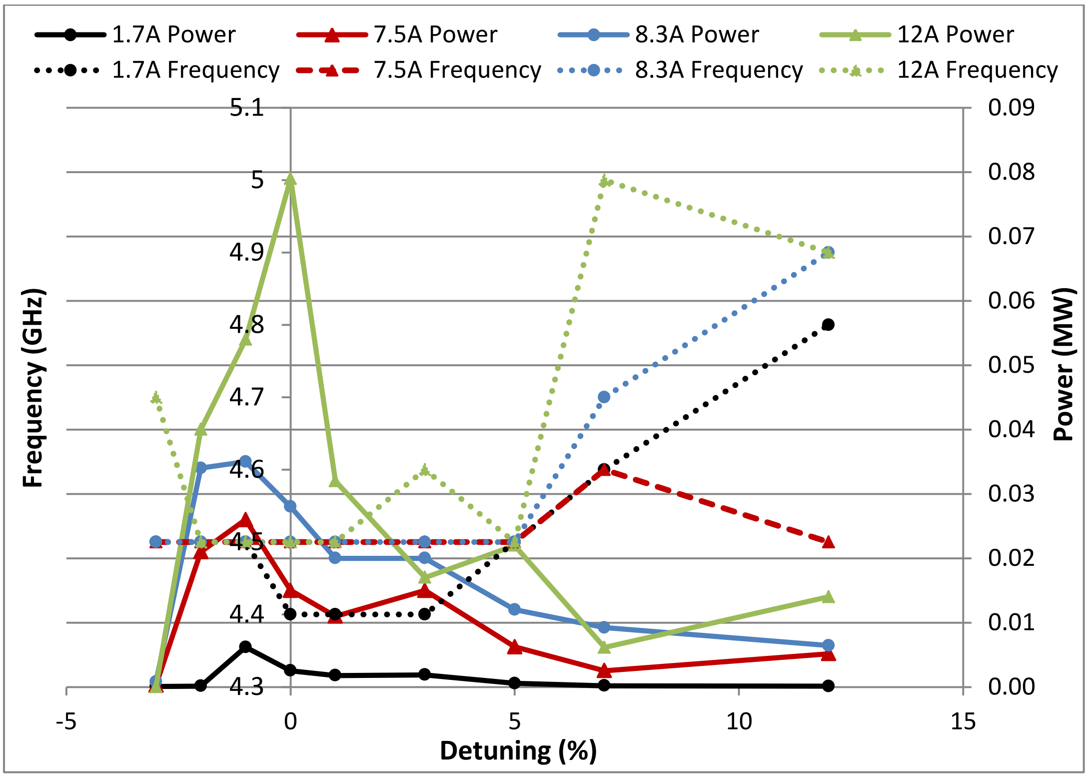

Figure 5.17**:** Resonant frequency and output power as a function of detuning ($(\omega_{ce}-\omega_{co})/\omega_{co}$) for Distribution 1 ($10^{o}$-$80^{o}$ horseshoe distribution).

Referring to the output frequency, it holds steady at around 4.5GHz in the vicinity of the resonance irrespective of detuning. However, with a sufficiently large detuning the wave power falls off rapidly whilst the wave frequency significantly increases.

From this it can be concluded that with sufficient beam current the instability tolerates the cyclotron frequency to exceed the transverse cut off by nearly 5%. This is consistent with the excitation of longitudinal modes above waveguide cut-off.

Figure 5.18 also illustrates how the detuning and beam current impacts on the output power and frequency. However, for the results presented in Figure 5.18 the horseshoe beam distribution function is concentrated on high pitch angles from 50° to 80° i.e. distribution 2.

For distribution 2, an increasing output power with increasing beam current is still observed. Increasing from 13kW for a beam current of 1.7A to a peak value of ~127kW for a beam current of 12A, this yields a maximum efficiency of 14%. In contrast, with distribution 1 a beam current of 12A gives a peak value of 79kW this yields an efficiency of ~9%. For a beam current of 1.7A the efficiencies for Distribution 1 and 2 are ~5% and 10% respectively. This clearly shows the importance of the high pitch electrons in providing the free energy to drive the instability for AKR emission.

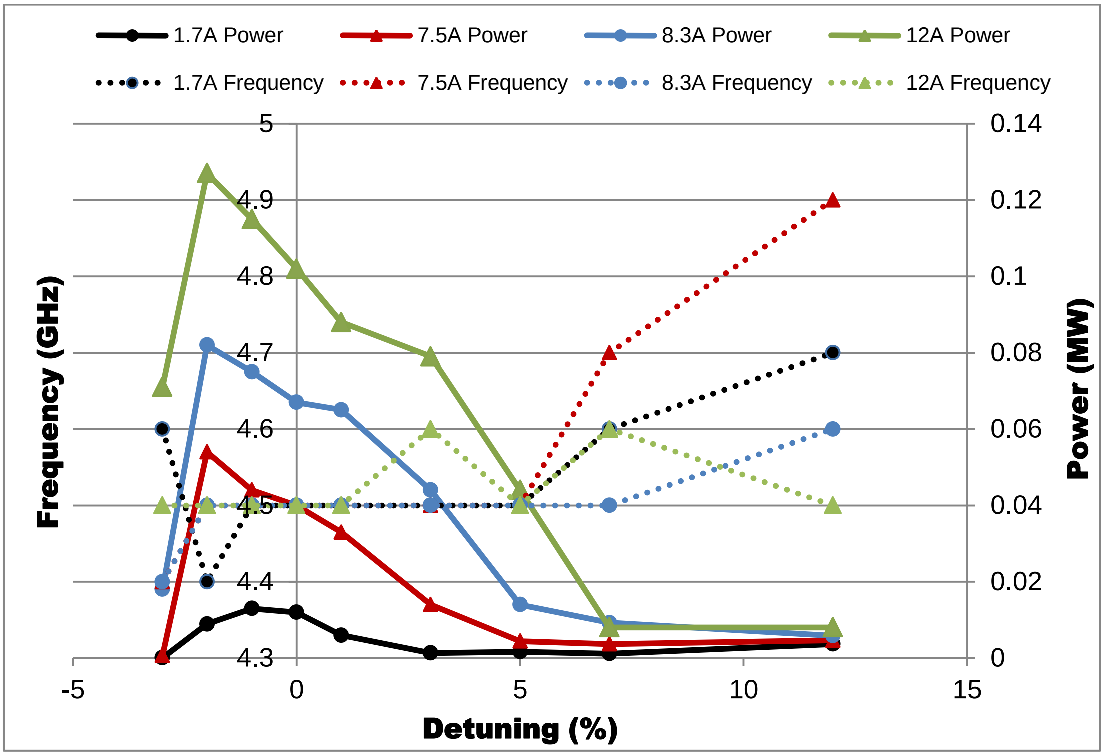

Figure 5.18**:** Resonant frequency and output power as a function of detuning, for Distribution 2 (50°-80° horseshoe distribution).

The toleration of the instability to detuning (-2 to +4-5%), plus the tendency to hold a given frequency (typically ~4.5GHz – 4.55GHz) irrespective of a significant change in gyro frequency is interesting. The frequency corresponds to a radiation propagation angle in the waveguide ~14° (arctan $k_z/k_\perp$) from perpendicular, suggesting emission is possibly away from exact perpendicular propagation in spite of relatively large velocity spread. This may be important to the wave propagation in the polar magnetosphere, particularly how the radiation is transmitted from the source region through the complex polar plasma to be observed by satellites as a free space wave. The significantly higher efficiencies seen here compared to earlier simulations suggests the effectiveness of the reflector and represents the first numerical indication that the wave may be preferentially emitted into a backwards propagating signal. This will be considered again in Section 5.7.1.

These results have shown that the pitch angle distribution of the electrons is vital in determining the strength of the instability. It is therefore interesting to consider the impact of progressive variation of the electron distribution in pitch angle. Distribution 3 has a range in pitch from 10 degrees to 80 degrees with increasing particle density, Table 5.3, such that there are twice the number of particles associated with 80° pitch angle as compared to those at 10°.

Figure 5.19 shows the variation of output power and frequency with electron current at a detuning of 2.8% for Distribution 3 showing that it has a higher output power compared to that of Distribution 1. The predicted wave emission frequency for both distributions rises from 4.4GHz to 4.5GHz as the beam current increases from ~3A to ~16A whilst the power increases with beam current. The spectra show clearly a transition from incoherent to coherent emission as time evolves in all cases, illustrated in Figure 5.19(b).

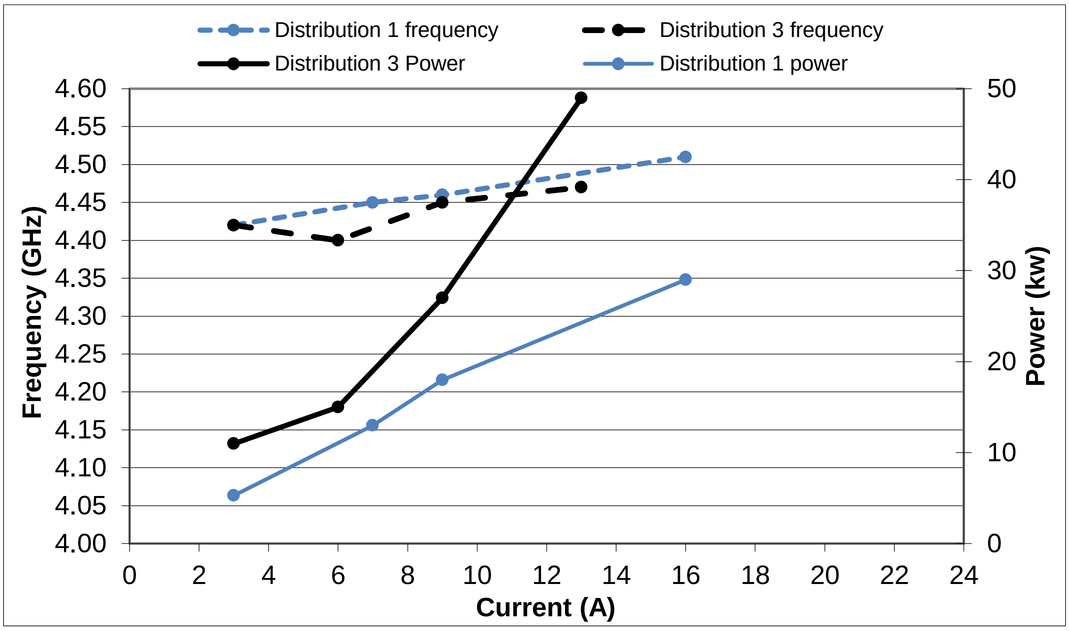

(a)

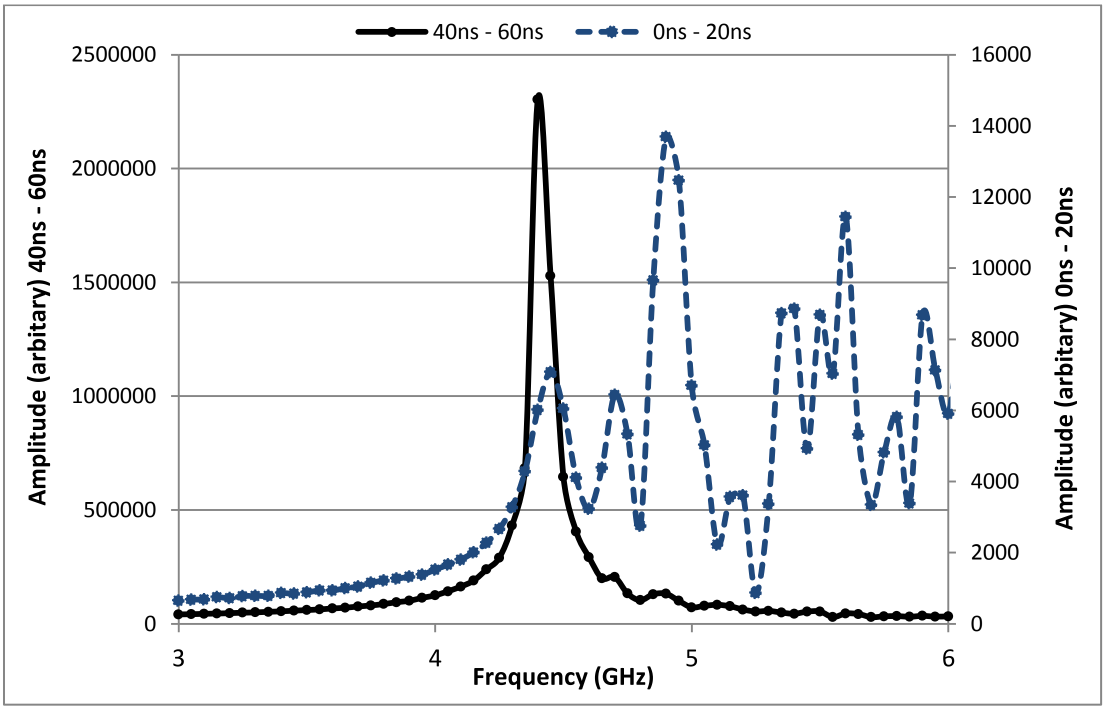

(b)

Figure 5.19**:** (a) Resonant frequency and output power as a function of current for a uniform particle distribution in pitch angle (Distribution 1) and for a progressively increasing distribution (Distribution 3) for a detuning of 2.8%. (b) Fourier transform of electric field spectrum, illustrating the transition from incoherent to coherent emission with increasing time.

5.3 Matching electron velocity distributions of 4.42GHz experiments and simulations

As illustrated in section 5.2, the distribution of particles is rather important in determining the strength of the instability. Therefore 3D simulations were conducted where the distribution of the electrons in velocity space was matched to the measurements obtained for the beams used in the 4.42GHz resonance regime experiment, defined in Table 5.4. This matching was not performed for the 11.7GHz resonance as there was no suitable number density distribution data available from these experiments to which to match. Modifying the numerical input parameters to provide a strong correlation to the experimental measurement will achieve a more comparable electron distribution function and should yield a more accurate prediction of the wave production efficiency. The beam was characterised in the experiment by measuring the ‘loss cone’ current as a function of the mirror ratio. The mirror ratio is calculated (for these purposes) as the ratio of the magnetic field at the cathode to the plateau magnetic field of the experiment.

Experiments at a mirror ratio of 9		**Experiments at a mirror ratio of 17**	
B_0 (T)	0.18	***B_0 (T)***	0.18
Energy (keV)	75	***Energy (keV)***	75
Current (A)	35	***Current (A)***	12

Table 5.4: Initial simulation parameters used to mould the number density distribution to that of the experiment for mirror ratios of 9 & 17. B_o is the plateau magnetic field required for resonance with the EM radiation at 4.42GHz.

The experimental estimates of the line density are shown as a function of pitch angle in Figure 5.20. The trend of the number density distribution for the particles in the simulation was read from Figure 5.20 and the software was loaded with a table (see Table 5.5) which defined the weighting associated with each pitch angle. This initial table was then iteratively evolved by comparing the simulated loss cone current versus the magnetic mirror ratio against that of the experiments. The simulations injected the particles at the plateaux B field of the experimental configuration and then the B field was slowly increased in z to determine the transmitted current as a function of the mirror ratio. The overall parameters used in the simulation are shown in Table 5.6.

Pitch angle (degrees)	*Mirror ratio 9*	*Mirror ratio 17*
10 - 20	8	1.9
20 - 30	5.9	1.6
30 - 40	4.2	1.4
40 - 50	3	1.3
50 - 60	1.8	0.9
60 - 70	1.3	0.6
70 - 80	1	0.5

Table 5.5: Values taken from experimental mirror plots used to input into KARAT to match the beam distribution.

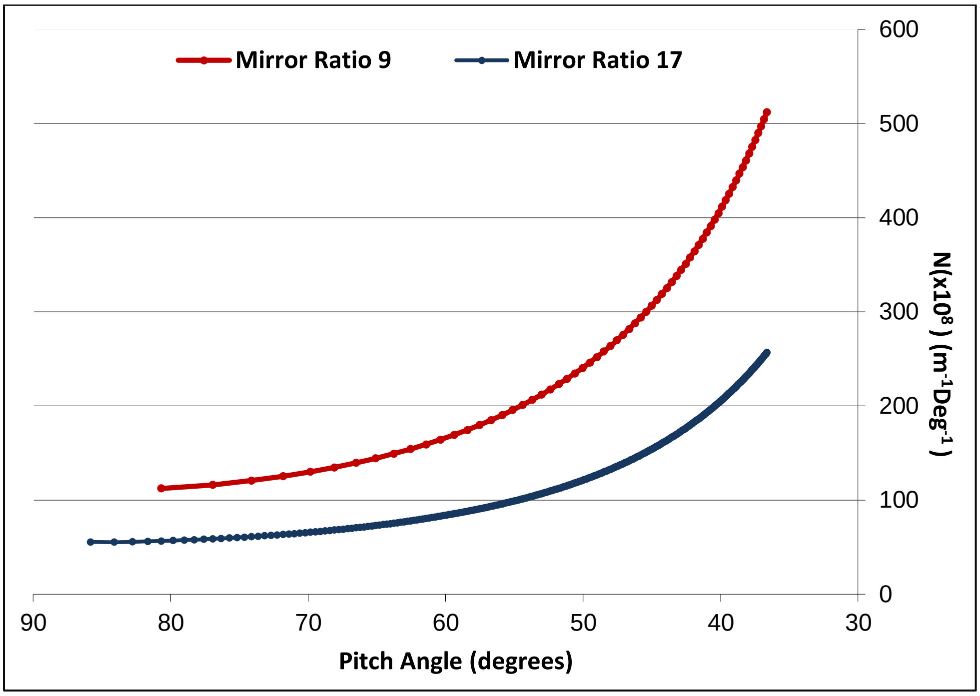

Figure 5.20**:** Experimentally estimated variation of the electron line density as a function of pitch angle. Utilised in matching the electron distribution in 3D KARAT simulations.

Geometrical Parameters	***Value or Range***
Axial length	2.5m
Radial width of interaction waveguide	0.0414m
Axial mesh spacing	0.2cm
Radial mesh spacing	0.2cm
Electron beam parameters	***Value or Range***
Electron beam current I_b	12A – 35A
Electron beam energy E	75kV
Injected electron beam pitch-factor spread	$\alpha = 0.36 – 11.4$
PiC particle merging factor	3×10^7 electrons/PiC particle
Number of PiC particles in system	~80,000 PiC particles
Constant magnetic field parameters	***Value or Range***
Axial magnetic field B_z0	0.17T - 0.5T
Length of constant axial field region	0.20m
Dielectric absorbent region post beam	***Value or Range***
Radial limits	0 → 0.01m
Axial limits	0.125 - 0.150 m
Conductivity	Isotropic with linear gradation 0 - 0.1Siemens/m
Relative dielectric permittivity $\boldsymbol{\varepsilon_r}$	3.2
Relative dielectric permeability μ_r	1

Table 5.6: Full simulation parameters used to mould the number density distribution to that of the experiment for mirror ratios of 9 & 17.

The simulated beam current corresponding to an experimental mirror ratio of 9 (cathode B-field 0.02T, resonant B-field 0.18T) is shown in Figure 5.21.

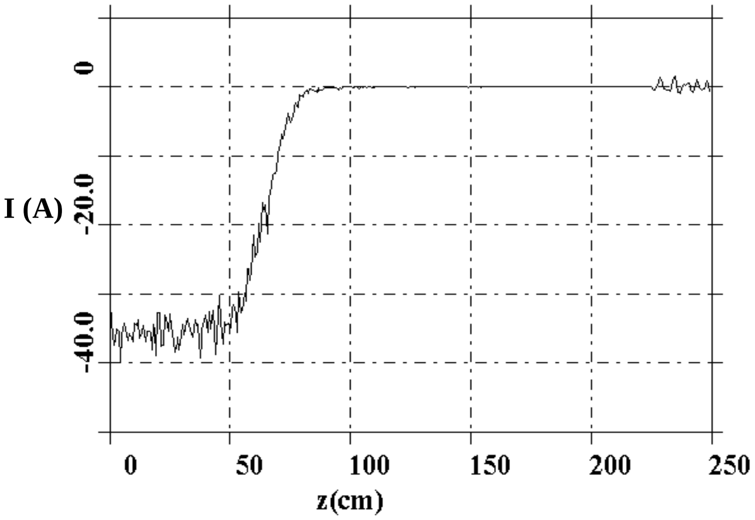

Figure 5.21: Beam current predicted by 3D KARAT simulations with electron distributions matched to experiment at a mirror ratio of 9. Current fluctuation at z=225-250cm is caused by an AC current in the absorbing dielectric.

The variation of the simulated transmitted beam current with mirror ratio as the plateau magnetic field, B, is increased progressively and gradually from the resonant value B_0 (~0.18T) to the maximum experiment magnetic fields of B=~0.5T is shown in Figure 5.22. Figure 5.23 and Figure 5.24 show the same data for a mirror ratio of 17 (cathode B-field 0.0105T, resonant B-field 0.18T).

The decrease in beam current as B_o increased was due to the electrons being mirrored. For both the experimental plateau/cathode mirror ratio's of 9 and 17 it can be seen the simulations matched reasonably well with the experimental measurement.

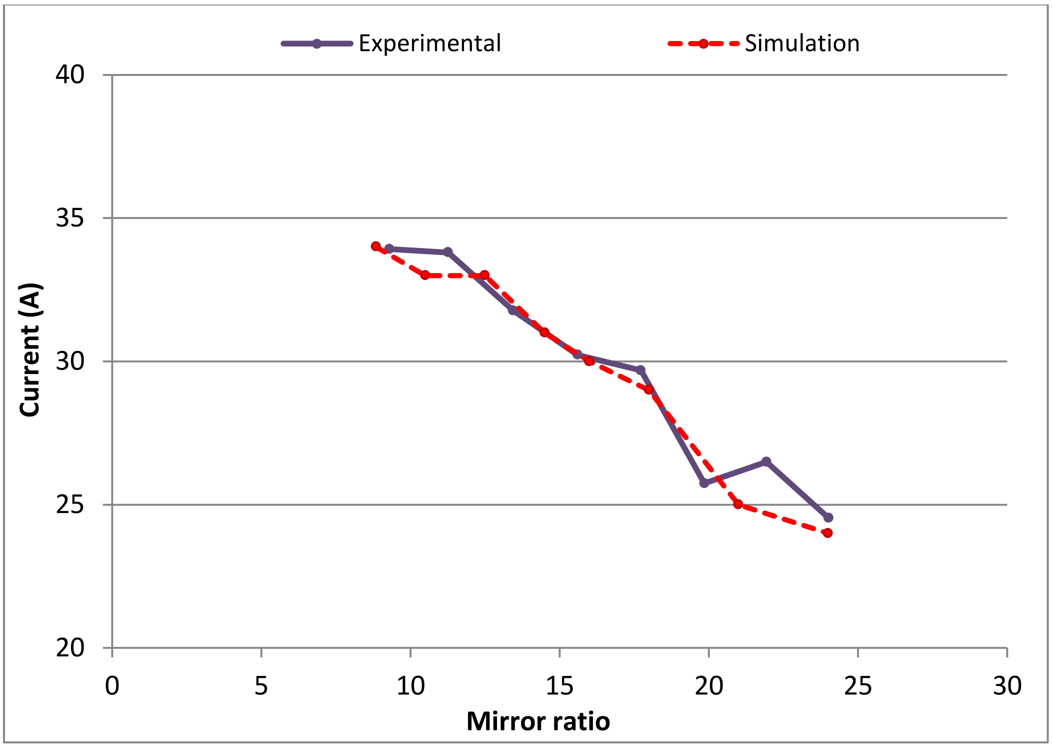

Figure 5.22**:** Matching of simulation electron distribution to experimental data for a plateau/cathode mirror ratio of nine.

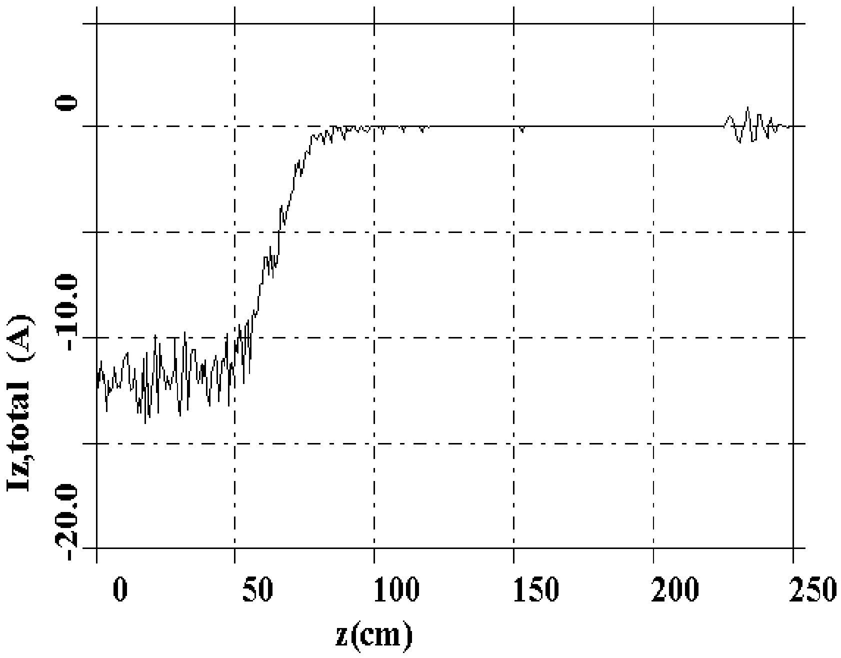

Figure 5.23**:** Beam current input to 3D KARAT simulations with electron distributions matched to experiment plateau/cathode mirror ratio of 17. Fluctuation in the current at z = 225 - 250cm is caused by an AC current in the absorbing dielectric.

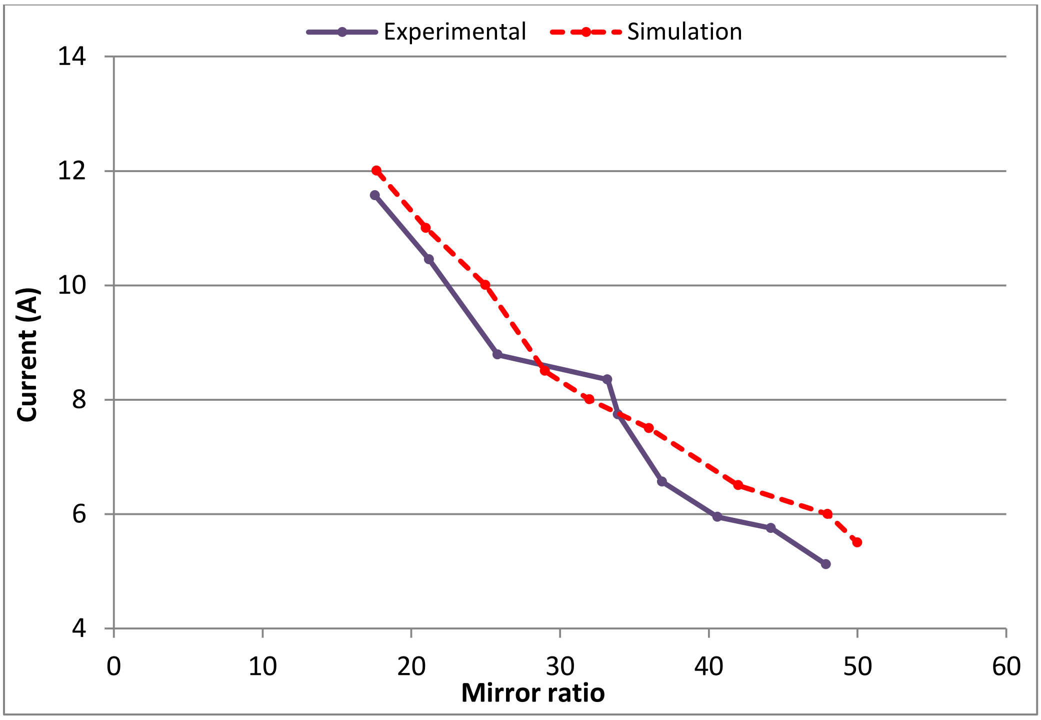

Figure 5.24**:** Matching of simulation electron distribution to experimental data for a plateau/cathode mirror ratio of seventeen.

Thus having arranged that the distribution of the electron number density in the simulation was comparable to the experiment it is possible to simulate the radiation emission process, also for comparison with the experimental measurements. These results are presented in section 5.5.

5.4 Experimental measurement & numerical mapping of the electron beam distribution in velocity space for B=0.11T & revised B=0.18T resonance configurations

Additional experimental measurements were performed in this project, at plateau fields of B=0.18T and B=0.11T. As the 2D simulations showed the distribution of electrons in velocity space was important in determining the strength of the instability, beam current measurements were taken as a function of magnetic field ratio (cathode to interaction space) by inserting a Faraday cup (see theory 4.3.5) into the interaction waveguide. The experimental data was recorded on an oscilloscope, Figure 5.25 illustrates the experimental measurements taken, for both B=0.11T and B=0.18T regimes. The minimum mirror ratio (~11) corresponds to a cavity operating magnetic field of B=0.11T, whilst the mirror ratio of 18 corresponds to an operating cavity magnetic field of B=0.18T, in each case the magnetic flux density through the cathode was B=0.01T. Increasing the plateau magnetic field over each of these values maps the corresponding electron velocity distribution by mirroring.

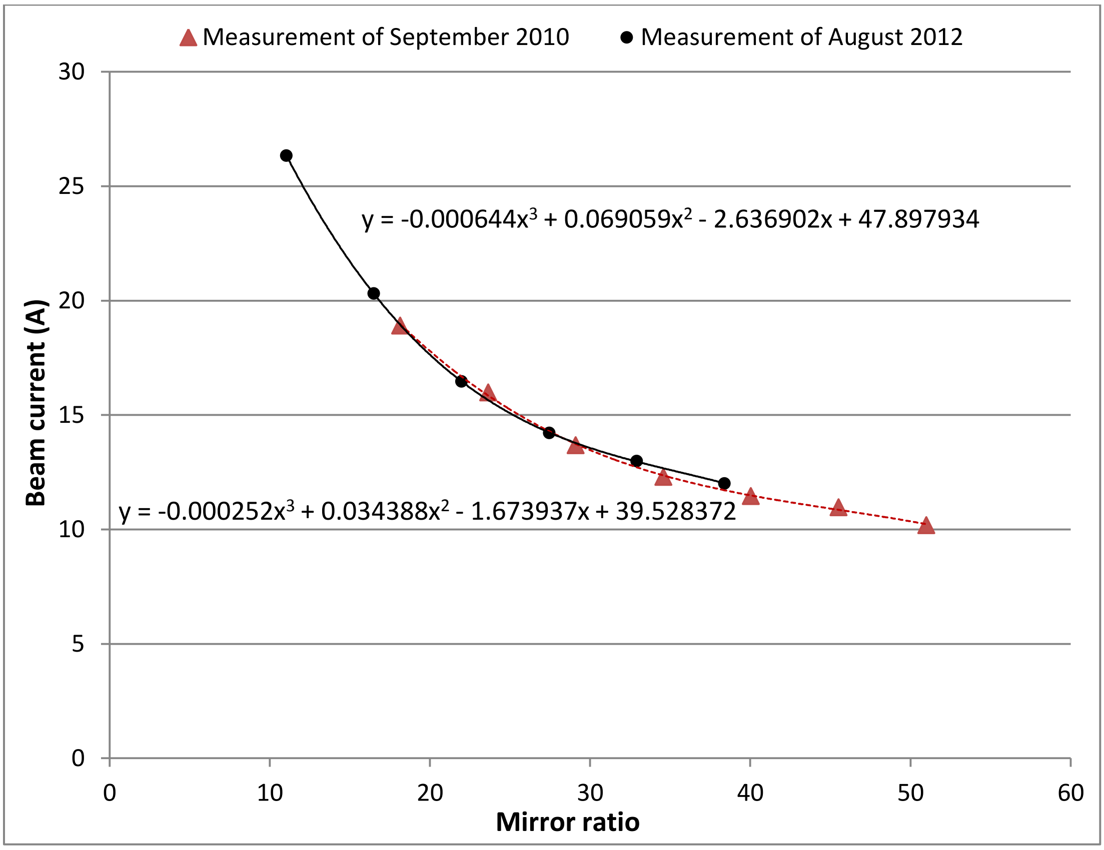

Figure 5.25**:** Experimentally measured beam current for B=0.11T and B=0.18T regimes, mapped with increasing plateaux magnetic field, cathode B=0.01T.

The method adopted in order to calculate the line density distribution of the experiments for input to the simulations from this set of data was to use a best fit trend line to each set of the data. The resulting equations shown in Figure 5.25 and Equation 5.01 and Equation 5.02. These equations were then used to calculate the one dimensional number density, as a function of pitch angle. Figure 5.26 illustrates the line densities implied by this method. The performance of the experiment was very stable as illustrated by detailed reproducibility over a two year period.

The equations used for calculation of the beam velocity distribution at a specified plateau magnetic field were as follows;

At a magnetic field of B=0.11T

$$I = -0.000644\ \mathrm{mirror}^3 + 0.069059\ \mathrm{mirror}^2 - 2.636902\ \mathrm{mirror} + 47.897934 \qquad \text{Equation 5.01}$$

For a magnetic field of B=0.18T

$$I = -0.000252\ \text{mirror}^3 + 0.034388\ \text{mirror}^2 - 1.673937\ \text{mirror} + 39.528372 \qquad \text{Equation 5.02}$$

A point of note is the equations co-efficients are written to six decimal places, the reasoning for this is that this is the minimum requirement that ensures the resultant fitted line matched well over the entire range. With any fewer decimal figures the quality of fit changes dramatically largely due to the x^3 term, giving inferior results.

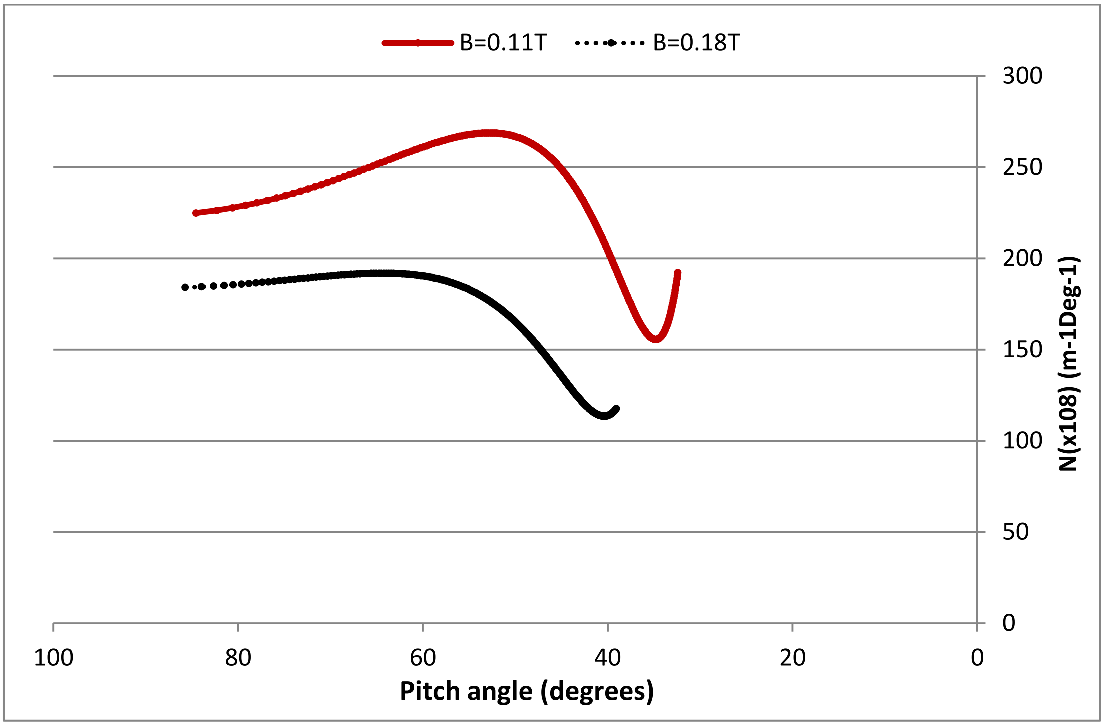

Figure 5.26: Estimated experimental beam distribution for resonances at B=0.18T and B=0.11T plateau magnetic fields.

5.4.1 Matching electron number density distribution of new experimental data to simulations

Matching the number density of the simulations to that of the experiment is as previously noted an important step to enable realistic simulations of the RF wave generation process in the experiment (and hence to understand the implications of the behaviour in the auroral region). The pitch angle distribution of Figure 5.26 was used to define the electron distribution in the simulations. They were then in turn tested by a mirroring simulation which can be directly tested against the initial experimental data, shown in Figure 5.25. The results of the numerical ‘mirroring’ test is shown in Figure 5.27. The mirroring analysis for the simulated electron beam allows the mapping of the 1D number density distribution in pitch angle, just as was done for the experimental data. This is shown in Figure 5.28.

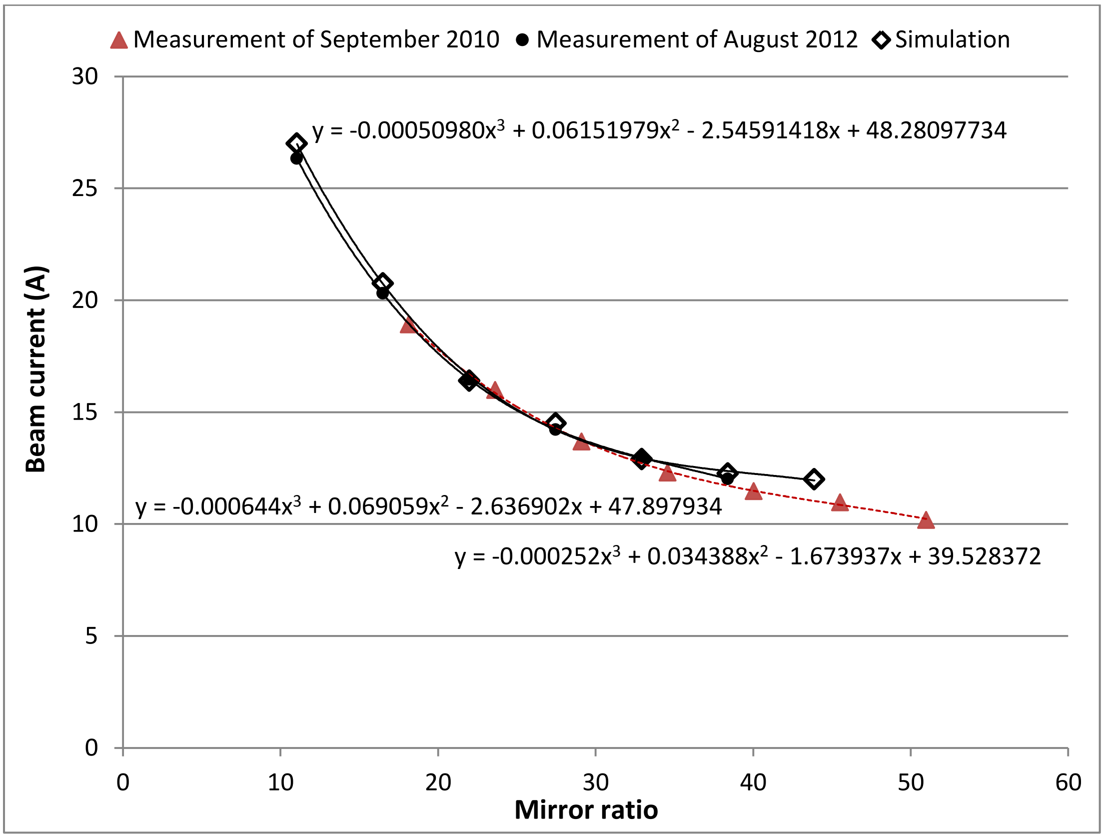

Figure 5.27**:** Experimentally measured beam current for B=0.11T and B=0.18T regimes, mapped with increasing magnetic field, cathode B=0.01T and the simulated beam current for B=0.11T.

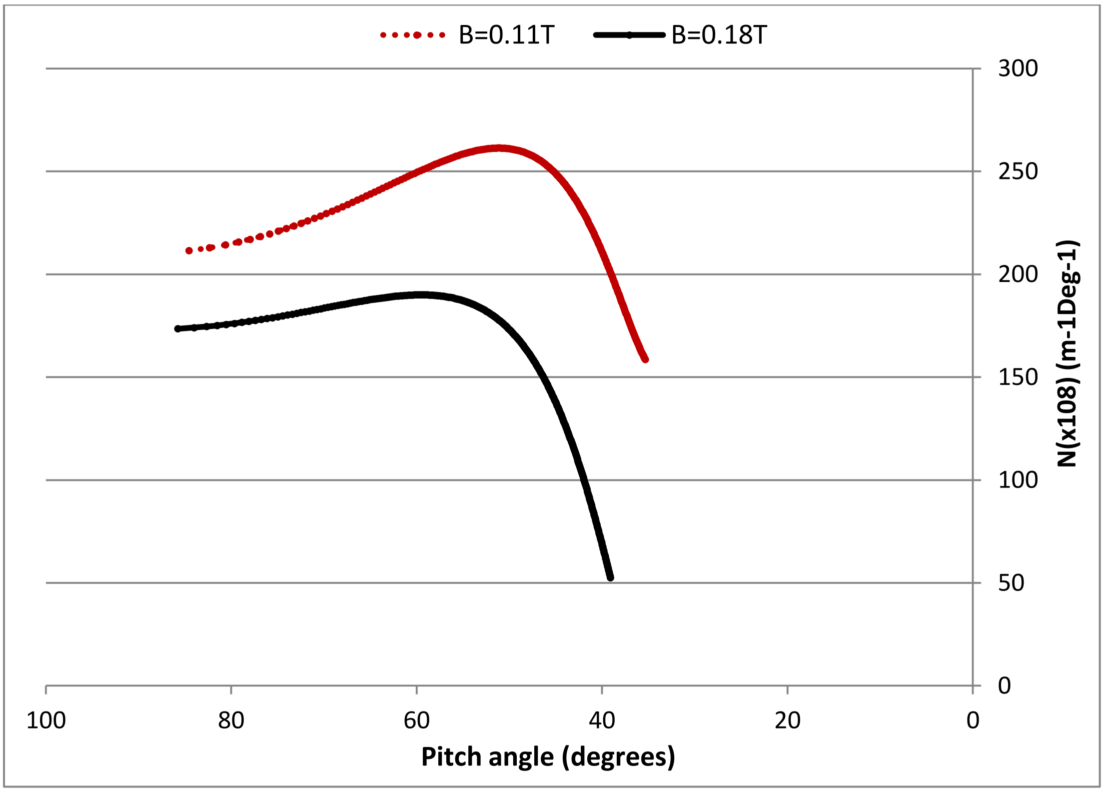

Figure 5.28**:** 1D electron beam distribution as a function of beam pitch angle in the simulation for B=0.11T and B=0.18T plateau magnetic fields.

It can be seen in Figure 5.29 the best fit line to the simulation data yields a good agreement between the experimental and the simulation estimates for the electron distribution in pitch angle, except at very low (~40^{o}) pitch angles which are underestimated by the simulations. But these are less important in driving the cyclotron instability.

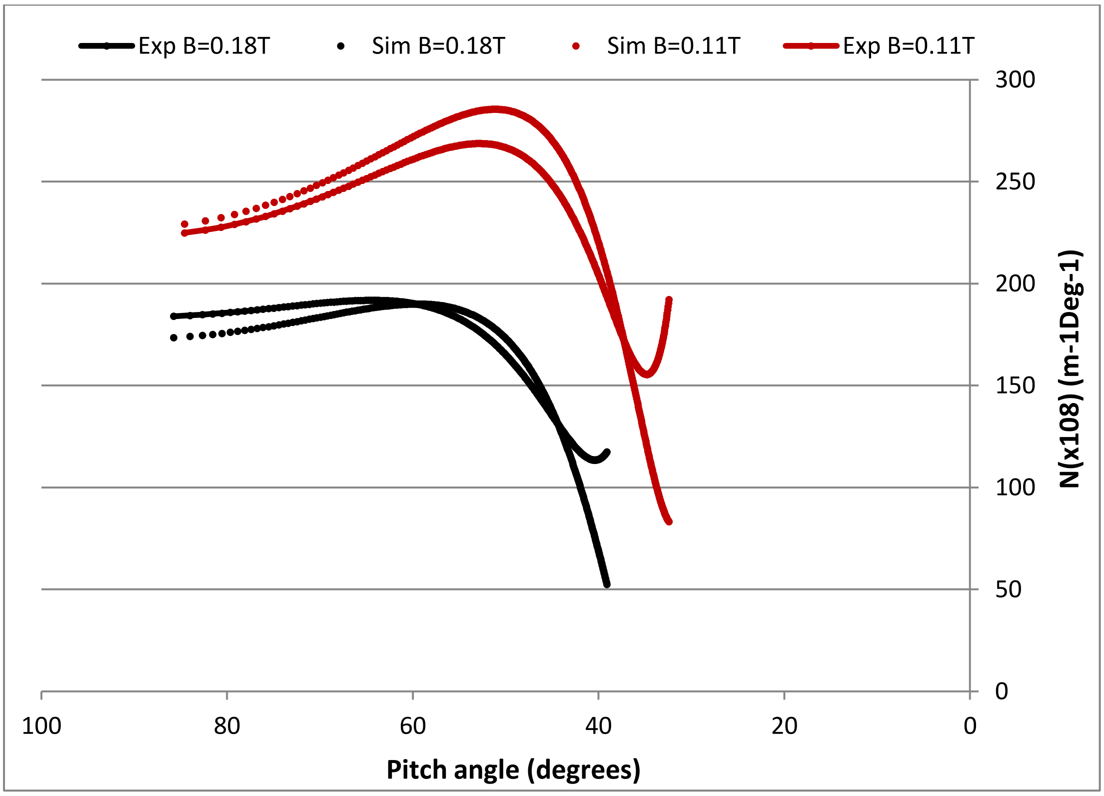

Figure 5.29**:** Comparison of simulation and experimental distribution of electrons in pitch angle.

5.5 3D simulation of electromagnetic emissions from realistic electron horseshoe distributions

3D simulations were undertaken to investigate microwave emissions as a function of detuning over a range from -3% to 14% using a numerical electron beam consistent with the experimental measurements obtained for a cathode magnetic field of B=0.02T and a resonant magnetic field of nominally B=0.18T, i.e. a mirror ratio of 9. The detuning is an important parameter in defining the behaviour of a cyclotron instability, defined in percentage as;

$$df/f = \left(\frac{f_{ce} - f_{co}}{f_{ce}} \right) \text{ x } 100 \qquad \text{Equation 5.03}$$

where; f_{ce} *is the cyclotron frequency and* f_{co} *is the cut-off frequency*

The highest radiation power of 70kW was predicted in the simulations for a detuning of 2%, Figure 5.30. The RF power decreased rapidly to 30kW, at a detuning of 6% and remained steady until 8%. It was seen that above ~8% detuning other transverse modes were being excited, in addition to the intended $TE_{0,1}$. From ~12% detuning and above the $TE_{3,1}$ (this is indicated by the dotted line) mode is clearly excited. The excitation of this mode allows for an increase in the output power after the decrease in the value of radiated power above 2% detuning. This arises since the cut-off of the $TE_{3,1}$ mode is above the $TE_{0,1}$ cut-off, so this mode can be excited effectively (since it is closer to perpendicular resonance).

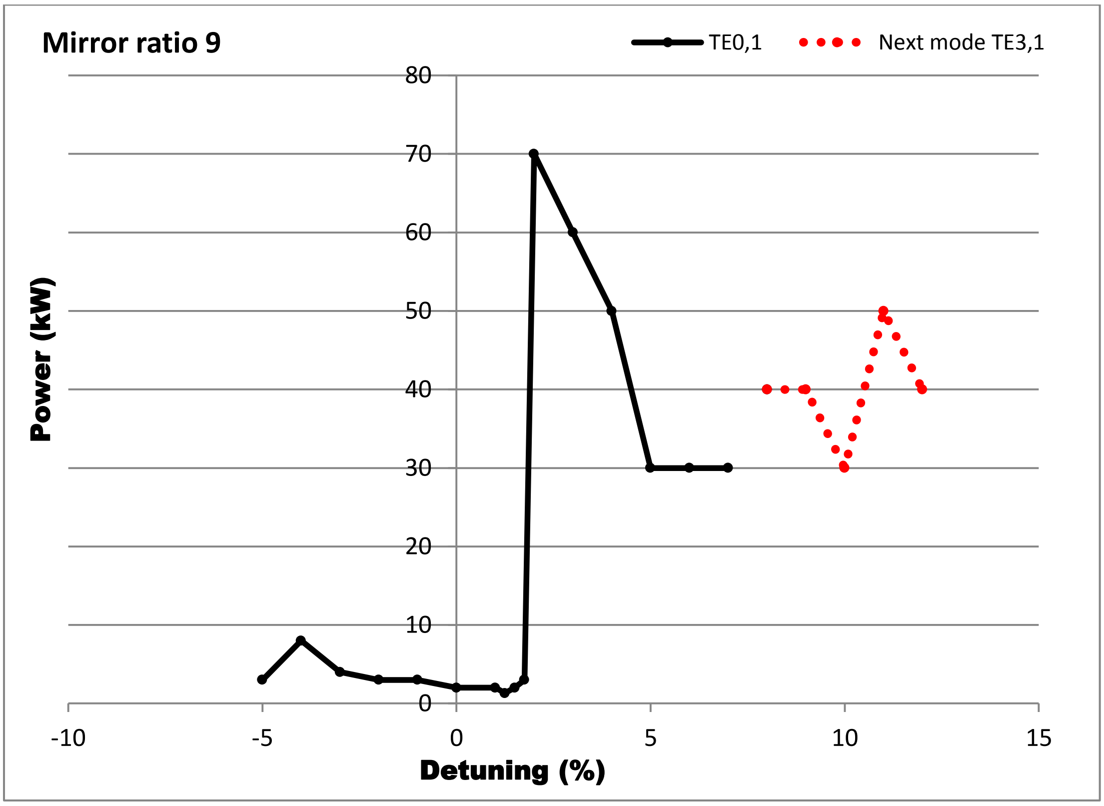

Figure 5.30**:** Simulated RF wave generation calculations consistent with the electron beam formed in the experiment at a mirror ratio of 9. 0% detuning corresponds to B=0.1769T.

The predicted variation of the output power with magnetic field is similar for the beam formed in the experiment at a mirror ratio of 17, corresponding to a cathode B=0.0105T and resonant magnetic field nominally B=0.18T. However the peak power predicted was lower at 45kW which turned on rapidly at a detuning value of 2%, and decreases much more quickly to a value of only 6kW, Figure 5.31.

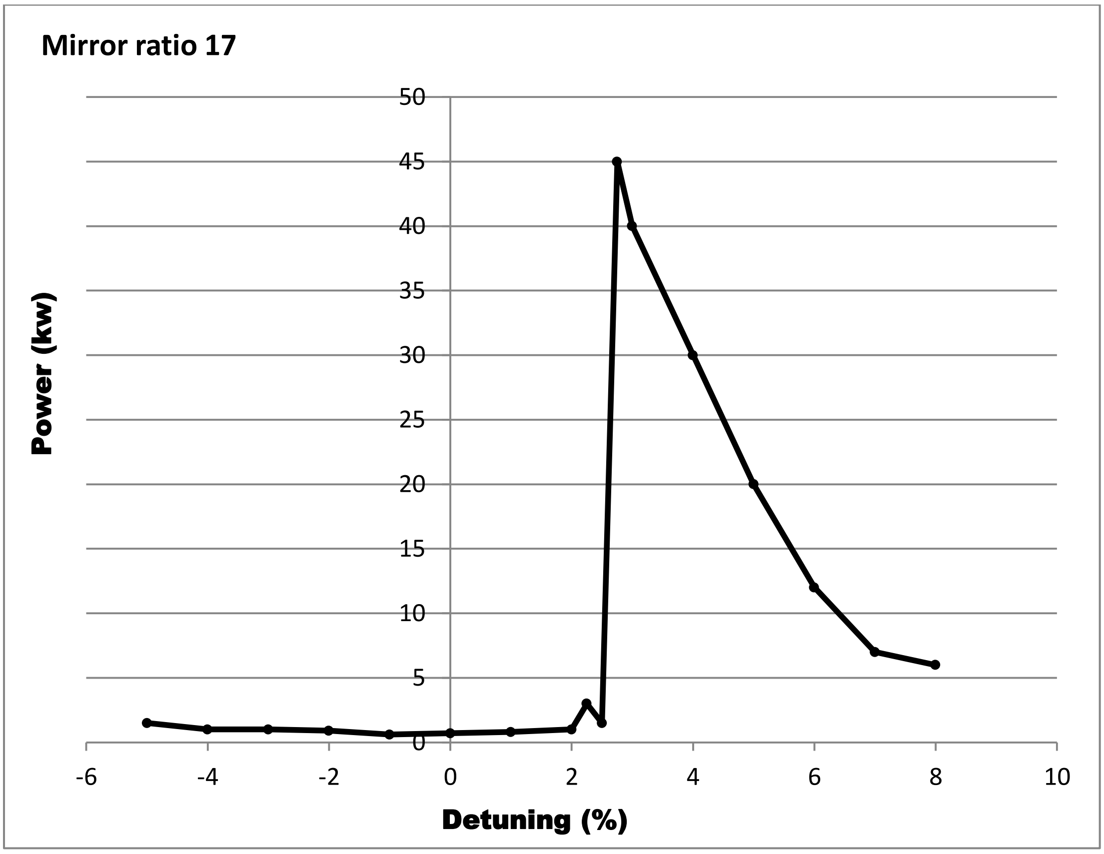

Figure 5.31**:** Simulated RF wave generation calculations consistent with the electron beam formed in the experiments at a mirror ratio of 17. 0% detuning corresponds to B=0.1769T.

Figure 5.32 illustrates the mode content predicted by the simulations corresponding to the experimental conditions at a mirror ratio of 9, (a) illustrates the resonant mode $TE_{0,1}$ at a detuning of 4.5% and (b) illustrating the $TE_{3,1}$ mode being excited at higher detuning of 10%, with slight distortions associated with mode competition from the $TE_{0,1}$. The Figure also shows the results of a spatial Fourier analysis of the spatial structure confirming the visual impression given by the field patterns. In the experiment when using a 35A beam formed with a compression factor of 9, an output power of ~35kW was estimated in $TE_{0,1}$ mode. Using the 12A beam formed at a compression ratio of 17 the experimental measurement indicated ~17kW. These are in reasonable agreement with the simulations presented here.

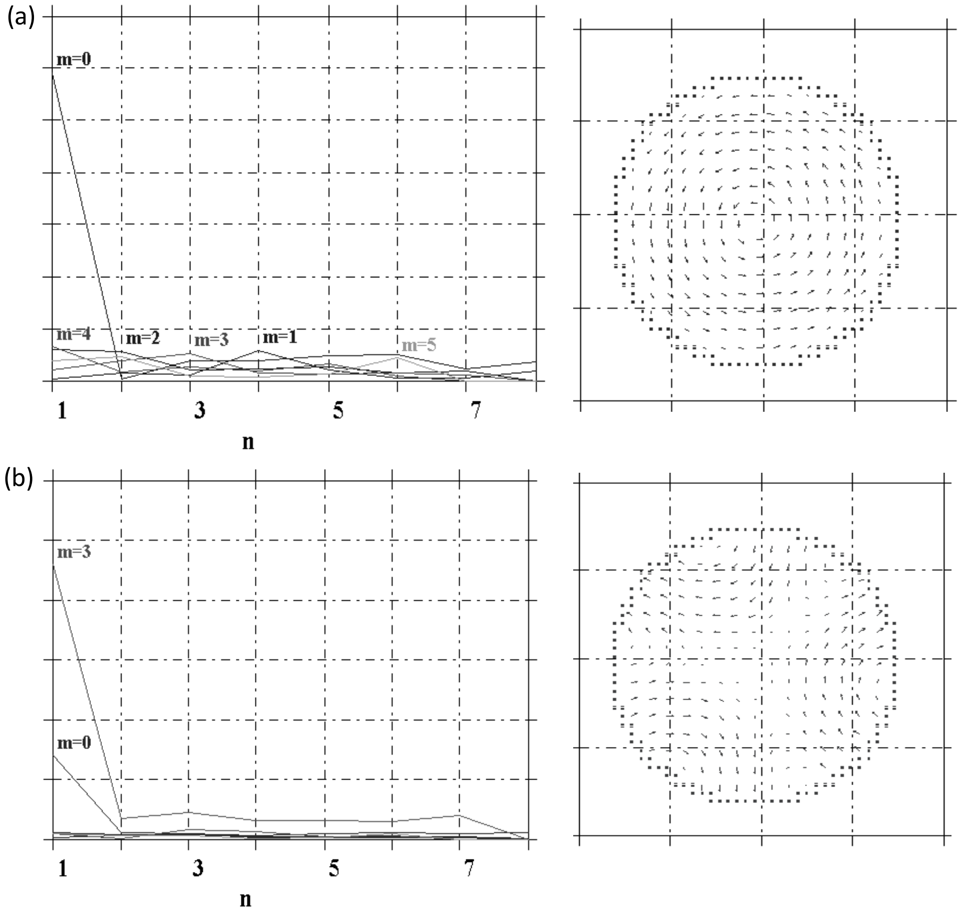

Figure 5.32: Mode content predicted by the simulations (a) $TE_{0,1}$ mode and corresponding electric field pattern predicted at a detuning of 4.5% (b) mode competition between the $TE_{0,1}$ and a strong $TE_{3,1}$ mode and corresponding electric field pattern predicted at a detuning of 10%. The electron beam was consistent with that used in the experiment at a cathode B=0.02T.

5.6 Simulation of mode competition in high frequency experiments

As previously seen in the electric field patterns predicted by the preliminary 3D 11.7GHz simulations (see theory section 5.1) at least two modes were excited, predominantly the $TE_{0,3}$ and the $TE_{2,3}$. These modes were also observed experimentally, which is an indication that there may be strong mode competition. This high magnetic field, high frequency, 11.7GHz regime was originally chosen as it is a rather overmoded regime (with λ considerably less than the transverse scale size of the interaction resonator). This more closely resembles the auroral region in that transverse field structure is less severely controlled by the boundary conditions.

Simulations were conducted to analyse this experimentally observed mode competition in more detail and to verify the modes thought to be excited. The parameters of these simulations are shown in Table 5.7 below. The detuning is measured as a fractional shift of the cyclotron frequency from the cut-off of the $TE_{0,3}$ mode.

Parameters	***Value or range***
B_o (T)	0.466 - 0.494
Energy (keV)	85
Pitch	0^o - 90^o
Current (A)	13 - 37

Table 5.7: Parameters for mode competition analysis simulations.

Figure 5.33 illustrates an example of the Fourier transform of the temporal evolution of the electric field in these simulations. A frequency of ~11.7GHz was excited as expected. The axial variation of the beam current in these simulations is shown in Figure 5.34, illustrating an injected beam current of 13A. After z=50cm the beam current decreases due to the fringing of the magnetic field, resulting in particles striking the walls.

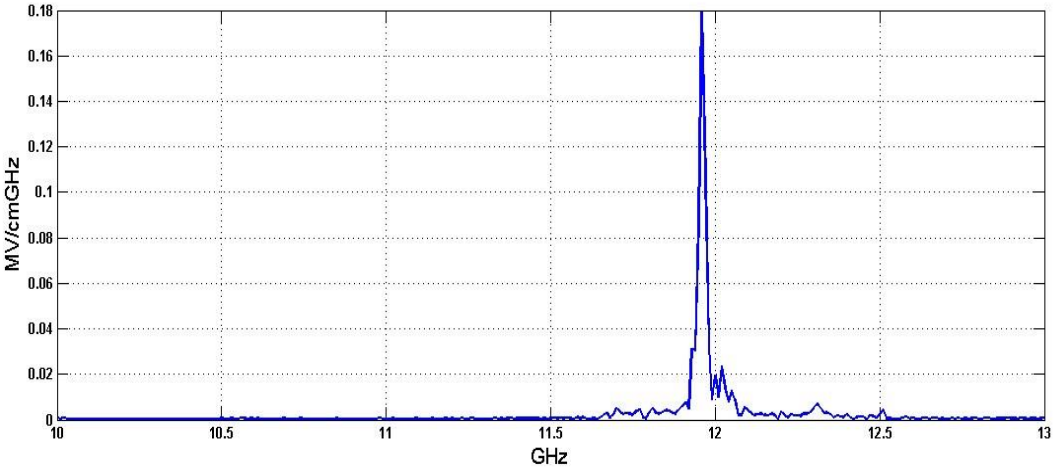

Figure 5.33**:** Fourier transform of the electric field illustrating the peak frequency of emission at 11.7GHz. There is also a small peak at around 12GHz indicating the possibility of mode competition.

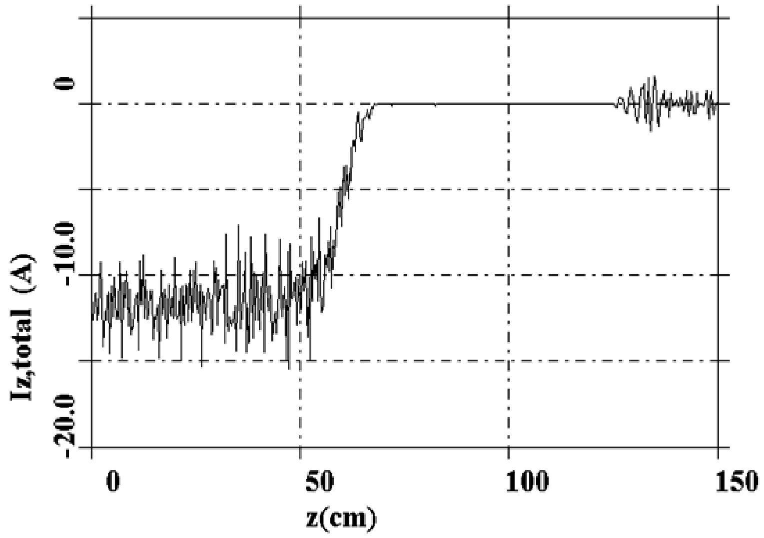

Figure 5.34**:** An example of the axial variation of the beam current, corresponding to an injected current of 13A, predicted by 3D KARAT simulations conducted for the mode competition analysis.

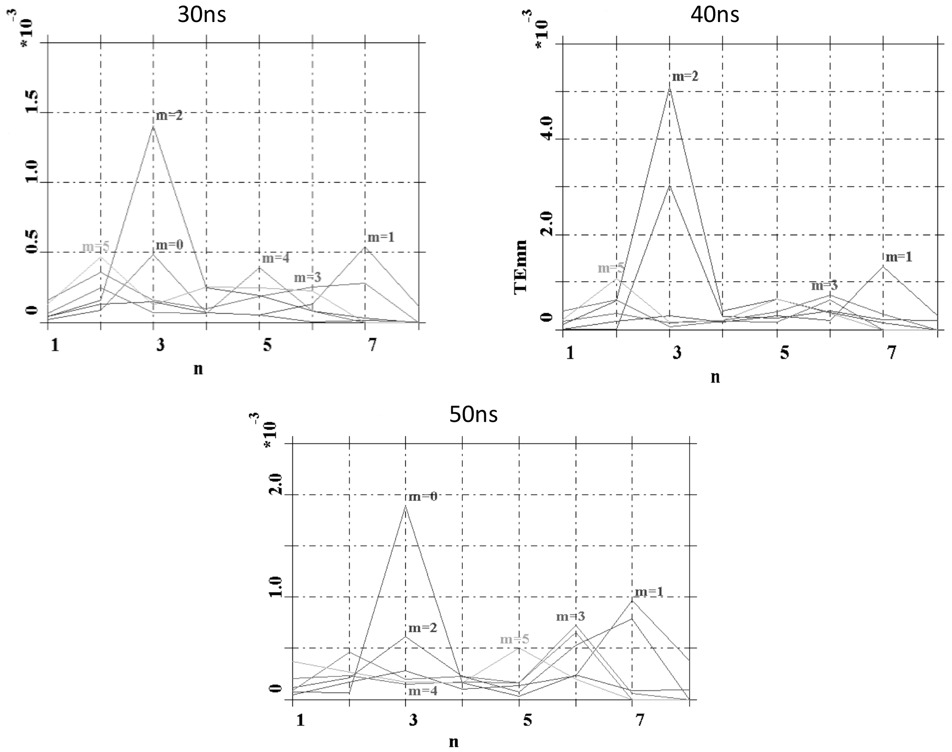

Figure 5.35**:** 3D KARAT output illustrating the modes excited by a 37A electron beam at a magnetic field of B=0.48T. It can be seen that at 30ns the predominant mode is the $TE_{2,3}$ with a weakly excited $TE_{0,3}$ mode , however with the elapsing of time at 50ns, the predominant mode is the $TE_{0,3}$ and the $TE_{2,3}$ is now the smaller mode. This illustrates mode competition, associated with different growth rates and saturation limits of the wave emission in these two modes. At 40ns it is clear to see that there is competition between the modes.

For illustrative purposes, Figure 5.35 shows the modes excited in some of the simulations. It can be seen that initially the predominant mode is the $TE_{2,3}$ whilst there is only weak excitation of the $TE_{0,3}$ mode. However after a further 20ns elapses, at 50ns, in the simulation the predominant mode is the $TE_{0,3}$ and the $TE_{2,3}$ is now the weaker mode. This “swap over” of modes illustrates competition.

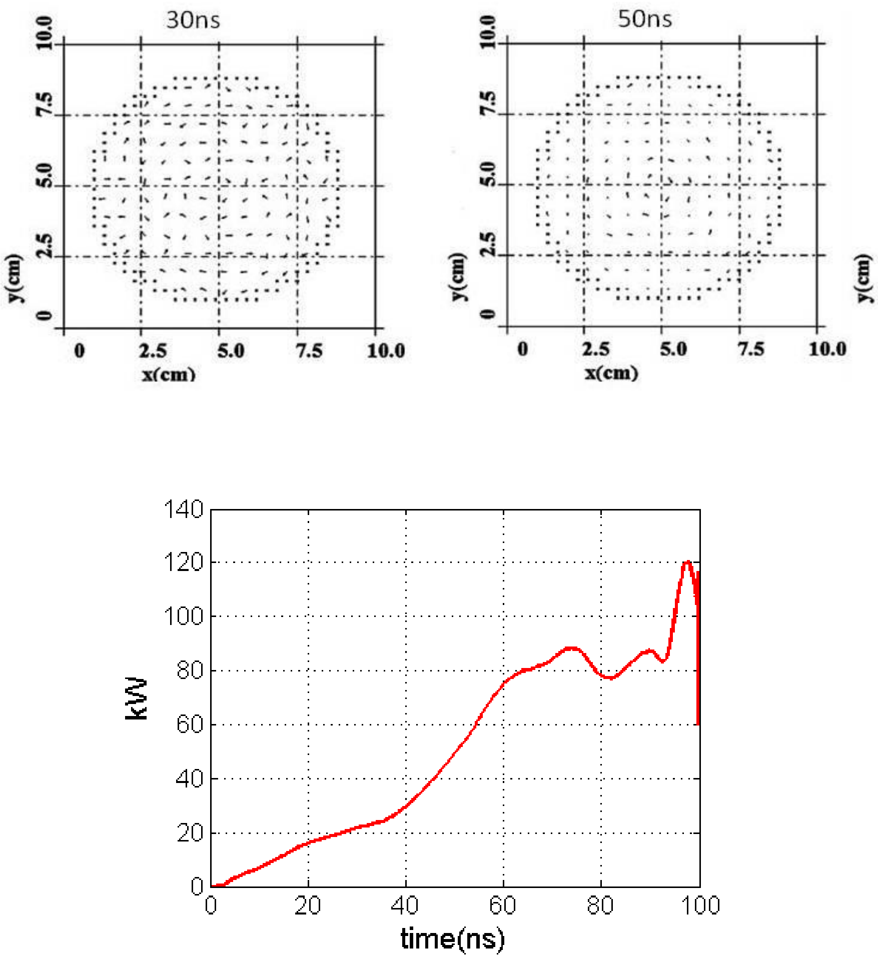

(a)

(b)

Figure 5.36**:** (a) 3D KARAT electric field vector plots predicted by the simulations, corresponding to an injected current of 37A and a magnetic field of B=0.48T, the pattern of the $TE_{2,3}$ mode is becoming disordered at 30ns showing the start of the competition between $TE_{2,3}$ and $TE_{0,3}$ modes and at 50ns it is illustrating the dominant excitation of the $TE_{0,3}$ mode. (b) Plot illustrating the power variation as the excited mode transitions from the $TE_{2,3}$ to $TE_{0,3}$ mode.

This mode ‘competition’ is clearly seen at 40ns, where both modes are being simultaneously excited at similar strength. Figure 5.36**a** illustrates the electric field vector plots from the simulation which also illustrate mode competition. Referring to Figure 5.36**b** the power rises slowly until 40ns then rapidly to 60ns then stabilises until ~100ns. The variation in power suggests that the instability started at relatively low power in the $TE_{2,3}$ mode then switched to a strong excitation of the $TE_{0,3}$ mode. The simulations investigated which modes were excited for a range of detunings using electron beam currents consistent with experimental conditions. Table 5.8 and Figure 5.37 illustrate the results from these simulations.

Current (A)	***Detuning range (%)***	***Mode initially excited***
13	-3 to 1	$TE_{2,3}$
	2 to 3	$TE_{0,3}$
16	-3 to 0	$TE_{2,3}$
	1 to 3	$TE_{0,3}$
37	-3 to -1	$TE_{2,3}$
	0 to 3	$TE_{0,3}$

Table 5.8: Results for mode competition simulations, illustrating how the excited modes varied with detuning and beam current.

Referring to Figure 5.37, it can be seen that there is a clear trend from the results output power generally increased with beam current (and hence beam power). Efficiency is relatively insensitive to current varying from a maximum ~5% to 1% as the magnetic field increased from B=0.465T to B=0.495T. When the magnetic field is below B=0.48T (which corresponds to exact resonance with the $TE_{2,3}$ mode) the predicted recurring dominant mode is the $TE_{2,3}$. When the detuning is increased above this limit the recurring mode excited is the $TE_{0,3}$.

Analysis of the transverse field distribution in the output aperture revealed that at significant negative detuning (-3%,-2%) the $TE_{2,3}$ mode was fairly stable. As the detuning approached zero (-1%, 0%) there was a tendency for the simulation to change oscillation mode (as illustrated in Figures 5.35 and Figure 5.36). Whilst at high positive detuning (1% or greater) the $TE_{0,3}$ mode was the most prominent throughout, however there was substantial mode competition with several modes weakly excited. It was also apparent that the higher the beam current the greater the tendency for multiple modes to be excited. There were also signs of the $TE_{5,2}$ mode (which is the next lowest mode) being excited.

Previous experimental results show multi-mode excitation with strong evidence of the $TE_{0,3}$, $TE_{2,3}$ and $TE_{5,2}$ modes in the measured antenna patterns. The mode content was seen to be a complex function of time and magnetic configuration. This is consistent with these simulations. It would therefore appear that as the magnetic field increased the mode content of the RF output shifts from predominantly $TE_{2,3}$ mode to becoming more multi-mode with strong evidence of both the $TE_{0,3}$ and $TE_{5,2}$ modes.

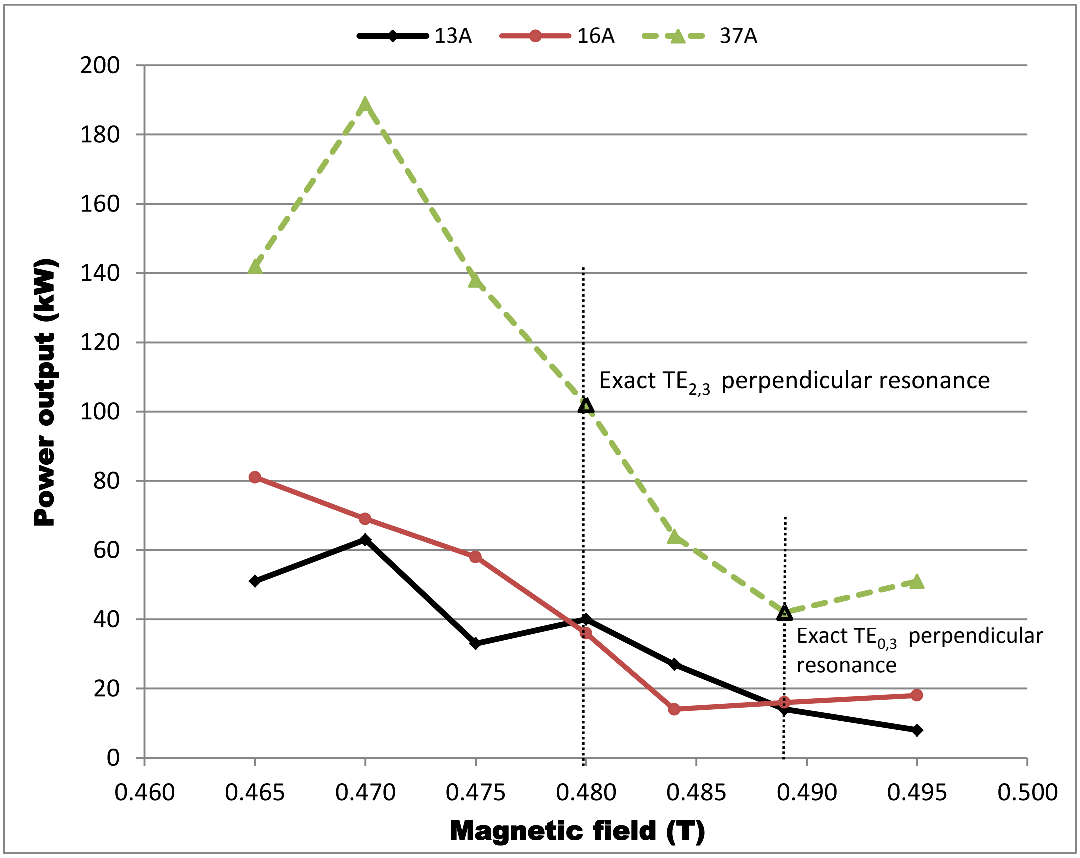

Figure 5.37**:** Results for mode competition simulations, illustrating how power varies with beam current and detuning, around a central frequency of 11.7GHz.

5.7 Investigation of backward wave instability

Whilst conducting some preliminary simulations it was regularly noted that the backward travelling wave had a higher amplitude and better defined mode pattern than the forward going wave.

Therefore a set of simulations, key parameters given in Table 5.9, with a reduced waveguide diameter were conducted to analyse the relative strength of the forwards and backwards propagating waves and hence test the apparent resilience of the backward wave interaction in a geometry where relatively few transverse modes can be excited over a large spectral range. They are not intended to be directly comparable to the experiment. The parameters for these simulations are shown in Table 5.9. Figure 5.38 & Figure 5.39, illustrate the Fourier transform of the AC waveforms from the simulations for two magnetic field values B=0.46T and B=0.5T respectively. Figure 5.40 shows the variation in wave power and frequency illustrating the backwards resonance is predicted to show a remarkable resilience to the Doppler shift, confirming indications from earlier simulations. The backwards going wave maintains a power >20kW even as the cyclotron frequency reached 11.7GHz, where perpendicular propagation corresponds to a frequency of 8.8GHz. In contrast the forward wave power falls below 10kW just above 9.5GHz. The AC waveform (and hence the spectra) of the forward wave is much ‘noisier’ than the backward wave.

As the magnetic field increases, i.e. the detuning from perpendicular resonance, in this analysis at B=0.36T, is increased, the spectrum loses coherence (particularly the forward wave, see Figure 5.38 and Figure 5.39) illustrating that detuning has an important effect on the strength of the interaction since it controls the Doppler spread of the resonance (much wider for forward wave interaction). Also notice that the amplitude of the Fourier transform is much larger for the backward wave consistent with the estimates of power flux. This would suggest that there is a preference for backwards wave emission. It can also be seen that the backwards and forwards radiation frequency for both resonances is almost equal. Implying that the high pitch angle electrons are the primary driver of the emission in both forwards and backwards direction. This refers back to section 5.2 and more specifically Figure

5.17 and Figure 5.18 which show that the efficiency of the emissions from the high pitch angle electrons is stronger. It was important to further investigate this evidence of backward resonance as this could have significant implications in the auroral density cavity in the magnetosphere where there is a cold tenous plasma in the resonant region. Backward wave emissions into an off-perpendicular radio wave may be important for AKR emissions as they may allow emission into the X-mode below cyclotron resonance and hence avoid possible absorption in the upper hybrid stop-band (which is only slightly above ω_{ce}). It is also thought that a backward wave interaction could explain the discrete character of the AKR frequency spectrum, the synchronous temporal change of frequencies of excited modes, as well as high-power regimes with complex frequency spectra [Savilov et al. 2007]. Moreover, radio waves emitted with a slight backward angle (from a descending electron flux) may experience upwards refraction in the complex plasma environment of the polar magnetosphere.

Geometrical Parameters	***Value or Range***
Axial length	1.5m
Radial width of interaction waveguide	0.01m
Axial mesh spacing	0.2cm
Radial mesh spacing	0.2cm
Electron beam parameters	***Value or Range***
Electron beam current I_b	11.5A
Electron beam energy E	75kV
Injected electron beam pitch-factor spread	$\alpha = 0.36 \rightarrow 11.4$ (uniform distribution)
PiC particle merging factor	3×10^7 electrons/PiC particle
Number of PiC particles in system	~80,000 PiC particles
Constant magnetic field parameters	***Value or Range***
Axial magnetic field B_{z0}	0.357T- 0.5T
Length of constant axial field region	0.30m
Dielectric absorbent region post beam	***Value or Range***
Radial limits	$0 \rightarrow 0.01$m
Axial limits	0.125 - 0.150 m
Conductivity	Isotropic with linear gradation 0 – 0.1Siemens/m
Dielectric permittivity ε_r	3.2
Dielectric permeability μ_r	1

Table 5.9: Parameters for initial simulations conducted for backward wave investigations at 8.7GHz – 12.18GHz.

Work by Mutel et al, using data from the Cluster mission, showed that the radiation from the auroral region undergoes strong refraction which is caused by the density inhomogeneity in the magnetospheric plasma with altitude. Mutel et al. have shown that the ray paths due to refraction are propagating at angles with respect to the magnetic field of between 10^o and 20^o well before they encounter the second harmonic layer, with much reduced attenuation at these angles [Mutel et al 2008][Menietti et al 2011]. Both these simulations and simulations conducted by Speirs [Speirs et al. 2010] and observation [Menietti et al 2011] suggest that the radiation is generated at a backward angle of a few degrees to the beam direction and not strictly perpendicular. This can then give rise to upward refraction due to the decreasing background plasma density with increasing altitude (see appendix 1 for more detail).

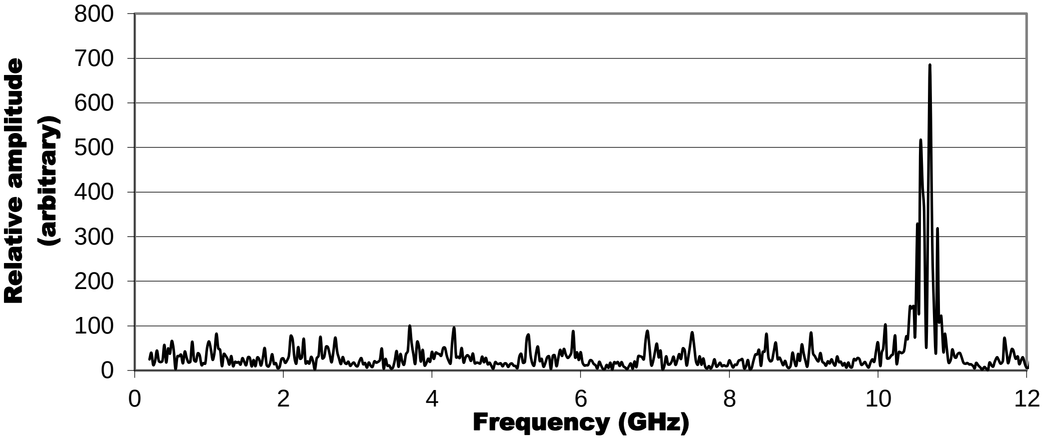

(a)

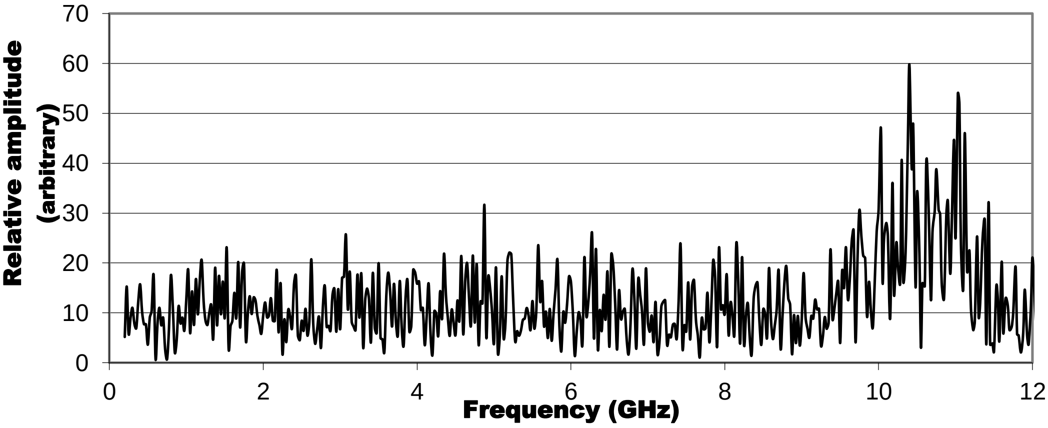

(b)

Figure 5.38**:** Fourier transform of electric field for B=0.46T (a) simulation spectrum for the backward wave (b) simulated spectrum for the forward wave. More energy is coupled into the backwards wave than the forward, indicating a backwards wave resonance. This is consistent with the form of the dispersion curves where the width of the forward wave resonance increases rapidly with detuning above cut-off whilst the backward wave resonance is less severely affected.

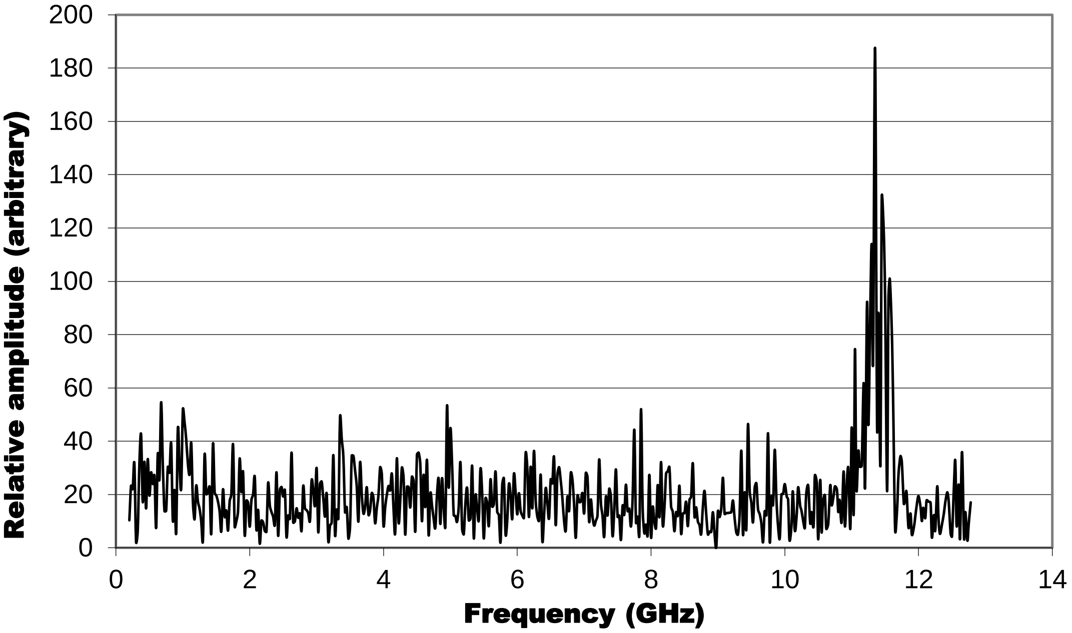

(a)

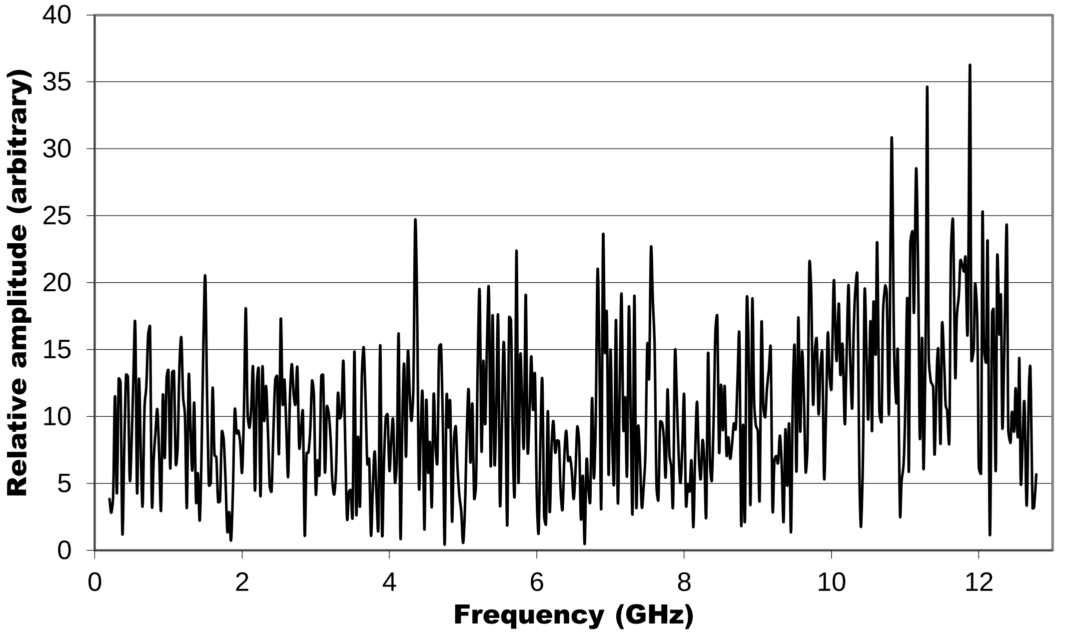

(b)

Figure 5.39**:** Fourier transform of electric field for B=0.5T (a) simulated spectrum for the backward wave and (b) simulated spectrum for the forward wave. More energy is coupled into the backwards wave than the forward, indicating a backwards wave resonance. Note that both are less well defined than Figure 5.38.

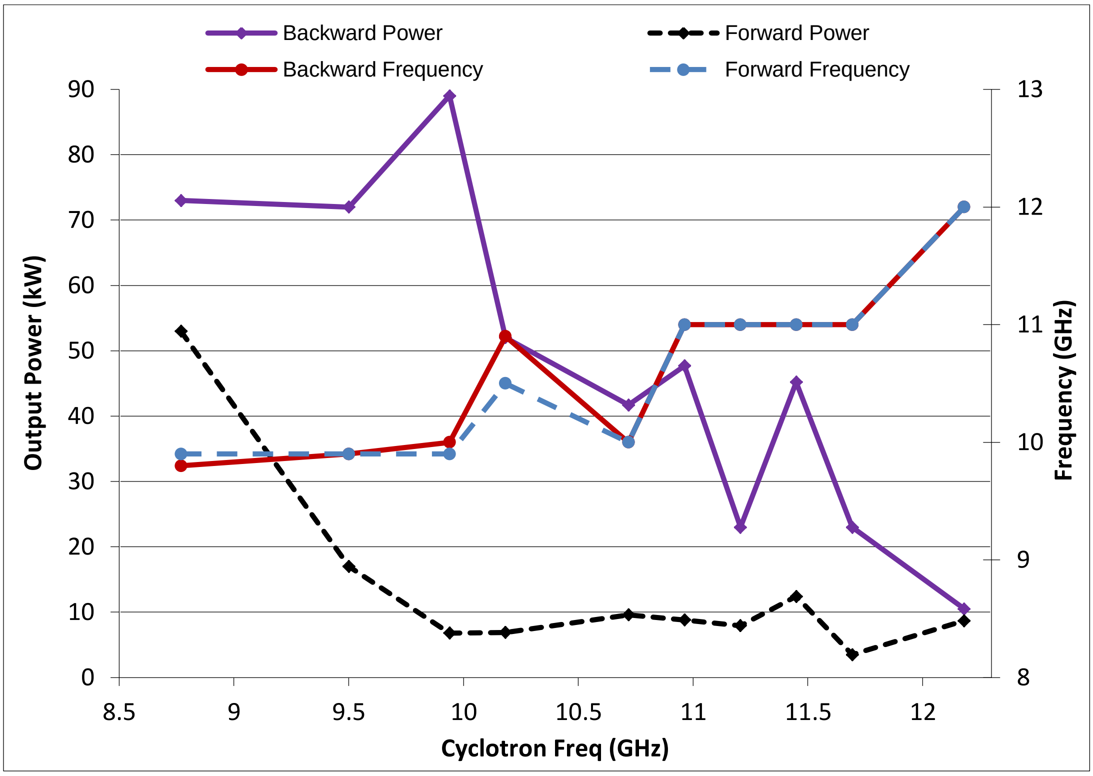

Figure 5.40**:** Backwards and forwards radiation frequencies are almost equal for both resonance conditions implying high pitch angle electrons are determining the interaction. The backwards resonance shows remarkable resilience to Doppler broadening.

5.7.1 Experimental and numerical comparative investigations of backward wave nature of the instability

Experiments were conducted to investigate the emissions from the electron beam as the resonant frequency is increased above cut-off. The experiment used a 4.14cm diameter waveguide in nominally the $TE_{0,1}$ mode which has a cut off frequency of 4.42GHz. Figure 5.41 illustrates the acceleration potential, diode current and illustrates the rectified microwave signal recorded in the experiments. Figure 5.42 illustrates the Fourier transform of the signal illustrating a wave frequency of 4.58GHz captured on a 12GHz real time digitising oscilloscope.

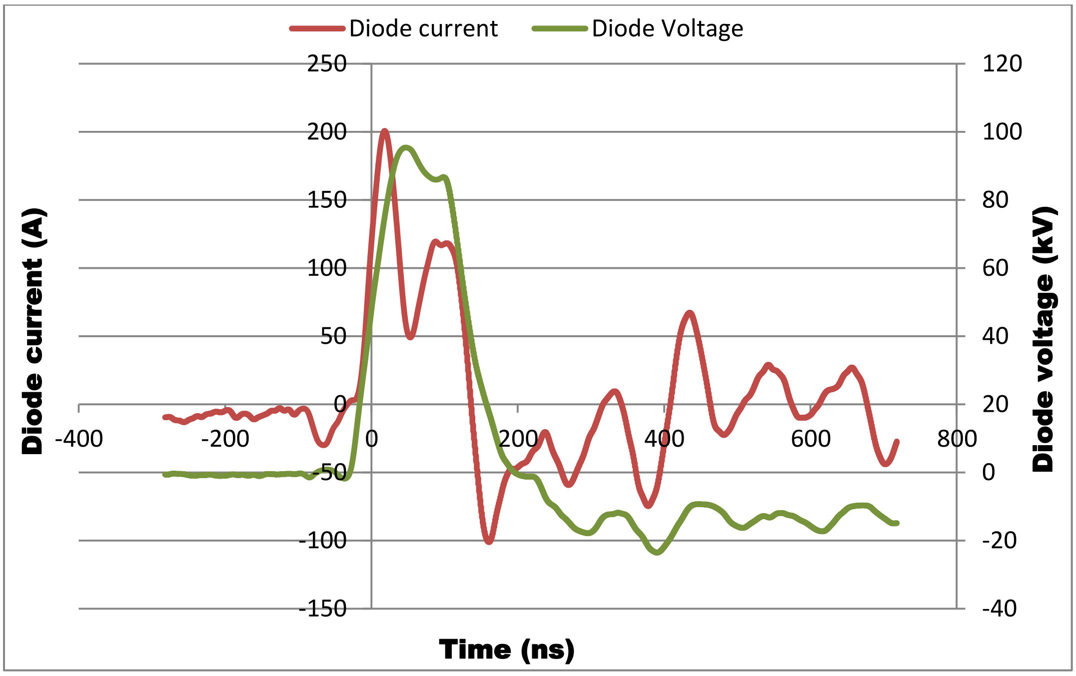

(a)

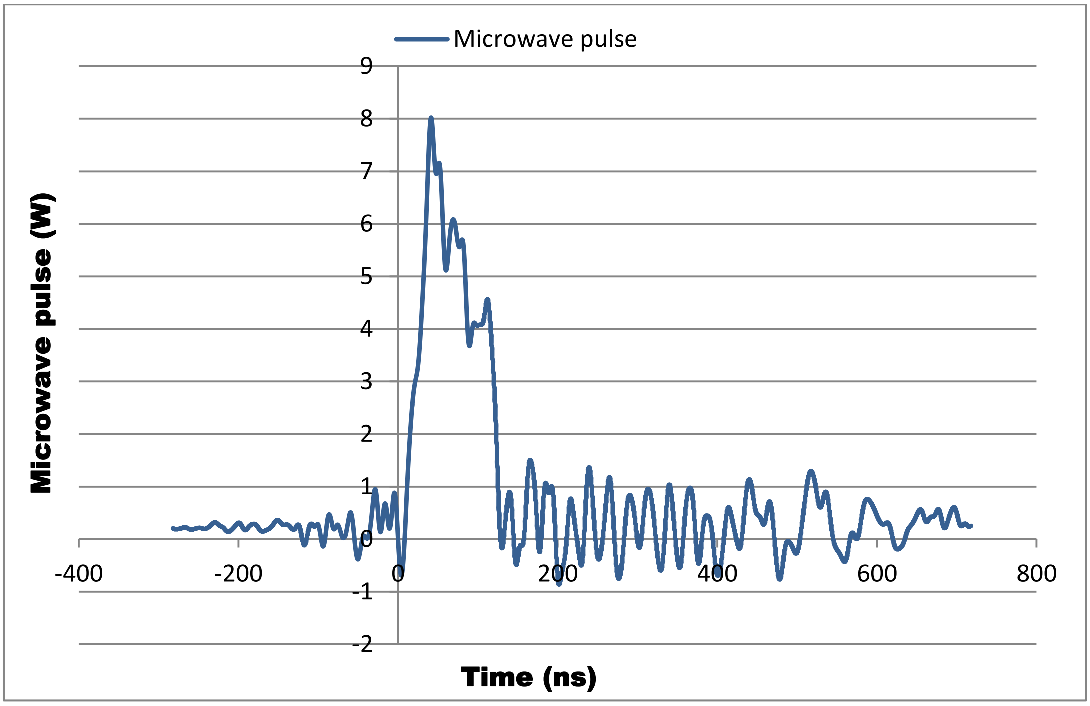

(b)

Figure 5.41**:** (a) Accelerating potential and diode current pulse (b) Rectified microwave output signal.

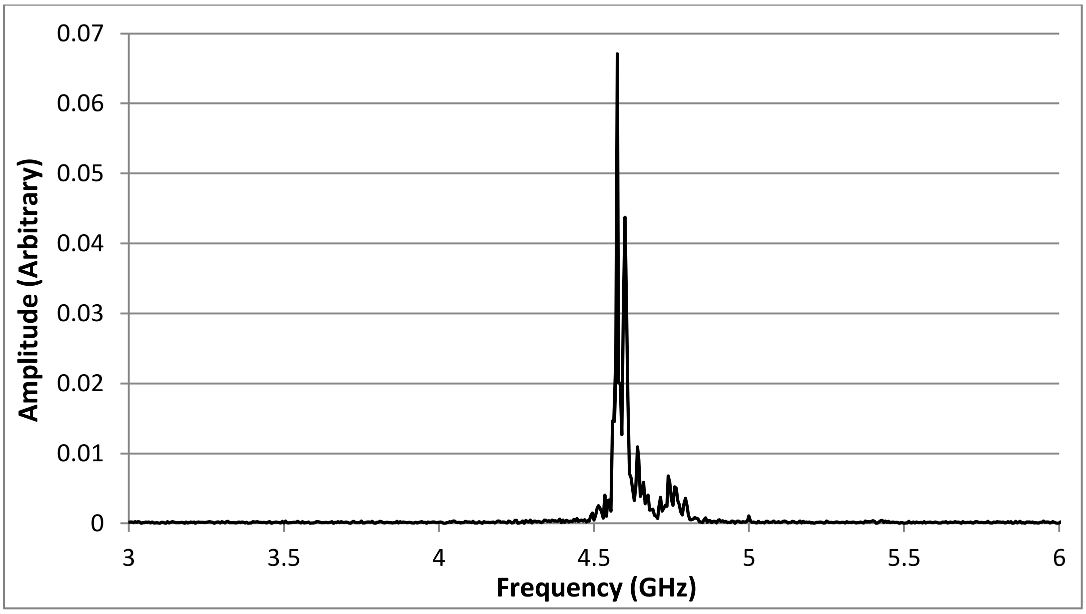

Figure 5.42**:** Fast Fourier transform of the AC wavepacket taken from the Oscilloscope. Illustrating a resonant frequency of 4.58GHz. This trace was taken from experiments conducted with a step reflector.

This variation of the wave amplitude and frequency was recorded as a function of the magnetic field. Three different resonator configurations were tested, one was open at both ends whilst the other two were terminated at the accelerator end, one with a plate having a 4cm diameter aperture and the other with a taper having an angle at 22.4^o & clear bore radius of 3cm. These reflectors would act to scatter the backwards wave into a forwards signal for measurement but did not affect beam transport. In the absence of a reflector any wave generated in the backwards direction would launch into the gun region and be relatively weakly observed at the output. The two reflectors would ensure the signals were observed at the output. The tapered reflector would be less likely to induce a mode conversion at the reflection point.

Figure 5.43 illustrates the results from this experiment. It can be seen that the output frequency increased more slowly than the cyclotron frequency, particularly when the resonator was completely open at both ends, or when closed by the planar reflector at the gun end. This indicates a backward wave resonance, consistent with its stronger tolerance to the high levels of velocity spread in this electron beam. Beam wave simulations were conducted with the same waveguide and beam parameters as the experiment with the tapered reflector showing strong agreement with the experimental measurements. The beam current and energy in this simulation are defined to match the experimental measurements, whilst the simulated electron distribution in velocity space exploits the measurements and analysis discussed in section 5.4 to conform to the experimental results. The simulation parameters are shown in Table 5.10 below.

Parameters	***Value or range***
Current (A)	17
B field (T)	0.182 – 0.21
Energy (keV)	75

Table 5.10: Simulation parameters for investigation of backward wave excitation.

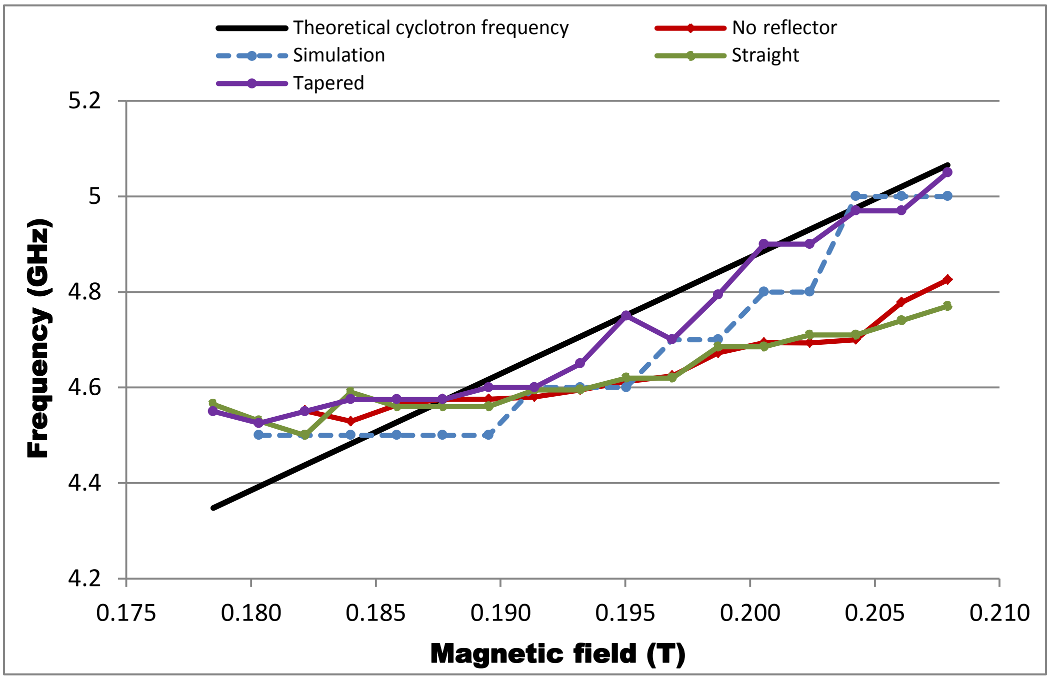

Figure 5.43**:** Experimental measurement of emission frequency as a function of the magnetic field. It can be seen that the wave frequency increases more slowly than the cyclotron frequency suggesting a backward wave instability.

The predicted variation in the output power was also plotted against the magnetic field as it increases through resonance, Figure 5.44. There was no wave generation until a magnetic field of B=0.184T was obtained. Whilst the signal declines above B=0.186T which is taken to correspond closest resonance with the first mode of the cavity. This gradual decline in power with increasing detuning combined with the slow increase in frequency is indicative of a backward wave resonance, as both the Doppler downshift and spread increase.

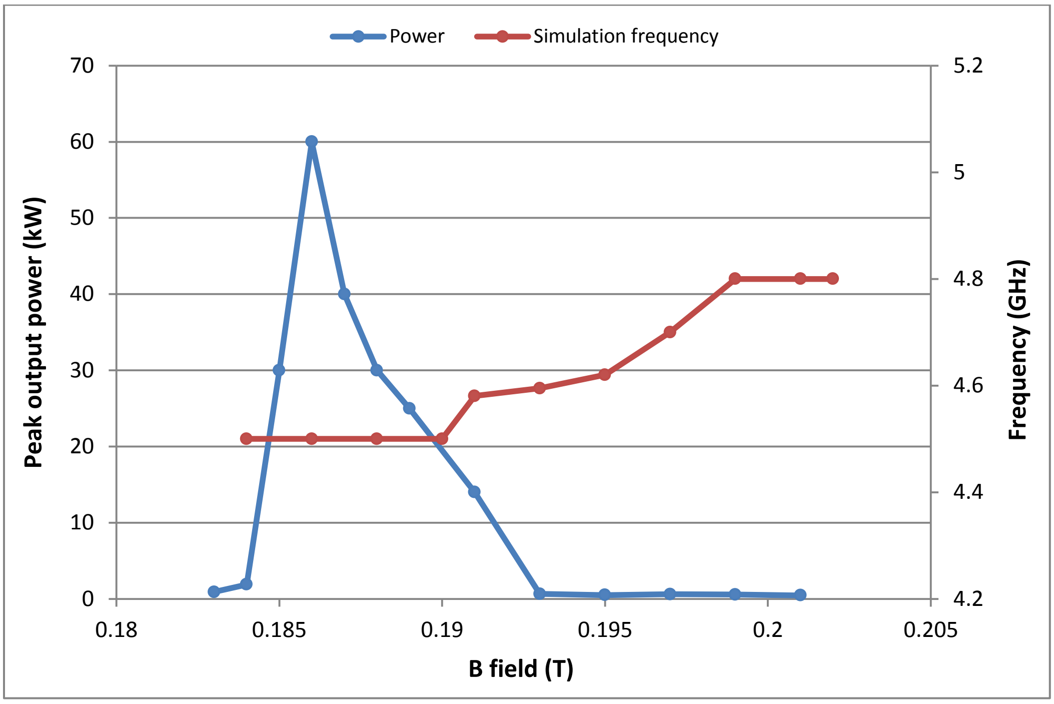

Figure 5.44**:** Variation in predicted radiation emission strength & frequency as the magnetic field is tuned through resonance. The frequency increases slowly with increasing magnetic field, illustrating a backward wave resonance.

5.7.2 Experimental measurements of wave polarisation, propagation and power

The experiment also allowed the variation in the strength of the wave emissions to be measured as a function of the detuning, and by using the set-up illustrated in section 4.5.4, measurements were taken of the microwave emissions from the experiment as a function of detector polarisation and position.

The measurements were taken in increments of 5^o. The power coupled into the receiving scanning waveguide was measured separately in two different orientations i.e. radial polarisation, where the antenna is polarised parallel to the scanning plane, and also azimuthal polarisation (where the antenna is polarised perpendicular to the scanning plane) for each of the three cavity configurations. For each waveguide orientation the strength of the emissions was measured as a function of position and then magnetic field. This latter measurement was performed at an angular position of 30 degrees, and the magnetic field was varied in steps of B=0.01T. The purpose of this experiment was to determine the variation in the output power and efficiency of the generated radiation.

The choice of the magnetic fields at which the antenna patterns were measured was determined by an analysis of the power coupled into the receiving waveguide as a function of the magnetic field as shown in Figure 5.45 at an angle of 30 degrees in azimuthal polarisation. One can clearly see a similar response for the tapered and planar reflectors, the antenna patterns were measured to look at the regions where the emission was weak (B=0.184T) and strong (B=0.192T) Integration of each of the individual mode plots, allows the RF power of the system to be obtained. The periodic variation of power with magnetic field, seen in Figure 5.45, is probably associated with excitation of different longitudinal modes of the cavity.

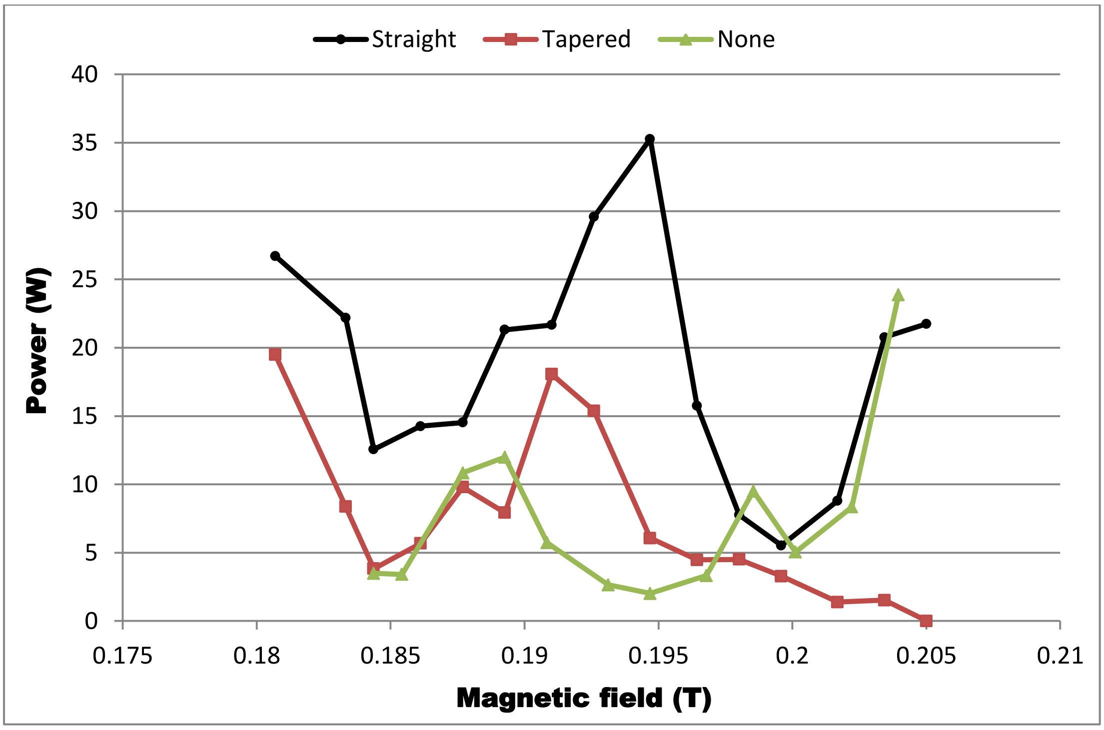

Figure 5.45: Experimental measurement of signal entering the receiver waveguide, for each type of reflector used, as a function of magnetic field at an angle of 30° in azimuthal polarisation.

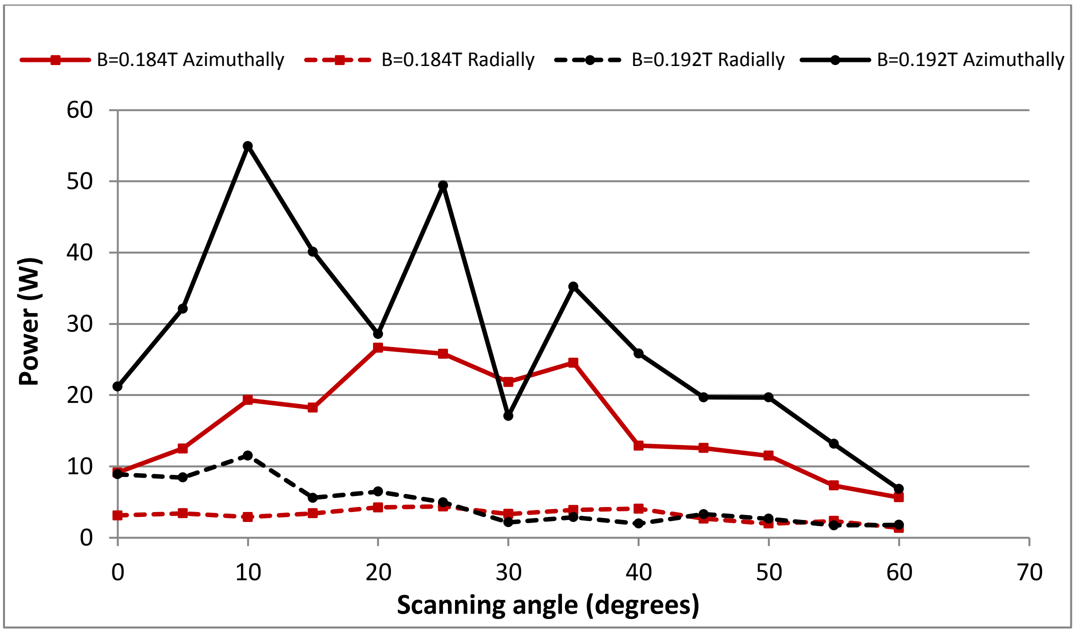

Figure 5.46: Variation of power incident on $5.6 \times 10^{-4} m^2$ aperture of the receiving waveguide (both radially and azimuthally polarised) with angular position, at B=0.184T & B=0.192T, consistent with the $TE_{0,1}$ mode (at B=0.184T). This data is for a *straight reflector*.

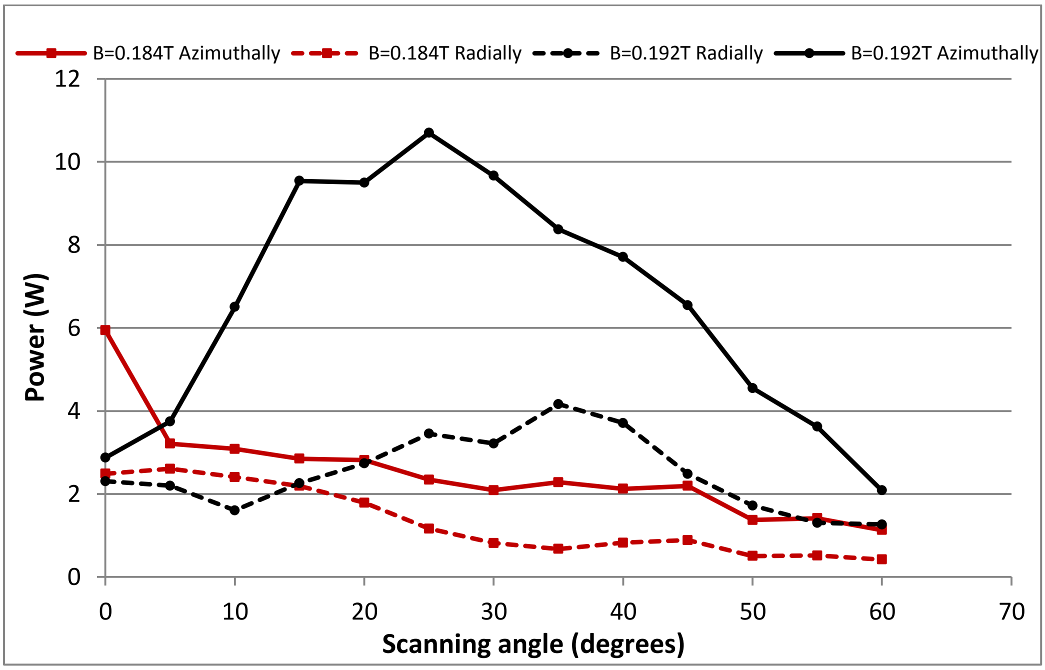

Figure 5.47: Intensity variation (both radially and azimuthally polarised) with angular position for azimuthal and radial polarisation, at a cyclotron frequency corresponding to B=0.184T and B=0.192T, clear radiation pattern maximum ~25^{o} at B=0.192T, indicating a $TE_{0,1}$ mode. This data is for a *tapered reflector*.

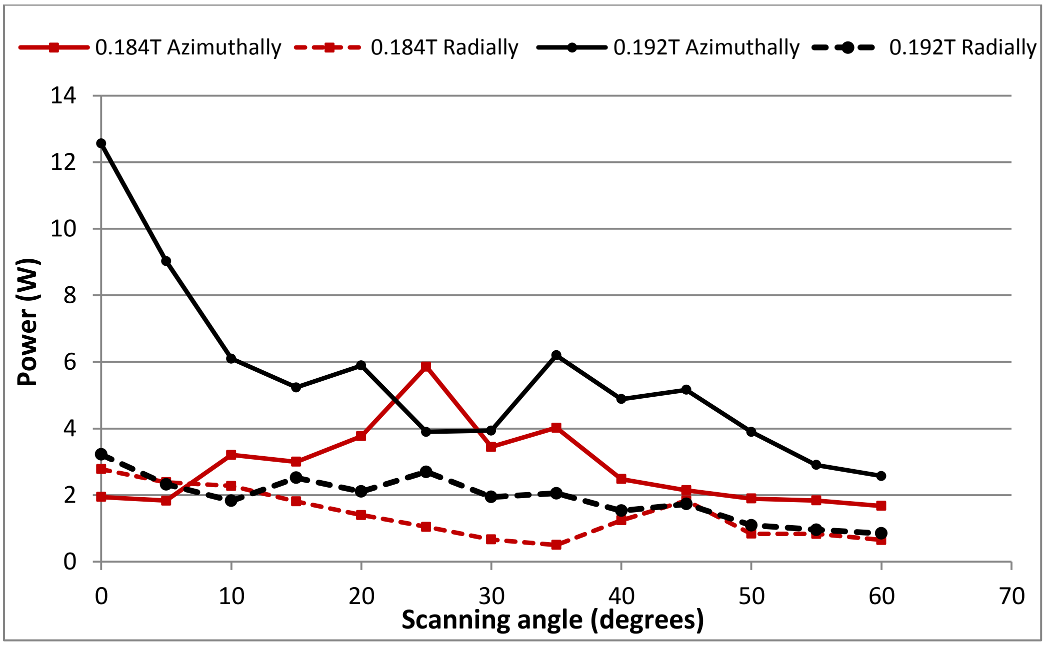

Figure 5.48**:** Variation of power incident on $5.6x10^{-4}m^2$ aperture of the recieving waveguide (both radially and azimuthally polarised) with angular position. At a cyclotron frequency of B=0.192T, power is primarily radiated down the centre implying a $TE_{1,1}$ like mode. This data is for *no reflector*. With B=0.184T the pattern is similar to a $TE_{0,1}$.

Figure 5.46-5.48 show the measurements of the output antenna patterns from the experiment at two different magnetic fields (B=0.184T and B=0.192T) in two different polarisations of the receiving antenna and for three different cavity configurations, plate reflector, tapered reflector and open resonator respectively.

In Figure 5.46 the azimuthal fields show lobe peaks at ~25^o for both magnetic fields (with some contamination at the higher magnetic field) indicative of a $TE_{0,1}$ mode (see Figure 5.49a). The $TE_{0,1}$ mode is, for these magnetic fields, closely associated with the near perpendicular X-mode. Figure 5.47 illustrates a clear $TE_{0,1}$ mode at the higher magnetic field of B=0.192T but a relatively weak homogenous radiation pattern is observed at B=0.184T when the accelerator end of the cavity is terminated by a tapered reflector.

Figure 5.48 shows the antenna patterns measured when no reflector was present in the cavity. At B=0.192T the signal was dominated by a strong and well resolved central lobe in azimuthal polarisation (similar to a $TE_{1,1}$ mode see Figure 5.49(b)) and at B=0.184T the pattern is peaked at ~25^o, consistent with a $TE_{0,1}$ signal. Figure

5.49a illustrates the power distribution for a $TE_{0,1}$ mode whilst Figure 5.49b shows the predicted pattern of a $TE_{1,1}$ mode radiated from the 8.28cm diameter aperture at a frequency of 4.5GHz. Note: $TE_{0,1}$ mode is peaked in azimuthal polarisation at 25^o-30^o whilst the $TE_{1,1}$ mode is centrally polarised and has a ~3dB point at 20^o.

To determine the power flux density estimates as a function of the scanned angle θ in both the radial and azimuthal polarisations, the rectifier calibration equations obtained from Figure 4.36 were used. Using this method it was possible to calculate the power that enters the receiver aperture in Watts. To reduce and quantify the random effects the values from these calculations are averaged over several pulses, these are then divided by the cross sectional area of the antenna, allowing for the attenuators in the feed waveguides, to estimate the intensity.

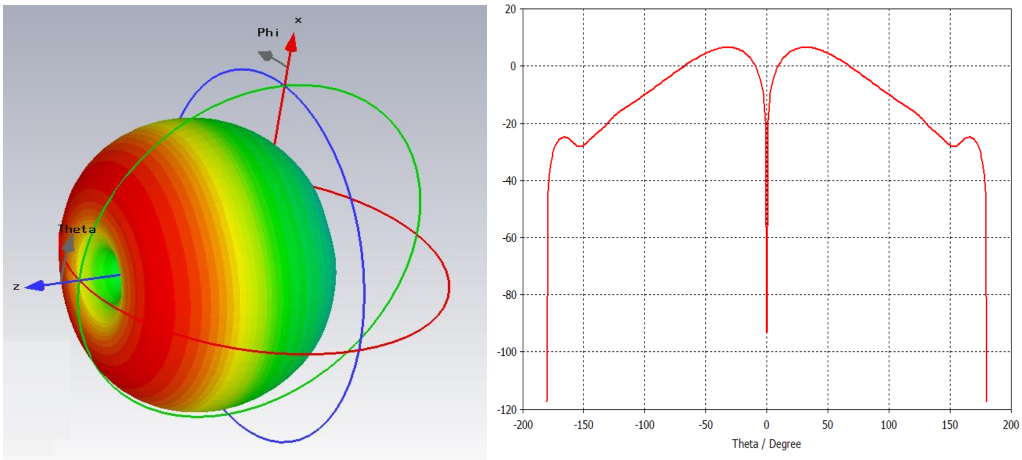

(a) Far field patterns illustrating $TE_{0,1}$ mode, notice lobe peak at ~25-30^o.

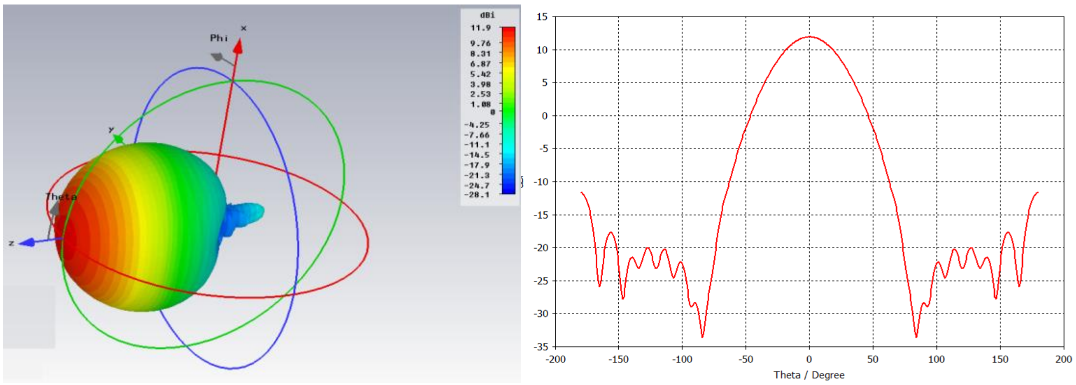

(b) Far field patterns illustrating $TE_{1,1}$ mode, note -3dB point at ~20^o.

Figure 5.49**:** Far field patterns for $TE_{0,1}$, and $TE_{1,1}$ modes.

When there was *no reflector* in the experiment at a magnetic field of B=0.184T an output power of 24.6kW was estimated by integrating the experimental antenna pattern. At a magnetic field of B=0.192T the total radiated power was estimated to be 31.6kW. These correspond to an efficiency of 2% to 2.4% respectively. When there was a *step reflector* in the experiment for a magnetic field of B=0.184T an output power of 99.1kW was estimated by integrating the experimental pattern. For the B=0.192T measurements a radiated power of 146.6kW was estimated, these suggest efficiencies of 7% to 11.5% respectively. For the case of *a tapered reflector* in the experiment for a magnetic field of B=0.184T an output power of 49.4kW was estimated by integrating the normalised experimental pattern. For the B=0.192T case the results were 108.8kW. These suggest efficiencies of 3.8% to 8.5% respectively.

5.8 O-mode and R-mode type resonances

Satellite measurements of AKR emissions have shown that they are predominately in the X-mode [Kaiser et al. 1978]. However it has been observed by at least eight different satellites, mainly Voyager 1 & 2 and DE-1 that there appears to be a weak O-mode component [Shawhan & Gurnett 1982] [Calvert 1981][Benson 1984] [Benson & Akasofu 1984].

The DE-1 satellite observations indicated the presence of both ordinary as well as extraordinary wave modes. When both modes are present simultaneously the O-mode generally occurs at lower frequencies and is smaller in amplitude by around a factor of 50. The harmonics associated with O mode AKR are less intense than the harmonics associated with X-mode AKR [Mellott 1984][Mellott et al. 1986].

The ISIS 1 observations of the O mode fundamental AKR is consistent with the O-mode observed by the DE-1 satellite whilst ISIS 1 revealed that O-mode AKR is present in locations outside the low-density source region of the intense AKR X-mode emission.

Satellite observations indicated the excitation of the O mode, so it was of interest to investigate the potential for the generation of O-mode like AKR emission from electron beams with horseshoe distributions in their velocity space. It is possible to tune the Strathclyde AKR experiment for generation of an electromagnetic mode which has characteristics close to the O-mode. Here it was decided to look for possible excitation of a $TM_{0,1}$ mode close to cut-off where its $E_{\perp}$ components $\rightarrow 0$ (i.e. the wave E field is parallel to, and the wave vector is perpendicular to the static magnetic field, like the O-mode). Simulations were also conducted to investigate the O-mode like regime of AKR emissions. The parameters used to define the simulation are shown in Table 5.11 below. Figure 5.50 illustrates the frequency and power output from these simulations.

Parameters	***Value or range***
B_o (T)	0.109 – 0.132
Pitch	$0^o – 90^o$
Energy (keV)	75
Current (A)	25

Table 5.11: Parameters of simulations conducted to investigate ‘R-mode’ and ‘O-mode’ emission.

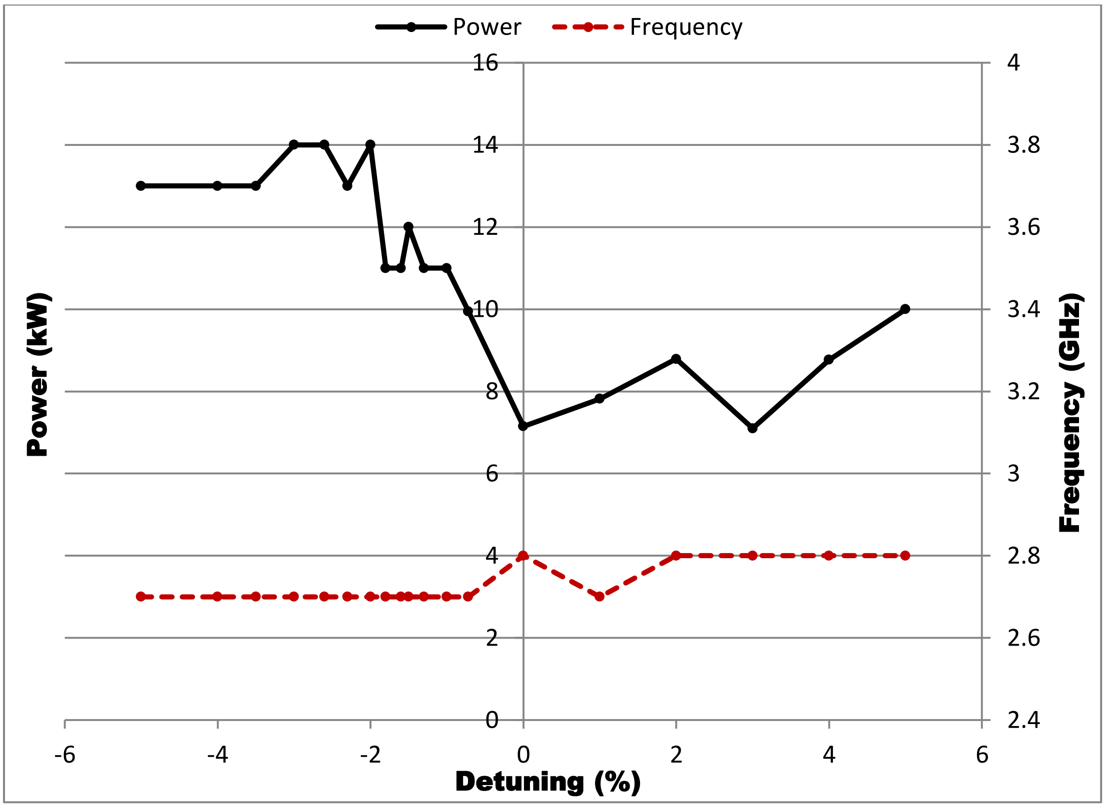

Figure 5.50**:** Predictions for power and frequency variation with magnetic field detuning for O-like and R-like excitation investigations, illustrating an output frequency ~2.7GHz.

Interestingly the same configuration will allow the electrons to excite a travelling R-like mode, here represented by a $TE_{1,1}$ wave, in a manner that may be relevant to the Earths radiation belt physics.

Figure 5.51 illustrates the geometry of the simulation. The cylindrical waveguide radius matched the experimental geometry at 4.14cm. The plateau region was 20cm long, consistent with the experimental plateau, whilst a taper is introduced at the injection end of the cavity. The beam can be seen dumping into the walls at z=100cm. At z=225cm there is a ‘numerical’ absorber with conductivity increasing from the left to the right side of the simulation geometry. The beam current in the simulation is shown in Figure 5.52.

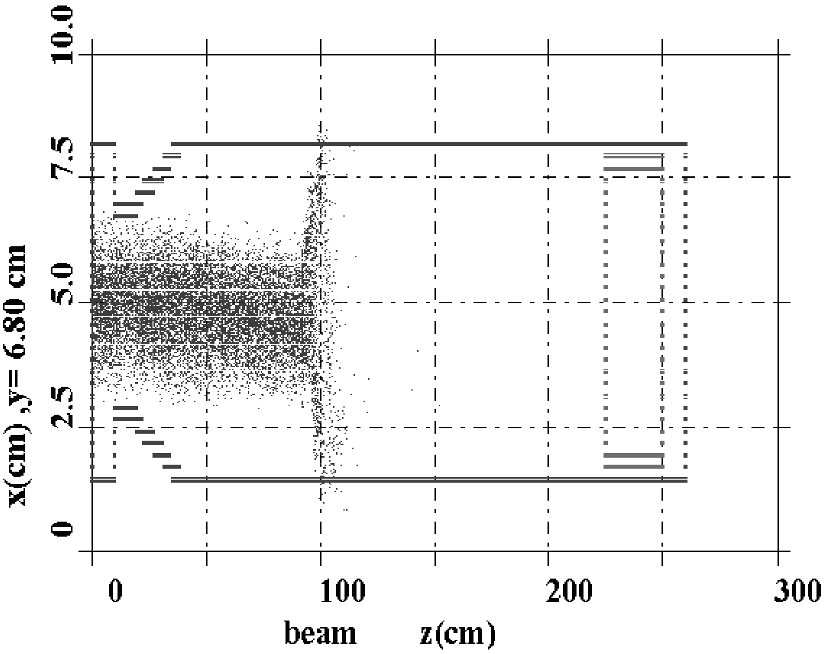

Figure 5.51: Simulation geometry, similar to the experiment with inserted taper, illustrating the waveguide and the electron beam PiC particle trajectories of the pre-defined horseshoe distribution.

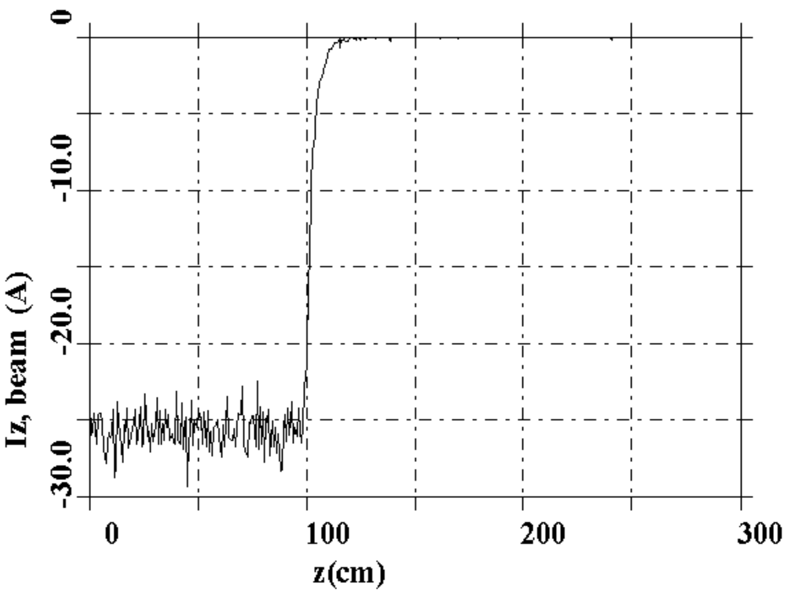

Figure 5.52**:** Simulation beam current, comparable to the experiment.

The cut-off for the $TM_{0,1}$ mode in this waveguide is 2.77GHz. This corresponds to a magnetic field of B=0.116T for cyclotron resonance with electrons having an energy of 75keV. Figure 5.53 is a plot generated by 3D KARAT illustrating the predictions of the excited modes. Here it can be seen that the predominant mode predicted is in fact the $TE_{1,1}$ (R like) rather than the $TM_{0,1}$ (O like) mode.

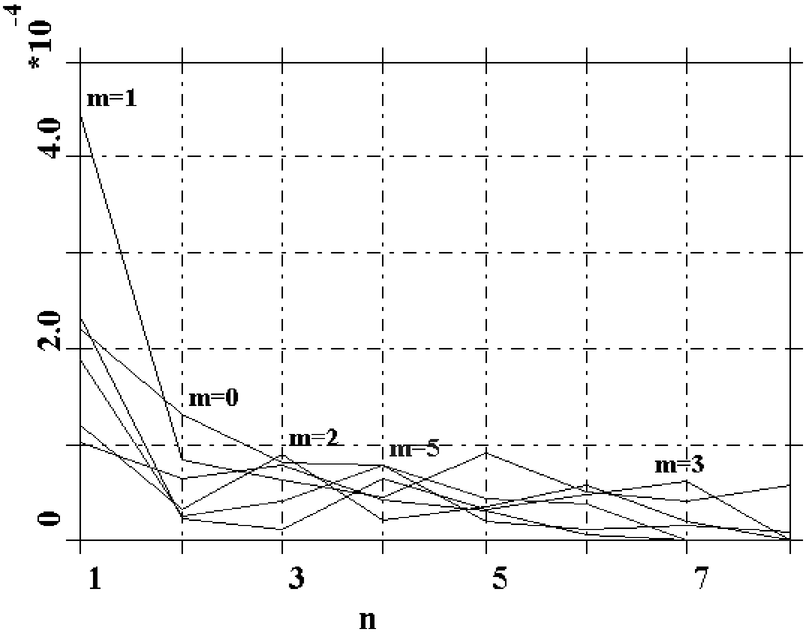

Figure 5.53**:** Representation of modes being excited in simulation, illustrating dominance of the $TE_{1,1}$.

Figure 5.54 is the Fourier transform of the electric field illustrating the peak frequency of predicted radio emission at 2.7GHz.

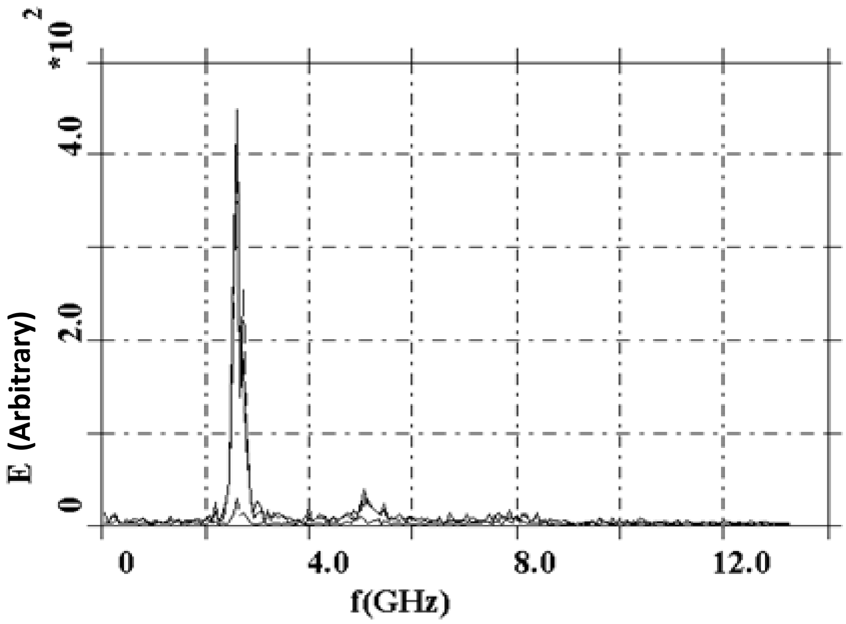

Figure 5.54**:** Fourier transform of the electric field illustrating a peak frequency of emission at 2.7GHz.

Although these simulations were intended to investigate the possible excitation of O-modes in AKR emissions, it was observed that in fact the $TM_{0,1}$ mode is not predicted but that the $TE_{1,1}$ mode has been excited at a frequency significantly above its cut-off (2.12GHz) and close to (but slightly below) the cyclotron frequency.

The $TE_{1,1}$ polarisation and propagation properties in this regime are closer to the properties of the R-X mode being excited with a significant axial wave-vector.

Following the results obtained from these simulations it was fitting to conduct experiments to verify their predictions. Plotting experimental data of the predicted frequency of emission against the cyclotron frequency, Figure 5.55, it is seen that the frequency of emission increases nearly linearly with (but at a downshift from) the cyclotron frequency. Figure 5.56 illustrates the Fourier transform of a signal illustrating the peak wave frequency of 2.66GHz captured on a 12GHz real time digitising oscilloscope.

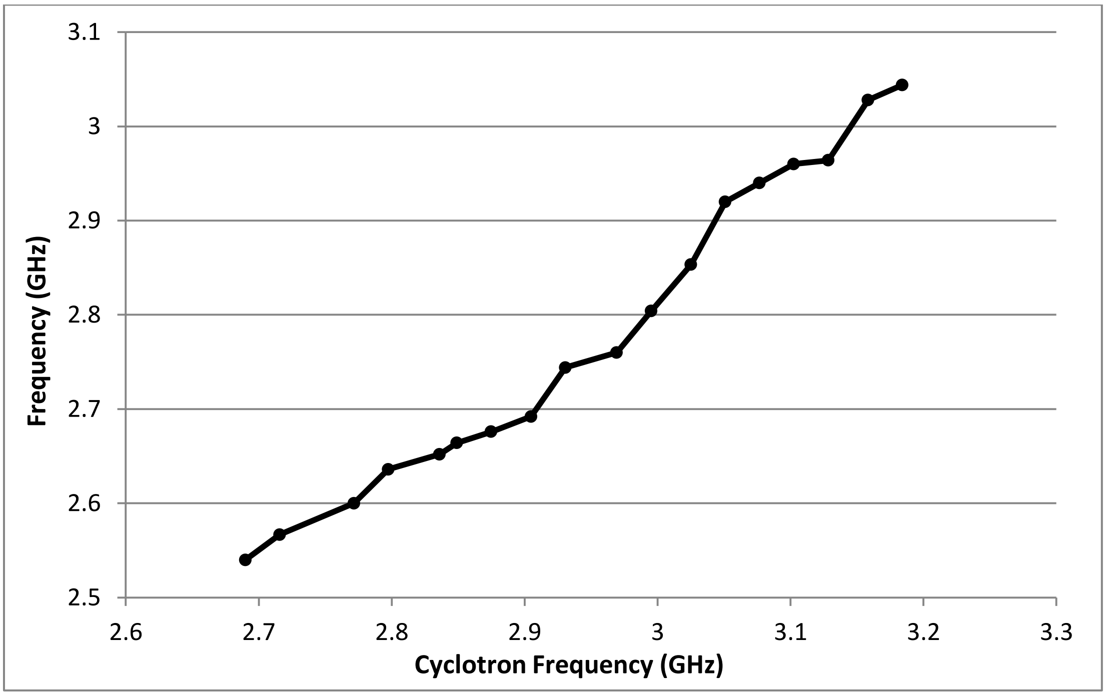

Figure 5.55**:** Measurement of radiation frequency as the cyclotron frequency increases in "O-mode"/"R-mode" experiments.

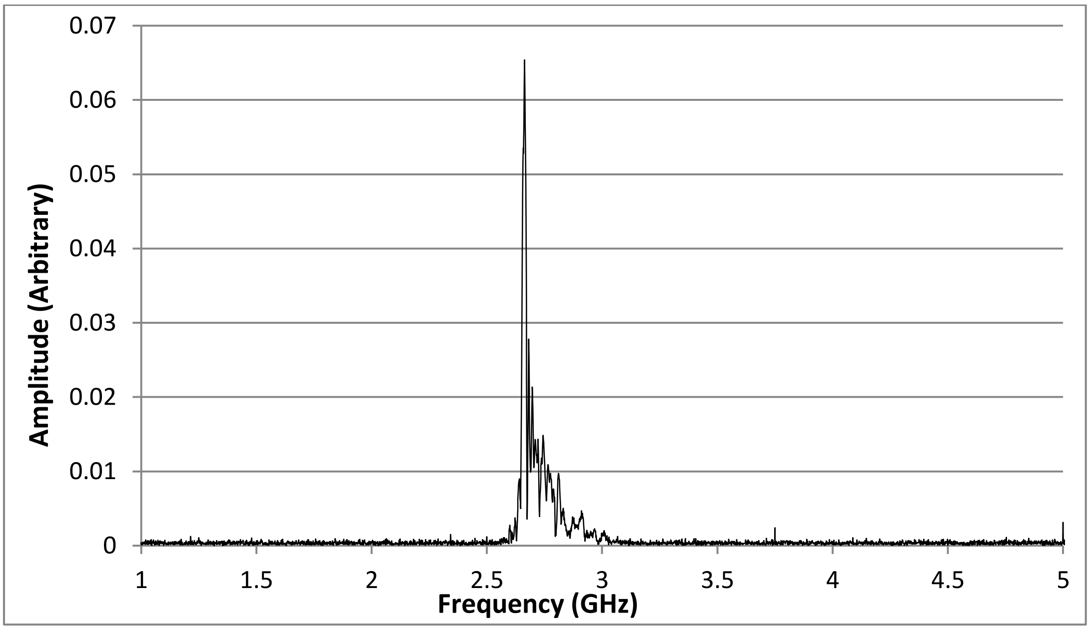

Figure 5.56**:** Fast Fourier transform of the AC wavepacket taken from the oscilloscope, illustrating a frequency of 2.66GHz. These experiments were conducted to investigate the possibility of the R or O-mode excitation.

Using the same method as previously described and the set-up shown in section 4.5.5 measurements were taken for the variation in the strength of the wave emissions as a function of the detuning and angular position. Figure 5.57 illustrates the power flux density variation with angular position. This has a structure that is broadly similar to the $TE_{1,1}$ mode, i.e. the electron beam appears to be exciting an R like mode rather than an O like mode. The variation of power received by the detector system, for these experiments, as a function of the magnetic field at a position of 30 degrees and in azimuthal polarisation is shown in Figure 5.58.

Integration of the antenna patterns allows the RF power of the system to be obtained. For the B=0.116T regime, corresponding to a cyclotron frequency of 2.85GHz, an estimate of the output power of 54kW was obtained at a frequency of 2.66GHz by direct integration of the experimental data. This corresponds to a remarkably high efficiency of 2.88% for an electron beam of such wide velocity spread radiating into a wave propagating at 37^o from the normal to the waveguide axis. Moreover, the efficiency remained as high as ~1% - 1.5% up to a cyclotron frequency of 3.14GHz generating radiation of 2.96GHz corresponding to a wave propagation angle of 45^o to the waveguide normal.

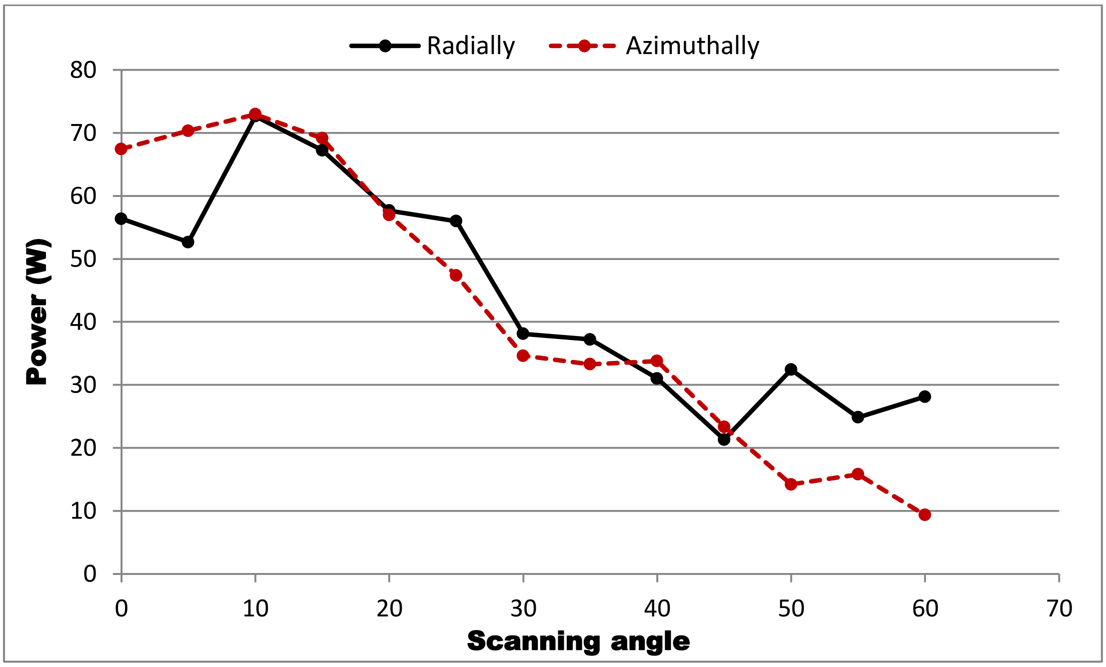

Figure 5.57**:** Intensity variation with angular position for azimuthal and radial polarisation of the detector. Magnetic field B=0.116T.

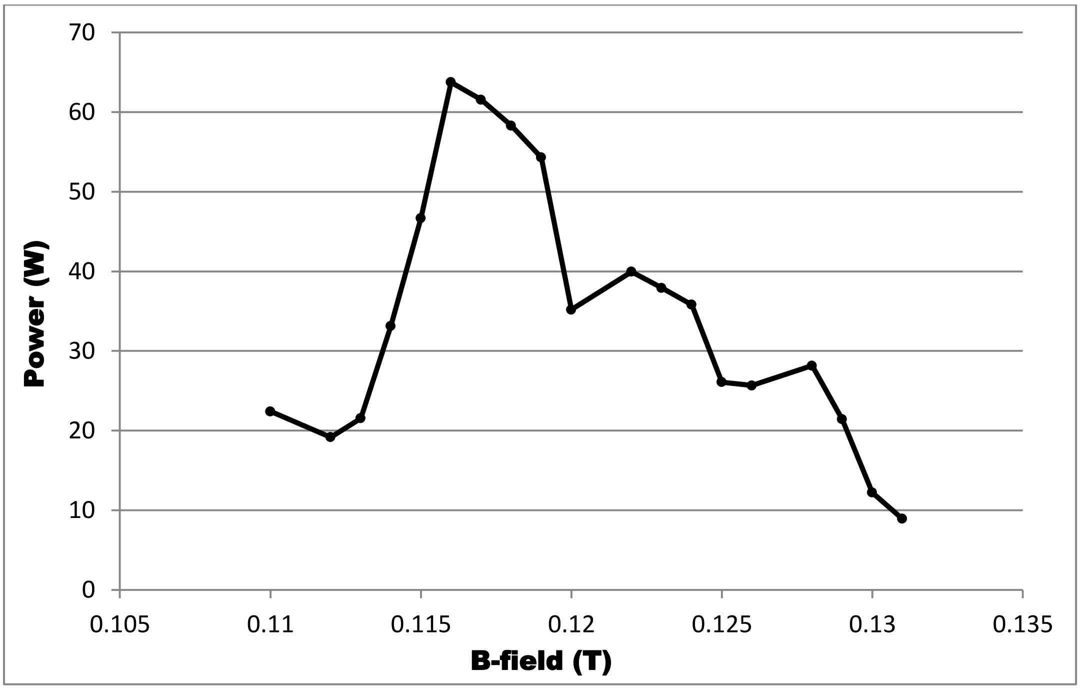

Figure 5.58**:** Measurement of power output with increasing magnetic field for the R and O-mode investigation experiments.

Chapter 6

Discussions, conclusions and future work

This chapter presents a discussion and comparison of the results obtained from 2D and 3D particle in cell code (PiC) simulations and laboratory experiments. The chapter will also present overall conclusions and comparisons with the geophysical environment.

6.1 Overview

The work described in this thesis was undertaken to enhance the understanding of electron beam behaviour and beam wave instabilities associated with the formation and subsequent evolution of an electron horseshoe distribution in velocity space. Electron horseshoe distributions form due to the conservation of the magnetic moment, μ, when an electron beam is incident on a region of increasing axial magnetic field. Electron horseshoe distributions have been observed to occur naturally within the terrestrial auroral zone and are believed to be unstable with respect to a cyclotron maser instability that is responsible for generating AKR [Ergun et al. 2000][Bingham & Cairns 2000].

In the work undertaken for this thesis, a series of numerical simulations were conducted utilising the PiC code KARAT to model the electromagnetic wave generation from an electron beam having a horseshoe distribution in velocity space. These simulations were either compared to existing experimental measurements or to new experiments conducted concurrently, exploiting a laboratory apparatus to replicate certain features of the auroral density cavity.

The simulations predicted the RF output signals, corresponding emission spectra, output power/Poyntings flux and RF conversion efficiencies. A novel feature of the 3D simulations presented here are that they are able to consider the excitation of the full spectrum of natural transverse modes available to the experiment. The simulations were developed exploiting experimental measurements quantifying the electron distribution in velocity space to define consistent distributions in the numerical models. The sensitivity of the cyclotron emissions to the electron beam current, electron velocity distribution and cyclotron detuning was investigated for resonances with near perpendicular X-like modes. Simulations and experiments were also undertaken to investigate emission into O-like perpendicular and R-X like off perpendicular propagating waves.

6.2 Simulations demonstrating importance of velocity distribution

The importance of the electron distribution in velocity space, the beam current and the magnetic detuning were demonstrated in 2D KARAT simulations. This allowed study and analysis of a wide range of parameters rapidly within a simpler simulation system as in a 2D simulation the azimuthal structure is discounted which eliminates the requirement to mesh one of the transverse dimensions.

The proposed theoretical models for the AKR cyclotron maser instability suggest that the instability is driven by a positive gradient in the transverse velocity profile of the electron velocity distribution (see theory section 2.5) [Wu & Lee 1979][Bingham & Cairns 2000]. The transverse velocity profile is observed to smear-out in velocity space as the interaction progresses; this causes a progressive decrease in the positive gradient across the transverse velocity profile leading to a saturation effect that limits the maximum radiation power.

The analysis illustrated that, naturally, when the input beam current increased the output power generally increased. There was a sharp resonance when the cyclotron frequency is close to the waveguide cut-off frequency (corresponding to perpendicular wave propagation) with sharp drops in emission efficiency for either increasing or decreasing detuning.

With a uniform electron distribution (10^o-80^o in pitch angle) simulations predicted a maximum efficiency of ~9% and a resonance width (where a strong interaction is observed) of ~3%. With a distribution of electrons focussed from 50^o to 80^o degrees in pitch angles, the maximum efficiency increased to ~14%, with a much wider resonance range ~6-7%. These simulations illustrated clearly the importance of the high pitch electrons in providing free energy to drive the instability for AKR emission. These enhanced efficiencies compared to previous simulations and experiments (~1-3%) suggest the reflector included in these models was significant and indicated the potential importance of backwards wave resonances.

This verified that in order to conduct realistic simulations of the experiments and thus better understand the implications of the experimental measurements of the RF wave generation process for the behaviour in the auroral region, the distribution of the electrons in velocity space in the simulations would need to be matched to the number densities obtained from the experimental studies.

6.3 Experimentally consistent electron velocity distribution

Unlike the previous 2D simulations conducted [Speirs et al. 2008][Speirs et al. 2010] the 3D simulations did not simulate the electron gun. This was due to computational restrictions. The 3D simulations instead injected a predefined horseshoe distribution in velocity space; an example of this distribution can be seen in Figure 5.3. Here, the beam progresses along the waveguide and dumps into the wall at the end of the interaction region. Initially the electrons have a spread in their transverse and axial momentum associated with the horseshoe distribution.

Given the obvious impact of the electron velocity on wave generation (see theory section 6.2) it was vital to ensure that the electron distribution in the simulations was matched to the experimental data. Excellent agreement was obtained with experiments which were shown to be stable over a period of several years, as shown in Figure 5.27.

6.4 Experimentally consistent 3D simulation of wave generation

This work represents the first attempt to conduct simulations of the wave emissions from horseshoe distribution electron beams in 3D. Previous numerical studies had investigated the formation and evolution of an electron horseshoe distribution, using a 2D version of KARAT [Speirs et al. 2008][Speirs et al. 2010]. 2D simulations can only allow for axisymmetric modes to be identified, which means that the impact and role of modes with azimuthal structure cannot be predicted. Therefore, in conducting 3D simulations a more complete representation of the interaction dynamics is considered.

These simulations are compared to a laboratory experiment scaled to microwave frequencies built to replicate major aspects of the configuration of the auroral density cavity situated in the Earth’s polar magnetosphere (see theory section 4 for experimental apparatus). The simulations are compared to prior experiments at cyclotron frequencies of 4.42GHz and 11.7GHz (near cut off for the $TE_{0,1}$ and $TE_{0,3}$ modes of the interaction waveguide, radius 4.14cm) and with new experiments undertaken at ~4.42GHz and ~2.67GHz cyclotron frequency. The length of the interaction region was ~20cm. Measurements taken from the experiment defined the electron beam current and energy in the interaction waveguide and its velocity space distribution (i.e. the horseshoe distribution function), in the simulations as described in Section 6.3.

For the 11.7GHz interaction regime, the 3D simulations predicted spectra at close to the cyclotron frequency with strong mode competition. The simulations predicted the same dominant modes (the $TE_{2,3}$ and $TE_{0,3}$) that had been identified experimentally [McConville et al. 2008][Speirs et al. 2005]. The analysis of this regime was discussed in section 5.6.

The simulations gave reasonable agreement with the experimental measurements of the output power with a predicted power ~15kW - 40kW from the 3D simulations (at magnetic fields of B>0.48T) compared to the 2D simulation predictions of 20kW and the experimental measurements of 10kW from a beam of ~16A. The 3D simulations predict output powers of ~40kW – 100kW in a configuration where an experimental measurement of 30kW was obtained from a beam of 37A. It should be noted here that the experiments did not fully explore the lower range of magnetic fields presented in Figure 5.37.

Secondly when the cyclotron frequency was below the $TE_{0,3}$ cut-off frequency, the predicted mode was normally the $TE_{2,3}$ and was stable. However, when the detuning was increased above the $TE_{2,3}$ cut-off frequency the predicted mode was the $TE_{0,3.}$ Overall it was seen that the higher the beam current the tendency for excitation of multiple modes increased. These modes (as noted above) closely match the modes observed in the experiment. This strong correlation between the 3D PiC code and the experiment provides confidence in the accuracy of the simulation techniques, whilst also confirming the interpretation of the experimental measurements [McConville et al 2008].

In general, the simulations also agreed strongly with the spectral content of the radiation measured in the experiment, clearly showing evidence of emission of waves close to the cyclotron frequency.

Analysing the RF output power or Poynting flux corresponding to the 4.42GHz resonance regime the 3D simulations predicted an output power in the range 10kW-40kW as a function of the precise tuning of the resonance for a beam at 75keV and 12A compared to an experimental measurement of 19kW for a similar electron beam velocity distribution. An alternative regime predicted power ~30kW-70kW for a beam configuration which produced ~35kW in the experiment. The 3D simulations also agreed strongly with the previous 2D simulations which predicted output of 20kW and 50kW for these two configurations. The excitation of the expected $TE_{0,1}$ mode, was confirmed in these 3D simulations.

One point of particular interest in the spectral output is shown by the spectra of the 4.42GHz 3D simulation. The spectra indicated a second harmonic at ~8GHz. This second harmonic was seen in the experiments conducted for these regimes, but could not be identified in the simulations conducted [Speirs et al. 2008] in two dimensions. This confirms that the three dimensional simulations provide a more comprehensive representation of the experiment, by being able to predict harmonic content excited in non-symmetric modes.

6.5 Preferential backwards wave emission

In various initial simulations it was regularly noted that a backward travelling wave was excited that was stronger than the forward going wave. The forward wave spectrum was also observed to be noisier than the backward going wave, although the centre frequency of the forward and backward wave were nearly equal illustrating that the high pitch electrons (which have nearly no Doppler shift in either direction) were the primary driver for the emissions. Additional simulations and experiments were conducted to investigate this. The output frequency was observed to increase more slowly with the magnetic field than the cyclotron frequency which indicates a backwards wave resonance with a stronger tolerance to the high velocity spread present in these electron beams. It was also seen that there was a gradual decline in RF power with increasing detuning which is also characteristic of a backward wave resonance. Experiments were conducted with reflectors in the interaction waveguide to ensure that the detectors were able to measure emissions in the backward wave mode. It was seen that when there was no reflector present there was significantly less output power, supporting the premise of a preference for backward wave emission.

Once the spectral output had been examined from both the experiments and simulations a scan of the output antenna pattern was conducted in order to identify the interacting waveguide modes present at different magnetic mirror ratios. The experimental set-up for these measurements is illustrated in Chapters 4 and 5. The variation in the strength of the wave emissions was measured as a function of detuning. The antenna measurements were compared to a transverse spatial Fourier analysis in the simulations which predicted the modes which could be excited. The results showed that adding the reflector to the system increased efficiency from ~1% - 3% to up to ~8% - 11%, clearly showing the preference for emission into contra propagating waves. It is possible that the enhanced emission is associated with the increase of the Q of the resonator caused by the introduction of the reflector. However, the preliminary simulations, section 5.7, showed that ~10% efficiency in the backward wave was achievable without the use of any closed resonator configuration, supporting the suggestion that the enhanced efficiency in the experiment is associated with forward scattering of a wave primarily generated in the backwards direction.

This evidence of backward resonance may have significant implications in the auroral density cavity in the magnetosphere where there is a cold tenous plasma in the resonant region since it may allow for AKR emission into the X-mode below the cyclotron frequency and hence below the upper hybrid stopband. It is also thought that a backward wave interaction could explain the discrete character of the AKR frequency spectrum [Savilov et al. 2007].

When radio waves emit with a slight backward angle they may experience subsequent upwards refraction in the complex plasma environment of the polar magnetosphere which can explain the measurements taken from the Cluster satellite [Mutel et al 2008][Menietti et al 2011]. This premise is supported by calculations undertaken by colleagues at St Andrews University and simulations by D Speirs at Strathclyde University.

6.6 Emission into R-like modes

Radial and azimuthal antenna pattern scans were carried out for magnetic fields of B=0.116T to establish if these unusual electron beams would radiate in O-like modes at close to the cyclotron frequency (and near to the cut-off of the $TM_{0,1}$ mode). In these experiments (and numerical investigations) the power was observed to be radiated along the centre of the antenna pattern suggesting that instead of the expected O-like $TM_{0,1}$ mode, a $TE_{1,1}$ mode had been excited relatively far from its cut-off 2.12GHz at a frequency close to but slightly below the cyclotron frequency ~2.85GHz. The $TE_{1,1}$ polarisation and propagation properties at these frequencies appear to be similar to the properties of the R-X mode being excited with a significant axial wave-vector, having propagation angles as low as 45^o from the waveguide axis.

Using the same method as previously described and the set-up shown in section 4.5.4. Measurements were taken for the variation in the strength of the wave emissions as a function of the detuning and angular position. The variation of power received by the detector system, for these experiments, as a function of the magnetic field at a position of 30 degrees and in azimuthal polarisation is shown in Figure 5.58.

Integration of the antenna patterns allows the RF power of the system to be obtained. For the B=0.116T regime an estimate of output power of 54kW was obtained by direct integration of the experimental data. This corresponds to an efficiency of 2.9%. This is a remarkably high efficiency for emission so far from perpendicular propagation (37^o from perpendicular to the waveguide axis) and may be relevant to events like triggered whistlers and other equatorial cyclotron wave effects connected to the radiation belts. It may also be relevant in applied physics to future high frequency sources where suppression of wall loss may be more important than electronic efficiency, by simultaneous excitation of both forward and backward travelling waves at the cyclotron frequency.

6.7 Comparison to the magnetosphere

The simulations (both 2D and 3D) compare well to the scaled experiments and provide insight into parameters hard to directly measure. The agreement encompasses efficiency, frequency and wave propagation and polarisation properties.

The waveguides used in these investigations support a range of TE and TM modes. Near to cut-off TE modes in a waveguide aligned with a static magnetic field have a close relationship with the polarisation and propagation properties of the X-mode observed in the magnetosphere.

One of main aims of this research was to investigate whether there is enough free energy in the AKR emission process to account for the efficiency of radiation emission ~1-2%, as measured from the magnetosphere corresponding to a power of ~1GW. The power of the emitted radiation in both the experiment and the simulations ranged from ~17kW – 60kW which correspond to efficiencies of between 1% - 3%. In fact higher efficiencies were measured in the backwards propagating waves. The simulations largely agree with these experimental measurements and the simulation software is now being used to analyse the unbound environment to predict the efficiency of the wave generation in the natural situation.

The 11.7GHz resonance mode of the experiment (exciting the $TE_{0,3}$ and $TE_{2,3}$ modes) illustrated that the systems peak efficiency would not be seriously impeded in overmoded conditions where the transverse field configuration is not well defined. This suggests the results have significant relevance for the magnetospheric environment which also presents an overmoded transverse field structure [Speirs et al. 2005][Cairns et al. 2005] with weakly defined radiation boundaries. In all cases preference for emission in X-modes at around the cyclotron frequency was confirmed.

Near to cut-off TM modes are close approximations to the O-mode (propagating perpendicular to the magnetic field but polarised parallel to the magnetic field). Magnetospheric observations suggested that radiation polarised in O-mode is sometimes observed though at a relatively weak level. Experiments investigating excitation of near to cut-off TM modes at close to the cyclotron frequency did not in fact observe radiation in this mode. Instead these experiments observed excitation of a mode that appeared close to the $TE_{1,1}$ mode, somewhat above its cut-off frequency. This mode seems likely to be related to the emission of whistler modes in the equatorial region of the Earth’s magnetosphere.

The success of the 3D simulations in reproducing the experimental performance provides justification for the use of these simulation methods (as well as the previously validated 2D simulations) in investigations of the actual geophysical environment.

In the research conducted for this thesis the simulation and experimental results support the proposal that the descending auroral electron flux can provide the driving energy to give rise to generation of AKR in the auroral density cavity. They agree well with the theoretical predictions for the electron cyclotron maser instability associated with this descending electron beam.

6.8 Future work

An important development of the simulations, building on the demonstration that they can give reasonable predictions for the behaviour of the experiment, would be to conduct simulations with unbounded geometry, this would represent the auroral density cavity more closely as there would be no ‘hard’ boundary conditions as arise with waveguides. This is an activity pursued by the authors colleague D.C. Speirs.

It was noticed in Penning trap plasma experiments [McConville et al. 2011] that when a background plasma was generated in the experiment it was seen that the nature of the radiation generation was significantly affected. Specifically, the background plasma reduced the efficiency of the wave generation and introduced strong statistical variation in the strength of the wave interaction. More experiments, with a background plasma, could be conducted to research the regimes discussed in this thesis (backward wave emission and R-X like modes). The trap may also be extended from the previous length of 20cm, providing a larger plasma region. This would be particularly interesting for the sort of extended interactions one might expect for R-branch instabilities. This would develop the interesting result from the present thesis which showed reasonably strong emissions from these unusual electron beams into co-propagating dipole radiation modes which appear similar in some respects to R-type plasma modes.

This would necessitate the removal of the cathode mesh of the Penning trap to allow for egress of circularly polarised radiation. These experiments might allow the investigation of the chorus and triggered whistler phenomenon which occur along the magnetic field lines in the Earth’s equatorial magnetosphere [Santolik et al. 2003].

REFERENCES

Agapov I, Blair G.A, Woodley M, “Beam emittance measurement with laser scanners in the International Linear Collider beam delivery systems”, Physical Review Special Topics, Accelerators and Beams, Vol **10**, 112801, 2007.

Aikio A.T, Mursula K, Buchert S, Forme F, Amm O, Markland G, Dunlop M, Fontaine D, Vaivads A, Fazakerley A, “Temporal evolution of two auroral arcs as measured by the Cluster satellite and coordinated ground-based instruments”, Annales Geophysicae, Vol **22**, pp4089-4101, 2004.

Anderson S.G, Rosenzweig J.B, Le Sage G.P, Crane J.K, “Space-charge effects in high brightness electron beam emittance measurements”, Physical Review Special Topics, Accelerators and beams, Vol **5**, 014201, 2002.

Andre M, “Waves and wave-particle interactions in the auroral region”, Journal of Atmospheric and Solar-Terrestrial Physics, Vol **59**, pp1687-1712, 1997.

Beneditkov E.A, Getmansev G.G, Sazonov Y.A, Tarasov A.F,” Preliminary results of measurement of the intensity of disturbed extraterrestrial radio-frequency emission at 75 and 1525KHz frequencies by the satellite Electron-2” Kosm. Issled, Vol **3**, pp614-617, 1965.

Benson R.F, Calvert W, “ISIS 1 observations at the source of Auroral Kilometric Radiation”, Geophysical Research Letters, Vol **6**, No 6, pp479-482 1979.

Benson R.F, “Auroral Kilometric Radiation: Wave Modes, Harmonics and Source Region Electron Density Structures”, NASA technical memorandum, 86101, 1984.

Benson R.F and Akasofu SI, “Auroral Kilometric Radiation/Aurora correlation”, Radio Science, Vol **19**, Issue 2, pp527-541, 1984.

Benson R.F, “Auroral Kilometric Radiation – Waves modes, Harmonics, and Source region electron-density structures”, Journal of Geophysical Research – Space Physics, Vol **90**, pp2753-2784, 1985.

Benson R.F, Webb P.A, Green J.L, Carpenter D.L, Sonwalkar V.S, James H.G, Reinisch B.W, “ Active wave experiments in space plasmas, The Z mode”, Lect Notes Phys, Springer-Verlag Berlin Heidelberg, Vol **687**, pp3-35, 2006.

Bingham R and Cairns R.A, “Generation of Auroral Kilometric Radiation by electron horseshoe distributions”, Physics of Plasmas, Vol 7, no.7, 3089, 2000.

Bingham R and Cairns R.A, Kellett B.J, “Coherent cyclotron maser radiation from UV Ceti”, Astronomy and Astrophysics, Vol **370**, pp1000-1003, 2001.

Bingham R, Cairns R.A, “A new Cyclotron Maser Radiation Mechanism in space plasmas”, Physica Scripta, Issue T98, pp160-162, 2002**a**.

Bingham R, Kellet B.J, Cairns R.A., Mendonca J.T and Spicer D.S, “Cyclotron Maser Radiation from Astrophysics shocks” The astrophysical Journal, Vol **595,** pp279-284, 2002**b**.

Bingham R, Kellett B.J, Cairns R.A, Vorgul I, Phelps A.D.R, Ronald K, Speirs D.C, “Cyclotron maser radiation in space and laboratory plasmas”, Plasma Phys, Vol **44**, No 5-6, pp382-387, 2004.

Birdsall C.K, “Plasma physics via computer simulation”, McGraw-Hill Book, New York,1985.

Bott I B, “Tuneable Source of Millimeter and Sub millimeter Radiation”, Proc. IEEE Vol **52**, pp330-331, 1964.

Bujarbarua S, Sarma S.N, Nambu M, “Auroral Kilometric Radiation due to a new plasma instability”, Physical Review A, Vol **29**, No4, pp2171-2178, 1984**a**.

Bujarbarua S, Nambu M, “On the theory of Auroral Kilometric Radiation”, Physica Scripta, Vol **30**, pp201-211, 1984**b**.

Cairns R.A, Speirs D.C, Ronald K, Vorgul I, Kellett B.J, Phelps A.D.R, Bingham R, “A cyclotron maser instability with application to space and laboratory plasmas”, Physica Scripta, Vol **T116**, pp23-26, 2005.

Cairns R.A, Vorgul I, Bingham R, Ronald K, Speirs D.C, McConville S.L, Gillespie K.M, Bryson R, Phelps A.D.R, Kellett B.J, Cross A.W, Robertson C.W, Whyte C.G, He W, “Cyclotron maser radiation from inhomogeneous plasmas”, Physics of Plasmas, Vol **18**, 022902, 2011.

Calvert W, “The Auroral plasma cavity”, Geophysical Research Letters, Vol **8**, pp919-921, 1981.

Chow K.K and Pantell R.H “The cyclotron resonance backward wave oscillator”, Proc IEEE, Vol **48**, pp330-331, 1964.

Chu K.R, “The electron cyclotron maser”, Reviews of Modern Physics, Vol **76**, pp490-493, 2004.

Collin H.L, Peterson W.K, Lennartsson O.W, Drake J.F, “The seasonal variation of auroral ion beams”, Geophysical Research Letters, Vol **25**, No 21, pp4071-4074, 1998.

Collin R.E, “Foundations for microwave engineering”, IEEE press series, 2nd edition, Ohio, 2001.

Cole K.D, Pokhotelov O.A, “Cyclotron solitons – source of Earths Kilometric radiation”, Plasma Physics, Vol **22**, pp595-608, 1980.

Davydovskii V.Y, “On the possibility of accelerating charged particles by electromagnetic waves in a constant magnetic field” Zh,Eksp, Teror.Fiz., 13: 886-88 (Soviet Physics JETP, 16 (1963) : 629-30), 1962

Delroy G.T, Ergun R.E, Carlson C.W, Muschetti L, Chaston C.C, Peria W, McFadden J.P, “FAST observations of electron distributions within AKR source regions.”, Vol **25**, No 12, pp2069-2070, 1998.

Ergun R.E, Carlson C.W, McFadden J.P, Delroy G.T, Strangeway R.J, Pritchett P.L, “Electron-cyclotron maser driven by charged-particle accelecration from magnetic field-aligned electric fields”, The Astrophysical Journal, Vol **538**, pp465-466, 2000.

Ergun R.E, Carlson C.W, McFadden J.P, Mozer F.S, Delory G.T, Peria W, Chaston C.C, Temerin M, Elphic R, Strangeway R, Pfaff R, Cattell C.A, Klumpar D, Shelly E, Peterson W, Moebius E, Kistler L, “FAST satellite wave observations in the AKR source region”, Geophysical Research Letters, Vol **25**, No 12, pp2061-2064, 1998.

Eriksson A and Wahlund J, “Charging of the Freja Satellite in the Auroral Zone”, IEEE Transactions on Plasma Science, Vol **34**, No 5, pp2038-2044, 2006.

Feinstein J, “Research on electronic Interaction with the fields of Mirror Resonators”, Proc. Int. Cong. Microwave Tubes 5th., Paris, pp506-508, 1964.

Engel A.V, “Ionized Gases”, American Institute of Physics, New York, 1997.

Felba J, “Emittance of high-power-density electron beam”, Vacuum, Vol **55**, pp223-233, 1999.

Gapanov A.V.,“Interaction between electron fluxes and Electromagnetic waves in waveguides”, IZV.VUZ. Radiofizica,” Vol **2**, pp460-462, 1959.

Gillespie K.M, Speirs D.C, Ronald K, McConville S.L, Phelps A.D.R, Bingham R, Cross A.W, Robertson C.W, Whyte C.G, He W, Vorgul I, Cairns R.A, Kellett B.J, “3D PiC code simulations for a laboratory experimental investigation of Auroral Kilometric Radiation mechanisms”, Plasma Physics and Controlled Fusion, Vol **50**, 124038 (11pp), 2008.

Gilmour A.S, “Microwave tubes”, Artech House, Massachusetts, 1986.

Grabbe C.L, “Theory of the fine structure of Auroral Kilometric Radiation”, Geophysical Research Letters, Vol **9**, No 2, pp155-158, 1982.

Granatstein V.L and Alexeff I, (Editors) “High-Power Microwave Sources”, Artech House, Boston, London, pp104-203, 1987.

Green J.L, Gurnett D.A, Shawhan S.D, “The Angular distribution of Auroral Kilometric Radiation”, Journal of Geophysical Research, Vol **82**, No13, pp1825-1838, 1977.

Gurnett D.A, “The Earth as a radio source; Terrestrial kilometric radiation” J.Geophys Res, Vol **79**, pp4227-4238, 1974.

Gurnett D.A, Huff R.L, Pickett J.S, Persoon A.M, Mutel R.L, Christopher I.W, Kletzing C.A, Inan U.S, Martin W.L, Bougeret J.L, Alleyne H.St.C, Yearby K.H, “First results from the Cluster wideband plasma wave investigation”, Annales Geophysicae, Vol **19**, pp1259-1272, 2001.

Handbook of Atmospheric electrodynamics Volume II. Radioastronomical Institute, Germany. Edited by Hans Volland. CRC Press.

Helliwell R.A, “A tale of two magnetospheres – the cold and the hot”, Journal of Atmospheric and Solar-Terrestrial Physics, Vol **63**, pp110-1116, 2001.

Hirshfield J.L, Wachtel J.M, “Electron cyclotron maser”, Physical Review Letters, Vol **12,** No 19, pp533-536, 1964.

Hirshfield J.L and Granatstein V.L, “The Electron Cyclotron Maser-An historical Survey”, IEEE Transactions on Microwave Theory and Techniques, Vol **mtt-25,** No 6, pp522-526, 1977.

Hosotani A, Ono T, Iizima M, Kumamoto A, “Second harmonics of Auroral Kilometric Radiation observed by the Akebono satellite”, Adv. Polar Upper Atmos Res, Vol **17**, pp146-154, 2003.

Huff R.L, Calvert W, Craven J.D, Frank L.A, Gurnett D.A, “ Mapping of Auroral Kilometric Radiation Sources to the Aurora”, Journal of Geophysical Research, Vol **93**, pp11,445-11,454, 1988.

Humphries S. Jr, “Principles of Charged Particle Acceleration”, University of New Mexico, John Wiley & Sons, 1999.

Imhof W.L, Anderson R.R, Chenette D.L, Mobilia J, Petrinec S.M, Walt M, “The correlation of rapid AKR variations with changes in the fluxes of precipitating electrons”, Adv. Space Res, Vol **23**, No10, pp1747-1752, 1999.

Kaiser M.L, Alexander J.K, Riddle A.C, Pearce J.B and Warwick J.W, “Direct measurements by Voyagers 1 and 2 of the polarization of terrestrial kilometric radiation”, Geophysical Research Letters, Vol **5**, pp857-860, 1978.

Kasaba Y, Matsumoto H, Hashimoto K, Anderson R.R, “The angular distribution of Auroral Kilometric Radiation observed by the GEOtail spacecraft”, Geophysical Research Letters, Vol **24**, Issue 20, pp 2483-2486, 1997.

Kumamoto A and Oya H, “Asymmetry of occurrence – frequency and intensity of AKR between summer polar region and winter polar region sources”, Geophysical Review Letters, Vol **25**, Issue 13, pp2369-2372, 1998.

Kumamoto A, Ono T, Oya H, “Seasonal dependence of the vertical distributions of Auroral Kilometric Radiation sources and auroral particle acceleration regions observed by the Akebono satellite”, Adv Polar Upper Atmos, Res, Vol **15**, pp32-42, 2001.

Kumamoto A, Ono T, Iizima M, “Seasonal and solar cycle dependences of the correlation between Auroral Kilometric Radiation and the AE index”, Adv. Polar Upper Atmos, Res Vol **19**, pp10-20, 2005.

Kuril’chik V.N, “Observations of the Auroral Hectometric Radio Emission onboard the INTERBALL-1 Satellite, Cosmic Research, Vol **45**, No 3, pp248-252, 2007.

Kurth W, Baumback M.M, Gurnett D.A, “Direction-Finding Measurements of Auroral Kilometric Radiation”, Journal of Geophysical Research, Vol **80**, No 19, pp2746-2770, 1975.

Kurth W.S, Gurnett D.A, “Auroral Kilometric Radiation integrated power flux as a proxy for A_E”, Adv.Space Res, Vol **22**, No1, pp73-77, 1998.

Labelle J, Treumann R.A, “Auroral Radio emissions, 1. Hisses, Roars, and Burst”, Space Science Reviews, Vol **101**, pp295-440, 2002.

Lamy L, Zarka P, Cecconi B, Hess S, Prnage R, “Modelling of Saturn kilometric radiation arcs and equatorial shadow zone”, Journal of Geophysical Research, Vol **113**, A10213, 2008.

Louarn P, Roux A, De Feraudy H, Le Queau D, Andre M, Matson L, “Trapped electrons as a free energy source for the auroal kilometric radiation”, Journal of Geophysical Research, Vol **95**, No A5, pp5983-5995, 1990.

Louarn P, Le Queau D, “Generation of the Auroral Kilometric Radiation in plasma cavities – I. Experimental study”, Planet, Space. Sci, Vol **44**, No 3, pp199-210, 1996**a**.

Louarn P and, L’Queau D, “Generation of the Auroral Kilometric Radiation in plasma cavities-II The cyclotron maser instability in small size sources”, Planet Space Sci, Vol **44**, No 3, pp211-224, 1996**b**.

Lysak R.L and Andre M, “Particle Acceleration and Wave Phenomena in the Auroral Region”, Phys. Chem. Earth, Vol **26**, No1-3, pp3-12, 2001.

Marklund G.T, “Auroral phenomena related to intense electric fields observed by the Freja satellite”, Plasma Phys. Control Fusion, Vol **39**, a195-a226, 1997.

McConville S.L, Speirs D.C, Ronald K, Phelps A.D.R, Cross A.W, Bingham R, Robertson C.W, Whyte C.G, He W, Gillespie K.M, Vorgul I, Cairns R.A, Kellett B.J, “Demonstration of auroral radio emission mechanisms by laboratory experiment, Plasma Physics and Controlled Fusion, Vol **50**, 074010 (13pp), 2008.

McConville S.L, “Scaled experimental and numerical investigation of auroral radiation phenomena”, PhD thesis, University of Strathclyde library, 2009.

McConville S.L, Koepke M.E, Gillespie K.M, Matheson K, Whyte C.G, Robertson C.W, Speirs D.C, “Characterization of a Penning discharge for investigation of auroral radio wave generation mechanisms”, Plasma Physics and Controlled Fusion, Vol **53**, 124020 (9pp), 2011.

Mellott M.M, Huff R.L, Gurnett D, “Ordinary mode Auroral Kilometric Radiation fine structure observed by DE 1”, Journal of Geophysical Research, Vol **93**, No A7, pp7515-7520, 1988.

Melrose D.B and Dulk G.A, “Electron-cyclotron masers as the source of certain solar and stellar radio bursts”, The Astrophysical Journal, Vol **259**, pp844-858, 1982.

Melrose D.B, Hewitt R.G, Dulk G.A, “Electron – cyclotron maser emission: Relative growth and damping rates for different modes and harmonics”, Journal of Geophysical Research, Vol **89**, No A2, pp897-904, 1984.

Melrose D.B, “Coherent emission”, Universal Heliophysical Processes Proceedings, IAU Symposium, No 257, 2008.

Meng C.I, Liou K, Newell P.T, “Asymmetric sunlight effect on dayside/nightside auroral precipitation”, Phys.Chem.Earth, Vol **26**, No1-3, pp43-47, 2001.

Menietti J.D, Persoon A.M, Pickett J.S, Gurnett D.A, “ Statistical study of Auroral Kilometric Radiation fine structure striations observed by Polar”, Journal of Geophysical Research, Vol **105**, No A8, pp18,857-18,866, 2000.

Menietti J.D, Kurth W.S, “Ordered fine structure in the radio emission observed by Cassini, Cluster and Polar”, Planetary Radio Emissions VI, pp265-272, 2006.

Menietti J.D, Mutel R.L, Santolik O, Scudder J.D, Christopher I.W, “Striated drifting Auroral Kilometric Radiation burst: Possible stimulation by upward traveling EMIC waves”, Journal of Geophysical Research, Vol **111**, A04214, 2006.

Menietti J.D, Donovan E.F, Honary F, Spanswick E, “AKR breakup and auroral particle acceleration at substorm onset”, Journal of Geophysical Research, Vol **113**, A09213, 2008.

Menietti J.D, Donovan E.F, Honary F, Spanswick E, “Simultaneous radio optical oobservations of aurroral structures: implications for AKR beaming”, Journal of Geophysical Research, Vol **116**, A12219, 2011.

Mesyats G.A and D.I Proskurovsky, “Pulsed Electrical Discharge in Vacuum”, Springer – Verlag Germany, 1989.

Miller R.B, “Mechanism of explosive electron emission for dielectric fiber (velvet) cathodes”, Journal of Applied Physics, Vol **84**, No 7, 3880, 1998.

Moen J, Berry S.T, Kersley L, Lybekk B, “Probing discrete auroral arcs by ionospheric tomography”, Annales Geophysical, Earth and environmental science, Vol **16**, No 5, Springer Berlin/Heidelberg, 1998.

Morgan D.D, Menietti J.D, Wingless R.M, Wong H.K, “Perpendicular electron heating by absorption of Auroral Kilometric Radiation”, Planetary and Space Science, Vol **48**, pp41-49, 2000.

Morioka A, Miyoshi Y, Tsuchiya F, Misawa H, Yumoto K, Parks G.K, Anderson R.R, “AKR breakup and auroral particle acceleration at substrom onset”, Journal of Geophysical Research, Vol **113**, A09213, 2008.

Morozova E.A, Mogilevsky M.M, Hanasz J, Rusanov A.A, “The fine structure of the AKR Electromagnetic Field as Measured by the Interball-2 Satellite”, Cosmic Research, Vol **40**, No 4, pp404-410, 2002.

Mutel R.L, Gurnett D.A and Huff R.L, “VLBI studies of Auroral Kilometric Radiation and solar type III bursts using the wideband data plasma wave instrument”, Proc Cluster II workshop on Multiscale/Multipoint plasma measurements, London, ESA SP-449, 2000.

Mutel R.L, Gurnett D.A and Christopher I.W, “Spatial and Temporal Properties of AKR Burst Emission Derived from Cluster WBD VLBI studies”, Annales Geophysicae. Vol **22**, pp, 2625-2632. 2004.

Mutel R.L, Menietti J.D, Christopher I.W, Gurnett D.A, Cook J.M, “Striated AKR Emission: A remote Tracer of Ion Solitary Structures”, Journal of Geophysical Research, Vol **111**, A10203, 2006.

Mutel R.L, Christopher I.W, Pickett J.S, “Cluster multi-spacecraft determination of AKR angular beaming”, Geophysical Research Letters, Geophysical Research Letters, Vol **35**, L07104, 2008.

Nusinovich G.S, “Introduction to the Physics of Gyrotrons”, John Hopkins University press, Maryland, 2004.

O’Shea P.G, “Reversible and irreversible emittance growth”, Physical Review, E**57**, No 1, pp1081-1087, 1998.

Omidi N, Wu C.S, Gurnett D.A, “ Generation of Auroral Kilometric and Z mode Radiation by the cyclotron maser mechanism”, Journal of Geophysical Research, Vol **89**, No A2, pp883-895, 1984.

Oya H, “Origin of Jovian dacameter wave emissions-conversion from the electron cyclotron plasma wave to the ordinary mode electromagnetic wave”, Planetary Space Science, Vol **22**, pp687-708, 1974.

Pantell R.H, “Backward wave oscillations in an unloaded waveguide” Proc. IRE, Vol **47**, pp1146, 1959.

Parrot M, Lefeuvre F, Rauch J.L, Santolik O and Mogilevski M.M, “ Propagation characteristics of Auroral Kilometric Radiation observed by the MEMO experiment on INTERBALL 2”, Journal of Geophysical Research, Vol **106**, pp315-325, 2001.

Pazamickas K.A, Green J.L, Gallagher D.L, Boardsen S, Mende S, Frey H, Reinisch B.W, “Correlation between low frequency Auroral Kilometric Radiation (AKR) and auroral structures”, Archive.org/details/NASA/techdoc20050212155.

Perraut S, De Feraudy H, Roux A, Decreau E, Paris J, Matson L, “Density measurements in key regions of the Earth’s magnetosphere cusp and auroral region”, Journal of Geophysical Research, Vol **95**, pp5997-6014, 1990.

Pickett J.S, Chen L.-J, Mutel R.L, Christopher I.W, Santolik O, Lakhina G.S, Singh S.V, Reddy R.V, Gurnett D.A, Tsurutani B.T, Lucek E, Lavraud B, “Furthering our understanding of electrostatic solitary waves through Cluster multispacecraft observations and theory”, Advances in Space Research, Vol **41**, pp1666-1676, 2008.

Pickett J.S, Grison B, Omura Y, Engebretson M.J, Dandouras I, Masson A, Adrian M.L, Santolik O, Decreau P.M.E, Cornilleau-Wehrlin N, Constantinescu D, “Cluster observations of EMIC triggered emission in association with Pc1 waves nears Earth’s plasmapause, Geophysical Research Letters, Vol **37**, L09104, 2010.

Poezd E.D, Fiala V, Triska P, “Coupling between Auroral Kilometric Radiation and auroral radio noise based on wave-particle resonance interaction”, Studia geod, Vol **31**, pp73-84, 1987.

Pozar D.A, “Microwave engineering”, 3rd edition, John Wiley and Sons, Massachusetts, Inc, 2005.

Pottelette R, Treumann R.A, Berthomier M, "Auroral plasma turbulence and the cause of Auroral Kilometric Radiation fine structure", Journal of Geophysical Research, Vol **106**, No 5, pp8465-8476, 2001.

Rhee M.J, "Refined definition of the beam brightness", Phys. Fluids, Vol **4**, (6), P1674, 1992.

Ronald K, "Gyrotron experiments using explosive electron emission cathodes", PhD thesis, University of Strathclyde library, 1996.

Ronald K, Speirs D.C, McConville S.L, Phelps A.D.R, Robertson C.W, Whyte C.G, He W, Gillespie K.M, Cross A.W, Bingham R, "Radio frequency structure and diagnostic measurements for a laboratory simulation of Auroral Kilometric Radiation", Physics of Plasmas, Vol **15**, 056503, 2008**a**.

Ronald K, McConville S.L, Spiers D.C, Phelps A.D.R, Robertson C.W, Whyte C.G, He W, Gillespie K.M, Cross A.W, Bingham R, "Electron beam measurements for a laboratory simulation of Auroral Kilometric Radiation", Plasma Physics and Controlled Fusion, Vol **17**,035011 (8pp), 2008**b**.

Ronald K, Speirs D.C, McConville S.L, Gillespie K.M, Phelps A.D.R, Bingham R, Vorgul I, Cairns R.A, Cross A.W, Robertson C.W, Whyte C.G, Kellett B.J, "Auroral magnetospheric cyclotron emission processes: numerical and experimental simulations", Plasma Physics and Controlled Fusion, Vol **53**, 074015 (11pp), 2011.

Roux A, Hilgers A, De'Feraudy, Le'Queau, Louran P, Perraut S, "Auroral Kilometric Radiation Sources; In Situ and Remote observations from Viking", Geophysical Research Letters, Vol **98**, NoA7, pp11657-11670, 1993.

Saflekos N.A, Burch J.L, Gurnett D.A, Anderson R.R, Sheehan R.E, "Kilometric Radiation power flux dependence on area of discrete aurora", NASA technical report, N89-23040/3, 1989.

Santolik O, Gurnett D.A, "Transverse dimensions of chorus in the source region", Geophysical Research Letters, Vol **30**, No 2, 1031, 2003.

Sato A, Wright D.M, Ebihara Y, Sato M, Mutata Y, Doi H, Saemundsson T, Milan S.E, Lester M, Carlson C.W, " Direct comparison of pulsating aurora observed simultaneously by the FAST satellite and from the ground at Syowa", Geophysical Research Letters, Vol **29**, No 21, 2041, 2002.

Savilov A.V, Bespalov P.A, Ronald K, Phelps A.D.R, "Dynamics of excitation of backward waves in long inhomogeneous systems", Physics of Plasmas, Vol **14**, 113104, 2007.

Schneider J, “Stimulated emission of radiation by relativistic electrons in a magnetic field”, Phys. Rev Lett. Vol **2**, No 2, pp504, 1959.

Schreiber R, Santolik O, Parrot M, Lefeuvre F, Hanasz J, Brittnacher M, “Auroral Kilometric Radiation source characteristics using ray tracing techniques”, Journal of Geophysical Research, Vol **107**, A11, 2002.

Schreiber R, “A simple model of the Auroral Kilometric Radiation visibility”, Journal of Geophysical Research, Vol **110**, A11, 2005.

Shawhan S.D and Gurnett D.A, “Polarization mesuarments of aorural kilometric radiation by dynamics explorer – 1”, Geophysical Review Letters, Vol **9**, No 9, pp913-916.

Shepherd S.G, LaBelle J, Trimpi M.L, “ Further investigation of auroral roar fine structure”, Journal of Geophysical Research, Vol **103**, No A2, pp2219-2229, 1998.

Sigsbee K, Cattell C.A, Lysak R.L, Carlson C.W, Ergun R.E, McFadden J.P, Mozer F, Elphic R.C, Strangeway R.J, Tsuruda K, Yamamoto T, Kokubun S, Fairfield D, Pfaff R, Parks G, Brittnacher M, “FAST – Geotail correlative studies of magnetosphere – ionosphere coupling in the nightside magnetosphere”, Geophysical Research Letters, Vol **25**, pp2077-2080, 1998.

Spark S.N, Cross A.W, Phelps A.D.R, Ronald K, “ Megawatt, 33Hz PRF tunable gyrotron experiments”, International Journal of Infrared and Millimeter Waves, Vol **15**, No 12, 1994.

Speirs D.C, Phelps A.D.R, Konoplev I.V, Cross A.W, He W, “ Stimulation of high power broadband cyclotron autoresonance maser amplifier and electron beam experiments”, Review of Scientific Instruments, Vol **75**, pp826-831, 2004.

Speirs D.C, Vorgul I, Ronald K, Bingham R, Cairns R.A, Phelps A.D.R, Kellett B.J, Cross A.W, Whyte C.G, Robertson C, “A laboratory experiment to investigate Auroral Kilometric Radiation emission mechanisms”, Journal of Plasma Physics, Vol **71**, Part 5, pp665-674, 2005.

Speirs D.C, “Cyclotron maser emission from space and laboratory plasma”, PhD thesis, University of Strathclyde library, 2006.

Speirs D.C, McConville S.L, Gillespie K.M, Ronald K, Phelps A.D.R, Cross A.W, Bingham R, Robertson C.W, Whyte C.G, Vorgul I, Cairns R.A, Kellett B.J, “Numerical simulation of auroral cyclotron maser processes”, Plasma Physics and Controlled Fusion, Vol **50**, 074011 (15pp), 2008.

Speirs D.C, Vorgul I, Ronald K, McConville S.L, Phelps A.D.R, Cross A.W, Bingham R, Robertson C.W, Whyte C.G, He I, Vorgul I, Cairns R.A, , Kellett B.J, “Numerical investigation of auroral cyclotron maser processes”, Physics of Plasmas, Vol **17**, 056501, 2010.

Sprangle P and Drobot A.T, “The linear and self-consistent nonlinear theory of the electron cyclotron maser instability”, IEEE Transactions on Microwave Theory and techniques, Vol **mtt-25**, No 6, 1977.

Strangeway R.J, Kepko L, Elphic R.C, Carlson C.W, Ergun R.E, McFadden J.P, Peria W.J, Delory G.T, Chaston C.C, Temerin M, Cattel C.A, Mobius E, Kistler L.M, Klumpar D.M, Peterson W.K, Shelley E.G, Pfaff R.F. “FAST observations of VLF waves in the auroral zone: Evidence of very low plasma densities”, Geophys Res Letter, Vol **25**,pp2065-2068. 1998.

Stix T.H, “Waves in Plasmas”, Springer, NY, 1992.

Swann W.F, “Application of Liouvilles Theorem to electron orbits in the Earth’s magnetic field”, Physical Review, Vol **44**, pp224-227, 1933.

Tarakanov V, “KARAT manual”, pp1-4.

Tsimring S.E, “Electron Beams and Microwave Electronics”, John Wiley & Sons, New Jersey, 2007.

Twiss R.Q, “Radiation transfer and the possibility of negative absorption in radio astronomy”, Australian J. Phys., Vol **11**(4), pp564, 1958.

Ungstrup E, Bahnsen A, Wong H.K, Andre M, Matson L, “Energy source of generation mechanism for Auroral Kilometric Radiation”, Journal of Geophysical Research, Vol **95**, pp5973-5981, 1990.

Vanderlinde, “Classical Electromagnetic theory”, John Wiley & Sons, Dordrecht, pp240-242, 1993.

Vorgul I, Cairns R.A, Bingham R, “Analysis of a cyclotron maser instability in cylindrical geometry”, Physics of Plasmas, Vol **12**, 122903, 2005.

Vorgul I, Kellett B.J, Cairns R.A, Bingham R, Ronald K, Speirs D.C, McConville S.L, Gillespie K.M, Phelps A.D.R, “Cyclotron maser emission: Stars, Planets and laboratory”, Physics of Plasmas, Vol **18**, 056501, 2011.

Von Engel A, “Ionized Gases”, American Institute of Physics, New York, 1997.

Worster J, “The brightness of electron beams”, Brit. J.Appl. Phys, Vol **2**, Issue 3, pp457-462, 1968.

Wu C.S and Lee L.C, “A theory of the terrestrial kilometric radiation”, The Astrophysical Journal, Vol **230**, pp621-626, 1979.

Wu C.S and Lee L.C., “Auroral radio emissions at the outer planets; observations and theories”, Journal of Geophysical Research, Vol **103**, pp20159-20194, 1998.

Yi- Jiun S, Ma L, Ergun R.E, Pritchett P.L, Carlson C.W, “Short-burst auroral radiations in Alfvenic acceleration regions: FAST observations”, Journal of Geophyiscal Research, Vol **113**, A08214, 2008.

Yoon P.H and Weatherwax A.T, “A theory for AKR fine frequency structure”, Geophysical Research Letters, Vol **25**, pp4461-4464, 1998.

Zanetti L, Potemra T, Erlandson R, Bythrow P, Anderson B, Lui A, Ohtani S, Fountain G, Henshow R, Ballard B, Lohr D, Hayes J, Holland D, Acuna M, Fairfield D, Slavin J, Baumjohann W, Engbretson M, Glassmeier K, Gustafsson G, Iijima T, Luhr H, Primdahl F, “ Magnetic field experiment on the Freja satellite”, Space Science Reviews, Vol **70**, pp465-482, 1994.

Zieball L.F and Yoon P.H, “Quasilinear analysis of loss-cone driven weakly relativistic electron cyclotron maser instability”, Physics of Plasmas, Vol **2** (4), 1285, 1995.

APPENDIX 1

Additional material

Terrestrial auroral processes

The aurora phenomenon

The phenomenon most commonly associated with the terrestrial auroral regions are the optical ionospheric emissions known as the “Aurora Borealis” in the northern hemisphere (or the Northern lights) and the southern counterpart named “Aurora Australis”. Aurora are natural phenomena that occur most often in the polar regions of the Earth. They present a complex behaviour that arises from interactions between plasma and the Earths electromagnetic fields. It takes the form of colourful irregular lights in the night sky with no two Aurora ever being the same. One of the terms to describe the Aurora is the “Arc” (which describes Aurora which form a simple curving arc of light across the sky). Another term is a band which refers to Aurora that have an irregular shape with kinks or folds.

The gases in the aurora glow with characteristic colours, green is the most common colour and is caused by atomic oxygen at altitudes of between 100km and 200km whereas purple colours are due to molecular nitrogen, Figure A.1a. Figure A.1b illustrates each of these colours. The striking image in Figure A.1c of the aurora was taken during a geomagnetic storm from the International Space Station (ISS). Aurora occur most often in the region known as the “auroral oval” these rings are roughly 2400km around the Earth’s North and South magnetic Poles. Figure 1d was also taken from the ISS and clearly illustrates the green aurora.

These ovals, Figure A.2, are constantly in motion and changing in brightness, moving by either expanding towards the equator or contracting towards the pole, due to severe magnetic storms. The Aurora is also a product of the accelerated electrons that form AKR. The electrons in the loss cone will penetrate the Earth’s ionosphere exciting the atoms and molecules which decay resulting in visible aurora.

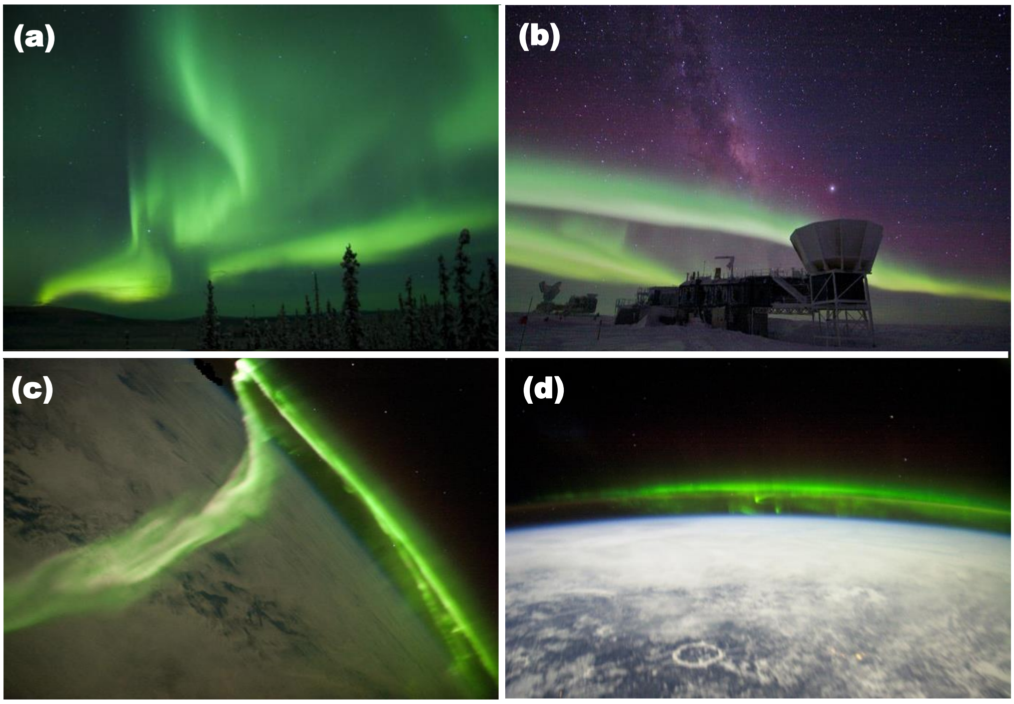

Figure A.1: (a) Illustration of aurora in the night sky, green is the most common colour in the aurora and is caused by atomic oxygen. (b) Illustration of an auroral arc, purple colours are due to molecular nitrogen. (c) Image of the aurora taken during a geomagnetic storm from the International Space Station (ISS). (d) Also taken from the ISS and showing the green aurora [NASA space agency].

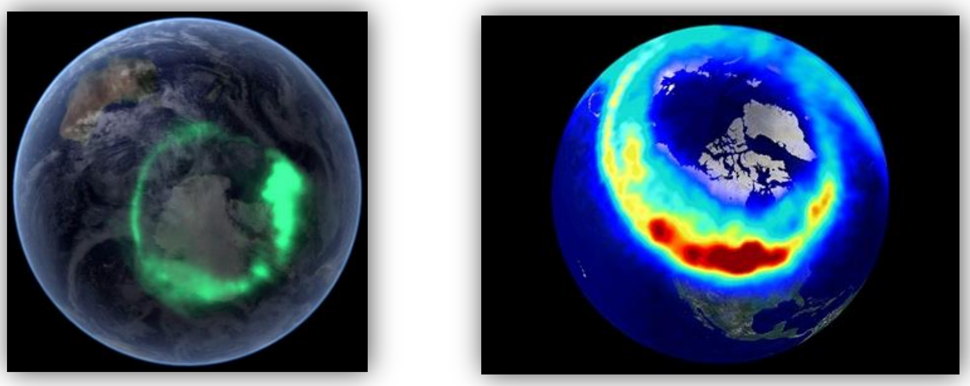

(a) (b)

Figure A.2: Illustration of auroral arcs (a) Aurora Australis captured by NASA’s IMAGE satellite. (b) Image taken from Cluster satellite [NASA space agency].

Shown here is the Aurora Australis, Figure A.3, taken by astronauts on board the International Space Station. The images were acquired on September 11, 2011 as the ISS orbit passed over eastern Australia, reached the "bottom" of the orbit, then changed direction to passing just east of New Zealand during the night hours, describing a wide "U" over the region.

The aurora displays a sinuous green ribbon shape with occasional hints of red near the upper extent. The unique viewing perspective from the ISS cupola allows for a sense of the 3-dimensional nature of the phenomena as it varies in apparent length, width, and thickness as the ISS orbits above it.

Understanding natural phenomenon such as the aurora and AKR is of importance as this area of research can contribute to the scientific understanding of complex natural processes [Humphries 1998].

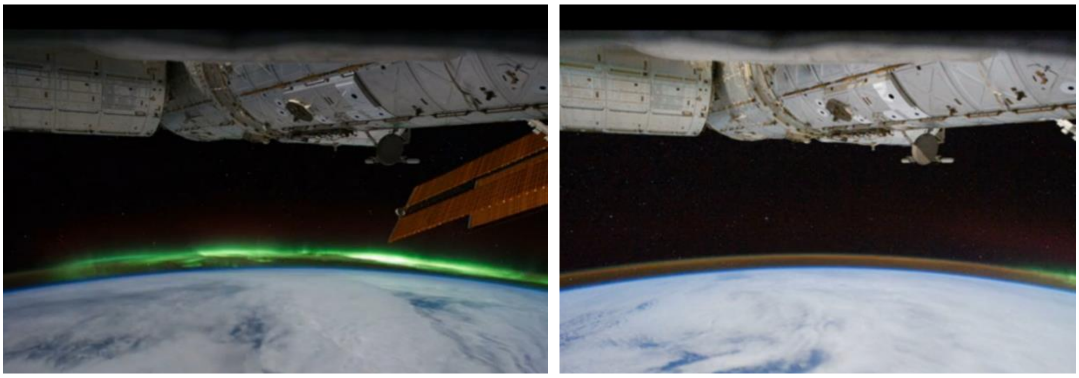

Figure A.3: Aurora Australis, South of Australia taken from the ISS [NASA space agency].

Experimental technical details

Safety interlocks

When using high voltage power supplies and generating microwaves and electron beams, particular caution must be taken for safety when experiments are being conducted. The laboratory utilises a safety interlock system to ensure a controlled and protected working environment for those concerned. The interlocks are based on pneumatic – electrical switchgear.

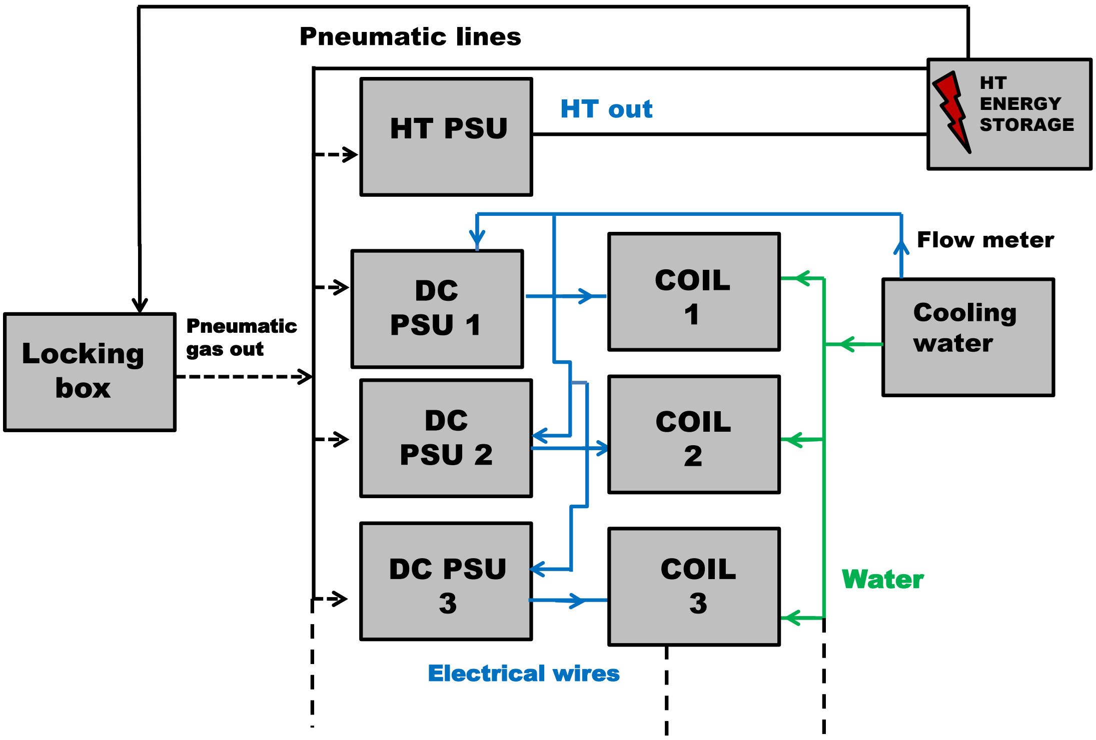

Figure A.4: The safety interlock system. Each item must be "OK" before the main interlock will allow power on the high voltage power supplies.

The high current and high voltage power supplies are centrally interlocked. In particular the high current power supplies are interlocked through water temperature and flow rate monitors, Figure A.4. In this instance if the solenoid water cooling flow falls to an unsuitable level for sufficient cooling, or if the temperature changes above a certain unsuitable level then the circuit monitor will drop the enable signal to the interlock which will in turn switch off the supplies. HT PSU's are interlocked with the door on the X-ray enclosure and the capacitor dump switches with pneumatic logic. Only when the door is shut can the system pressurise, lifting the dump switches and enabling the HT supplies.

For safety of personnel there is an EM dump button in the bay and on the interlock control box. This button can be depressed if one should ever need to immediately dump the power to the experiment or if someone were somehow accidently shut within the bay whilst the experiment is arming.

Vacuum Systems

A vacuum is created in the chamber of beam-wave instability experiments to allow the interaction between the charged particles and the electromagnetic field without any unnecessary collisions with the air molecules.

Vacuum systems can be divided into subsections for different ranges of pressures as vacuum technology extends over more than fifteen orders of magnitude in pressure, these divisions fall crudely into;

Vacuum type	***Pressure (mbar)***
Low vacuum	Atmospheric pressure to 1mbar
Medium vacuum	1mbar to 10^{-3}mbar
High vacuum	10^{-3}mbar to 10^{-8}mbar
Ultra high vacuum	10^{-8}mbar to 10^{-12}mbar
Extreme vacuum	Less than 10^{-12}mbar

Table A.1: Various vacuum conditions with indicative pressure ranges.

Evacuation of a chamber is not as simple as reducing the pressure in the chamber by removing air, there are other processes which need to be taken into account, which release gas into the vacuum system. These include leaks which can arise from O-rings that are damaged or badly designed or scratched sealing surfaces. If a component of the vacuum chamber is linked to the vessel by a small complicated path then it is possible for gas to leak very slowly from trapped volumes. It is therefore desirable to avoid threaded fittings inside vacuum vessels. A vacuum can be affected by gas trapped on the surface of the vessel and some processes that occur in the vacuum can produce gas for example when components are heated to eliminate absorbed gas from materials. Poor vacuums (or at any rate slow pump down times) can also result from poorly dried components which have been cleaned with water, so it is preferred to clean vacuum components with alcohol or acetone if possible.

Figure A.5, illustrates a volume of gas moving from one end of a pipe to the other along a pressure gradient i.e. a region of high pressure at one end and a region of low pressure at the other. If $p_1 > p_2$, then the flow shall be from region 1 to region 2. If the temperature remains unchanged then the number of gas molecules must fill a larger volume when the pressure is p_2 compared to that at p_1 where they started.

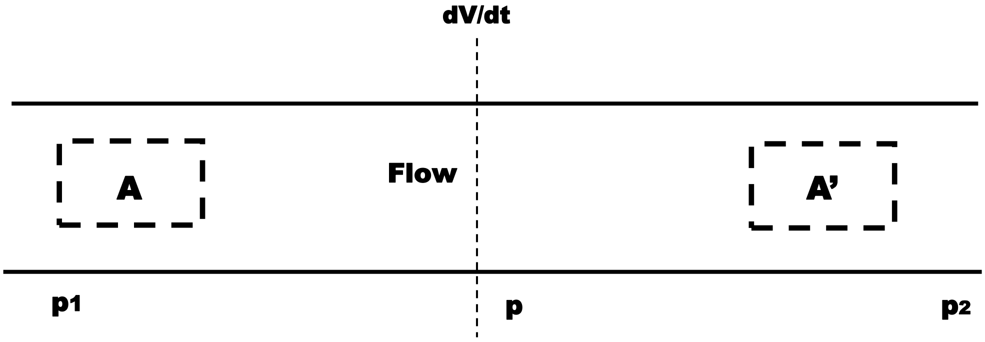

Figure A.5: Pipe having a pressure differential between the ends such that $p_1 > p_2$.

The pressure will be the same at any radial position across the pipe at any axial position; it is therefore possible to define the throughput of the system, from which the mass and the particle flow rate may be calculated. Calculating throughput;

$$Q = p.(dV/dt)$$

where, dV/dt - volumetric flow i.e. the speed (particularly to the inlet of a pump), p-chamber pressure

Rotary vane pump

The displacement pump used in the AKR experiment is one of the most widely used and well established primary pumps, the rotary pump. The mechanics of the rotary pump can be seen in Figure A.6, this figure illustrates a two stage pump where the exhaust from the first stage is internally connected to the inlet of the second stage, the basic mechanics for a single stage pump are the same although only half of the structure described here is required.

In the slots of the rotors, eccentrically located in the cavities of the structure, there are two sliding vanes, sealed by a fluid film, which are continuously in contact with the walls of the stator. The air expands through the inlet as the “leading” vane expands the volume under the inlet port. When the “trailing” vane isolates the lower chamber it then compresses the gas towards the exhaust port, into the transfer line to the second stage of the pump. The “trailing” vane also acts as the “leading” vane for a new “parcel” of gas and the process repeats. The second stage further compresses the gas and ultimately expels it through the spring loaded exhaust valve.

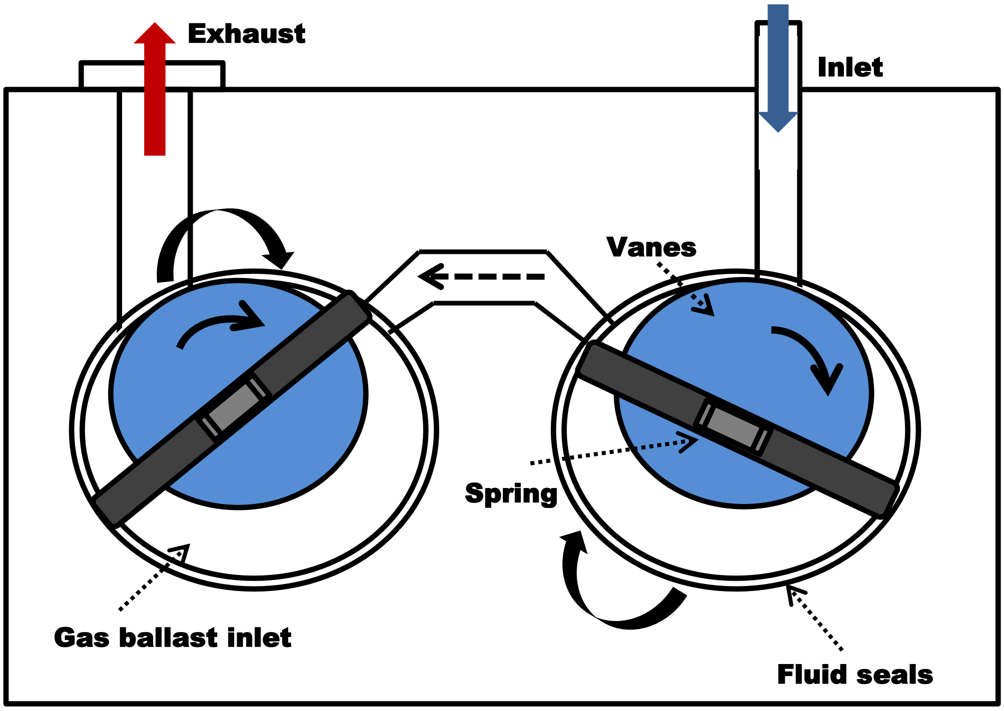

Figure A.6: Systematic diagram of rotary vane pump.

Like the vanes, the rotor and the stator are also sealed by fluid film. Rotary pump fluids need to be of a high quality with a low vapour pressure and also need to have good lubricating properties. In a rotary vane or piston pump the fluid provides a vacuum seal between the moving surfaces and lubricates and cools the bearings and sliding surfaces. The rotary pump used in the experiment is a two stage pump.

Diffusion pump

A diffusion pump works very differently from a mechanical pump, as in a mechanical pump air is removed from a chamber by a mechanical expansion and compression cycle using pistons, fins and lobes. A diffusion pump uses the vapour of a boiling fluid to form a jet and induce air molecules to drift in the direction of the jet. The fluid jet is condensed on a cooled surface and returned to the boiler reservoir. The heater sits at the bottom below the oil and as the oil becomes hot enough to vaporize, it rises up the centre of the pump and through the exit nozzles which are set at a downward angle.

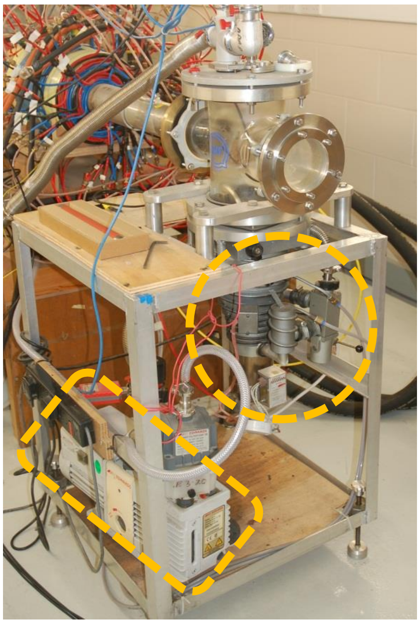

Figure A.7: Photograph of diffusion pump attached to the experiment, the rotary vane pump can be seen on the bottom left of the pump stand.

Due to the angling of the nozzles and that the arrangement is in a ring, a curtain of vapour will form and extends from the nozzles to the pump wall, air molecules that wander into the inlet collide with the curtain and collisional momentum transfer imparts a net downward momentum to the gas particles inducing an increasing pressure gradient down through the pump.

Clearly the jet velocity must be greater than the thermal velocity of the gas particles. When the oil vapour hits the cooled walls of the pump it cools and runs down the sides of the pump. If a gas molecule tries to travel upwards, it is caught by the vapour curtain and is forced downwards again.

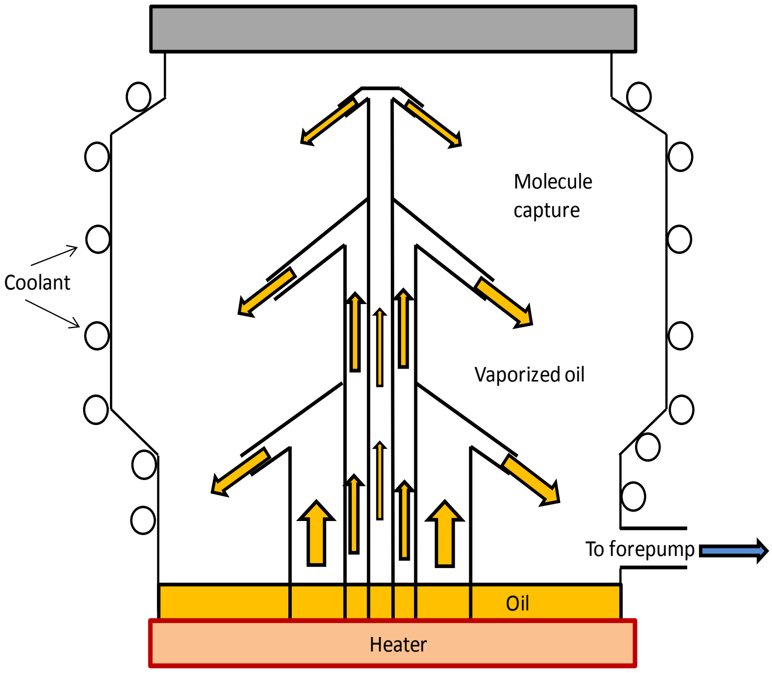

Figure A.8: Systematic diagram of diffusion pump.

The continuous forcing of the air molecules downwards will create an area at the bottom of the pump that is higher in pressure than the top of the pump, i.e. the pressure below each oil curtain is higher than at the top of each oil curtain when the pump is in operation. Typically silicone oil is used as the pump fluid because of its high vapour point and stability. Silicone oil will perform over long periods of time with little to no degradation.

Vacuum gauge diagnostics

The basic working principle of an ionization gauge, as the name would indicate, is the collection of ions formed from the neutral gas molecules. The rate of ionisation is measured by the current. Ion gauges date to 1909 when it was noticed that a triode valve could be used as a vacuum gauge. Thermionic ion gauges work by relying on the fact that an energetic beam of electrons will ionise the molecules in a low pressure gas. The source of electrons is a hot filament within the gauge, these electrons are accelerated towards a mesh anode beyond which is situated a high voltage cathode. The electrons oscillate around the anode driven by the repulsion from the two cathodic elements, some of these electrons will be collected by the anode as they strike it every now and then. As ionization of a gas particle occurs the ion is drawn towards the collector where the ion current is measured.

The current of the ions that arrive on the collector, I_i, is related to the current of the electrons leaving the cathodic electrode, I_e, by the probability of an electron striking and ionising a particle of gas molecule,

$$I_i = n\rho\sigma I_e$$

where, ρ *- path length of the electron from its emission until it is collected at the anode,*

n *- molecular density,* σ *- ionisation cross section*

A Bayard-Alpert gauge is used in ultra high vacuum conditions (UHV) and the only difference between this and a conventional gauge is that the Bayard-Alpert gauge collector surface area is much smaller. Conventional gauges can be used in systems above 10^{-7}mBar whereas Bayard-Alpert gauges can be used at around 10^{-10}mBar. Ion gauges are reliable but in order to take an accurate measurement the gauge must be first degassed.

Backward wave coupling

Kinetic theory of backward-wave coupling

Colleagues at the University of St Andrews have developed a kinetic description of the instability that predicts an enhanced growth rate for small negative axial wave numbers, in agreement with the results of laboratory experiments and numerical simulations conducted at the University of Strathclyde. This predication also represents a suitable precursor for a model of upward refraction and field-aligned escape of terrestrial auroral kilometric radiation as proposed by Mutel and Menietti based on Cluster satellite missions.

In the limit where the Larmor radius is small compared to the wavelength, the imaginary parts of all components of the dielectric tensor for near perpendicular propagation go approximately as;

$$\int dv_{//} v_{\perp} \frac{\partial f}{\partial v_{\perp}} \qquad (1)$$

with $v_{\perp}$ *determined as a function of* $v_{//}$ *by the resonance condition*

$$\omega - k_{//} v_{//} = \frac{\omega_c}{\gamma} \qquad (2)$$

This assumes that the relativistic factor can be put equal to one everywhere except in the resonance condition. If we take a typical horseshoe distribution, produced from an initial Maxwellian with drift speed 0.25c and thermal velocity 0.015*c* and subject to a magnetic compression by a factor 15, then a contour plot of $\partial f / \partial v_{\perp}$ (in the positive quadrants) is shown in Figure 4.9. Velocities in what follows will be in units of *c* and frequencies in units of ω_c.

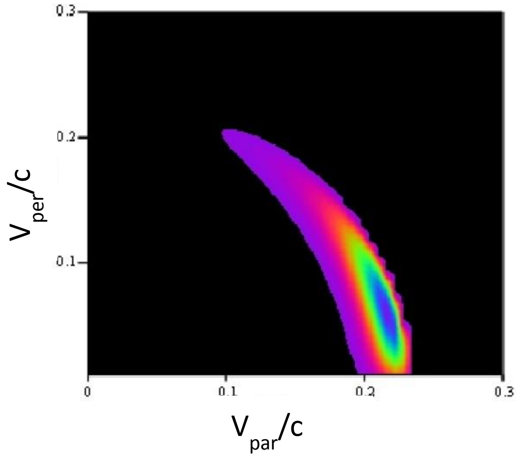

Figure A.9: Contour plot of positive gradient regions of horseshoe distribution, $v_{//}$ = 0.25c, v_{th} = 0.015c, B_z/B_{z0}=15.

An alternative representation as a surface plot is shown in Figure A.10.

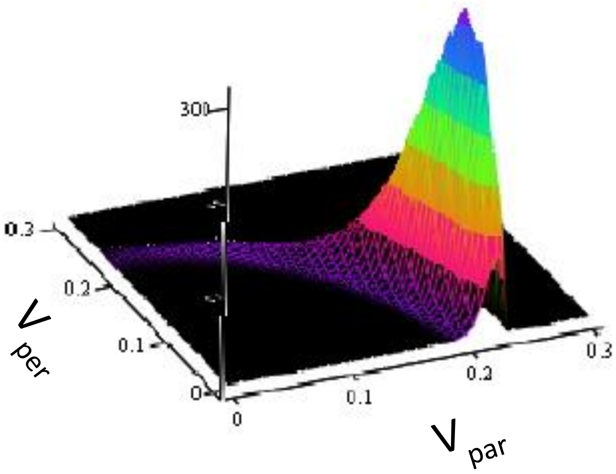

Figure A.10: Contour plot of positive gradient regions of horseshoe distribution, $v_{//}$ = 0.25c, v_{th} = 0.015c, B_z/B_{z0}=15.

This shows that maximum growth can be expected when the resonance curve passes through a fairly restricted area in velocity space. The shape of the resonance curve is indicated in the following diagram, plotted for ω = 0.97ω_c and three different values of $n_{//} = k_{//}c/\omega$.

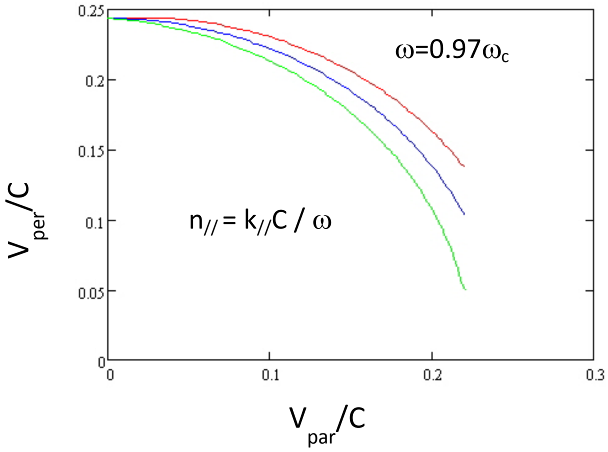

Figure A.11: Resonance curves for $n_{||}$ = 0.02 (red), 0 (blue) and -0.02 (green).

The point to note is that for positive $n_{//}$ the curve lies above the $n_{//} = 0$ curve, while for negative $n_{//}$ it lies below. The other relevant thing to notice is that increasing the frequency moves the whole curve downwards, starting at a lower point at $v_{//} = 0$. Combining these two pieces of information it can be seen that in order for the resonance curve to pass through the region of maximum $\partial f / \partial v_{\perp}$ it must have a higher frequency when $n_{//}$ is positive than when $n_{//}$ is zero, so that the lower starting point at $v = 0$ compensates for the smaller downwards curvature.

For negative $n_{//}$ maximum growth is to be expected at a lower frequency. This is illustrated by the following series of diagrams, in which the perpendicular gradient along the resonance curve is shown as a function of $v_{//}$ and of frequency. This shows the maximum value of the gradient occurring at higher frequencies when $n_{//}$ is positive.

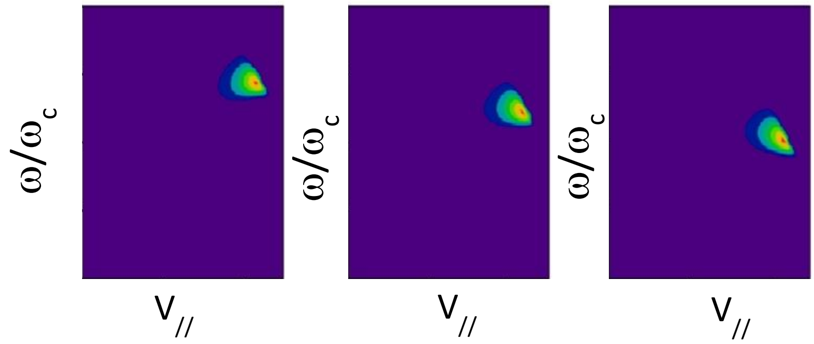

Figure A.12: Contour plots of perpendicular velocity gradient $\partial f / \partial v_{\perp}$ along resonance curves as a function of $v_{||}$ and frequency. From left to right the values of $n_{||}$ are 0.02, 0 and -0.02.

When the frequency is chosen so that the imaginary part of the dielectric tensor, estimated by (1) is a maximum for each value of $n_{//}$ then it does not vary greatly for small values of $n_{//}$, positive or negative. However, it needs to be noted that the growth rate is approximately

$$\omega_{im} = \frac{\mathrm{Im}(D)}{\frac{\partial}{\partial\omega}(\mathrm{Re}(D))} \tag{3}$$

where, $D = 0$ is the dispersion relation.

As an approximation to D we take the cold plasma result at perpendicular incidence, a reasonable approximation if $n_{//}$ is small and also the Larmor radius is small compared to the perpendicular wavelength. The value of $\partial D/\partial\omega$ as a function of frequency is shown in Figure A.12, for $\omega_p = 0{:}1\omega_c$.

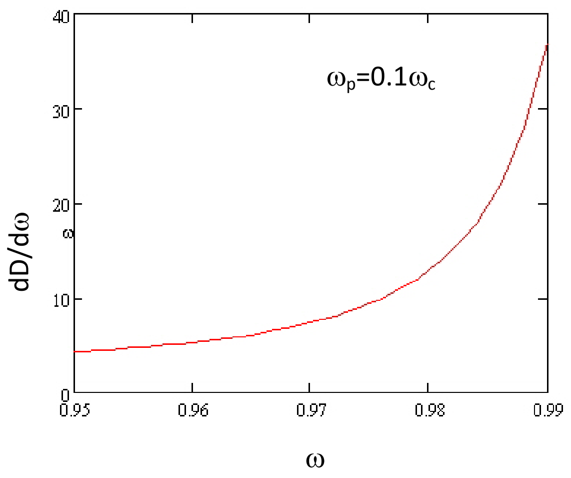

Figure A.13: Gradient with respect to frequency of dispersion function.

The crucial point to notice is that because of the proximity to the upper hybrid resonance, where D has a singularity, the gradient is strongly increasing with frequency. This means that the growth rate for positive $n_{//}$ components, for which (1) is greater for higher frequencies is supressed, while that for lower $n_{//}$ components is enhanced. This is illustrated in Figure A.14, which plots (for different values of $n_{//}$);

$$\frac{\int dv_{//} v_{\perp} \frac{\partial f}{\partial v_{\perp}}}{\frac{\partial}{\partial \omega}(\mathrm{Re}(D))} \tag{4}$$

Note that this is not the actual growth rate, since the numerator in this expression is not the imaginary part of the dispersion relation, just something proportional to it. This plot simply illustrates the relative growth rates and the units on the vertical axis are arbitrary.

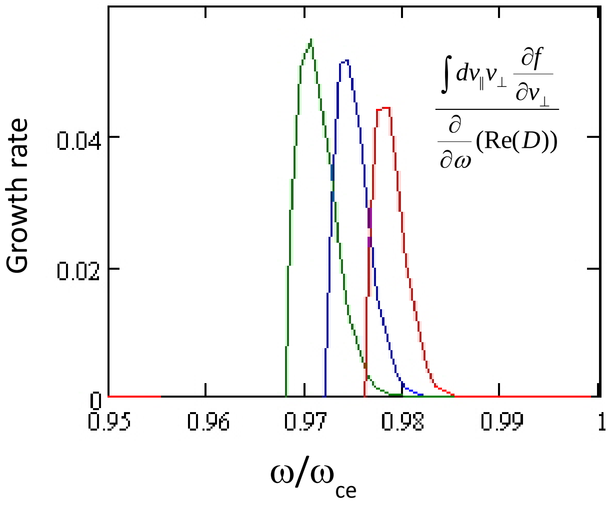

Figure A.14: Growth rate proportionality for $n_{\|} = 0.02$ (red), 0 (blue) and -0.02 (green).

If we go to higher values of $|n_{//}|$ the value of (1) tends to decrease since the resonance curve starts to pass through the region of optimum perpendicular gradient, illustrated in Figure A.9, at a more oblique angle. This is illustrated in Figure A.15 where now we have $n_{//} = \pm 0.1$.

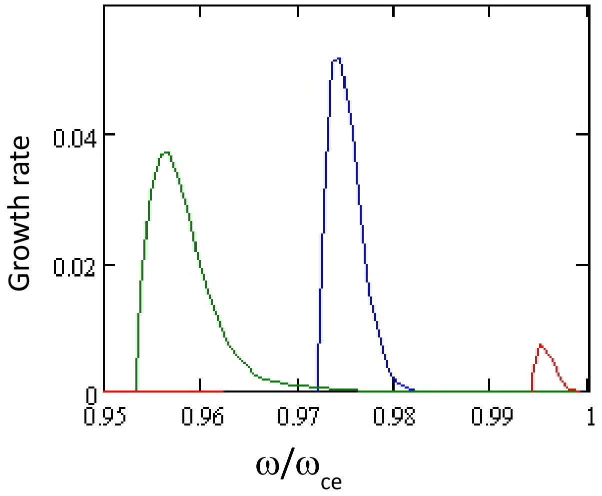

Figure A.15: Growth rate proportionality for $n_{||} = 0.1$ (red), 0 (blue) and -0.1 (green).

The conclusion we can reach is that the peak growth rate is for radiation at a few degrees from perpendicular in the backwards direction. The effect of changing other parameters can briefly be described as follows.

- The results are rather insensitive to the value of ω_p in the range $\omega_p < \omega_{ce}$.
- Anything which spreads the beam out, either an increase in the initial thermal spread or an increase in the magnetic compression, tends to produce a less marked increase in growth rate for negative $n_{//}$ over a smaller range of angles.

APPENDIX 2

Maple script

This is the Maple script used to calculate the magnetic field of the experiment in KARAT simulations. It calculates and plots the resultant axial magnetic field due to a set of finite coils. The coils are specified in terms of their geometries, currents and relative axial positions.

The script is very useful for the purpose of tuning for a specific magnetic field profile in experiments. It can also generate a delimited data file of the axial magnetic field profile for importation into PIC code modelling packages such as KARAT or Magic.

First the script parameters are cleared / initialised :-

```
restart;
```

The properties and positions of each individual solenoid are now consecutively specified. A unique numerical index is used to identify parameters associated with a specific solenoid. Solenoid 1 is set.

Solenoid 1

```
A1:=50;N1:=143;M1:=N1;L1:=0.5;dz1:=0.7;LA1:=4;Ri1:=0.105;Ro1:=(Ri1+LA1/M1);R1:=(Ri1+Ro1)/2;
```

Solenoid 2

```
A2:=40;N2:=143;M2:=N2;L2:=0.45;dz2:=dz1-L1/2-L2/2;LA2:=2;Ri2:=0.105;Ro2:=(Ri2+LA2/M2);R2:=(Ri2+Ro2)/2;
```

Solenoid 3

```
A3:=270;N3:=143;M3:=N3;L3:=0.5;dz3:=dz1+L1/2+L3/2;LA3:=10;Ri3:=0.05;Ro3:=(Ri3+LA3/M3);R3:=(Ri3+Ro3)/2;
```

Solenoids 4 and 5, shimming solenoids to extend the flat central field portion of the main solenoid 3.

```
A4:=230;N4:=143;M4:=N4;L4:=0.11;dz4:=dz1+L1/2+L4/2;LA4:=2;Ri4:=Ro3;Ro4:=(Ri4+LA4/M4);R4:=(Ri4+Ro4)/2;A5:=270;N5:=N4;M5:=N5;L5:=L4;dz5:=dz1+L1/2+L3-L5/2;LA5:=LA4;Ri5:=Ro3;Ro5:=(Ri5+LA5/M5);R5:=(Ri5+Ro5)/2;
```

```
A6:=0;N6:=143;M6:=N6;L6:=0.2525;dz6:=dz3;LA6:=4;Ri6:=0.124;Ro6:=(Ri6+LA6/M6);R6:=(Ri6+Ro6)/2;
b:=(mu*A*N/2)*(((L/2-(l-dz))/sqrt(R^2+(L/2-(l-dz))^2))-((-L/2-(l-dz))/sqrt(R^2+(-L/2-(l-dz))^2)));
```

```
B:=M*integrate(b,R=Ri..Ro);
mu:=Pi*4E-7;
B1:=eval(B,[A=A1,N=N1,M=M1,L=L1,dz=dz1,LA=LA1,Ri=Ri1,Ro=Ro1,R=R1]
);
lim1:=-L1/2+dz1;lim2:=L1/2+dz1;
plot(B1,l=lim1..lim2);

B2:=eval(B,[A=A2,N=N2,M=M2,L=L2,dz=dz2,LA=LA2,Ri=Ri2,Ro=Ro2,R=R2]
);


lim3:=-L2/2+dz2;lim4:=L2/2+dz2;
plot(B2,l=lim3..lim4);

B3:=eval(B,[A=A3,N=N3,M=M3,L=L3,dz=dz3,LA=LA3,Ri=Ri3,Ro=Ro3,R=R3]
);

B4:=eval(B,[A=A4,N=N4,M=M4,L=L4,dz=dz4,LA=LA4,Ri=Ri4,Ro=Ro4,R=R4]
);

B5:=eval(B,[A=A5,N=N5,M=M5,L=L5,dz=dz5,LA=LA5,Ri=Ri5,Ro=Ro5,R=R5]
);

B6:=eval(B,[A=A6,N=N6,M=M6,L=L6,dz=dz6,LA=LA6,Ri=Ri6,Ro=Ro6,R=R6]
);

lim5:=-L3/2+dz3;lim6:=L3/2+dz3;
plot(B6,l=lim5..lim6);
lim7:=-L3/2+dz3;lim8:=L3/2+dz3;
plot(B3+B4+B5+B6,l=lim7..lim8);

Btot:=B1+B2+B3+B4+B5+B6;
plot(Btot,l=lim3..lim8);
```

Work out limiting Larmor step and radius as a function of z from Btot and the electron energy (V), assume alpha is zero for Larmor step and infinite for Larmor radius

```
ce:=1.6E-19;me:=9.11E-
31;cl:=3E8;V:=100000;gmma:=1+ce*V/(me*cl^2);ve:=cl*sqrt((1-
1/gmma^2));freq:=ce*Btot/(2*3.1416*gmma*me);Lz:=ve/freq;Lr:=ve/(2*3.1416
*freq);plot([Lz,Lr],l=lim3..lim8,
color=[red,green]);plot((diff(Btot,l))*(Lz/Btot),l=lim3..lim8);
```

Write out the data for Bz on axis to a file called Bz for KARAT and or Magic, file format is [axial location/cm,field/G]

```
stepno:=1;steps:=88;minz:=0;maxz:=2.8;stepsize:=(maxz-minz)/steps;
fopen(Bz,WRITE,TEXT);printlevel:=0;
for step from minz by stepsize to maxz do
fprintf(Bz,"%d\t%f\t%f\n",stepno,evalf(step*100)+0.5,eval(10000*Btot,l=step))
;
stepno:=stepno+1;
end do;
fprintf(Bz,"%d\t%d\t%f\n",stepno,9999,0);fclose(Bz);printlevel:=1;
```

Solenoid1

```
totallength1:=0;
for counter1 from 1 by 1 to LA1 do
print (layer_sol1,counter1);
wirelength1:=L1*N1*(2*Pi*(Ri1+((counter1-1)*(1/M1))+(1/(2*M1))));
numwires1:=wirelength1/20;
print (number_of_wires, evalf(numwires1));
totallength1:=totallength1+wirelength1;
end do;
```

Solenoid2

```
totallength2:=0;
for counter2 from 1 by 1 to LA2 do
print (layer_sol2,counter2);
wirelength2:=L2*N2*(2*Pi*(Ri2+((counter2-1)*(1/M2))+(1/(2*M2))));
numwires2:=wirelength2/20;
print (number_of_wires, evalf(numwires2));
totallength2:=totallength2+wirelength2;
end do;
```

Solenoid3

```
totallength3:=0;
for counter3 from 1 by 1 to LA3 do
print (layer_sol3,counter3);
wirelength3:=L3*N3*(2*Pi*(Ri3+((counter3-1)*(1/M3))+(1/(2*M3))));
numwires3:=wirelength3/20;
print (number_of_wires, evalf(numwires3));
totallength3:=totallength3+wirelength3;
end do;
```

Solenoid 4

```
totallength4:=0;
for counter4 from 1 by 1 to LA4 do
print (layer_sol4,counter4);
```

```
wirelength4:=L4*N4*(2*Pi*(Ri4+((counter4-1)*(1/M4))+(1/(2*M4))));
numwires4:=wirelength4/20;
print (number_of_wires, evalf(numwires4));
totallength4:=totallength4+wirelength4;
end do;
```

Solenoid 5

```
totallength5:=0;
for counter5 from 1 by 1 to LA5 do
print (layer_sol5,counter5);
wirelength5:=L5*N5*(2*Pi*(Ri5+((counter5-1)*(1/M5))+(1/(2*M5))));
numwires5:=wirelength5/20;
print (number_of_wires, evalf(numwires5));
totallength5:=totallength5+wirelength5;
end do;
```

Solenoid 6

```
totallength6:=0;
for counter6 from 1 by 1 to LA6 do
print (layer_sol6,counter6);
wirelength6:=L6*N6*(2*Pi*(Ri6+((counter6-1)*(1/M6))+(1/(2*M6))));
numwires6:=wirelength6/20;
print (number_of_wires, evalf(numwires6));
totallength6:=totallength6+wirelength6;
end do;
```

Net small-bore conductor length required

```
multisolenoid_conductor_length:=totallength1+totallength2+totallength3+totallength4+totallength5+totallength6;
```

Power dissipation

Common Parameters

```
Rwi:=0.00125;Rwo:=0.0026;
```

Solenoid1

```
totalresistanceA1:=evalf(totallength1*0.0313/28.6);totalresistanceA1HOT:=evalf(totallength1*0.0363/28.6);totalresistanceB1:=(1.724E-8)*totallength1/(Pi*(Rwo^2-Rwi^2));totalresistanceB1HOT:=(1.16*1.724E-8)*totallength1/(Pi*(Rwo^2-Rwi^2));drivevoltageA1:=evalf(totalresistanceA1*A1);drivevoltageA1HOT:=evalf(totalresistanceA1HOT*A1);drivevoltageB1:=evalf(totalresistanceB1*A1);drivevoltageB1HOT:=evalf(totalresistanceB1HOT*A1);totalpowerA1:=drivevoltag
```

```
eA1*A1;totalpowerA1HOT:=drivevoltageA1HOT*A1;totalpowerB1:=drivevoltageB1*A1;totalpowerB1HOT:=drivevoltageB1HOT*A1;Vol_sol1:=totallength1*Pi*(Rwo^2-Rwi^2);totalweight_sol1:=evalf(8.89E3*evalf(Vol_sol1));
```

Solenoid2

```
totalresistanceA2:=evalf(totallength2*0.0313/28.6);totalresistanceA2HOT:=evalf(totallength2*0.0363/28.6);totalresistanceB2:=(1.724E-8)*totallength2/(Pi*(Rwo^2-Rwi^2));totalresistanceB2HOT:=(1.16*1.724E-8)*totallength2/(Pi*(Rwo^2-Rwi^2));drivevoltageA2:=evalf(totalresistanceA2*A2);drivevoltageA2HOT:=evalf(totalresistanceA2HOT*A2);drivevoltageB2:=evalf(totalresistanceB2*A2);drivevoltageB2HOT:=evalf(totalresistanceB2HOT*A2);totalpowerA2:=drivevoltageA2*A2;totalpowerA2HOT:=drivevoltageA2HOT*A2;totalpowerB2:=drivevoltageB2*A2;totalpowerB2HOT:=drivevoltageB2HOT*A2;Vol_sol2:=totallength2*Pi*(Rwo^2-Rwi^2);totalweight_sol2:=evalf(8.89E3*evalf(Vol_sol2));
```

Solenoid3

```
totalresistanceA3:=evalf(totallength3*0.0313/28.6);totalresistanceA3HOT:=evalf(totallength3*0.0363/28.6);totalresistanceB3:=(1.724E-8)*totallength3/(Pi*(Rwo^2-Rwi^2));totalresistanceB3HOT:=(1.16*1.724E-8)*totallength3/(Pi*(Rwo^2-Rwi^2));drivevoltageA3:=evalf(totalresistanceA3*A3);drivevoltageA3HOT:=evalf(totalresistanceA3HOT*A3);drivevoltageB3:=evalf(totalresistanceB3*A3);drivevoltageB3HOT:=evalf(totalresistanceB3HOT*A3);totalpowerA3:=drivevoltageA3*A3;totalpowerA3HOT:=drivevoltageA3HOT*A3;totalpowerB3:=drivevoltageB3*A3;totalpowerB3HOT:=drivevoltageB3HOT*A3;Vol_sol3:=totallength3*Pi*(Rwo^2-Rwi^2);totalweight_sol3:=evalf(8.89E3*evalf(Vol_sol3));
```

Solenoid 4

```
totalresistanceA4:=evalf(totallength4*0.0313/28.6);totalresistanceA4HOT:=evalf(totallength4*0.0363/28.6);totalresistanceB4:=(1.724E-8)*totallength4/(Pi*(Rwo^2-Rwi^2));totalresistanceB4HOT:=(1.16*1.724E-8)*totallength4/(Pi*(Rwo^2-Rwi^2));drivevoltageA4:=evalf(totalresistanceA4*A4);drivevoltageA4HOT:=evalf(totalresistanceA4HOT*A4);drivevoltageB4:=evalf(totalresistanceB4*A4);drivevoltageB4HOT:=evalf(totalresistanceB4HOT*A4);totalpowerA4:=drivevoltageA4*A4;totalpowerA4HOT:=drivevoltageA4HOT*A4;totalpowerB4:=drivevoltageB4*A4;totalpowerB4HOT:=drivevoltageB4HOT*A4;Vol_sol4:=totallength4*Pi*(Rwo^2-Rwi^2);totalweight_sol4:=evalf(8.89E3*evalf(Vol_sol4));
```

Solenoid 5

```
totalresistanceA5:=evalf(totallength5*0.0313/28.6);totalresistanceA5HOT:=evalf(totallength5*0.0363/28.6);totalresistanceB5:=(1.724E-8)*totallength5/(Pi*(Rwo^2-Rwi^2));totalresistanceB5HOT:=(1.16*1.724E-8)*totallength5/(Pi*(Rwo^2-Rwi^2));drivevoltageA5:=evalf(totalresistanceA5*A5);drivevoltageA5HOT:=ev
```

```
alf(totalresistanceA5HOT*A5);drivevoltageB5:=evalf(totalresistanceB5*A5);drivevoltageB5HOT:=evalf(totalresistanceB5HOT*A5);totalpowerA5:=drivevoltageA5*A5;totalpowerA5HOT:=drivevoltageA5HOT*A5;totalpowerB5:=drivevoltageB5*A5;totalpowerB5HOT:=drivevoltageB5HOT*A5;Vol_sol5:=totallength5*Pi*(Rwo^2-Rwi^2);totalweight_sol5:=evalf(8.89E3*evalf(Vol_sol5));
```

```
totalresistanceA6:=evalf(totallength6*0.0313/28.6);totalresistanceA6HOT:=evalf(totallength6*0.0363/28.6);totalresistanceB6:=(1.724E-8)*totallength6/(Pi*(Rwo^2-Rwi^2));totalresistanceB6HOT:=(1.16*1.724E-8)*totallength6/(Pi*(Rwo^2-Rwi^2));drivevoltageA6:=evalf(totalresistanceA6*A6);drivevoltageA6HOT:=evalf(totalresistanceA6HOT*A6);drivevoltageB6:=evalf(totalresistanceB6*A6);drivevoltageB6HOT:=evalf(totalresistanceB6HOT*A6);totalpowerA6:=drivevoltageA6*A6;totalpowerA6HOT:=drivevoltageA6HOT*A6;totalpowerB6:=drivevoltageB6*A6;totalpowerB5HOT:=drivevoltageB6HOT*A6;Vol_sol6:=totallength6*Pi*(Rwo^2-Rwi^2);totalweight_sol6:=evalf(8.89E3*evalf(Vol_sol6));
```

Net power dissipation in solenoid configuration

Using experimentally measured resistance:-

```
Net_powerA:=totalpowerA1+totalpowerA2+totalpowerA3+totalpowerA4+totalpowerA5+totalpowerA6;
Net_powerA_HOT:=totalpowerA1HOT+totalpowerA2HOT+totalpowerA3HOT+totalpowerA4HOT+totalpowerA5HOT+totalpowerA6HOT;
```

Using standard commercial OFC resistance:-

```
Net_powerB:=totalpowerB1+totalpowerB2+totalpowerB3+totalpowerB4+totalpowerB5+totalpowerB6;
Net_powerB_HOT:=totalpowerB1HOT+totalpowerB2HOT+totalpowerB3HOT+totalpowerB4HOT+totalpowerB5HOT+totalpowerB6HOT;
```

Net mass of copper in solenoid system

```
Totalweight_allsol:=totalweight_sol1+totalweight_sol2+totalweight_sol3+totalweight_sol4+totalweight_sol5+totalweight_sol6;
```

```
totallength:=totallength1+totallength2+totallength3+totallength4+totallength5+totallength6;
```

APPENDIX 3

Published papers & achievements

PUBLISHED PAPERS

KM Gillespie, DC Speirs, K Ronald, SL McConville, ‘3D PiC code simulations for a laboratory experimental investigation of Auroral Kilometric Radiation mechanisms’, Plasma Physics and Controlled Fusion, **50**, Art: 124038, 2008.

SL McConville, DC Speirs, K Ronald, ADR Phelps, AW Cross, R Bingham, CW Robertson, CG Whyte, W He, KM Gillespie et al, ‘Demonstration of auroral radio emission mechanisms by laboratory experiment’, Plasma Physics and Controlled Fusion, **50**, Art: 074010, 2008.

DC Speirs, SL McConville, KM Gillespie et al, ‘Numerical simulation of auroral cyclotron maser processes’, Plasma Physics and Controlled Fusion, **50**, Art: 074011, 2008.

K Ronald, DC Speirs, SL McConville, ADR Phelps, CW Robertson, CG Whyte, W He, KM Gillespie et al, ‘Radio frequency resonator structure and diagnostic measurements for a laboratory simulation of Auroral Kilometric Radiation’, Physics of Plasmas, **15**, Art: 056503, 2008.

K Ronald, SL McConville, DC Speirs, ADR Phelps, CW Robertson, CG Whyte, W He, KM Gillespie et al, ‘Electron Beam Measurements for a Laboratory Simulation of Auroral Kilometric Radiation’, Plasma Sources Sci. Technol., **17**, Art: 035011, 2008.

DC Speirs, K Ronald, SL McConville, KM Gillespie et al, ‘Numerical investigation of auroral cyclotron maser processes’, Physics of Plasmas, **17**, Art: 056501, 2010.

K Ronald, DC Speirs, SL McConville, KM Gillespie et al, ‘Auroral magnetospheric cyclotron emission processes: numerical and experimental simulations’, Plasma Physics and Controlled Fusion, **53**, Art: 074015, 2011.

RA Cairns, I Vorgul, R Bingham, K Ronald, DC Speirs, SL McConville, KM Gillespie et al, ‘Cyclotron maser radiation from inhomogeneous plasmas’, Physics of Plasmas, **18**, Art: 022902, 2011

I Vorgul, BJ Kellett, RA Cairns, R Bingham, K Ronald, DC Speirs, SL McConville, KM Gillespie et al, ‘Cyclotron maser emission - Stars, planets and laboratory’, Physics of Plasmas, **18**, Art: 056501, 2011.

SL McConville, ME Koepke, KM Gillespie et al, ‘Characterization of a Penning discharge for investigation of auroral radio wave generation mechanisms’, Plasma Physics and Controlled Fusion, **53**, Art: 124020, 2011.

DC Speirs, SL McConville, KM Gillespie et al, ‘Numerical simulations of unbounded cyclotron-maser emissions’, Journal of Plasma Physics, Vol **79**, (6), pp999-1001,2013.

ACHIEVEMENTS THROUGHOUT PhD

- Best student presentation, 3D PiC Modelling of a experiment to investigate Auroral Kilometric Radiation Mechanisms, 28th International Conference on Phenomena in Ionized Gases (ICPIG), International conference, Prague 2007.

- Best student oral presentation, PiC code Simulations of Auroral Kilometric Radiation Emission Mechanisms, University of Strathclyde, Physics Departmental Postgraduate Conference 2007.

- Certificate of achievement for poster presentation, 3D PiC code investigations of Auroral Kilometric Radiation mechanisms, 15th International Congress on Plasma Physics (ICPP), International conference, Chile 2010.

- Certificate of achievement for poster presentation, Numerical and laboratory studies of auroral cyclotron emission processes, National Astronomy Meeting (NAM), International conference, Manchester 2012.